Experimental Investigations of Correlated Electron Systems:

Alkali Fullerides and Sesquioxides

by

H. Esma Okur

Durham
University

A dissertation submitted to the University of Durham in fulfilment of the requirements for the award of the degree of Doctor of Philosophy.

February 2016

<u>Declaration</u>

I hereby declare that this thesis has not been submitted, either in the same or different form, to this or any other university for a degree.

Signature:

Acknowledgements

H. Esma Okur   **Durham University**   Degree: D. Phil

Abstract

Experimental investigations of correlated electron systems:

alkali fullerides and sesquioxides

The work reported in this thesis systematically investigates the structural, electronic and/or magnetic properties of fcc $A_xCs_{3-x}C_{60}$ fullerides (A = K and Rb) and of sesquioxide Cs_4O_6 under ambient and non-ambient temperature and pressure conditions, employing X-ray and neutron powder diffraction, muon spin relaxation, and SQUID magnetometry.

In the $A_xCs_{3-x}C_{60}$ alkali fullerides, unconventional superconductivity can emerge through tuning of intermolecular distances. While conventional BCS-like response is found in the underexpanded regime of the electronic phase diagram, significant deviations appear in the overexpanded region adjacent to the Mott boundary where strong electron correlations are prominent. In this work, the solid-state synthesis of fcc $K_xCs_{3-x}C_{60}$ ($0.12 \leq x \leq 2$) superconducting materials, with intermolecular distances controlled *via* adjusting the K^+/Cs^+ dopant ratio, is reported. Whilst the structural, electronic and magnetic properties of fcc $K_xCs_{3-x}C_{60}$ are reminiscent of those previously reported for fcc $Rb_xCs_{3-x}C_{60}$, *i.e.* the Mott boundary can be shifted to ambient pressure and the metal-insulator crossover temperature can be tuned by such chemical pressurisation of Cs_3C_{60}, cation-specific effects are of importance on the electronic properties of fcc $A_xCs_{3-x}C_{60}$. This work also provides strong evidence for correlated behaviour in the overexpanded regime through examining the presence or not of the Hebel-Slichter coherence peak and extracting the superconducting gap magnitude.

Crystallographically, the alkali sesquioxides A_4O_6 (A = Rb, Cs), at high and low temperature, had been reported to adopt a cubic structure which generates a single crystallographic position for dioxygen, implying charge disorder: $A_4(O_2^{(4/3)-})_3$. Conversely, spectroscopy studies at 5 K found evidence for two localized valence states of dioxygen, indicating charge ordering: $(A^+)_4(O_2^-)_2(O_2^{2-})$. This issue is addressed with the first systematic investigation of the temperature- and cooling-protocol-dependent structural evolution of Cs_4O_6, revealing the existence of a valence-ordered state at low temperature and also that valence disorder-order transitions can be induced by temperature, pressure and X-ray illumination.

CONTENTS

List of Figures

xiii

Chapter 1 Introduction

Correlated electron systems encompass a broad range of materials that show extraordinary physical phenomena such as metal-insulator transitions, anomalous metallicity, superconductivity and exotic forms of magnetism. Therefore this class of materials has aroused a lot of interest in modern condensed matter science. In particular, high-temperature unconventional superconductivity in highly correlated systems such as the cuprates has been at the centre of attention for three decades. The importance of correlated behaviour in producing the unconventional superconductivity in overexpanded molecular A_3C_{60} fulleride superconductors has been discovered only very recently. Various complex transition metal oxides exhibit different forms of magnetic interactions due to the correlations among the $3d$ electrons. In this class of materials, several degrees of freedom (spin, charge, lattice, and orbital) are simultaneously active and finely compete with each other leading to the emergence of important physical phenomena such as high-temperature superconductivity and colossal magnetoresistance. In addition to $3d$ systems, the correlations among $4f$ electrons can also lead to a wide variety of extraordinary physical phenomena such as superconductivity, heavy-fermion and mixed-valence behaviour, valence fluctuations, and charge disorder/order transitions. Recent experimental and theoretical studies conducted on the mixed-valence molecular sesquioxides have proposed the importance of electron-electron correlations, and the presence of strong coupling between the charge, orbital and spin degrees of freedom in open-shell p-electron systems as well.

This chapter will first summarise some key features of molecular and solid C_{60} (section 1.1), superconductivity in intercalated fullerides focusing on the alkali-metal-doped A_3C_{60} family, and early discoveries through to recent progress (section 1.2). Secondly, some key structural and magnetic properties of alkali oxides, focusing on the molecular sesquioxides, will be also summarised. Finally, an overview of the thesis contents will be presented.

1.1 Molecular and crystal structures of C_{60}

Fullerenes are the third allotropic form of pure carbon after graphite and diamond and take the form of hollow spheres, ellipsoids or tubes. The closed-cage carbon molecule C_{60}, the highly symmetrical and most stable member of the fullerene family, was discovered by Kroto *et al.* in 1985 by vapourizing a graphite target by laser irradiation [1]. Several years later, the discovery of a method for producing [2] and purifying [3], [4] significant quantities of bulk mixtures of fullerenes, especially the celebrated C_{60} molecule, has made research into the properties of fullerenes and their derivatives possible, and opened new fields of fullerene research in chemistry [5] and condensed matter-physics [6].

The C_{60} molecule consists of sixty carbon atoms located at the vertices of a truncated icosahedral structure (point group symmetry I_h), forming 32 faces; twelve pentagons and twenty hexagons. Whilst all carbon atoms are chemically equivalent, the structure contains thirty localised C-C double bonds fusing two hexagons (6:6 = 1.391 Å) and sixty C-C single bonds fusing a hexagon and a pentagon (6:5 = 1.455 Å) [7]. At room temperature, crystalline C_{60} adopts a face-centered cubic (fcc) structure (space group $Fm\bar{3}m$) with a lattice constant of 14.17(1) Å and a nearest neighbour centre-to-centre $C_{60} - C_{60}$ distance of 10.0 Å [8]. Solid-state ^{13}C NMR [9]–[12], quasi-elastic neutron scattering [13] and muon spin resonance studies (μSR) [14], [15] have shown that, at room temperature, individual C_{60} molecules rotate rapidly, resulting in time-averaging of the truncated icosahedron to a molecular unit with quasi-spherical symmetry. This reorientational motion is seen as orientational disorder in X-ray diffraction studies at room temperature [8]. However, the NMR spectra at low temperatures revealed that large-amplitude reorientations of C_{60} molecules become rare on the time scale of the NMR, which led to the question as to whether or not the C_{60} molecules order orientationally at low temperatures.

The temperature response of the C_{60} structure between 5 and 320 K revealed that there are 3 distinct regions; phase I (320 - 260 K), phase II (260 - 90 K) and phase III (90 - 5 K). In the phase I region, the C_{60} molecules rotate freely and nearly independently of each other. On cooling through 260 K, a first–order phase transition occurs from orientationally-disordered fcc (space group $Fm\bar{3}m$) to an

ordered primitive-cubic structure (space group $Pa\bar{3}$) [8], [16]. In phase II, there are two near-neighbour orientations which differ in the way electron-rich 6:6 bonds of one molecule are facing adjacent molecules – this can happen either to electron–poor pentagonal faces ('P') or to electron-rich hexagonal faces ('H'). The 'P' orientation is the one which is energetically favourable and is in the majority [17]. However, with further cooling below 90 K, in phase III, the C_{60} molecules can no longer flip between the two orientations leading to an orientational glassy phase. The relative ratio of the two orientations remains constant on further cooling to 5 K, with the major fraction of 'P' orientation invariant [16].

The closed-packed fcc C_{60} structure contains three interstitial cavities per C_{60} that are large enough to accommodate smaller atoms, ions or molecules as intercalants [18]. One site has octahedral (O_h) symmetry and a radius of 2.06 Å, larger than the size of any alkali ion. The other two cavities are smaller, with a radius of 1.12 Å and tetrahedral symmetry (T_d).

The electronic structure of C_{60} reveals that the lowest unoccupied molecular orbital (LUMO) is triply degenerate (t_{1u} symmetry), and the energy gap between the five-fold degenerate highest occupied molecular orbital (HOMO) and the LUMO is relatively small (~1.9 eV) [19], which makes the C_{60} molecule a good electron acceptor (Figure 1.1). The next unoccupied orbital (LUMO+1) is also triply degenerate (t_{1g}) and chemically accessible, with possible anion charges of up to 12 electrons.

Pristine C_{60} solid is a band insulator due to the fully occupied h_u and empty t_{1u} bands. However, a large variety of conducting compounds have been discovered by introducing electrons to the two empty t_{1u}- and/or t_{1g}-derived conduction bands, through chemical doping.
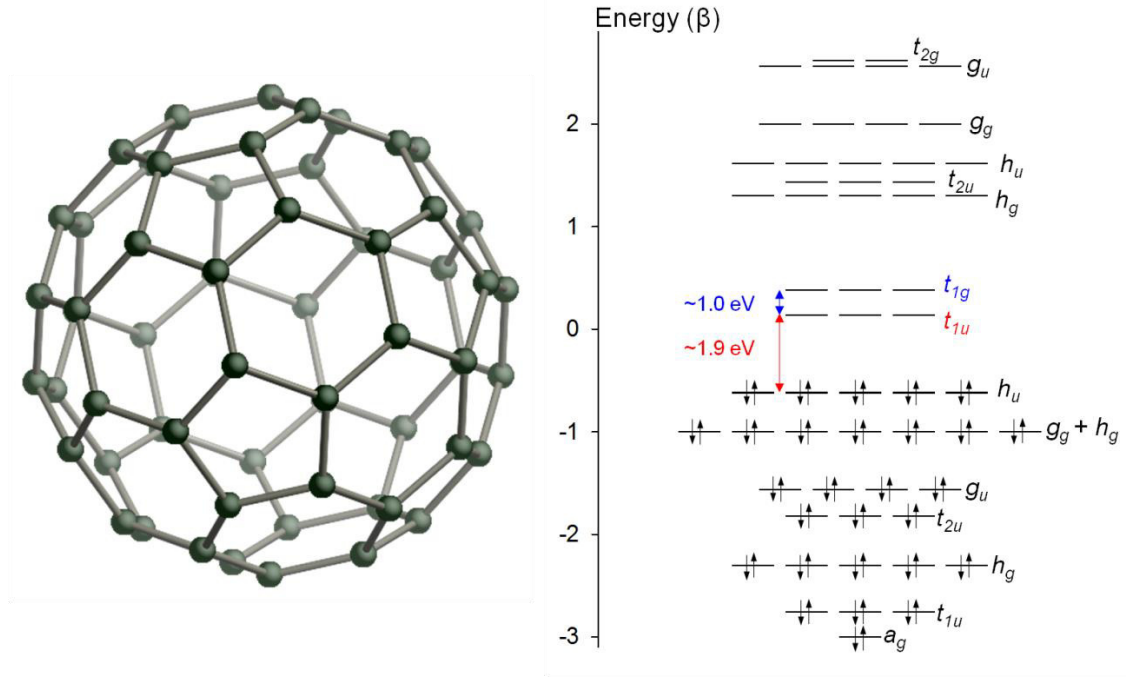
Figure 1.1 The C_{60} molecule (left) and its Hückel molecular orbital energy level scheme (right); adapted from ref. [20].

1.2 Superconductivity in intercalated fullerides

Metallic behaviour at 300 K was first observed by Haddon *et al.* in alkali-metal-doped Rb/C_{60} and K/C_{60} films [21]. Shortly afterwards, the first superconducting fulleride, K_3C_{60}, was discovered with a transition temperature, T_c, of 18 K [22], and the superconducting phase was later identified as an fcc-structured phase [23], [24]. This discovery was then followed by reported transition temperatures of 28 K [25] and 30 K for Rb_3C_{60} [23], 31 K for Rb_2CsC_{60} and 33 K for $RbCs_2C_{60}$ [26]. Ganin *et al.* reported the emergence of superconductivity in Cs_3C_{60} upon the application of hydrostatic pressure [27], [28]. Further superconducting compounds containing small alkali metals, *e.g.* $Na_2A_xC_{60}$ ($x \leq 1$, A = K, Rb, Cs) [29], [30] and Li_xCsC_{60} [31], and ammonia-containing compounds, *e.g.* $(NH_3)_4Na_2CsC_{60}$ [32], were also reported. The most-studied superconducting fullerides are those of the A_3C_{60} family (A = K, Rb, Cs or a combination thereof) in which the nominal electron count per C_{60} molecule (molecular valence), n, is three, leading to a half-filled t_{1u} band (t_{1u} superconducting fullerides).

Besides alkali-metal intercalation, the t_{1u}- and t_{1g}-derived bands can be accessed by alkaline-earth- and rare-earth-metal intercalation, which can lead to

higher molecular valence systems where the t_{1g}–derived band is partially filled. Several superconducting fulleride compounds, with $3 < n < 10$, were reported; $A_{3-x}Ba_xC_{60}$ (A = K, Rb, Cs) [33], Ca_xC_{60} ($x \sim 5$) [34], AE_4C_{60} (AE = Ba, Sr) [35], [36], $A_3Ba_3C_{60}$ (A = K, Rb) [37], [38] and $K_2Ba_4C_{60}$ [39]. The synthesis, structure and key magnetic and electronic properties of the A_3C_{60} fulleride superconductors, which are experimentally investigated in this work, are summarised in the following sections.

1.2.1 A_3C_{60} fullerides

The intercalated derivatives of fullerene solids (fullerides) exhibit different properties depending on the doping level, the nature of the dopant species and the way that the doping is employed. The synthetic technique employed in this work is exohedral doping, known as intercalation of dopant species into solid C_{60}. In this technique, the dopant occupies the interstitial holes in the sublattice which is formed by fullerene molecules in the solid crystalline C_{60}. Upon doping, if there is a charge transfer between the dopant and the host C_{60} acceptor molecules, the transferred electrons are delocalised over the molecular cage, resulting in the formation of C_{60}^{n-} molecular anions. If there is no charge transfer, they form clathrate compounds [40]. Intercalation of three alkali atoms donates three electrons per C_{60} to the t_{1u} band which leads to a half-filled t_{1u} band in A_3C_{60} fullerides and results in metallic behaviour, except for the overexpanded fulleride, Cs_3C_{60}. Structural studies of the single-phase superconducting A_3C_{60} compounds (A = K, Rb or a mixture) have confirmed that they adopt the cryolite-type fcc structure in which all T_d and O_h cavities are fully occupied by the alkali ions [41].

The size match between the O_h and T_d cavities and the alkali ions is important as it affects the structural properties of the A_3C_{60} compounds. For instance, the larger O_h cavity (r = 2.06 Å) can be intercalated with large alkali cations such as Cs^+ (r = 1.67 Å), Rb^+ (r = 1.52 Å) and K^+ (r = 1.38 Å), with a minor impact on the structure. However, the intercalation of larger cations into the T_d cavity (r = 1.12 Å) induces different structural behaviour, whereby the C_{60}^{3-} anions are no longer free to rotate and adopt a merohedrally-disordered structure even though the structure is still fcc. Merohedrally-disordered C_{60}^{3-} anions involve two equally-populated, randomly distributed molecular orientations which differ by a 90°

rotation about any twofold axis [24]. The merohedral disorder was found to be present at all accessible temperatures [42]. The merohedral disorder is either a dominant or a contributing factor to a number of the observed unique electronic properties of these systems. In contrast, when the T_d cavities are occupied by smaller ions, such as Na^+ or Li^+ as in Na_2CsC_{60}, the C_{60} ions continue to rotate. Such A_3C_{60} fullerides exhibit an analogous structural transition to that of the pristine C_{60}, undergoing a transition upon cooling from an orientationally-disordered high-temperature structure (space group $Fm\overline{3}m$) to an ordered primitive low-temperature cubic structure ($Pa\overline{3}$) [43].

Due to the smaller size of the T_d cavity, the lattice expansion (separation between C_{60} molecules) in A_3C_{60} fullerides directly relates to the size of the cation intercalated into the T_d site rather than the O_h site, and can be varied by systematically replacing the alkali dopants with larger alkali metals. Therefore, the most expanded member of the A_3C_{60} family is Cs_3C_{60}. In contrast to other A_3C_{60} compounds, Cs_3C_{60} has two distinct polymorphs (Figure 1.2); the so-called A15 structure based on body-centered-cubic (bcc) packing of orientationally-ordered C_{60}^{3-} anions [27], and fcc packing, which is isostructural to the less-expanded A_3C_{60} series (A = K, Rb, Cs or a combination) [28].
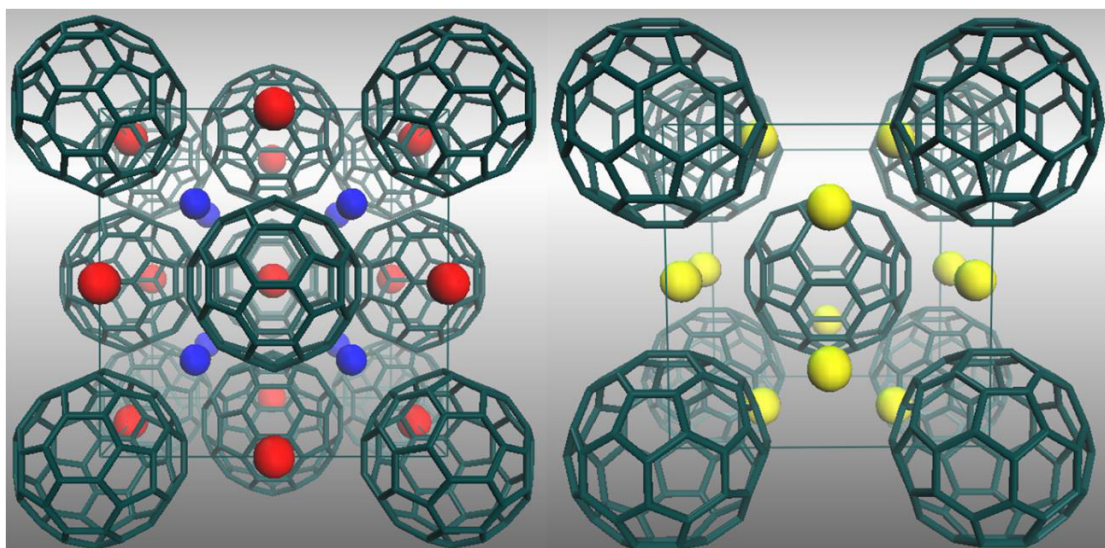
Figure 1.2 From left to right, schematic crystal structures of fcc A_3C_{60} and A15 Cs_3C_{60}. In the fcc structure, only one of the two C_{60} orientations is depicted for visual clarity, and octahedral and tetrahedral cations in the fcc A_3C_{60} are shown in red and blue, respectively.

1.2.2 Synthesis of alkali metal fullerides

Several synthetic routes have been developed to synthesise A_xC_{60} compounds, with x = 1, 3, 4 and 6 and A = K, Rb and Cs. In the case of smaller alkali metals, Na and Li, x can vary between 1 and 11. They can be prepared by exposing solid C_{60}, in the form of polycrystalline films, microcrystalline powder or single crystals, to alkali metal vapour, which diffuses into the host at temperatures of ~100 – 410°C; the reaction temperature varies with the dopant. All the A_xC_{60} compounds, except Cs_3C_{60}, can be prepared with this 'direct reaction method', including the intermetallic mixtures of these alkali metals, $A_xA'_{3-x}C_{60}$ [40]. Tanigaki and co-workers also used the direct reaction method (at 390°C) to synthesise $RbCs_2C_{60}$ [26]. Both alkali metals and A_xC_{60} solids are very air-sensitive; therefore, reactions must be undertaken in inert oxygen- and water vapour-free atmospheres.

The saturated A_6C_{60} (A = K, Rb, Cs) compounds can be prepared either with stoichiometric reagent amounts or with an excess of alkali metal. In this study, both ways were used to synthesise the K_6C_{60} and Cs_6C_{60} compounds which were used as precursors for further reactions with C_{60}. The A_6C_{60} compositions can be produced by a vapour-transport method, in which a temperature gradient is used to transfer the metal vapour to the C_{60}, and any excess unreacted metal is removed by reversing the temperature gradient upon cooling [44]. In this study, the vapour-transport method was employed for the synthesis of single-phase Cs_6C_{60} compounds, whereas the K_6C_{60} fullerides were synthesised using the direct reaction method. Finally, these compounds were used as precursors for the synthesis of $K_xCs_{3-x}C_{60}$ compounds ($0.12 \leq x \leq 2$).

In addition to the solid-state synthetic protocols, various solution-based routes have also been reported for producing alkali-metal fullerides. The first easily reproducible solution-based technique was described by Wang and co-workers for synthesising superconducting alkali metal fullerides from toluene, with T_c values of 18 K and 29 K for K_xC_{60} and Rb_xC_{60}, respectively [45], [46]. Several different protocols were then developed for alkali-metal intercalation using different solvents, such as liquid ammonia [47], [48], methylamine [49], [50] , THF [51], n-propylamine and n-butylamine [52].

Synthesis of the most expanded member of the A_3C_{60} family, Cs_3C_{60}, and more expanded fcc A_3C_{60} fullerides than $RbCs_2C_{60}$ using either conventional direct reactions or solution-based methods had failed. The reason for this failure can be traced to the thermodynamic instability associated with the introduction of the large Cs^+ cation (r = 1.67 Å) into the small tetrahedral hole (r = 1.12 Å). Due to this size mismatch, the compounds that are attempted to be synthesised disproportionate into CsC_{60} and Cs_4C_{60} phases. Dahlke *et al.* synthesised a series of fcc-rich compounds $A_xCs_{3-x}C_{60}$, where A is either Rb or K (0.3 ≤ x ≤ 1), using a liquid ammonia route, obtaining a wider range of compositions with higher fcc phase fractions than synthesis by solid-vapour reaction had allowed before. However, reducing the Rb content of the $Rb_xCs_{3-x}C_{60}$ phase to x < 0.32 to increase the interfullerene separation led only to smaller fcc phase fractions and to no increase in fcc unit cell volume, implying a higher fraction of Rb in the fcc phase than the nominal stoichiometry one, with CsC_{60} and Cs_4C_{60} also forming [53].

Kelty and co-workers reported superconductivity at ambient pressure in Cs_xC_{60} (x = 1.2 – 3) at T_c = 30 K with a low shielding fraction (~1%). They used binary alloys of CsM_x (M = Hg, Tl, Bi) as dopants due to their lower reactivity than pure Cs metal [54]. Several years later, Palstra *et al.* synthesised nominal Cs_3C_{60} using a liquid ammonia route, and reported superconductivity at 40 K with shielding fraction at the <0.1% level, under hydrostatic pressure of 15 kbar. However, the resultant materials were multi-phase and poorly crystalline which led to difficulties in the identification of the putative superconducting phases [55]. Until 2008, all attempts to synthesise bulk superconducting Cs_3C_{60} were unsuccessful, and the identification of the reported superconducting phases remained unresolved.

In 2008, Ganin *et al.* reported bulk superconductivity in A15 Cs_3C_{60} with a shielding fraction of 67% and a maximum T_c = 38 K at ~7 kbar. They employed a low-temperature solution-based technique, in which Cs metal or Cs_6C_{60} was reacted with C_{60} in methylamine at −65 °C followed by solvent removal under vacuum. The phase fraction of the superconducting A15 phase was reported as 77.7(6)%, and the remaining minor phases were identified as the fcc polymorph of Cs_3C_{60} and bco Cs_4C_{60} [27]. Soon after, fcc Cs_3C_{60} was also isolated in high yields of

up to 86%, with bulk superconductivity appearing under hydrostatic pressure with a maximum T_c of 35 K (the highest found in the fcc A_3C_{60} family) [28]. More recently, McLennan *et al.* reported a new solvent-based method for the synthesis of fcc-rich Cs_3C_{60} , involving THF together with an organometallic salt reducing agent [56].

1.2.3   BCS theory and its applicability for the A_3C_{60} superconductors

The classic mechanism of superconductivity, namely, the 'BCS' theory of superconductivity, was described by Bardeen, Cooper and Schrieffer in 1957 [57]. The essence of the BCS theory is the formation of 'Cooper pairs', which are bound pairs of electrons, condensed into an ordered state by interaction with each other, and with equal but opposite spin and angular momentum. The theory assumes that the only important energy difference between the normal and superconducting states arises from the formation and interaction of the Cooper pairs, and that the attractive interaction between the electrons is mediated by the phonons. Whilst an electron moves through a lattice of cations, it can distort the lattice around it by disturbing the motion of the cations; then, the positive ions create a cloud of increased positive charge density by crowding in on the electron. This cloud of positive charge in turn attracts a second electron resulting in the formation of the Cooper pairs, by overcoming the Coulomb repulsion of the first electron.

The Cooper pairs in a superconductor form a condensed state, act as bosons and occupy the same quantum state (the BCS ground state) which is separated by an energy gap from the excited states. The lowest quantum state is stable below an energy gap value of 2Δ (Δ = superconducting gap). The gap size of 2Δ, which is opened at the Fermi level, reflects the required energy for breaking up a Cooper pair, whereby two single electrons are produced in the lowest possible energy state just above the gap. When the Cooper pairs start breaking up at elevated temperatures due to the thermal fluctuations, the energy of the collective ground state is reduced because of the reduced number of the Cooper pairs, which results in a reduced superconducting gap value. Finally, the gap completely vanishes, the superconducting state is destroyed at T_c, and the material becomes a normal metal. Measurements of the superconducting gap and comparison of its value with that predicted by BCS theory are essential for researching whether the

superconductivity is driven by the electron-phonon interaction, the effective electron-electron attraction *via* the interaction of electrons with lattice vibrations.

The C_{60} molecule has discrete energy levels which are only weakly broadened in solid C_{60}, leading to a set of non-overlapping bands with a relatively narrow band width $W \simeq 0.5$ eV due to the relatively large distance between the nearest carbons of adjacent molecules (weak C_{60}-C_{60} interaction) [58], [59]. In A_3C_{60}, transferred electrons become delocalised due to overlapping of t_{1u} orbitals between neighbouring molecules. Since t_{1u} orbitals exhibit mostly p_z character, they radiate out from the C_{60} surface, resulting in non-negligible overlapping of t_{1u} orbitals.

C_{60} has intramolecular vibrations (phonons) with energies up to $\omega_{ph} \sim 0.2$ eV. In A_3C_{60}, only high-frequency phonons with H_g symmetry couple to the t_{1u} electrons [58]. It was reported very early that the superconductivity is driven by the coupling between these phonons and the t_{1u} electrons [60], whereas the other phonon modes, such as librations, C_{60}-C_{60} vibrations and alkali-C_{60} vibrations, play a minor role in the emergence of the superconductivity. However, it had also been argued that an electronic mechanism might drive the superconductivity [61]–[63].

In systems where the pairing is driven by a phonon-induced attraction, the Migdal-Eliashberg theory provides a method in which T_c can be estimated from the McMillan equation and formulated as a function of the electron-phonon and Coulomb interaction coupling constants, as follows [64]:

$$T_c = \left(\frac{\theta_D}{1.45}\right) \exp\left[\frac{-1.04(1+\lambda)}{\lambda - \mu^*(1+0.62\lambda)}\right] \qquad \text{Equation 1.1}$$

Here λ is the dimensionless electron-phonon coupling constant, μ^* is the Coulomb pseudopotential (effective Coulomb repulsion strength), and θ_D is the Debye temperature defining the characteristic phonon frequency, $\theta_D = \hbar\omega_D / k_B$. Estimates of the electron-phonon coupling constant in A_3C_{60}, $\lambda \simeq 0.5 - 1$, were found to be in the right range to explain the experimental T_c values with a BCS model [65].

Fleming *et al.* prepared a series of fcc A_3C_{60} (between K_3C_{60} and Rb_2CsC_{60}) superconductors and showed that T_c increases monotonically with the lattice

parameter. Extended Hückel band-structure calculations revealed that there is a monotonic increase in the density of states at the Fermi level, $N_{\varepsilon(F)}$, with increasing lattice parameter [41]. This increase in $N_{\varepsilon(F)}$ can be interpreted as resulting from a narrowing of the band at the Fermi level due to the weaker overlap between nearest-neighbour t_{1u} orbitals. Based on this explanation, the change in T_c with interfullerene spacing observed in A_3C_{60} fullerides was inferred using a BCS-type weak coupling relation [25]:

$$k_B T_c = \hbar\omega \exp[-\frac{1}{V \, N_{\varepsilon(F)}}]$$

<div align="right">Equation 1.2</div>

Here k_B is the Boltzmann constant, $\hbar\omega$ is the frequency of the pairing-mediating excitation, and V describes the extent of coupling between the lattice vibrations and the electrons. A wide variety of experimental work, including the measurement of the density of states at the Fermi level in K_3C_{60} and Rb_3C_{60}[25], was found to be in agreement with the BCS–like scaling of T_c with $N_{\varepsilon(F)}$.

Dahlke and co-workers reported that the variation of T_c with fcc lattice parameter in the series of overexpanded $Rb_xCs_{3-x}C_{60}$ ($0.32 \leq x \leq 1$) compounds shows an unexpected behaviour; T_c reaches a maximum at $x = 1$, then starts to decrease with lattice expansion [53]. In 2010, a significant breakthrough was achieved by Ganin and co-workers with the bulk synthesis and characterisation of the fcc superconducting polymorph of Cs_3C_{60} [28]. In contrast to all other reported fcc A_3C_{60} compounds (A = K, Rb, or a combination including Cs), fcc Cs_3C_{60} is a magnetic insulator at ambient pressure, becoming superconducting under applied pressure. The superconducting T_c initially increases with pressure, reaching a $T_{c(max.)}$ of 35 K (the highest found in the fcc A_3C_{60} family); this discovery then led to several intense theoretical debates concerning the applicability of the BCS theory and its derivatives for the more expanded members of the fcc A_3C_{60} family. Moreover, a non-BCS-like 'dome'-shaped scaling of T_c with pressure was also reported for the A15 superconducting polymorph of Cs_3C_{60} [28].

McDonald and co-workers extended the earlier work on $Rb_xCs_{3-x}C_{60}$ and synthesised high-quality Cs-rich superconducting samples covering the compositional range $0 \leq x \leq 0.5$ using a solid-state synthetic route. They reported that the superconducting T_c initially increases upon applying pressure in each of

these systems, reaches a maximum, and then decreases upon further pressurisation, forming 'dome' shapes ('$T_c(P)$ domes'), which contrasts sharply with the BCS-like monotonic scaling of T_c with pressure [66].

In a more recent study, a series of high-quality fcc-rich 'overexpanded' $Rb_xCs_{3-x}C_{60}$ samples were prepared with x systematically varied between 2 and 0.35. Bulk superconductivity was confirmed in all samples. Zadik *et al.* undertook extensive structural and magnetic characterisation of the series at both ambient and elevated pressures, and showed that the T_c responds sensitively to applied pressure, exhibiting distinct superconductivity $T_c(P)$ domes for all compositions except Rb_2CsC_{60}, which still shows a non-linear $T_c(P)$ response at low pressure (Figure 1.3) [67].
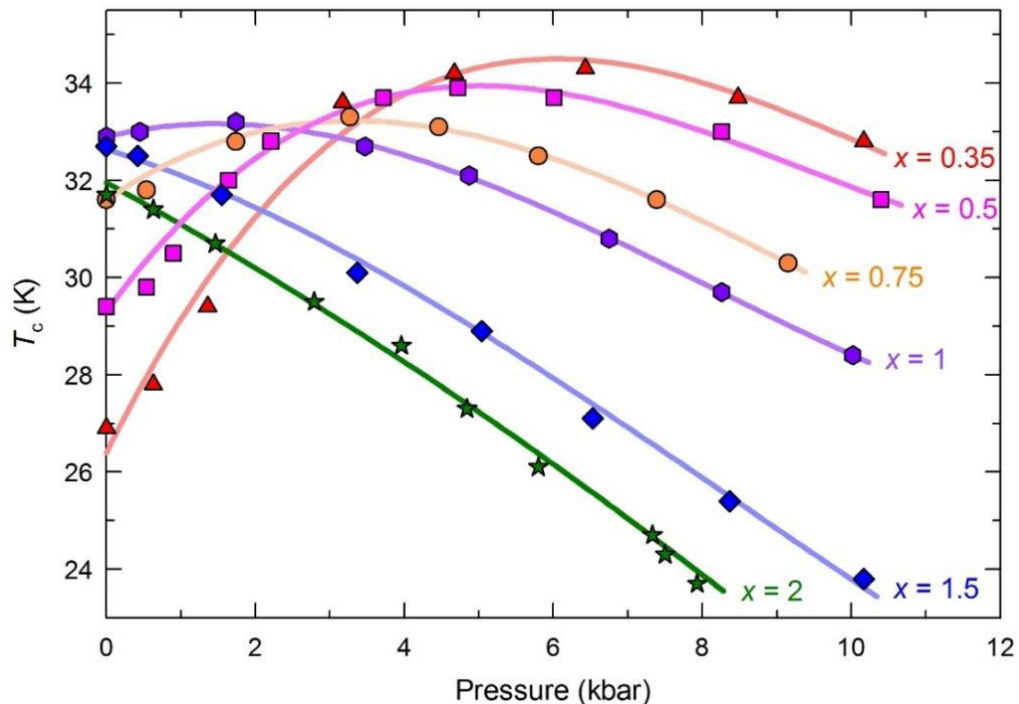
Figure 1.3 The variation of superconducting T_c with pressure for $Rb_xCs_{3-x}C_{60}$ ($0.35 \leq x \leq 2$). The lines through the data are guides to the eye. Datasets are from ref. [67].

Within the weak-coupling limit of BCS theory, the high-frequency intramolecular phonons ($\omega_{ph} \sim 1000\text{-}1600$ cm^{-1}) take part in the superconducting pairing mechanism [25], [41], [59]. On the other hand, the non-monotonic variation of T_c with interfulleride separation could have been explained if the electron-phonon coupling strength, V, changes from weak- to strong-coupling with increasing interfulleride separation. However, this would have necessitated a

switch-over from the involvement of the high to that of the low-frequency intermolecular phonons (ω_{ph} ~100 cm^{-1}) [68] in the pairing interaction [69] for overexpanded systems. This would have then implied that the high- and low-frequency phonons would be active in different parts of the electronic phase diagram. This is unlikely as the high-frequency phonon modes are always present and cannot be active only in one distinct region of the phase diagram, and also there is no obvious changes in the crystal and electronic structures [70]. As a result, the applicability of the conventional BCS-like explanation of superconductivity is questionable for overexpanded A_3C_{60} superconducting materials.

As mentioned previously, measurements of the superconducting gap and comparison of the values with predicted ones based on the BCS theory is a common way to investigate to what extent the BCS model is applicable for the A_3C_{60} superconductors. The BCS theory in the limit of weak coupling predicts that the reduced gap $2\Delta/k_BT_c$ has a material-independent BCS value of 3.52; larger experimental values would indicate strong coupling. Very early measurements of Δ for Rb_3C_{60} using STM yielded significantly larger $2\Delta/k_BT_c$ values of 5.3 [71] and 5.4 [72], indicating a broadened BCS-like density of states. More experiments have been employed to measure the gap for Rb_3C_{60} and K_3C_{60} superconductors using different techniques (such as NMR, μSR, optical measurements and photoemission), and $2\Delta/k_BT_c$ values obtained from those measurements have varied substantially, ranging from the BCS value to ~4.2 [58].

Kiefl *et al.* studied the temperature dependence of the longitudinal-field muon spin-relaxation rate, $1/T_1$, in the normal and superconducting states of Rb_3C_{60}, where endohedrally formed muonium ($Mu@C_{60}$) undergoes spin exchange scattering with electronic excitations. They reported that the temperature dependence of $1/T_1$ just below T_c fits the theory of Hebel and Slichter describing spin relaxation for a BCS-type superconductor. The gap for electronic excitations was found to be $\Delta/k_B = 53(4)$ K, corresponding to $2\Delta/k_BT_c = 3.6(3)$ ($T_c = 29.4$ K), in agreement with the prediction of the weak-coupling BCS limit [73].

MacFarlane and co-workers also performed μSR studies of Rb_3C_{60}, K_3C_{60} and Na_2CsC_{60} superconductors and observed the relaxation of $Mu@C_{60}$ in

longitudinally-applied magnetic fields. In metals, the Korringa mechanism is the expected spin-lattice relaxation mechanism in which $1/T_1 T$ is temperature independent. They showed that the temperature dependences of the relaxation rates exhibited Korringa behaviour above the T_c, and a small field-dependent 'Hebel-Slichter' coherence peak just below T_c (Figure 1.4). The reduced gap values were found to be in between 3.2 and 4, which are expected values for the less expanded A_3C_{60} fullerides [74].
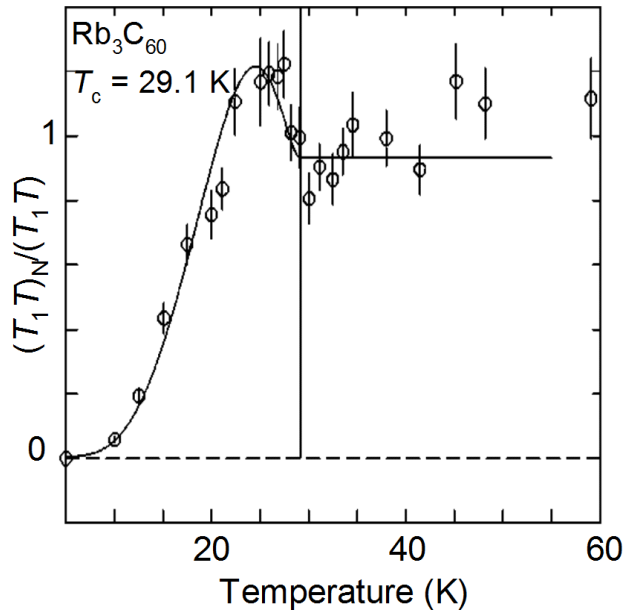
Figure 1.4 Temperature dependence of the spin-relaxation rate of Mu@C_{60} in fcc Rb_3C_{60} (copied from ref. [74]) at a field of 1.5 T. $1/T_1$ is normalised to the rate in the normal state just above T_c. Black solid line through data points is the fit to the Hebel-Slichter function. Solid vertical line mark the superconducting T_c.

Extensive experimental and theoretical investigations have indicated that the superconducting pairing in the family of A_3C_{60} fullerides is driven by a phonon-induced attraction, where electrons are paired in a pair-state of s-wave symmetry (observed in *e.g.* elemental metals), as predicted by the BCS theory [58]. However, the region between the well-explored conventional BCS-type superconductors (underexpanded A_3C_{60}) and the highly-expanded Cs_3C_{60} was not studied in any detail until the very recent extensive study of ref. [67] in which this unexplored region was investigated with fcc-rich $Rb_xCs_{3-x}C_{60}$ ($0.35 \leq x \leq 2$) materials. It has become increasingly clear that the electronic phase diagram of A_3C_{60} fulleride superconductors has similar features to those of other unconventional high-temperature superconductors; in the aforementioned study, the superconducting

14

gap increased with increasing unit cell volume, to values far higher than those predicted for the BCS weak-coupling limit [67], in agreement with the results of earlier high-pressure NMR studies on fcc and A15 Cs_3C_{60} polymorphs, examining the volume dependence of $2\Delta/k_BT_c$ [70], [75].

1.2.4 Strong electron correlations in A_3C_{60} fullerides

When two electrons are added to a C_{60} molecule, they will repel each other due to the Coulomb interaction. The magnitude of this on-site Coulomb interaction energy, the so-called Hubard U, can be obtained in different ways. U was calculated as $\simeq$ 3 eV using density functional theory for a free C_{60} molecule. Experimentally it was found to be $\simeq$ 3.3 eV [6]. For solid C_{60}, this large repulsive Coulomb interaction can be strongly screened by the polarisation of the surrounding molecules. Measurements of the on-site U in solid C_{60} ($U \simeq$ 1.6 eV) performed by Lof *et al.* using Auger spectroscopy on a K_3C_{60} film suggested that the ratios of U to the bandwidth (W), U/W, for doped C_{60} are comparable to those of high-T_c cuprates, and thus doped C_{60} should be considered as a highly correlated electron system [76].

The metal-insulator transition in a correlated system is usually discussed in terms of the U/W ratio [77]. Electrons in a solid containing ~1 electron per lattice site can lead to a Mott insulating state when the Coulomb repulsion U exceeds W (the one-particle bandwidth); in the contrasting case where $U/W <<$ 1, metallic behaviour is expected. When $U/W >>$ 1, the free motion of electrons is prevented by the large energy cost of having one site doubly-occupied, and thus electron localisation occurs. Therefore, a first-order metal-insulator transition occurs at a critical ratio of U/W close to 1*.*

U is a molecular property and remains essentially constant across the A_3C_{60} family, whereas W depends on the interfullerene separation, and therefore U/W increases with lattice expansion. Despite the fact that less expanded A_3C_{60} materials show relatively high values of U/W, they exhibit a metallic behaviour rather than the expected Mott-insulating behaviour. This results from the t_{1u} orbital degeneracy (the cubic symmetry retains the triple degeneracy of the t_{1u} orbitals) which allows additional hopping channels to the neighbouring molecules. As a result, the relevant bandwidth for the metal-insulator transition to occur is

smaller by a factor equal to the square root of the orbital degeneracy [78]. The boundary for the metal-insulator transition (MIT) therefore shifts to much higher values of the (U/W) ratio, and the metallic state survives. The frustration inherent in the fcc lattice can further stabilise the highly correlated metallic state by raising the critical ratio to even higher values, *i.e.* (U/W)$_c$ $\simeq$ 2.3, compared to non-frustrated topologies such as those based on bcc packing, with (U/W)$_c$ $\simeq$ 1.3 [79]. In summary, the high critical ratio for the fcc A_3C_{60} compounds results from a combination of orbital degeneracy and frustration effects.

With further band narrowing (increased interfullerene separation), a transition to a Mott insulating state due to electron localisation is expected. The parent compound Cs_3C_{60} should therefore be close to the Mott transition. Following the discovery of bulk superconductivity at 38 K in A15 Cs_3C_{60} [27], Takabayashi *et al.* reported that superconductivity emerges out of a localised electron antiferromagnetic Mott-Hubbard insulating state, with T_N = 46 K (at ambient pressure), with the application of pressure [80]. Soon after, superconductivity under moderate pressures ($T_{c(max.)}$ = 35 K) and Mott-Hubbard antiferromagnetic ordering below T_N = 2.2 K (at ambient pressure) in fcc Cs_3C_{60} was reported [28].

In spite of the structural differences between the two cubic Cs_3C_{60} polymorphs, T_c scales in a dome-like relationship, independently of structure, in proximity to the Mott metal-insulator transition [28]. This result demonstrates that the superconductivity of the A15 and fcc Cs_3C_{60} phases is identical in origin and implies that the strong electron-electron interactions responsible for the Mott state are likely to control the Mott metal-insulator transitions and also the superconducting states in both polymorphs [28], [80], [81]. These features of the Cs_3C_{60} polymorphs are characteristic of other high-temperature superconducting materials [82].

The icosahedral symmetry of the C_{60} molecule and strong electron-phonon coupling between C_{60} intramolecular phonons and t_{1u} electrons play another important role. The high molecular symmetry leads to a high degree of degeneracy in the electronic states, the origin of the Jahn-Teller (JT) effect [83]. The JT effect in a non-linear molecule with degenerate electronic levels removes this degeneracy

by distorting the molecule. A C_{60} molecule will have 180 total degrees of freedom, but the number of vibrational degrees of freedom is 174 (−3 translational and −3 rotational modes). Fortunately for symmetry reasons, only the highly symmetric A_g and the five-fold-degenerate H_g phonon modes can couple to the t_{1u} levels. However, only the H_g phonon modes can lead to JT distortion; the A_g modes do not lift the degeneracy due to their high symmetry [83].

When a vibration of H_g symmetry is excited, the three-fold degeneracy of the t_{1u} level is lifted (the t_{1u} level is no longer degenerate) which makes the C_{60} molecules unstable to the JT distortion [58]. The JT coupling of electrons to the H_g molecular vibrations near to the Mott transition in C_{60}^{3-} can reverse Hund's rule and favour a low-spin ($S = 1/2$) state [84]. Such a scenario has received strong support with the discovery of Cs_3C_{60} polymorphs that are Mott insulators at ambient conditions, with the C_{60}^{3-} ions in a low-spin ($S = 1/2$) electronic state [28], [80], [85].

Tunnelling between equivalent distortions can lead to pseudorotation which dynamically re-establishes the full icosahedral symmetry– this is the dynamic JT effect. This dynamical distorted state can therefore lead to a gap in the electronic spectrum and a maximally-paired electron configuration without any static lattice symmetry breaking [61]. The presence of the dynamic JT effect has been recently confirmed in fcc and A15 Cs_3C_{60} using infrared spectroscopy, defining the insulating state of both polymorphs as that of magnetic Mott-Jahn-Teller insulators [86] (MJTI, Figure 1.5 [67]). However, due to the rapid interconversion rate ($< 10^{11}\,s^{-1}$) between different conformations, the temporally- and spatially-averaged cubic crystal symmetry is still experimentally observed by diffraction, although the JT effect locally distorts the molecular C_{60}^{3-} ions [86].

A so-called 'new state of matter' - the unconventional correlated Jahn-Teller metal (JTM) [67] - has recently been reported in highly overexpanded $Rb_xCs_{3-x}C_{60}$ (e.g. $x = 0.35, 0.5$) that emerges upon compression from the MJTI state (Figure 1.5). It survives for a large part of the phase field until it gradually fades away into the normal metallic state. It was demonstrated that JT distortions can coexist with metallicity: in JTMs, the hopping electrons spent long enough on the molecular C_{60} units allowing the molecular JT distortions to be observed by IR spectroscopy,

leading to an inhomogeneous co-existence of localized JT active and itinerant electrons. Applying chemical pressure to the parent fcc Cs_3C_{60} phase (through substitution of the smaller Rb^+ for the Cs^+) first transforms the MJTI into the JTM. Subsequently, upon further decrease in intermolecular distances, a gradual disappearance of the localised features occurs and a conventional metal is encountered in Rb_2CsC_{60} and Rb_3C_{60} (Figure 1.5) – the molecular JT distortion is no longer discernible; the degeneracy of the t_{1u} levels and the symmetry of the C_{60} units are restored [67].
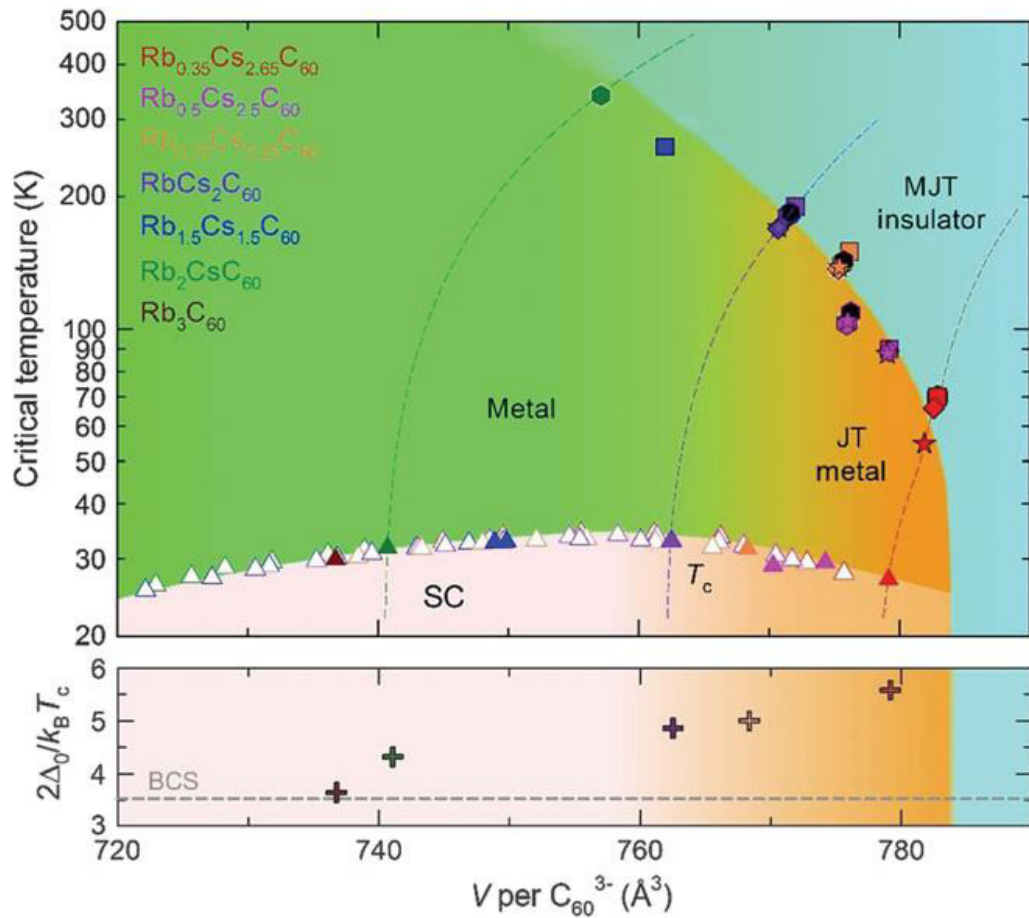
Figure 1.5 Electronic phase diagram of fcc $Rb_xCs_{3-x}C_{60}$ showing the evolution of T_c as a function of V (solid and unfilled triangles signify data collected at ambient and high pressures, respectively) and the MJTI-to-JTM crossover temperature, T' as a function of V (XRPD: squares; $\chi(T)$: stars; ^{13}C, [87]Rb and [133]Cs NMR spectroscopy: hexagons with white, color and black edges, respectively; IR spectroscopy: diamonds). Within the metallic (superconducting) regime, gradient shading from orange to green schematically illustrates the JTM to conventional metal (unconventional to weak-coupling BCS conventional superconductor) crossover. Dashed lines mark experimental $V(T)$ tracks for selected compositions. The lower panel shows the variation in superconducting gap divided by T_c, $2\Delta_0/k_BT_c$, with V (from ref. [67]).

To conclude, molecular features play an important role in producing the unconventional superconductivity forming from JTMs upon cooling in the overexpanded regime of the fcc A_3C_{60} fullerides. The boundary with the JTM directly affects superconductivity: although the s-wave nature of the superconducting gap is retained right across the entire V range extending from a conventional metal (Rb_3C_{60}) to highly overexpanded $Rb_xCs_{3-x}C_{60}$ (*e.g. x* = 0.35, 0.5), the superconducting gap increases monotonically with increasing interfullerene separation to values far higher than those predicted for the BCS weak-coupling limit ($2\Delta/k_BT_c$ = 5.6(2) for $Rb_{0.35}Cs_{2.65}C_{60}$; Figure 1.5 [67]), probed by NMR spectroscopy [67], [70] and [75]. As the JT effect fades away at small interfullerene separations, the size of the gap returns to the value characteristic for conventional BCS superconductors and conventional $N_{\varepsilon(F)}$ dependence of T_c reappears.

The recent findings about the electronic properties of A_3C_{60} fullerides close to the Mott insulator boundary discussed above are not consistent with the BCS phenomenology and imply the importance of electron-electron interactions. Thus they confirm the A_3C_{60} fullerides as members of the class of strongly correlated superconducting materials. In this work, additional findings will be presented on the structural and electronic properties of these systems, providing further evidence about the dominance of strong correlations in determining the unconventional superconductivity in overexpanded fcc A_3C_{60} fullerides.

1.3 Molecular alkali oxides

Solid dioxygen is an intriguing material in which *p*-electron-derived magnetic ordering occurs. It exhibits an AFM transition with T_N = 24 K [87], becomes metallic at room temperature at pressures above 95 GPa concurrently with the onset of a structural transition [88] and shows superconductivity with a T_c of 0.6 K at pressures around 100 GPa [89]. Materials containing dioxygen have attracted considerable research interest and many structural, optical, and magnetic studies of solid oxygen at high pressures have been reported [87], [90], [91].

The majority of magnetic materials involve systems incorporating transition or rare-earth metal ions with open *d*– or *f*– electron shells. However, comparative behaviour in *p*-electron systems is not widely observable and there is a limited number of examples of such materials known. In particular, materials containing

molecular oxygen in different oxidation states are particularly intriguing and typically magnetically active. This is associated with the presence of the doubly degenerate LUMO which for dioxygen is occupied by two electrons leading to a $S = 1$ ground state.

Reduction or oxidation of dioxygen, O_2, leads to ionic forms *via* the population or depopulation of the doubly-degenerate antibonding π^* molecular orbitals with one or two additional electrons. Figure 1.6 shows the molecular orbital diagrams of molecular oxygen and of the superoxide, O_2^-, and peroxide, O_2^{2-}, anions. The superoxide O_2^- anion contains a single unpaired spin and is therefore paramagnetic ($S = 1/2$). The O_2^- anion exists in the presence of low-valent, non-oxidizable and highly electropositive metal cations. The alkali superoxides, AO_2, where A = Na, K, Rb and Cs, are the best known examples [92]. They are orange-yellow in colour and are rare examples of magnetic materials where the magnetism is of *p*-orbital origin. On the other hand, the O_2^{2-} anion has an even number of electrons, 14, and is thus diamagnetic. In contrast to the alkali superoxides, the absence of colour is also a characteristic feature of diamagnetic alkali peroxides, A_2O_2 [92].
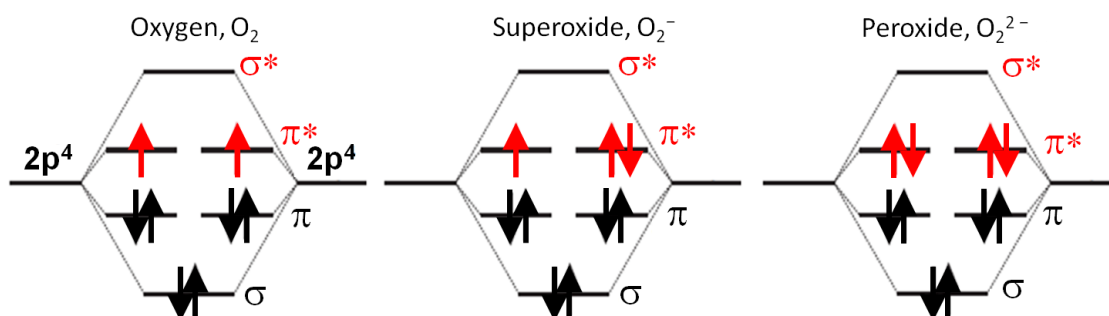
Figure 1.6 Molecular orbital diagrams of diatomic molecular oxygen ions

Among the alkali oxides, the black-coloured molecular sesquioxides with a composition of A_2O_3 fall into the *p*-electron mixed-valence systems with dioxygen in two different oxidation states. Electroneutrality considerations have led to the formulation of sesquioxides as $(A^+)_4(O_2^-)_2(O_2^{2-})$ (A = Rb and Cs), with three molecular anions per formula unit - one closed-shell non-magnetic O_2^{2-} anion and two open-shell magnetic O_2^- anions [93]–[95].

In alkali superoxides (AO_2), the relative orientations of the dioxygen anions play a crucial role in determining the adopted crystal structure and magnetic properties [92], [96]. The interactions between the superoxide units give rise to a series of crystallographic phase transitions on cooling, involving changes of the orientation pattern [97] and of the magnetic properties [98]. The structures of the different phases of the AO_2 compounds are described comprehensively in [92], [97] and [99]. The relative alignment of the O_2^- anions, as well as the state of partially-filled antibonding π^* molecular orbitals, yields a rich variety of magnetic properties of alkali superoxides. KO_2, RbO_2, and CsO_2 have been reported to be antiferromagnetic with T_N of 7, 15, and 9 K, respectively [92], [96].

1.3.1 Conflicting structural and magnetic properties of sesquioxides

Thermodynamically-stable alkali superoxides and sesquioxides can be synthesized using metals with large atomic numbers such as Rb and Cs, as the thermodynamic stability of the alkali oxides increases with atomic number [92]. The so-called sesquioxides Rb_4O_6 and Cs_4O_6 were first characterized by X-ray powder diffraction by Helms and Klemm in 1939 [93]. Both sesquioxides crystallize with the cubic anti-Th_3P_4 structure (the Pu_2C_3 structure was unknown at that time). In 1991, Jansen *et al.* performed X-ray diffraction on Rb_4O_6 single crystals and confirmed adoption of the cubic Pu_2C_3 structure (space group $I\overline{4}3d$) [94]. Elastic and inelastic neutron scattering have also been used to study the structure and excitations of Rb_4O_6 [95]. Neutron diffraction revealed that Rb_4O_6 is also isostructural to cubic Pu_2C_3. Moreover, it is stable down to 5 K, and no reduction of symmetry or ordering of the dioxygen anions takes place. In this structure, there is a single crystallographic position for both Rb^+ and oxygen. On the other hand, vibrational spectroscopy studies of Rb_4O_6 have revealed the existence of distinct O_2^{2-} and O_2^- anions. While dioxygen appears crystallographically single valent, spectroscopy has provided unambiguous evidence for two localized valence states of dioxygen [95], [100]. No crystallographic evidence has been found so far for two localized valence states of dioxygen in sesquioxides. Due to the single crystallographic position of oxygen in the cubic structure, only the presence of equivalent valency-delocalised $O_2^{(4/3)-}$

anions can be inferred, implying charge disorder and a general formula $Rb_4(O_2^{(4/3)})_3$.

The mixed-valency in the sesquioxides results in complicated magnetic response. Electronic structure calculations using the local spin-density approximation proposed half metallic ferromagnetism in Rb_4O_6 [101]; however, experimental investigation of the temperature-dependent magnetization of Rb_4O_6 has shown that it is a magnetically-frustrated insulator that exhibits spin-glass-like behaviour in a magnetic field. This peculiar behaviour was explained by a random charge ordering of the three charged dioxygen molecules in each formula unit [102]. Electronic structure calculations have also confirmed the insulating ground state with a large number of frustrated non-collinear magnetic configurations in Rb_4O_6. The magnetic order has been reported to be quite exotic, due to the existence of non-magnetic peroxide and magnetic superoxide anions that assemble in a frustrated antiferromagnetic configuration [103]. Frustrated magnetic ordering, which is of geometric origin and caused by the peculiar symmetry of A_4O_6, has also been proposed for Cs_4O_6 [100]. Magnetic and geometric frustrations are found often in d−electron systems, such as the spinel LiV_2O_4 [104] or the cubic vanadates [105]. However, in the case of the A_4O_6 compounds, the magnetic moment is carried by the p electrons of the anionic superoxide.

Recent experimental work by Arčon *et al.* has revealed intimate coupling between the charge, orbital and spin degrees of freedom in the sesquioxide Cs_4O_6 [106]. Two competing phases were discovered in the temperature evolution of the electron paramagnetic resonance (EPR) and [133]Cs NMR spectra: quenched high-temperature cubic and low−temperature low-symmetry phases. They reported that slow cooling leads to a transition to a low-symmetry orbitally-ordered structure; conversely, rapid cooling results in retention of the cubic structure. The two competing structures differ in the orientation of O_2^- anion axes, the ordering of π* molecular orbitals, and the superexchange interactions through the Cs^+ bridges. They stated that this orientational ordering of O_2 units, which is coupled to the orbital ordering, controls both the superexchange interactions through the Cs^+ bridges and the low-temperature magnetic properties of the two competing phases [106].

1.4 Outline of the thesis

The aim of this work is to systematically investigate the structural, electronic and magnetic properties of fcc $A_xCs_{3-x}C_{60}$ fullerides (A = K and Rb) across the superconductivity dome and of sesquioxide Cs_4O_6 under ambient and non-ambient temperature and pressure conditions. In Chapter 2, a wide variety of experimental characterisation techniques under ambient and non-ambient temperature and pressure conditions (X-ray and neutron powder diffraction, muon spin relaxation, and SQUID magnetometry) together with their theoretical aspects are outlined.

Chapter 3 is a comparative study focussing on the series of fcc $K_xCs_{3-x}C_{60}$ (0.12 ≤ x ≤ 2) superconductors which allow us to probe their electronic behaviour in a broad range of interfullerene separations extending from close to the Mott boundary, over the maximum of the dome and well into the underexpanded regime. It describes the evolution of their structural and magnetic properties at ambient and at elevated pressures and places them in the general context of our understanding of the rapidly-developing rich electronic phase diagram of fulleride superconductors. Connection of the two extremes (underexpanded and overexpanded regimes), of the electronic phase diagram, is achieved by hydrostatic and by 'chemical' pressure application through the adjustment of the alkali stoichiometry. Interfullerene spacing is also tuned by temperature. Tuning of interfullerene spacing allows us to balance the molecular and itinerant character of the electrons, leading to the highest known T_c among molecular superconductors.

Chapter 4 focuses on measurements of the temperature dependence of the longitudinal-field muon spin relaxation (LF-μSR) rate of endohedrally-formed muonium, Mu@C_{60} in superconducting fullerides. Observation of a 'Hebel-Slichter' coherence peak in underexpanded Rb_3C_{60} and K_3C_{60} had been taken as clear evidence of BCS-type superconductivity in the family of fcc A_3C_{60} fullerides. However, the critical region close to the Mott boundary as well as any compositions past the 'dome' maximum were not studied before. The work examines systems on either side of the 'superconductivity dome' and attempts to extract signatures of the importance of correlated behaviour through the search of the existence or not of the Hebel-Slichter coherence peak and the determination of the superconducting gap magnitude and its evolution with lattice spacing.

Chapter 5 describes the structural properties of the sesquioxide Cs_4O_6 and their evolution with temperature and pressure and under X-ray light illumination. It aims to resolve the conflicting reports on the structural properties of this material and establish the true crystallographic symmetry of the valence ordered state accessible by temperature and pressure. A valence order-disorder transition in Cs_4O_6, accompanied by a symmetry-lowering structural phase transition, is triggered under extreme experimental conditions. As the magnetic and molecular orderings are strongly coupled to each other, our findings shed new light on the magnetic behaviour of this family of materials.

Finally, Chapter 6 summarises the key results and contributions to knowledge arising from the present work, and proposes future directions.

Chapter 2 Instrumentation, theory and methodology

2.1 Introduction

The purpose of this chapter is to outline the experimental techniques and analysis methods which have been employed in the investigation of the structural, electronic and magnetic properties of the triply-doped fcc fullerides and the mixed-valence caesium sesquioxide, Cs_4O_6. Powder X-ray and neutron diffraction as a function of temperature, and of pressure, and muon spin relaxation techniques were employed in this extensive investigation. The magnetic properties of the samples were investigated using SQUID magnetometry at both ambient and high pressures. This chapter will detail the characterisation techniques together with relevant theoretical background. The synthetic part of the study will be presented in subsequent relevant chapters.

2.2 Powder Diffraction

Powder diffraction is the most widely used structural characterisation technique in solid state chemistry in situations where only polycrystalline samples are available. In 1916, the powder diffraction method using conventional X-ray sources was devised by Debye and Scherrer in Germany [107], [108]. The common applications of the technique such as phase identification, determination of the unit cell dimensions and the analysis of the structural imperfections were well established over the next half century. The applications of the technique peaked in the 1970s following the introduction of a powerful method for refining crystal structures from powder data by Rietveld in 1969 [109].

The Rietveld method has been extensively used since then to extract 3-dimensional structural information from 1-dimensional X-ray or neutron powder diffraction patterns. Over time, there has been a dramatic increase in diversity in the types of powder diffraction experiments being carried out, using X-rays from a laboratory generator or from a high-energy storage ring optimised for the generation of synchrotron radiation, or using neutrons produced in a reactor or a

spallation source. In this work, both X-ray and neutron scattering techniques were used.

2.2.1 Unit cell and crystal symmetry

The understanding of how atoms and molecules are arranged in space and how they form crystalline solids are essential to understand the diffraction technique and for the interpretation of the diffraction patterns. The presence of a systematic long-range order is a characteristic of a solid in the crystalline state, with atoms or molecules periodically arranged in space.

A crystal is made of repeating structural motifs whose locations are represented by points within a crystal lattice. Therefore, the entire crystal structure can be represented as a regular periodic array of points, which are known as lattice points, generated by translation of the unit cell. A unit cell is an imaginary parallelepiped within the crystal lattice, from which a complete crystal structure can be built using translational symmetry operations. In three dimensions, the unit cell has three sides: a, b and c and three angles between these pairs of sides: α, β and γ, which are termed as unit cell dimensions or lattice parameters. In crystallography, there are 7 different crystal systems defined by the geometry of the unit cells. The 7 crystal systems are: triclinic, monoclinic, hexagonal, trigonal, cubic, tetragonal and orthorhombic (Table 2.1). The unit cell can be primitive (P) or non-primitive. Whilst the term primitive designates when lattice points are only at each corner of the unit cell, non-primitive unit cells contain one extra lattice point either at the centre of each face (face centered (F)) or at the centre of each of two opposing faces (*e.g*. C centered) or at the centre of the unit cell (body centered (I)). This internal combination creates another additional 7 lattice types, resulting in a total of 14 types of lattices which are known as Bravais lattices [110].

In addition to the geometry, the distribution of the atoms in the repeating unit and the way that the unit cells build the crystal should be established using translational symmetry operations. A symmetry operation is an operation that does not make any difference in the appearance of the object operated. In crystallography, there are 4 different types of symmetry operations: rotation, reflection, inversion and translation. A symmetry element is a geometrical

26

visualization of one or more symmetry operations such as a rotation about an axis, a mirror reflection in a plane, an inversion through a point or a translation about a vector.

Table 2.1 The seven crystal systems

System	Axial lengths and angles	Number of Bravais lattices
Cubic	$a = b = c$, $\alpha = \beta = \gamma = 90°$	3
Tetragonal	$a = b \neq c$, $\alpha = \beta = \gamma = 90°$	2
Orthorhombic	$a \neq b \neq c$, $\alpha = \beta = \gamma = 90°$	4
Hexagonal	$a = b$, $\alpha = \beta = 90°$, $\gamma = 120°$	1
Trigonal	$a = b = c$, $\alpha = \beta = \gamma < 120°$, $\neq 90°$	1
Monoclinic	$a \neq b \neq c$, $\alpha = \gamma = 90°$, $\beta \neq 90°$	2
Triclinic	$a \neq b \neq c$, $\alpha \neq \beta \neq \gamma$	1

Combination of symmetry elements builds some complex symmetry elements. For example, simultaneous rotation/inversion and rotation/translation create an inversion axis and a screw axis, respectively. Combination of reflection/translation gives a glide plane. The Hermann-Mauguin notation is used to represent the symmetry elements in space groups, which are the description of given crystal structures and structure types. The characteristic assembly of symmetry operations is described by a point group, and in crystallography there are 32 crystallographic point groups that, when combined with the 14 Bravais lattices, lead to 230 different space groups. Space groups represent all possible distributions of atoms or molecules in the lattice to create the whole repeating unit cell that builds up the three-dimensional crystal structure through translational symmetry. More detailed information can be found in the *International tables for Crystallography, Volume A* [111] that contains lists of the equivalent positions for the 230 space groups.

2.2.2 Diffraction

Since the illustration of diffraction from crystals is difficult to visualise, 'lattice planes' which do not exist in real crystals are introduced to the

crystallography world. Lattice planes intersect lattice points and they are parallel to each other and equally spaced with every lattice point lying on one of the planes. The distance between the planes is known as *d*-spacing. Crystal lattice planes are described by Miller indices using three integers *h*, *k*, and *l*. Miller indices divide unit cell edges (*a*, *b* and *c*) into *h*, *k*, and *l* equal parts, respectively. If a plane is parallel to the *b*- and *c*- edge of the unit cell (no intercept on *b* and *c* axes), and intercepts the *a* axis at 1, the Miller indices of this plane are (100). The interplanar spacing for a particular set of planes, d_{hkl}, of a cubic unit cell with lattice parameter *a*, can be expressed as follows:

$$\frac{1}{(d_{hkl})^2} = \frac{(h^2 + k^2 + l^2)}{a^2} \qquad \text{Equation 2.1}$$

2.2.3 Reciprocal lattice and Ewald construction

A Bragg reflection is a radial distribution of the scattered intensity in reciprocal space where a diffraction pattern is collected. The concept of the reciprocal lattice was introduced by Ewald to present the physics of diffraction by a crystal [112]. The imaginary reciprocal lattice consists of points on a regular grid and each point is represented with a Miller index which corresponds to planes from which we imagine diffraction is occurring in so-called reciprocal space. The angular information of the Bragg reflections or spots can be transformed to a simple lattice in reciprocal space to relate the Bragg reflections and scattered intensity with the planes of the real space (direct) lattice. Each set of direct lattice planes is now a point in the reciprocal lattice carrying the same Miller indices as the corresponding direct lattice planes and the same symmetry with the direct lattice. The reciprocal lattice points are generated from the direct lattice and the conversions from one lattice to the other are defined as:

$$\mathbf{a}^* = \frac{\mathbf{b} \times \mathbf{c}}{V} \qquad \mathbf{b}^* = \frac{\mathbf{c} \times \mathbf{a}}{V} \qquad \mathbf{c}^* = \frac{\mathbf{a} \times \mathbf{b}}{V} \qquad \text{Equation 2.2}$$

with the inverse relationship of these two lattices given by:

$$\mathbf{a} = \frac{\mathbf{b}^* \times \mathbf{c}^*}{V^*} \qquad \mathbf{b} = \frac{\mathbf{c}^* \times \mathbf{a}^*}{V^*} \qquad \mathbf{c} = \frac{\mathbf{a}^* \times \mathbf{b}^*}{V^*} \qquad \text{Equation 2.3}$$

where **a**, **b**, **c** are the elementary translations of the direct lattice, and **a***, **b***, and **c*** are the elementary translations of the reciprocal lattice and defined as vectors. V and V^* are the volumes of the unit cell in the direct and reciprocal lattice, respectively [113].

The Ewald sphere concept is a convenient way to demonstrate the diffraction from reciprocal space. If a sphere is drawn around a crystal with a radius of $1/\lambda$ and positioned in such a way that Bragg's law (section 2.2.4) is satisfied, diffraction occurs whenever a reciprocal lattice point touches the surface of the Ewald sphere. Figure 2.1 demonstrates the Ewald sphere where O is the origin of the reciprocal space and P is a reciprocal lattice point (h, k, l), and $OP = $ **d*** is the reciprocal lattice vector which is perpendicular to the direct lattice plane and inversely proportional to d *via* the following relationship: **d*** $= 1/d_{hkl}$. The reciprocal lattice vector **d*** has to be equal to the scattering vector h to satisfy Bragg's law and so for diffraction to occur: $|h| = |s - s_0| = 1/d$, where S_0 and S signify the directions of propagation of the incident and scattered beam, respectively.
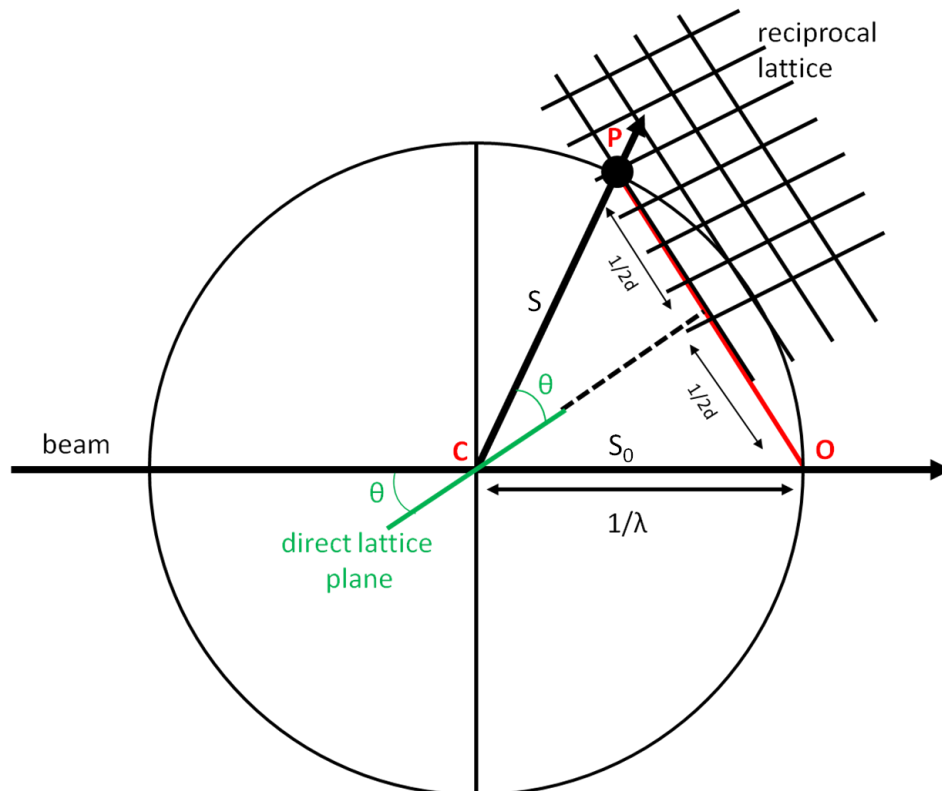
Figure 2.1 Two-dimensional representation of the Ewald sphere construction.

The orientation of the crystal reorients the reciprocal lattice which results in bringing different reciprocal lattice points on to the Ewald sphere surface. An ideal

polycrystalline sample contains individual crystallites which should orientate in all possible directions with equal probability. Therefore, all reciprocal lattice points become smeared out onto spherical shells that are centered at the origin of reciprocal space. These spherical shells intersect the surface of the Ewald sphere in circles. The circular intersections of these smeared reciprocal lattice points with the Ewald sphere in three dimensions generates co-axial cones, the so-called Debye-Scherrer cones [114].

The Debye-Scherrer cones appear as rings in the case of using a two dimensional detector, such as film or image plate, which is positioned perpendicular to the incident beam. The intensity around these rings is isotropic in an ideal powder, and thus the intensity of the rings will be uniform. If it is a grainy non-ideal powder, the ring intensity will not be uniform giving arbitrary intensities for the reflections in a one-dimensional cut (Bragg-Brentano geometry) through the rings. To remove granularity effects, the powder samples are generally rotated during the measurement.

The diameter of the Ewald sphere, $2/\lambda$, determines the lowest d-spacing reflections accessible in the experiment. The number of detectable reflections can be increased by decreasing the wavelength of the incident beam. In the case of an energy-dispersive experiment such as time-of-flight neutron powder diffraction, with no fixed wavelength but continuous distribution of wavelengths from λ_{min} to λ_{max}, all Debye-Scherrer cones can be detected [114].

2.2.4 Bragg's law

We can treat the lattice planes as mirrors which are periodically repeated, oriented to the incident beam at a specific angle and which reflect the incident beam. W. L. Bragg introduced a simple explanation of beam diffraction from a crystal; the incident beam is diffracted only at certain angles which are known as Bragg angles, θ, where constructive interference occurs and Bragg's law is satisfied. Figure 2.2 schematically demonstrates Bragg's law for reflection of incident waves from two lattice planes.
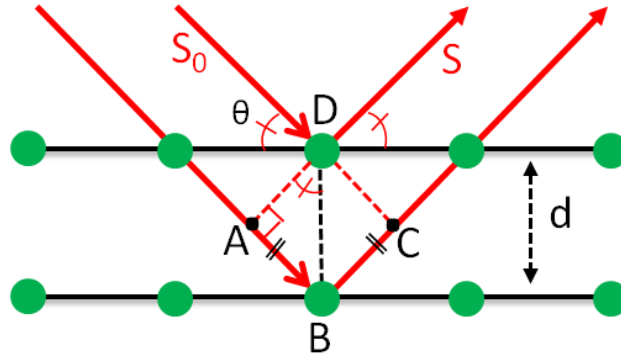
Figure 2.2 Schematic representation of the Bragg equation with reflection of two incident waves from two lattice planes belonging to the family of lattice planes with indices *h, k, l. d* is the interplanar spacing. S_0 and *S* signify the directions of propagation of the incident and scattered beam by the family of planes, respectively.

The difference in path between the scattered waves at B and D equals AB+BC=2*d*sinθ. Bragg's law states that the constructive interference occurs when the path difference is an integral multiple (*n*) of the wavelength (λ); *n* λ = 2*d* sin θ. The following expressions can be shown to relate the Ewald construction which satisfies the Bragg's law whilst diffraction takes place:

$$|h| \; = \; |s - s_0| \; = \; \frac{1}{d} \; = \; \frac{2 \; \sin \theta}{\lambda} \qquad\qquad \text{Equation 2.4}$$

and

$$|Q| = \frac{4 \; \pi \; \sin \theta}{\lambda} = \frac{2\pi}{d} \qquad\qquad \text{Equation 2.5}$$

The vector *Q* is the momentum transfer on scattering and differs from the scattering vector *h*, by a factor of 2π [114]. Powder diffraction data consists of a set of intensity values and is measured at a set of *Q* values which is stated as 2θ settings. They can also be collected with fixed 2θ whilst varying wavelength *e.g.* in time-of-flight neutron diffraction. The Bragg angle depends on d_{hkl} and the wavelength of the incident beam. X-rays and neutrons are widely used radiation sources in diffraction studies as their wavelength can be tuned to values similar to those of atomic distances (approximately 1 Å).

2.2.5 X-ray diffraction

In X-ray diffraction measurements, the incident X-rays are scattered by electrons in orbitals surrounding the atomic nucleus. A single electron scatters as a

point source. The scattering amplitude of an atom is proportional to the total number of core electrons in the atom. The scattering ability of different atoms as a function of $\sin \theta / \lambda$ is defined by the X-ray scattering factor f_0 [113]. The scattering amplitude from the unit cell is termed as the structure factor, F_{hkl}. The amplitude, $|F_{hkl}|$, is proportional to the square root of scattered intensity, I(hkl) as expressed by the following relation [115]:

$$|F_{hkl}|^2 = sI(hkl)$$ Equation 2.6

where s is a variable that is dependent on the sample and experimental setup, and can be expressed as follows:

$$s = \left(\frac{I_o \lambda^3 I_S}{8\pi r}\right) K_R\, K_G\, \frac{J_h}{V_c^2} L_p$$ Equation 2.7

I_0 = the intensity of the incident beam,

λ = the wavelength of the beam,

I_s = the height of the detector slit,

r = the distance between the sample and detector,

J_h = the multiplicity for reflection (hkl),

V_c = the unit cell volume,

L_p = the combination of the Lorentz and polarisation factors for the diffractometer geometry,

$K_R = (e^2/m_e c^2)^2$ where e and m_e are the charge and mass of an electron and c the speed of light,

$K_G = (1/8)\mu$ for X-ray Bragg-Brentano geometry (where the sample mount is tilted by an angle θ while the detector rotates by 2θ) and $K_G = V/4$ for X-ray Debye-Scherrer geometry (also known as transmission geometry where the sample rotates on an axis to minimise the effect of preferred orientation while the detector moves by 2θ), where μ is the linear absorption coefficient of the sample and V is the volume of the sample irradiated by the beam.

The structure factor can be defined as a Fourier series by summing over all atoms in the crystal structure as follows [115]:

$$F_{hkl} = \Sigma_i\, f_i\, e^{2\pi i(hx_i + ky_i + lz_i)}$$ Equation 2.8

where f_i is the X-ray scattering factor (or form factor) of atom-i, x_i, y_i and z_i are the fractional coordinates of atom-i in the unit cell and h, k and l are the Miller indices. The X-ray scattering factor, f can be given by the sum of $f_0 + f' + if''$ where f' and f'' are the real and imaginary components, respectively, of the anomalous scattering factor which depend on both atom type and the wavelength of the radiation source, and f_0 is the normal atomic scattering factor of the atom which is a function of $\sin\theta/\lambda$ [113].

In a real material, the atoms are not fixed within the crystal lattice but are in an oscillation about their average positions that depends on temperature. There will be an additional weakening of the scattering power of the atoms by the so-called Debye-Waller factor due to the thermal displacements of the atoms [114]. This Debye-Waller factor is angle-dependent and affects the high angle reflections substantially. The scattering amplitude decreases monotonically at higher diffraction angles at temperatures $T > 0$ K. These effects can be accounted for using the Debye-Waller equation [115]:

$$f = f_0\, e^{\left(\frac{-B\, sin^2\theta}{\lambda^2}\right)}$$

Equation 2.9

where f is the scattering factor under experimental conditions, f_0 is the scattering factor at 0 K, and B, the Debye-Waller factor, is defined as $B = 8\pi^2\langle u^2\rangle$. $\langle u^2\rangle$ signifies the mean square displacement of the atom from its equilibrium position. These displacements can be either isotropic or anisotropic. The anisotropic displacements are not the same in all directions giving an ellipsoidal distribution about their equilibrium position, with a 3 x 3 symmetric matrix: $\beta_{11}, \beta_{22}, \beta_{33}, \beta_{12}, \beta_{13}$ and β_{23}.

The number of electrons present in the atom determines the scattering power. Larger atoms that contain larger number of electrons give better scattering than that which have a small number of electrons; hence it is difficult to determine the atomic coordinates of those atoms with small atomic numbers, such as hydrogen, by this technique. While Equation 2.9 is expressed for an individual atom, it can be expanded to include all the atomic scattering factors for individual atoms in a unit cell containing n atoms and their Debye-Waller factors as follows [114]:

$$F_{hkl} = \sum_{i=1}^{n} f_i \, exp\left[-B_i \frac{sin^2 \theta}{\lambda^2}\right] exp[2\pi i(hx_i + ky_i + lz_i)]$$ Equation 2.10

where B_i is the Debye-Waller factor which accounts for the thermal motion of atom-i.

2.2.6 Neutron diffraction

Unlike X-rays, neutrons are predominantly scattered by the nuclei of atoms *via* the strong force. Since neutrons are spin-1/2 particles, for nuclei with spin, there is also an electromagnetic interaction between the neutron and the nucleus. The magnitude of this interaction depends on the spin state of the nucleus [116].

Whilst the X-ray scattering power of an atom is proportional to the total number of electrons, in the case of neutron diffraction, since the scattering process involves the interaction between the neutron and the atomic nucleus, the scattering power only depends on the nucleus itself. Therefore, neutron diffraction is the technique of choice to study light elements such as hydrogen, oxygen or lithium especially in the presence of heavier ones. Neutrons also interact with unpaired electrons *via* their spin and magnetic moments, which allows studying of magnetic order in a material.

When neutrons are concerned, the angular-independent term 'scattering length, b' is used rather than the angular-dependent form factor, f [114]. The scattering length measures the strength of the neutron–nucleus interaction. If a nucleus-j has a spin or different isotopes, b takes different values for different species. The mean value $\overline{b_j}$ for element j is called the coherent scattering length which is expressed in femtometers (1 fm = 10^{-15} m) [113]. The coherent scattering length is independent of the Bragg angle and the corresponding factors remain constant for any Bragg reflection. The area of each nucleus seen by a neutron is represented by the coherent cross section σ_c, and can be expressed as follows [117]:

$$\sigma_c = 4\pi\left(\overline{b_j}\right)^2$$ Equation 2.11

The sum of the corresponding macroscopic coherent σ_c, incoherent σ_i, and absorption σ_a cross sections gives the total cross section per unit volume with a unit of cm^{-1}. The neighbouring elements in the periodic table as well as isotopes

can have different scattering lengths and in some cases negative coherent scattering lengths are observed such as for Li, Ti and Mn, signifying that the neutron is subjected to an attractive potential of the nucleus rather than a repulsive potential. The best known form factors for X-rays and scattering lengths for neutrons of all chemical elements are listed for common isotopes and their naturally occurring mixtures (neutrons) and for neutral atoms and common ions (X-rays) in the *International tables for Crystallography, Volume C* [118].

There are two types of neutron diffraction methods based on determination either of wavelength using the Bragg condition for a single-crystal monochromator (constant wavelength neutron diffraction), or of velocity, measuring the time a neutron takes to travel a known distance (time-of-flight neutron diffraction) which differ according to the choice of the neutron source [114].

The monochromatic neutron diffraction technique is commonly used at a nuclear reactor source where a beam of neutrons with a constant wavelength is selected by a monochromator and directed toward a crystalline material. On the other hand, at a pulsed neutron source, a pulsed beam of neutrons with a wide spectrum of energies is directed toward a sample. Diffracted neutrons are recorded by sets of detector banks positioned at different fixed scattering angles. The energy and hence the wavelength of the diffracted neutrons is determined by recording the flight time at which each diffracted neutron arrives at the detector. In this work, the time-of-flight (tof) technique has been used for the neutron diffraction studies.

For the tof technique, the Bragg equation must be combined with the de Broglie relationship to extract the interplanar *d*-spacing values. The wavelength of a neutron is related to its momentum through the de Broglie relationship, which is expressed as $\lambda = h/mv$ where h is Planck's constant, m is the neutron mass and v is the neutron velocity defined as $v = L/t$, where L is the total flight path in metres and t is the time-of-flight measured in microseconds. The following relation is obtained between the time-of-flight and the *d*-spacing by combining the de Broglie and Bragg equations:

$$t = \frac{2mLdsin\theta}{h}$$ <div align="right">Equation 2.12</div>

The integrated intensity of a Bragg reflection in a tof neutron diffraction can be described as follows [119]:

$$I_{hkl} = cI_o(\lambda)\varepsilon(\lambda)\lambda^4 V_s A_{hkl}(\lambda) \times E_{hkl}(\lambda)j |F_{hkl}|^2 \frac{cos\theta\Delta\theta}{4V_c^2 sin^2\theta}$$ <div align="right">Equation 2.13</div>

where c is a normalising constant which is proportional to counting time, $I_o(\lambda)$ represents the incident neutron flux at wavelength λ, $\varepsilon(\lambda)$ symbolizes the detector efficiency at wavelength λ, $A_{hkl}(\lambda)$ is the attenuation coefficient for reflection hkl, $E_{hkl}(\lambda)$ represents the extinction coefficient for reflection hkl, V_s and V_c are the sample and unit cell volume, respectively, j represents the reflection multiplicity, F_{hkl} is the structure factor, and $\Delta\theta$ is the angular width of the detector.

2.2.7 Radiation sources

X-rays, a type of electromagnetic radiation, have wavelengths from ~0.1 to ~100 Å, between those of ɣ-radiation and ultraviolet rays. The most commonly used X-ray wavelength range in crystallography is ~0.1 - 5 Å (corresponding to ~125 – 2.5 keV), wavelengths of the same order of magnitude as the shortest interatomic distances observed in both organic and inorganic materials [116].

X-rays are generated using two different types of source. The first type, where X-rays are generated by bombarding a metal plate with high energy electrons, is termed a conventional X-ray tube. In X-ray tubes, a filament is heated to produce high energy electrons which are accelerated in a vacuum by a high electric field towards a metal target. After bombarding the metal plate, core electrons of the metal are excited to higher energy orbitals, and the energy of the relaxation of electrons is emitted as X-rays.

Two types of X-rays are emitted in this process: a continuous range of wavelengths knows as white (Bremsstrahlung) radiation, and characteristic radiation. White radiation is always emitted due to the collisions of the accelerated electrons with the core electrons of the metal atom. Characteristic radiation is obtained when the energy of the accelerated electrons is higher than a certain threshold value and it shows characteristic peaks. The energy of these

characteristic peaks depends on the metal target. After the collision, electrons from one of the inner electron shells of the metal atom are ejected. The ejected electrons are then replaced by electrons from a higher energy level which emit the energy difference of the two levels as X-rays with characteristic wavelengths. If the electrons fall into the K shell (n=1), the emitted X-rays are defined as K-radiation and are labelled K_α or K_β. Two transitions occur in the case of copper. One is a transition from 2p to 1s which produces radiation labelled as $K_{\alpha1}$ = 1.5406 Å and $K_{\alpha2}$ = 1.5443 Å due to the splitting of the 2p orbitals in copper. The second one is a transition from 3p to 1s, labelled as K_β = 1.3922 Å. Monochromators are used to filter out the undesired X-ray wavelength [113], [116].

The second type of X-ray source is generated at synchrotron radiation facilities where the electromagnetic radiation is emitted by charged particles in circular orbits tuneable to a wide range of wavelengths (10^3 - 10^{-1} Å). Today, so-called third generation synchrotron radiation facilities are in operation. Their brilliance (the measure of the quality of the source) exceeds the conventional X-ray sources by nearly ten orders of magnitude. In this study, third generation synchrotron sources were used for the X-ray diffraction experiments. Basic fundamentals of each of the different synchrotron facilities will be addressed separately in a different section.

Neutrons are uncharged subatomic spin-1/2 particles with mass 1,839 times that of an electron, and as previously mentioned they are produced either from nuclear reactor sources (*e.g.* the Institute Laue Langevin, ILL) or pulsed (spallation) neutron sources (*e.g.* ISIS Rutherford Appleton Laboratory). At a nuclear reactor, neutrons are produced by the fission of ^{235}U nuclei. The average energy of the generated neutrons in a reactor after each fission event is approximately 190 MeV which causes the neutrons to be very fast. Since only slow neutrons can be captured by a ^{235}U nucleus the generated fast neutrons must be slowed down by a moderator to increase their capture probability in reactors. During the moderation process, the fast neutrons are slowed down and they gain a wavelength suitable for neutron diffraction experiments. The neutrons after the moderation process, named thermal neutrons, have a kinetic energy of about 0.025 eV. Nuclear reactors produce continuous neutron beams with a wide range

of neutron wavelengths. Therefore, a produced neutron beam must be monochromated to narrow the range of neutron wavelengths for most of neutron diffraction experiments. This results in loss of flux from the source which is one of the biggest disadvantages of the reactor-based neutron sources. This problem is resolved in the new generation of highly intense pulsed (spallation) neutron sources.

In a pulsed (accelerator-based) neutron source, bunches of protons are accelerated to high energies in a particle accelerator and then each bunch of protons is released as a pulse to bombard a heavy metal target such as uranium, tantalum or tungsten, where spallation occurs. High energy neutrons are produced after the collision of each proton with the nuclei in the target. High energy neutrons are then slowed down by a moderator. At the end of the process a pulsed neutron flux is generated, which is an ideal source for the tof neutron diffraction technique as there is no need to use a monochromator for this technique. As a result the loss of the flux is removed [113], [116], [117]. The final flux obtained for the tof diffraction experiments is $\sim 10^2$ times higher, with shorter wavelength neutrons, than that produced in a reactor source, even though the raw flux produced by a reactor is higher than a pulsed neutron source. This allows the spallation source diffractometers to measure very small d-spacings without reaching the 'sinθ limit'. The smallest d-spacing with constant wavelength diffractometers is limited to $d_{min} = \lambda/2$, assuming that the detector can be positioned at 2θ = 180°.

2.3 Powder Diffraction Data Analysis

2.3.1 The Rietveld method

All collected X-ray and neutron powder diffraction data were analysed using the Rietveld refinement technique, which was first devised for the analysis of neutron diffraction data at fixed wavelength by Hugo Rietveld [109], then extended later for conventional X-ray and synchrotron X-ray diffraction data.

In the Rietveld method, an initially proposed starting structural model is fitted to the X-ray or neutron powder diffraction data. It is a least squares algorithm-based technique to optimise the fit between the observed data points

and a calculated diffraction pattern by adjusting parameters of the model and instrument, which is used for the data collection. This method is used for a variety of purposes including refining crystal structures, determining the crystallite sizes in samples, calculating the amount of disorder and quantitatively determining the percentages of different phases in samples [120], [121].

The Rietveld refinement technique was performed in this work using a set of programs known as General Structure Analysis System (GSAS) which is written in the FORTRAN language. Since it is difficult to view various options and the refined parameters, a graphical user interface (GUI) was used. EXPGUI is a GUI to GSAS and provides many useful utilities for viewing fits and refinement results, and applying different profile functions (depending on factors such as the features of the beam and the diffractometer) [122].

2.3.2 Peak intensity calculation

The Rietveld technique uses the entire diffraction pattern rather than separating it into a set of integrated intensities for each of the Bragg reflections. The reflection contributions are corrected for all geometric and sample dependent factors and the calculated intensity, y_c, at position $2\theta_i$ in the diffraction pattern can be described as:

$$y_c(2\theta_i) = y_b(2\theta_i) + s \sum_k j_k \ (LP)AA_sP_k|F_k|^2\Phi_k(2\theta_i - 2\theta_k) \qquad \text{Equation 2.14}$$

where y_b is the background intensity, s is a scale factor, j_k is the multiplicity factor, LP are the Lorentz and polarisation factors, A is the attenuation coefficient, A_s is an asymmetry correction factor, P_k is the preferred orientation correction, F_k is the structure factor and $\Phi_k(2\theta_i - 2\theta_k)$ is a reference to the peak shape profile function [120].

A residual function (M), is generated to fulfil the principle of the Rietveld refinement to minimise the difference between the calculated and observed diffraction pattern intensities. During the refinement, the residual function is minimised by adjusting the calculated pattern as follows [123]:

$$M = \sum_{2\theta_i} w_i \ (y_o(2\theta_i) - y_c(2\theta_i))^2 \qquad \text{Equation 2.15}$$

where $y_o(2\theta_i)$ is the observed intensity at position $2\theta_i$, and w_i is a statistical weighting function which is expressed as:

$$w_i = \frac{1}{y_o{}^t(2\theta_i)} \qquad \text{Equation 2.16}$$

where $y_o{}^t(2\theta_i)$ is the total intensity measured which is the sum of the observed intensity, $y_o(2\theta_i)$, and the background intensity, $y_b(2\theta_i)$, at position $2\theta_i$.

2.3.3 Peak shape determination

The shape of the observed peaks depends on the measured sample (domain size, defects, and stress/strain) and the settings of the instrument (the radiation source, geometry and slit sizes), which change as a function of 2θ. This complex dependence requires a complex peak shape function rather than using a simple Gaussian profile, and thus several functions are employed to model the peak shape over the whole range of diffraction angles for which data were collected [123]–[126].

In the case of using a constant wavelength X-ray beam, a complex function is applied to model the peak shape known as the pseudo-Voigt which is a combination by addition of Gaussian and Lorentzian functions [126]. The relation between the Gaussian and Lorentzian functions and the pseudo-Voigt function, $\Phi_k(2\theta_i - 2\theta_k)$ ($2\theta_k$ is the calculated position of the Bragg peak) can be expressed with the following relation [124], [125]:

$$\Phi_k(2\theta_i - 2\theta_k) = \eta \cdot L(2\theta, H_L) + (1 - \eta).\,G(2\theta, H_G) \qquad \text{Equation 2.17}$$

$$G(2\theta) = \frac{2}{H_G}\left[\frac{ln2}{\pi}\right]^{\frac{1}{2}} exp\left(\frac{-4ln2}{H_G{}^2}(2\theta - 2\theta_B)^2\right) \qquad \text{Equation 2.18}$$

$$L(2\theta) = \frac{2}{\pi H_L}\left(1 + \frac{4(\sqrt{2} - 1)}{H_L{}^2}(2\theta - 2\theta_B)^2\right)^{-1} \qquad \text{Equation 2.19}$$

where η is the mixing parameter defining the ratio of the peak shape between a Gaussian (where η = 0) and a Lorentzian (where η = 1) function, 2θ is the scattering angle, and $2\theta_B$ is the Bragg angle. H_G and H_L represent the full width at half of the maximum peak height (FWHM) of the Gaussian and Lorentzian peaks, which show angular dependences and can be expressed as [126]:

$$H_G = \left[U \tan^2 \theta + V \tan \theta + W + \frac{P}{\cos^2 \theta} \right]^{\frac{1}{2}} \qquad \text{Equation 2.20}$$

$$H_L = X \tan \theta + \frac{Y}{\cos \theta} \qquad \text{Equation 2.21}$$

where *U, V, W* and *P* are Gaussian, and *X* and *Y* are Lorentzian peak shape parameters which should be treated as adjustable variables in the refinement.

In this work, the analysis of the CW X-ray diffraction patterns was carried out using 'profile function 3 in GSAS' which includes both Gaussian and Lorentzian peak shape parameters (*GU, GV, GW, GP, LX* and *LY*) and some other parameters related with the diffractometer and sample used for the data collection. Low angle peak asymmetry (arising from axial divergence) can be modelled in GSAS by adjusting or refining the profile terms; in CW profile function 3, these are *S/L* and *H/L* where *L* is the diffractometer radius, *H* and *S* are the sample and detectors heights, respectively [127]. Ideally, these two terms should be fixed for a specific diffractometer; however, they can be refined if low angle peaks are present.

Another profile term included in profile function 3 is transparency, *trns*, which describes the X-ray penetration depth into a flat plate sample in Bragg-Brentano (reflection) geometry. However, since all my samples were measured in a Debye-Scherrer (transmission) geometry, the '*trns*' term was not refined during the analysis and kept at zero. In addition to those, two more parameters can be included for an accurate determination of the peak shape function; an anisotropy coefficient, *stec*, to define the Lorentzian broadening of the peaks, and strain broadening effects, *ptec* [127]. These two peak shape broadening terms were not needed to be refined and kept at zero. Apart from those, another term, '*shft*', can be included in the analysis to describe vertical displacement of a flat plate sample in Bragg-Brentano geometry. Instead of the '*shft*' option, a different term can be used

for the both geometries which is known as the 'ZERO' term which describes any shift (error) in the absolute 2θ = 0 position for the data and is measured in units of centidegrees.

In order to fit the peak shape of the tof neutron diffraction patterns, diffractometer constants to calculate the time-of-flight positions of the Bragg reflections must be known. There are three diffractometer constants, DIFC, DIFA and ZERO, which are determined by fitting the data collected from a standard sample during the calibration process and are given in an instrument parameter file. DIFC describes the relation between the total flight path, *L*, *d*-spacing and scattering angle, 2θ, of a detector. It should be kept in mind that DIFC varies from one detector bank to another due to the different scattering angles of detector banks. In general, DIFC is not refined and remains fixed, however in situations where both low and high resolution histograms obtained from different detector banks are present, DIFC can be refined. DIFA is sample-dependent and used to introduce small corrections to the expected time-of-flight of a reflection to allow peaks to shift due to absorption in the sample. ZERO is only instrument-dependent, thus it should not be refined and accounts for small differences between the various timing signals in the ISIS accelerator and the instrument data acquisition system [128].

The peak shape of the tof neutron diffraction pattern is modelled using the pseudo-Voigt function. The FWHM values of which are expressed in GSAS differently from those of the CW X-ray profile functions. The widths of the reflections using the Gaussian (Equation 2.22) and Lorentzian (Equation 2.23) parts of the pseudo-Voigt function can be modelled as:

$$\sigma^2 = \sigma_0{}^2 + \sigma_1{}^2 d^2 + \sigma_2{}^2 d^4 \qquad \text{Equation 2.22}$$

$$\gamma = \gamma_0 + \gamma_1 d + \gamma_2 d^2 + (\gamma_{1e} d + \gamma_{2e} d^2) \cos \emptyset \qquad \text{Equation 2.23}$$

where σ_0, σ_1, and σ_2 are Gaussian and γ_0, γ_1 and γ_2 are Lorentzian peak profile parameters. The equations above show that the width of a reflection is proportional to its *d*-spacing. However, in some cases where anisotropic line broadening is present, this profile function might not provide a satisfactory fit for

the peak shape. In such cases other profile functions provided in GSAS should be considered. Further information can be found in the GSAS manual [127].

2.3.4 Background determination

The background scattering originates from various sources depending on the material studied (amorphous and disordered phases, fluoresced X-rays, thermal diffuse scattering caused by lattice thermal vibrations, scattering of X-rays from air) and on the instrument itself (detector noise, misalignment of the incident and divergence slits, thickness and material of the sample holder). In this work, due to the air sensitivity of samples, glass capillaries were used as sample holders, and hence a contribution to the background from the amorphous glass is observed.

There are two ways to deal with the background contribution. It can be either estimated by selecting a number of baseline points away from the Bragg peaks in the pattern and then applying a linear interpolation between these points or it can be modelled by an empirical or semiempirical function which contains several refinable background coefficients. Since the background contribution arises from several different factors and appears differently from one diffraction pattern to another, GSAS provides eight different functions for modelling different types of background contributions [127].

Fitting of the background and the refinement of the background coefficients should be performed properly because there is always a strong correlation between the determination of the background and other parameters such as Debye-Waller displacement factors, peak shape and zero-point error. Therefore, in the early stage of the refinement procedure only a linear interpolation should be applied between the selected points without refining the background coefficients and then the unit cell parameters, peak shape and profile parameters can be refined. Once a reasonable starting model has been obtained, the background coefficients, Debye-Waller displacement factors and zero error can be refined, otherwise the refinement procedure results in a wrong starting model with incorrect parameters which can hinder the convergence process.

2.3.5 Reliability of Rietveld refinement

In Rietveld analysis, the least squares algorithm minimizes the differences between the observed and calculated diffraction profiles. In GSAS, the agreement between the two different profiles is quantified by the R-factors listed in the .LST file which is written and updated after each cycle of the refinements. The most straightforward discrepancy term is the weighted profile R-factor, R_{wp} which is defined as follows [120]:

$$R_{wp}^2 = \left[\frac{\sum_{2\theta_i} w_i |y_o(2\theta_i) - y_c(2\theta_i)|^2}{\sum_{2\theta_i} w_i |y_o(2\theta_i)|^2} \right] \qquad \text{Equation 2.24}$$

where $y_o(2\theta_i)$ and $y_c(2\theta_i)$ are the observed and calculated intensity at position $2\theta_i$, and w_i is a statistical weighting function.

If the calculated model is the best possible model that can ever be obtained for a given set of data, the best possible R_{wp} value can be obtained which is termed as the *expected R*-factor. The R_{exp} reflects the statistical quality of the data and the number of variables used in the refinement, and described as:

$$R_{exp}^2 = \left(\frac{N - P + C}{\sum_{2\theta_i} w_i |y_o(2\theta_i)|^2} \right) \qquad \text{Equation 2.25}$$

where N is the number of observations, P is the number of parameters refined, and C is the number of constraints applied to the model.

Another related statistical term is the agreement χ^2 factor, which can be calculated using the following equation [129]:

$$\chi^2 = \left(\frac{R_{wp}}{R_{exp}} \right)^2 = \frac{\sum_{2\theta_i} |y_o(2\theta_i) - y_c(2\theta_i)|^2}{(N - P + C)} \qquad \text{Equation 2.26}$$

If the calculated model is ideal and the standard uncertainties are correct, χ^2 approaches 1. A value of $\chi^2 < 1$ generally indicates that there are more parameters in the model than justifiable by the quality of the data [129]. Thereby for the accuracy of the refinement model the χ^2 should be monitored during the refinement procedure.

2.3.6 Modelling volume compression and thermal expansion

Volume Compression

Unit cell parameters vary systematically with temperature and pressure, and a number of approaches have been developed to parameterize these changes which relate to volume compression and thermal expansion. The study of the temperature and pressure response of materials presented in this work, with Rietveld analysis, enabled changes in unit cell volume to be extracted. Thus, the changes in electronic and magnetic properties were parameterized as a function of temperature or pressure obtained through other techniques in terms of the unit cell volume.

When pressure, P, is applied on a volume, V, the work done, W, is given by the expression $W = -P \Delta V$, resulting in negative ΔV in all materials under compression. The magnitude of these changes is directly related to interatomic forces, and hence an analysis of structural changes with pressure might reveal much about these interatomic forces [130].

The bulk modulus, K, is an important parameter, used to describe the stiffness of a solid, which relates the change of volume with P. The variation of the volume of a solid with pressure, at constant temperature can be described as follows:

$$K = -\frac{V \delta P}{\delta V}$$

Equation 2.27

Measured EoS are usually parameterized in terms of the values of the bulk modulus, and its pressure derivatives, evaluated at zero pressure [131]. These zero-pressure moduli are normally denoted by a subscript '0' such as K_0 or K'_0.

'Equations of state' (EoS) can be used to define the elastic relationship of volume to intensive variables, and hence enables the compressibility behaviour of solids to be described. Different assumptions can be made about how K changes with P, or how V varies with P. Unlike 'ideal gases,' there is no absolute thermodynamic basis for specifying the correct form of the EoS of solids. Commonly used EoS are established on various assumptions; however the validity of these can only be evaluated by considering whether the EoS can be successfully

applied to the experimental data. In this work, the Murnaghan and Birch-Murnaghan EoS were employed to extract the compressibility behaviour of the studied materials from the isothermal P-V data sets.

The Murnaghan EoS is based on the supposition that K varies linearly with pressure ($K = K_0 + K'_0 P$). Integration yields the following equation at constant temperature [132]:

$$P = \frac{K_0}{K'_0}\left[\left(\frac{V_0}{V}\right)^{K'_0} - 1\right]$$

<div align="right">Equation 2.28</div>

where V_0 is the volume at 'zero-pressure' and K'_0 is the pressure derivative of K_0. The Murnaghan EoS yields correct values of the room pressure bulk modulus for compressions up to about 10% (*i.e.* $V/V_0 > 0.9$), and has the advantage of algebraic simplicity.

The Birch-Murnaghan EoS is a finite strain EoS and assumes that the strain energy of a compressed solid can be described as a Taylor series in the Eulerian finite strain, f_E, defined as follows [133]:

$$f_E = \frac{(V_0/V)^{\frac{2}{3}} - 1}{2}$$

<div align="right">Equation 2.29</div>

The third-order Birch-Murnaghan EoS was employed using the following expression:

$$P = 3K_0 f_E (1 + 2f_E)^{\frac{5}{2}}\left[1 + \frac{3}{2}(K'_0 - 4)f_E\right]$$

<div align="right">Equation 2.30</div>

Thermal expansion

The addition of heat to an ionic crystal increases the energy of the crystal, principally in the form of lattice vibrations or phonons. If ionic bonds are treated as classical harmonic oscillators, the principal calculated effect of temperature is just increased vibration amplitude, resulting in breakage of bonds at high temperature due to extreme amplitudes. However, in real crystals, the purely harmonic model of atomic vibrations is not adequate to explain many properties of crystals. The equilibrium bond length does not change in the harmonic model, which leads to zero thermal expansion. Ideally, anharmonic vibration terms should

be employed in any analysis of the effect of temperature on crystal structure as its consequences include thermal expansion, and hence the change in equilibrium bond distance with temperature [130].

To interpolate the variations of lattice parameters over a temperature range, a method described by Sayetat and co-workers, which combines the early methodology of the Debye model for specific heat and the Grüneisen theory of the thermal expansion of solids, is used. Using this method, any eventual thermal anomalies, which may arise due to a phase transition or valency ordering/disordering can be shown, and phonon contributions from the thermal expansion curves of the lattice parameters can be extracted [134]. In this work, these curves were investigated using X-ray and neutron powder diffraction techniques over a temperature range.

According to Grüneisen's empirical law, thermal expansion coefficient, α, is described by the following relation:

$$\alpha = \gamma \frac{C_V K}{V} \qquad\qquad \text{Equation 2.31}$$

where γ is the anharmonic Grüneisen parameter which describes the effect that changing the volume of a crystal lattice, V, has on its vibrational characteristics. K symbolises the isothermal compressibility and C_V defines the specific heat at constant volume, which is expressed as:

$$C_V = C_V^{\text{lat}} + \sum_i C_V^i \qquad\qquad \text{Equation 2.32}$$

where C_V^{lat} describes the phonon contribution to the specific heat and C_V^i symbolises the additional contributions *e.g.* magnetic and electronic. Thus, using this model, once the modelled phonon contributions are subtracted, extra contributions to the thermal expansion can be extracted [134]. Grüneisen's empirical law states that when the phonons are the only contribution to the specific heat at constant volume, the thermal expansion of the crystal volume can be written as follows:

$$V \simeq V_0 \left(1 + K\,\gamma \int_0^T \frac{C_V^{\text{lat}}}{V}\,\mathrm{d}T \right) \qquad\qquad \text{Equation 2.33}$$

where V_0 is the crystal volume at 0 K.

The Debye model is a method developed by Peter Debye in 1912 to estimate the phonon contribution to the specific heat in a solid (specific heat and thermal expansion are correlated data) [135]. Debye's model describes the variation of C_V^{lat} with temperature, T as follows:

$$C_V^{\text{lat}} = (\delta/\delta T)\left[9k_B NrT(T/\theta_D)^3 \int_0^{\theta_{D/T}} \frac{x^3}{e^x - 1}\, dx\right]$$

Equation 2.34

where N is the number of primitive cells in the crystal, and r is the number of atoms in the polyatomic basis [134]. In the Debye approximation, γ can be defined as follows:

$$\gamma = -\left(\frac{\delta \ln \omega_D}{\delta \ln V}\right)$$

Equation 2.35

where ω_D is the Debye frequency, defining the maximum frequency of the crystal lattice vibrations of the crystal ($\omega_D \propto v_s/a$, v_s is the sound velocity, a is the crystal lattice constant), related to the characteristic Debye temperature, θ_D, as follows:

$$\theta_D = \frac{\hbar\omega_D}{k_B}$$

Equation 2.36

k_B and $\hbar$ are the Boltzmann and reduced Planck constants, respectively [134].

A combination of Equations 2.33 and 2.34 provides the simplest theoretical description of the lattice thermal expansion:

$$V \simeq V_0 + I_V T \varphi\left(\frac{\theta_D}{T}\right)$$

Equation 2.37

where $I_V = 3k_B rK\gamma$, and φ is the Thacher's approximate function of (θ_D/T). The coefficients of the function φ, expanded to the fourth power in T, are given in Sayetat et al [134]. Equation 2.37 is used to fit the experimental temperature dependence of the crystal volume with least-squares refinement of the θ_D, γ, and V_0.

2.4   µSR Spectroscopy

µSR stands for muon spin 'rotation', or 'relaxation', or 'resonance', depending on how the method is being used, or simply muon spin research, and has been extensively used to probe a wide range of phenomena in condensed matter and molecular science such as magnetic ordering, superconductivity and defects in

semiconductors [136]–[139]. Basically, μSR monitors the time evolution of the spin polarisation of implanted positive, spin-polarised muons into a sample of interest by detection of positrons emitted after the asymmetric decay of muons. A brief summary of the properties, production, implantation and decay of muons is included in this section.

2.4.1 Muon production, implantation and decay

A muon is an unstable elementary particle produced by the decay of pions; it decays to a positron, e^+ and two neutrinos, and has a life time of 2.2 μs [136]. While both charge states of muons exist, in the μSR technique mostly positive muons, μ^+, are employed. The positive muon can be treated as a light proton with a mass one ninth that of the proton and a spin of $^1/_2$. The success of the μSR technique relies on two circumstances: the intrinsic polarisation of the muons during their production from pions: $\pi^+ \rightarrow \mu^+ + \nu_\mu$ and the anisotropy of the positron emission in their subsequent decay to positrons and neutrinos: $\mu^+ \rightarrow e^+ + \overline{\nu}_e + \nu_\mu$ [136]. Positive pions, π^+ (lifetime 26 ns) are generated when a graphite target is bombarded with high energy proton beams. Muons are also present in cosmic rays but with lower intensities.

The lifetime of muons is long enough to be collected and delivered to the muon instruments where they are implanted in the samples. Since muons are charged particles, they are collected and delivered to beamlines by dipole and quadrupole magnets [35]. In this work, the ISIS pulsed muon source, which serves four μSR instruments with excellent data rates for time-resolved μSR studies, was used.

The high spin polarisation of the muon beam is provided by the beamline magnets which are tuned to select muons of a particular momentum to make their spins almost fully aligned along the beam direction. Even during the implantation, the polarisation of the muon beam is preserved close to 100% regardless of sample temperature or applied magnetic fields, which differs from typical magnetic resonance experiments that depend on the temperature and magnetic field, and the initial spin polarisation of the latter is not as high as that of the μSR technique [140].

As mentioned above, muons decay to positrons and neutrinos. These positrons are emitted preferentially in the direction of the muon spin at the moment of decay. As a result, the observation of decay positrons (asymmetric decay of muons) enables the direction of the spin to be monitored and displayed as a function of time following implantation inside the sample. In other words we detect the decay positrons, not muons themselves, which stop and decay inside the samples of interest. Once the muons have been implanted inside any material (in solid, liquid or gas form), since the muons are very sensitive to their magnetic environment thanks to their magnetic moments, a magnetic interaction arises between the muon spins and local magnetic fields. This magnetic interaction is the primary source of information in µSR and renders the muons an excellent probe of frustrated or weakly-magnetic systems [141]–[144].

2.4.2   µ$^+$ in matter

The implanted muons that have very high energy are slowed down to thermal energies on the nanosecond timescale while the initial polarisation is mostly preserved. The way that µ$^+$ interacts with its surroundings depends on the physical state and chemical properties of the material in which the muons are implanted. In certain materials during the slowing down process, a fraction of the muons can pick up an electron to form muonium, Mu (µ$^+$ e$^-$) that can be treated as a light isotope of hydrogen, as the mass of Mu is one ninth that of hydrogen and the chemical properties are similar to that of hydrogen. Muonium atoms can exist in three different states; a free (vacuum) muonium atomic state, muonium-containing free radicals (RMu·) in which muonium reacts with organic molecules due to its unpaired electron, leading to paramagnetic states, and finally a diamagnetic state where there is no interaction [138], [145]–[147]. While µSR is applied for the characterisation of a large variety of materials using different instruments and techniques, in this section, only the technique for the measurement of muon spin relaxation 'T_1' in A_3C_{60} fullerides in longitudinal fields is included, being the experimental µSR technique employed in this work.

2.4.3 Longitudinal Field Muon Spin Relaxation

Longitudinal Field Muon Spin Relaxation (LF-µSR) involves the application of an external magnetic field parallel to the initial direction of the muon spin polarisation, and the measurements of the time evolution of the muon polarisation along its original direction. Since the applied field is longitudinal in the absence of competing local fields within the samples, the muons are implanted in a stationary spin state and their initial polarisation preserved. The time evolution of the polarisation is known as relaxation function [136].

When muons are implanted in A_3C_{60} fullerides, a muonium atom is trapped inside the C_{60} cage, denoted as $Mu@C_{60}$ [148]. The spin exchange interactions with electronic excitations open a relaxation pathway for the muon spin in $Mu@C_{60}$ [73]. The muon spin relaxation of the endohedrally-formed muonium in A_3C_{60} fullerides shows up in longitudinal fields. The LF-µSR studies were performed using a high field muon spectrometer (HiFi) which is designed for measurements in longitudinal fields up to 5 Tesla. At HiFi, only 10-20% of muons form muonium inside the C_{60} cage, others implant elsewhere exohedrally in the structure [74]. A typical instrumental setup for the LF-µSR studies is depicted in Figure 2.3. The same setup can be also used for experiments in the absence of an external field, known as Zero Field Muon Spin Relaxation (ZF-µSR). The polarized muon beam goes through the hole in the backward positron detector then stops in the sample. The asymmetric decay of muons gives different counts at the forward and backward counters. If there is a relaxation of the muon spin polarisation, the counting rate of the two detectors will change with time. Conversely, in the absence of any relaxation, the ratio between the forward and backward detectors stays constant and does not change with time.
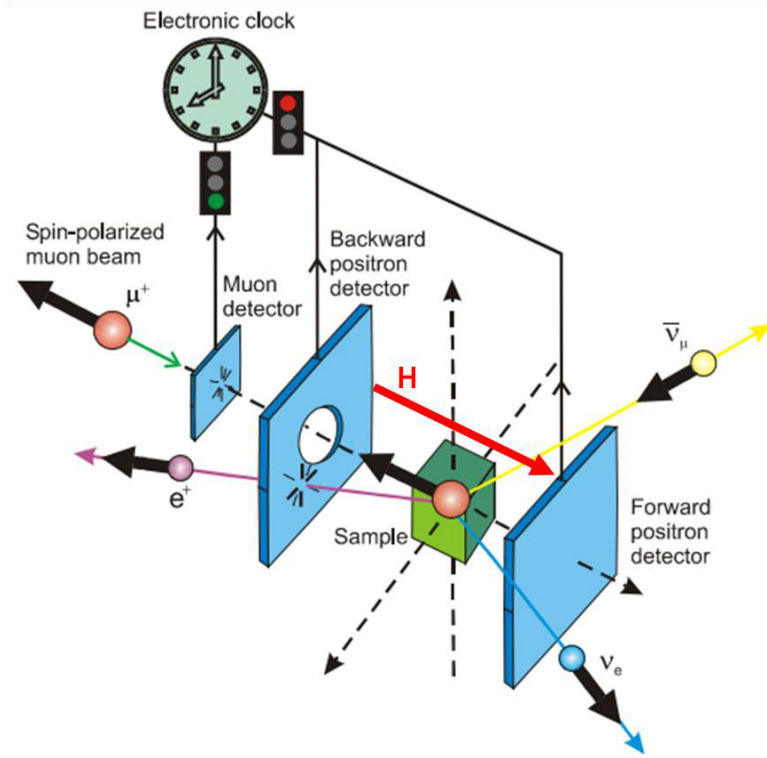
Figure 2.3 Schematic diagram of a LF-µSR set up, copied from ref. [149].

When a free muonium atom which is a two-spin-$^1/_2$ system like hydrogen is formed in its 1s ground state, the muon spin interacts with that of the single bound electron leading to a large isotropic hyperfine interaction (also known as Fermi or contact interaction) between the muon and single bound electron which results in a multitude of spin states. For an isotropic muonium in its electronic ground state, the hyperfine spin Hamiltonian can be expressed as [74], [150]:

$$H/_h = \gamma_e \, S_e \cdot B \; + \; \gamma_\mu \, S_\mu \cdot B \; + A_\mu \, S_e \cdot S_\mu \qquad \text{Equation 2.38}$$

where γ_e and γ_μ are the gyromagnetic ratios (the ratio of its magnetic dipole moment to its angular momentum) of the electron and muon, A_μ is the isotropic hyperfine coupling constant (hfcc) of Mu (A_μ = 4.46 GHz and A_H = 1.42 GHz) which is proportional to the unpaired spin density at the nucleus, S_e and S_μ are the electron and muon spins and B is the applied magnetic induction. This Hamiltonian provides the field dependence of the hyperfine energy levels which is shown in a Breit-Rabi diagram in Figure 2.4 [74].
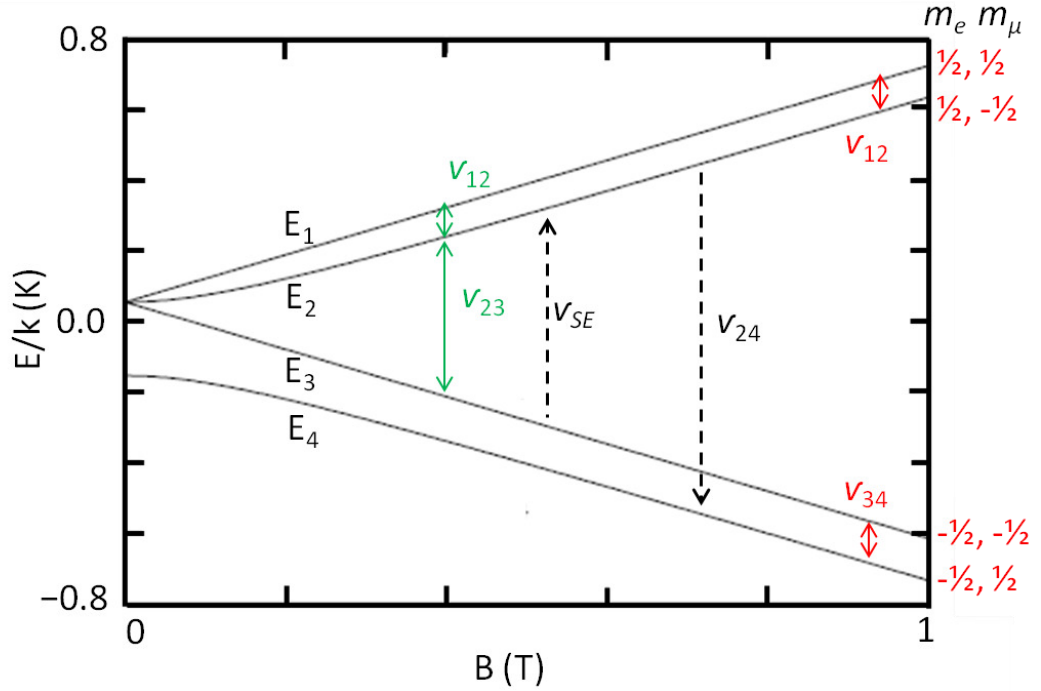
Figure 2.4 A representative Breit-Rabi diagram to show the field dependence of the hyperfine energy levels of an isotropic two-spin-$1/2$ muonium atom (adapted from [74]).

As seen in the Breit-Rabi diagram, the electronic ground state of muonium splits into four different energy levels. The possible observable transitions in high fields are $(1/2, 1/2) \rightarrow (1/2, -1/2)$ designated as v_{12} and $(-1/2, -1/2) \rightarrow (-1/2, 1/2)$ designated as v_{34}, and at low fields they are expressed as v_{12} and v_{23}. Due to the spin exchange of the muonium atom, the behaviour of the T_1 muon spin relaxation rate is separated into two zones at the point where the rate of spin exchange events (v_{SE}) is equal to v_{24} (2-4 muonium hyperfine frequency). If $v_{24} \ll v_{SE}$, which defines the fast region, the relaxation rate is almost field-independent. Conversely, in the slow region where $v_{24} \gg v_{SE}$, it is field-dependent. The relaxation rate in the slow region can be expressed as [74]:

$$T_1^{-1} \approx \frac{A_\mu^2 v_{SE}}{2[A_\mu^2 + ((\gamma_e + \gamma_\mu)B)^2]}$$

Equation 2.39

The origin of this relaxation lies in the field dependence of the spin eigenstates of Mu, as detailed in ref. [151]. These transitions between different energy levels, with repeated rapid electron spin-exchange scattering, involve a random flip of the

muonium electron spin (Figure 2.5). This random switch in the local field and muonium lead to relaxation of the muon's spin.
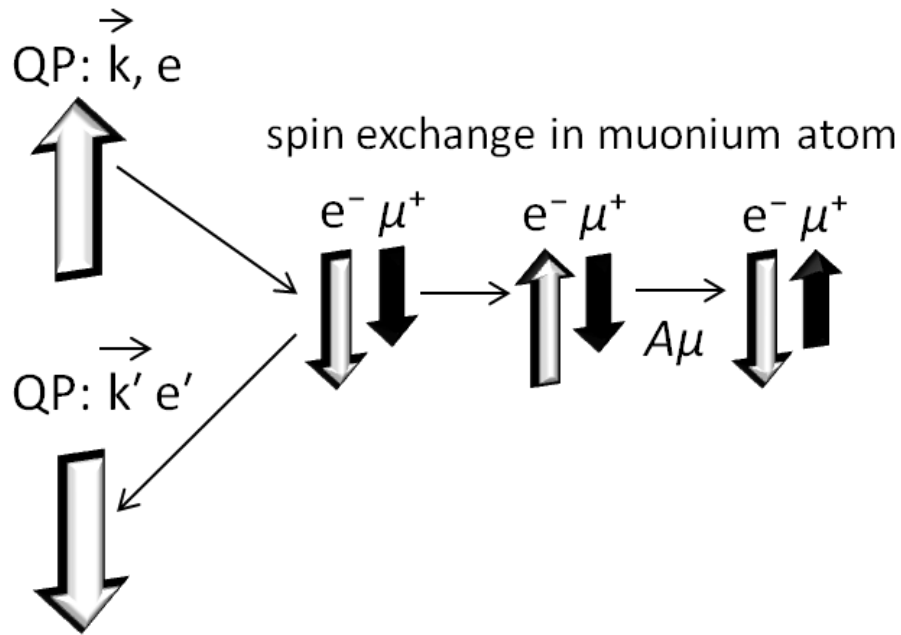
Figure 2.5 Spin exchange of a muonium atom with subsequent evolution due to muon-electron hyperfine interaction. QP stands for quasi particle at the Fermi surface with initial momentum k, and e is the magnetically scattered energy from the local moment; adapted from [74].

For detailed information, the reader is referred to the books of Schenck [152] and Yaouanc [139], the review articles of Cox [136], [138] and Patterson [150], and the PhD thesis of MacFarlane [153].

2.5   Radiation Facilities

2.5.1   European Synchrotron Radiation Facility (ESRF)

The European Synchrotron Radiation Facility (ESRF) is a third-generation X-ray light source located in Grenoble, France. The ESRF accelerator complex consists of a linear accelerator (LINAC), a booster and storage ring. Electrons are produced using an electron gun and then transferred into the LINAC and are accelerated to ~200 MeV by pulsed electric fields. Accelerated electrons by pulsed electric fields are then injected into the booster where electrons are accelerated using radio frequency waves until electrons reach kinetic energy of ~6 GeV. Finally, an injection system transfers them from the booster ring to the storage ring of 844 m where the electrons circle close to the speed of light [116].

The storage ring consists of 32 straight and 32 curved sections equipped with bending magnets and insertion devices. The bending magnets are used to bend the electrons into a non-linear trajectory around the circumference of the storage ring. This results in an emission of a spray of X-rays (fan-shaped). Furthermore, the magnets keep the electrons circulating in their ideal orbit and group them into bunches, which provide a maximum current of 200 mA for a beam lifetime of ~50 hours [154]. A general schematic illustration of a synchrotron storage ring is shown in Figure 2.6.

Insertion devices are made up of periodic arrays of small magnets and consist of two different types, wigglers and undulators, placed in the straight sections of the storage ring to create characteristic X-rays for different beamlines. Insertion devices deliver the X-ray beams to the beamlines located around the storage ring [116], [154]. For this project, X-ray powder diffraction data collection at ambient pressures was carried out at beamline ID31.
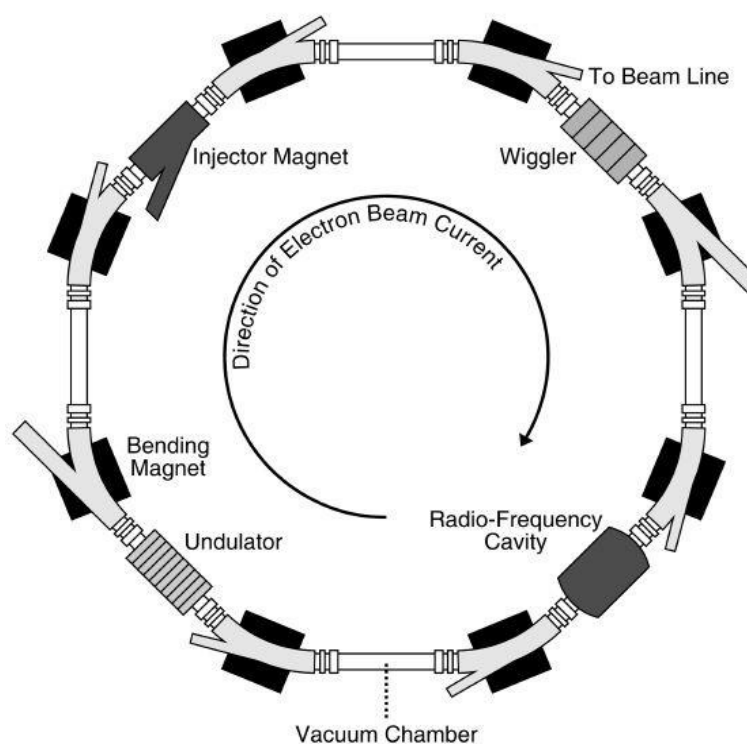
Figure 2.6 Schematic diagram of the ESRF accelerator complex (copied from [116]).

ID31 - High-resolution X-ray powder diffraction

Beamline ID31 was designed for high-resolution powder diffraction studies with very high energy resolution and fast data acquisition times. It was closed in

December 2013 and an upgraded version of the whole setup was transferred to beamline ID22.

The highly collimated beam from the undulator source was directed towards a cryogenically-cooled Si (111) double-crystal monochromator before hitting the sample. The diffractometer arm of ID31 was equipped with nine Si (111) crystal analysers and nine detectors (channels separated by ~2°). The 9 detectors moved simultaneously and produced 9 high-resolution diffraction patterns as a function of 2θ in parallel which then can be summed in different combinations, using the program 'id31sum' [155], [156]. The offsets between the channels were calibrated accurately after a new wavelength was selected. The calibration was carried out using a highly crystalline Si standard. ID31 operated in the energy range 5 – 60 keV and hence provided a broad range of wavelengths varying from 2.48 to 0.21 Å. Furthermore, ID31 was well optimised for capillary samples with a high speed capillary spinner (1200 rpm) to minimise preferred orientation effects and provides a robotic sample changer (with capacity for 50 capillaries) compatible with cryostream and hot-air blower [157]. Since all my samples are air-sensitive they were measured in capillaries (flat plate mode is also available at ID31).

2.5.2 SPring-8 Synchrotron Radiation Facility

The Spring-8 synchrotron radiation facility is located in Hyōgo Prefecture, Japan. The name "SPring-8" is derived from "**S**uper **P**hoton **ring**-**8** GeV'. The Spring-8 accelerator complex has 4 components: a 1 GeV linac, an 8-GeV booster synchrotron, an 8-GeV storage ring and a 1.5-GeV NewSUBARU storage ring. While the 8 GeV storage ring is used for the generation of brilliant X-rays, NewSUBARU is facilitated for the usage of short-pulse soft X-rays. The maximum energy of the generated beam is 8 GeV (cf. 6 GeV at ESRF). The procedure to produce X-ray radiation is similar to that of the ESRF. The storage ring is also composed of bending magnets and insertion devices with the same purposes as explained in section 2.5.1. In this study, variable temperature X-ray diffraction experiments at ambient and high pressure were performed at beamlines BL44B2 and BL10XU of SPring-8, respectively.

BL44B2 High-resolution X-ray powder diffraction

Beamline BL44B2 is designed for high-resolution powder diffraction studies and operates in the energy range 10 – 35 keV. X-rays are monochromated with a Si (111) double-crystal monochromator; thereafter they are focused with a Pt-coated bent cylinder type mirror to the sample to be measured. A hybrid detector system is installed on beamline BL44B2 which is equipped with a high-resolution Debye-Scherrer camera. The hybrid detector system consists of a conventional detector, an off-line imaging plate (IP) which allows high d-resolution measurements, and a CCD detector allowing angle-resolution measurements [158]. In this study, we used the imaging plate for variable temperature XRPD experiments. Using a mask with a 10 mm width slit, twenty data could be collected on one IP which covers an angular range between 2° and 75° with a 0.01° interval. The XRPD data collected on an IP are then scanned to retrieve the profiles digitally using the local programmes 'image reader' and 'ipv32.exe' which are provided on BL44B2 beamline computers. The sample temperature can be ranged between 100 and 1000 K by using a low- and high-temperature N_2 open-flow system.

BL10XU - High pressure research

BL10XU is a specially designed beamline for high-pressure X-ray diffraction studies using a diamond anvil cell (DAC). A DAC is a widely used device to generate extreme pressures by static compression and is composed of two opposing diamond anvils [159]. Pressure inside the DAC is monitored using a reference material whose behaviour is known under pressure. At BL10XU the pressure is determined using the calibrated ruby fluorescence line shift with pressure. Since the laser induced ruby fluorescence R_1 line shifts with pressure, the calibrated pressure dependence of the wavelength of the R_1 line allows us to determine the pressure [160]. The sample is placed in a chamber created between the perfectly parallel culet faces of the two opposing diamond anvils and a gasket that is a thin sheet of material with a tiny hole where the culets are facing each other, used to encapsulate the sample. The gasket can be made of Kapton, Cu, Be or stainless steel.

Since a hydrostatic pressure is desired for high pressure experiments, a pressure-transmitting medium is needed inside the sample chamber together with

the sample and the ruby. In the absence of a pressure-transmitting medium, the conditions are non-hydrostatic implying some unquantifiable deviations from the true structure metrics and also leading to broadening of the Bragg peaks. He gas was used as the pressure medium for data collection at BL10XU.

High pressure studies require high X-ray energies due to the high absorption of the diamond windows of the DAC, limited angular range available for X-ray diffraction and the very small sample size. The collimated beam is monochromatised using a Si (111) double crystal and the monochromatic X-rays have a kinetic energy of 14 – 58 keV. X-ray refractive lens system has been used as focusing optics which increases the intensity of X-rays about 10 times. A flat image plate (IP) detector (Rigaku R-AXIS IV++, 300×300 mm^2 area, 0.100 mm pixel size) has been used in this work to record images of the Debye-Scherrer rings, accompanied with a goniometer for the DAC, an ionisation chamber to monitor the beam intensity, four blade slits to adjust the spot size, attenuators, a beam stopper and a microscope to monitor the position of the DAC. The recorded data on the imaging plate were then converted into one-dimensional intensity as a function of diffraction angle by azimuthal integration, using the program WinPIP [161].

Integration of two-dimensional powder X-ray diffraction data collected at beamline BL10XU

The software WinPIP has been used to process the collected data by converting them into tables of scattered intensities *vs.* scattering angle 2θ [161]. If an IP detector is aligned perpendicular to the Debye-Scherrer cones' axes, the diffracted intensity appears as a series of concentric rings termed as Debye-Scherrer rings, on the detection plane (section 2.2.3). If the sample is an ideal powder, the intensity on each ring should be uniform. However, in practice, the small sample volume in the DAC causes real powder rings to be spotty or discontinuous which results in a fundamental problem with data quality from high pressure experiments. Therefore, the intensity as a function of ring radius is most reliably extracted by averaging over numerous radial scans taken over larger uniform, unbroken segments of the Debye-Scherrer rings. The recorded data on the detection plane are integrated along circles around the centre of the Debye-Scherrer rings, with radii ranging from zero to the IP detector border.

To extract data of intensity *vs.* effective radius, the x_0 and y_0 coordinates to define the position of the centre of the Debye-Scherrer rings on the image, and two further parameters, the tilt plane rotation angle and the tilt angle to define the shape and orientation of the integration ellipses, must be known before the integration. To convert these data into data of intensity *vs.* 2θ, the X-ray wavelength and the sample-to-detector distance must also be known which is determined by calibration with an external standard.

Some areas of the IP recording might include shadows cast on the detection area from diffracted radiation hitting the beam stopper, or the DAC, or overexposed spots. Therefore, these areas must be excluded before the data integration using masking tools provided within the WinPIP software without changing the image itself. There might be also some contributions from the crystalline diamond anvils and the ruby pressure calibration standard. If these contributions are non-overlapping and identifiable, they are generally masked prior to integration. Finally, the integrated data is ready to be analysed using *e.g.* the Rietveld method.

2.5.3 ISIS Rutherford Appleton Laboratory

The ISIS facility is a pulsed neutron and muon source located at the Rutherford Appleton Laboratory (RAL) in Oxfordshire, UK. The ISIS accelerator consists of an ion source, a Radio Frequency Quadrupole (RFQ) accelerator, a linear accelerator (linac) and a synchrotron. The ion source is the start point of the proton accelerator where H^- ions are produced. H^- ions are then transferred into the RFQ accelerator which focuses, accelerates and bunches the ions. The accelerated ions are then directed to the linac for further acceleration to 70 MeV with high intensity radio-frequency (RF) fields. Finally, 200 μs long and 22 mA H^- pulses are transferred to the synchrotron for the final acceleration. The synchrotron is equipped with ten dipole bending magnets and quadrupole magnets which bend and focus the beam to travel in a circular ring of 163 m circumference. Once the H^- pulses enter into the synchrotron, the electrons of the ions are separated using an aluminium oxide stripping foil to collect sufficient protons which are accelerated by radio-frequency electric fields [162].

The whole acceleration process is repeated 50 times per second and the beam makes 10,000 circles in the ring during the acceleration, and finally a mean current of 200 µA is delivered to the target stations and muon target. While Target Station – 1 (TS1) and Target Station – 2 (TS2), which include different type of instruments using characteristic neutrons, produce neutrons by bombarding a tungsten target with high energy protons by the spallation process, muons are produced by bombarding a thin graphite target with high energy protons [163]. In this work two different instruments were used: the General materials powder diffraction (GEM) diffractometer at TS1 and the high field muon spectrometer (HiFi) at the muon target.

General materials powder diffraction diffractometer

GEM is a new generation pulsed source diffractometer designed for the tof neutron diffraction technique. The basic principles of the tof technique were given in section 2.2.6. The GEM diffractometer has an incident flight path of $L = 17$ metres and a scattered flight path which varies from 1 metre to 2.9 metres. The special feature of the GEM diffractometer arises from the specially designed banks of detectors which cover a wide range of scattering angles from 1.1° to 169.3° with high resolution [59]. The position of the banks of detectors and the scattering angle range of each bank are shown in Figure 2.7. All the detectors are crossed-fiber ZnS/^{6}Li scintillation type detectors. The resolution of the detector banks in the 2θ direction is determined by the 5 mm width of the ZnS/^{6}Li scintillation elements which minimises the angular contribution to the resolution [163], [164].
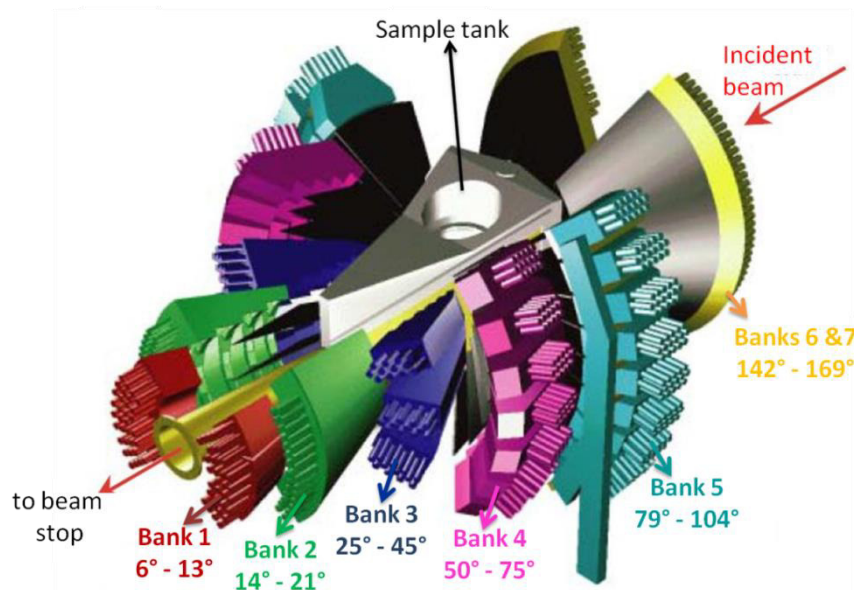
Figure 2.7 A schematic diagram of detector banks from 1 to 7 of the GEM detector array. Copied from [164].

The software MANTID, developed for the analysis and visualization of scientific data, was used for this work to process, visualise and/or analyse the neutron diffraction data [165], [166]. MANTID is provided at ISIS beamline computers for experimenters. Since the neutron diffraction data in this work was analysed by Rietveld method, MANTID was only used to monitor the data collection during the experiment and to sum the continuously collected tof diffraction patterns into appropriate groups, depending on the statistics of the data and applied external perturbations such as temperature and pressure.

High field muon spectrometer

The high field muon spectrometer (HiFi) at ISIS is designed for measurements in longitudinal fields of up to 5 Tesla. A 5T superconducting split-pair magnet is used. The μSR measurements in high magnetic fields require a homogeneous field over the sample volume, thus the magnetic axis has to be well-aligned with the beam direction and any possible stray field must be eliminated. In addition to the 5T superconducting magnet there are other magnets; z-axis coils that create fields used for the field switching (auxiliary field) up to 400 G, and x- and y-axis coils which create transverse fields of up to 200 G for the compensation of the stray field and calibrations. Apart from the importance of the magnetic field, the design of the detectors must be established carefully. The Forward (F) and

Backward (B) detectors should be as close as possible to the sample and cover the largest possible area around the sample to maximise the amount of detected positrons. The HiFi spectrometer can be equipped with a dilution fridge, ^{4}He and flow cryostats, a CCR and a reflector furnace to provide users with as many sample environment as possible [165], [167]. In this work, the WiMDA program suite was used to analyse muon depolarisation spectra [168].

2.6 Magnetism

Magnetism is a property of matter, used to describe the way that materials behave in the presence of an external magnetic field. Magnetic moments of an electron arise from two different sources. One originates from its orbital motion around the nucleus and the other one originates from electron spin. These two rotations result in the generation of a small magnetic field by creating a small current loop and having magnetic moments along the axis of rotation. If the cancellation of electronic moments is incomplete, the atom has a net magnetic moment which can exhibit paramagnetic, antiferromagnetic or ferromagnetic ordering. On the other hand, if there is a complete cancellation of both orbital and spin magnetic moments, this leads to diamagnetism.

The externally applied magnetic field or magnetic field strength is designated by H and the magnitude of the internal field strength (also known as magnetic induction or magnetic flux density) within a substance which is subjected to an H field is denoted by B. The magnetic flux density can be expressed as:

$$B = \mu_0 \left(H + M \right) \qquad \text{Equation 2.40}$$

where μ_0 is the permeability of a vacuum through which the applied field H passes and B is measured, and M is the volume magnetisation (magnetic moment per unit volume) which is proportional to H and can be represented as:

$$M = \chi H \qquad \text{Equation 2.41}$$

where χ is the volume magnetic susceptibility indicating the degree of magnetisation in response to an applied field, H. Since Equation 2.41 is given in the SI system, in which M and H are measured in the same unit Amperes/meter (A/m), χ is dimensionless. The susceptibility can be also defined as mass magnetic susceptibility or molar magnetic susceptibility (referring to the number of moles in

the material) with the units of emu g^{-1} Oe^{-1} and emu mol^{-1} Oe^{-1}, respectively in the cgs-emu system. The most widely performed magnetic measurements are the magnetisation as a function of temperature, $M(T)$ and/or the magnetisation as a function of applied field strength, $M(H)$. In the case of $M(H)$ measurements, the field is changed to suggested values while the temperature is fixed [169].

2.6.1 Diamagnetism

Diamagnetism is a very weak type of non-permanent magnetism, induced by changing the motion of core electrons due to an applied magnetic field. The considerably small magnitude of the induced magnetic moments (in the direction opposite to that of the applied magnetic field) causes a weak contribution to the response of a material to the external magnetic field. Diamagnetic materials have a relative magnetic permeability, μ_r, that is less than or equal to 1, and hence this yields a magnetic susceptibility less than or equal to 0, because the magnetic susceptibility (which is both temperature- and field-independent) and the relative permeability (which is a measure of the degree of being magnetised) are related as follows: $\chi = \mu_r - 1$. An $M(H)$ plot for diamagnetism should be linear and reversible but with a negative slope.

Whilst the magnetic contribution of diamagnetism is vastly outweighed by other effects such as paramagnetism, this contribution is very large in superconductors, leading to perfect diamagnetism as long as the superconducting state is kept. While diamagnets repel the external magnetic flux lines, paramagnets pull the lines into the material.

2.6.2 Paramagnetism

Paramagnetism, known to be the simplest form of magnetisation, arises when the magnetic moments of a material preferentially align along the direction of the external magnetic field. This results in the enhancement of the relative permeability, and therefore positive magnetic susceptibility is observed with paramagnetic materials. A typical paramagnetic material shows a linear $M(H)$ behaviour at constant temperature, which is reversible, following the same curve upon reducing the field as when increasing it. This paramagnetic behaviour, where atoms with unpaired electrons are present (Curie-type paramagnetism), can be

described with the following equation, indicating that the susceptibility of a paramagnetic material is inversely proportional to the temperature:

$$\chi(T) = \frac{C}{T}$$
Equation 2.42

where C is the material-specific Curie constant which is proportional to the square of the sample's effective magnetic moment. Figure 2.8 shows a schematic plot of $1/\chi$ against T, with a straight line through the origin. The Curie constant can be determined from its slope.
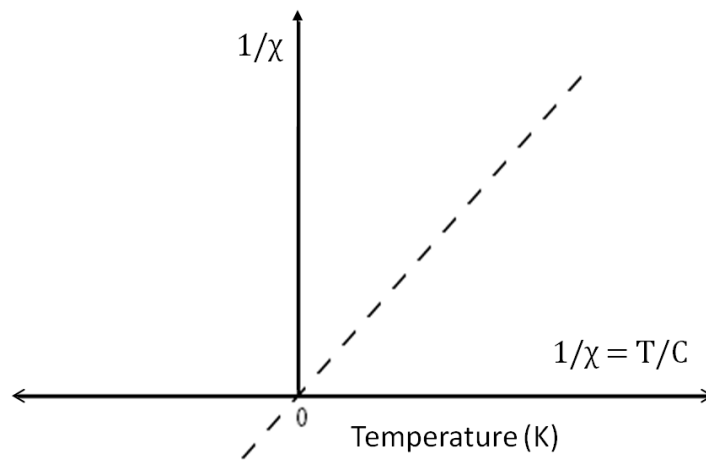
Figure 2.8 Schematic plot of $1/\chi$ vs T for a Curie-type paramagnetic material.

2.6.3 Ferromagnetism and Antiferromagnetism

Ferromagnetic materials have permanent magnetic moments with very large magnetisations even in the absence of an external magnetic field due to strong interaction between the magnetic moments of adjacent atoms or molecules, which can result in the formation of long-range magnetic ordering below a certain temperature. They show a non-linear $M(H)$ curve which is not reversible (*i.e.* magnetic hysteresis is found). Antiferromagnets also display long-range magnetic ordering, but have magnetic moments ordered such that adjacent moments are aligned anti-parallel with one another.

The magnetic behaviour of this type of magnetism can be described by the Curie-Weiss law, which defines the temperature dependence of the susceptibility

for systems with ferromagnetic and antiferromagnetic interactions above the magnetic ordering temperature:

$$\chi(T) = \frac{C}{T - \Theta}$$ Equation 2.43

where Θ is the material-specific Weiss temperature and can be obtained from the x-axis intercept of a plot of $1/\chi$ against T (Figure 2.9). If Θ is positive, the magnetic moments are aligned parallel with one another, and the material is ferromagnetic below the Curie temperature, T_C (Figure 2.9, $\Theta > 0$). On the other hand, if Θ is negative anti-ferromagnetic interactions occur and the magnetic moments are aligned anti-parallel with one another below the Néel temperature, T_N (Figure 2.9, $\Theta < 0$).
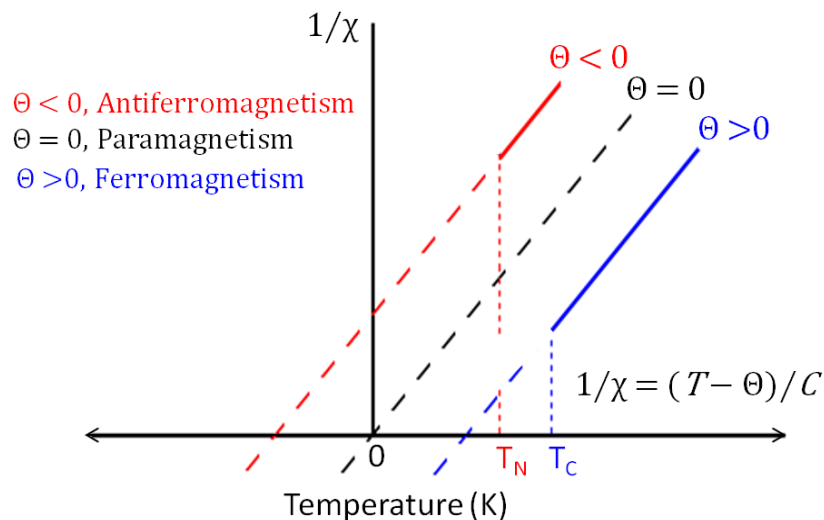
Figure 2.9 Schematic plot of $1/\chi$ *vs* T for various magnetic systems.

A schematic $\chi(T)$ plot for different types of magnetism is shown in Figure 2.10: The alignments of the magnetic moments are destroyed above the Curie (T_C) or Néel (T_N) temperature, thus the material becomes paramagnetic.
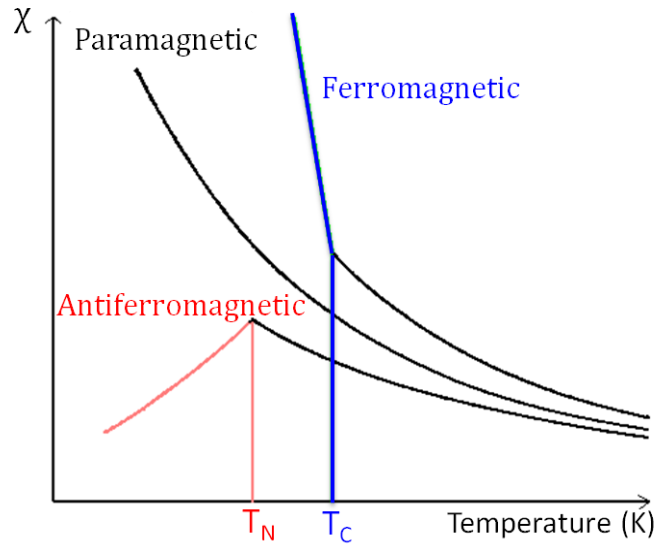
Figure 2.10 A Schematic plot of χ vs *T* for different types of magnetic behavior.

2.6.4 Superconductivity

The phenomenon of superconductivity has been known since 1911, with the discovery of superconductivity in mercury. Superconductors are materials which show no resistance to the flow of electricity and exhibit perfect diamagnetism by the repulsion of the interior magnetic field, known as the so-called Meissner effect which states that inside a superconductor in the superconducting state, magnetic flux density is zero. The direct-current (dc) electrical resistance of a superconductor drops abruptly to zero when it is cooled below its 'critical temperature', T_c, which is material-dependent.

Superconductors are classified into two different types: type-I and type-II, depending on their behaviour within an applied magnetic field. Most elemental superconductors and some alloy superconductors display type-I behaviour: the negative magnetisation increases linearly with field up to a critical field, H_c, below which the penetration of magnetic lines of flux into the material is prevented by the surface current of the material. The magnetisation falls abruptly to zero with further increase in field, as the superconducting state is completely destroyed, and the normal state appears.

In the case of a type-II superconductor, rather than a sharp transition, an initial transition on exceeding a small field, H_{c1} (the lower critical field) is observed from bulk superconductivity to a mixed state where superconductive and

66

insulating or metallic phases coexist (Figure 2.11). On increasing the field further to an upper critical field H_{c2}, the magnetisation decreases with constant slope until the field is increased to the H_{c2}, where superconductivity is destroyed completely and the normal state appears [169], [170].
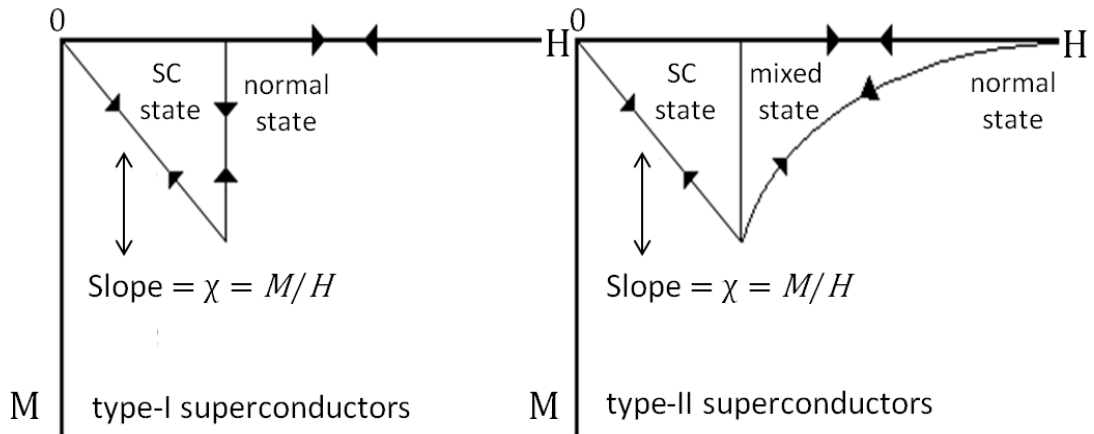
Figure 2.11 Magnetic behavior as a function of field for type-I and type-II superconductors; adapted from [169].

2.6.5   SQUID magnetometer

In this work, magnetic properties of samples over a temperature range between 1.8 and 300 K and over a range of applied magnetic fields up to 5 Tesla were studied using the Magnetic Property Measurement System (MPMS XL). The heart of the MPMS is the Superconducting Quantum Interference Device (SQUID) which is a very sensitive magnetometer used to measure extremely small magnetic fields, magnetic moments and subtle changes within the material. All data were collected using direct-current (dc) magnetometry.

The SQUID does not measure the magnetisation directly from the sample; instead, its sensors detect variations in the SQUID output voltage which is proportional to the magnetic moment of the sample. During the measurements, the sample moves in a series of discrete steps through some superconducting detection coils which are connected to the SQUID input coil with superconducting wires, allowing the current from the detection coils to inductively couple to the SQUID sensor [169].

While the sample moves through these coils, the magnetic moment of the sample induces an electric current in the detection coils (Figure 2.12). A closed

superconducting loop is generated by the detection coils, superconducting wires, and SQUID input coil, and consequently any change of magnetic flux in the detection coils will cause a change in the persistent current in the detection circuit, which is proportional to the change in magnetic flux.

Since the SQUID can function as a highly linear current-to-voltage convertor, the changes of the current in the detection coils produce corresponding changes in the SQUID output voltage which are proportional to the magnetic moment of the sample. The detected output voltage as a function of position gives a highly accurate measurement of the magnetic moment resulting from the sample [169] as soon as the sample is well-centered in the detection coil. Calibration of the system is required from time to time for accurate measurements of the voltage changes. The system can be accurately calibrated using a small piece of material with a known mass and magnetic susceptibility such as a small sphere of nickel.
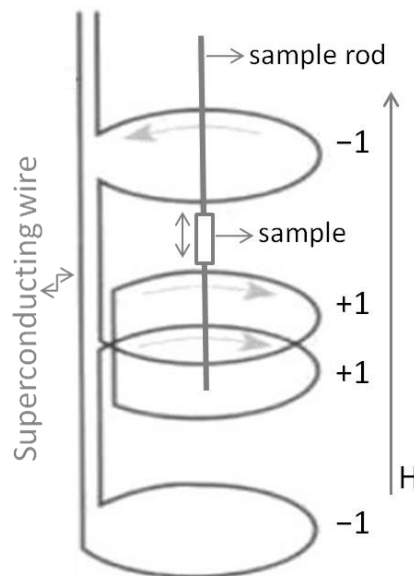
Figure 2.12 Schematic configuration of the superconducting detection coil: a single piece of superconducting wire wound in a set of three coils configured as a second-order (second derivative) gradiometer [169].

The sample chamber is, surrounded by the superconducting detection coils, kept at a low pressure with static helium gas. The sample is attached to the end of a rigid straight sample rod using Kapton tape, which is non-magnetic and resistant to low temperatures. Before lowering the sample into the sample space, the user

must ensure that the sample will not disengage from the rod during the measurements.

Furthermore, the sample space has to be free from moisture or air, if not the user must warm the SQUID magnetometer to room temperature and then perform a rigorous pumping procedure. Thereby, it is essential to perform the pumping procedure after each insertion/removal process of the sample rod into/from the sample space for the evacuation of air and moisture.

It should be also noted that after long measurements at high magnetic fields, there may be a remnant magnetic field present even after zeroing the field for subsequent low field measurements. This remnant field can be reset using a degaussing procedure which oscillates the magnetic field from a positive magnetic field to a negative magnetic field and gradually reduces the amplitude of oscillation. After the degaussing procedure, the superconducting magnet can be also reset.

The Sample Handling System controls the vertical motion of the rod during data acquisition. Since the sample rod moves vertically, the longitudinal (direction of the movement through the coil) moment (reported in emu) of the sample is extracted from the integration of the area under the voltage *vs.* position plot. For the results contained in this work, the iterative regression method was used to analyse the SQUID output signal which is available in the software MPMS MultiVu™. The measured longitudinal moment was converted to magnetisation using the following equation:

$$M = \mu/n$$
<div align="right">Equation 2.44</div>

where μ is the longitudinal moment (emu) and n is the number of moles of measured sample.

2.6.6 Ambient pressure magnetic measurements

The superconducting transition temperature (T_c) was obtained by low-field magnetisation measurements as a function of temperature at ambient pressures. Knowing that the superconducting state can be defined by its ability to expel the interior magnetic field, T_c can be determined as the temperature where the diamagnetic response is suppressed and paramagnetic behaviour appears in the

normal state. In measurements conducted in this work two types of dc magnetisation measurements were performed: field-cooled (FC) and zero-field-cooled (ZFC). In the case of the ZFC protocol, the sample was cooled down in zero applied magnetic field and the longitudinal moment was measured on warming. At temperatures above T_c the sample does not show diamagnetism anymore. For the FC protocol, the sample was cooled in a weak magnetic field and then the longitudinal moment was again measured on warming. Since magnetic flux inside the sample above T_c is trapped by the shielding currents on the surface during cooling, the sample will expel the flux less compared to the ZFC protocol, and hence the magnitude of the FC diamagnetic susceptibility will be reduced compared to the ZFC susceptibility. In other words, while the ZFC curve shows the flux exclusion, FC curve shows the flux expulsion. As a result, the temperature where the ZFC and FC curves deviate can be defined as the onset T_c of the superconducting material. This hysteresis of the diamagnetic susceptibility below T_c, the so-called Meissner effect, is definitive proof of superconductivity. The shielding fraction (SF) of samples was calculated from the ZFC magnetisation data using the following expression:

$$\text{SF} = \frac{4\pi\rho\Delta\mu}{Hm} \times 100 \text{ \%}$$

Equation 2.45

where ρ is the density of the sample (g cm^{-3}), H is the applied external field (Oe), m is the mass of the measured sample (g) and $\Delta\mu$ is the change in the longitudinal moment from the paramagnetic to the superconducting state.

High-field magnetisation measurements were also performed in order to investigate the magnetic susceptibility behaviour in the normal state. All samples measured at ambient pressure in this work were sealed inside thin-walled 5 mm-diameter high-purity Suprasil® quartz ampoules (due to their air-sensitivity), and attached to a sample rod using a plastic straw and Kapton tape.

2.6.7 High pressure magnetic measurements

High pressure magnetic measurements were carried out under applied pressures of up to 10 kbar using an 'easyLab Mcell 10', a cylindrical hydrostatic pressure cell based on a single walled-design [171]. The high pressure cell is

composed of many components and correct assembly is imperative for successful measurements. The cell body should be clean from dust or remaining debris from previous measurements and the cell components must be correctly and tightly packed. Figure 2.13 schematically shows the entire setup of the high pressure cell.

A perfect assembly of the cell is required for accurate measurements as well as for the consistency of the background measurements with the actual measurement, and hence good care must be taken of the cell components. The minimum position of the upper locking nut 'Zmin', should be measured on a regular basis by inserting a ceramic piston cap into the upper part of the HP cell, fully screwing the upper locking nut, and then measuring the distance between the top of the cell body and the top of the upper locking nut using a Vernier calliper. 'Zmin' should never be exceeded, to avoid damage to the piston cap. Before anything is loaded in the PTFE sample capsule, the user should make sure that the PTFE capsule goes right through the cell and the pistons and caps should be checked under the microscope to ensure that they are not cracked or defective [171].
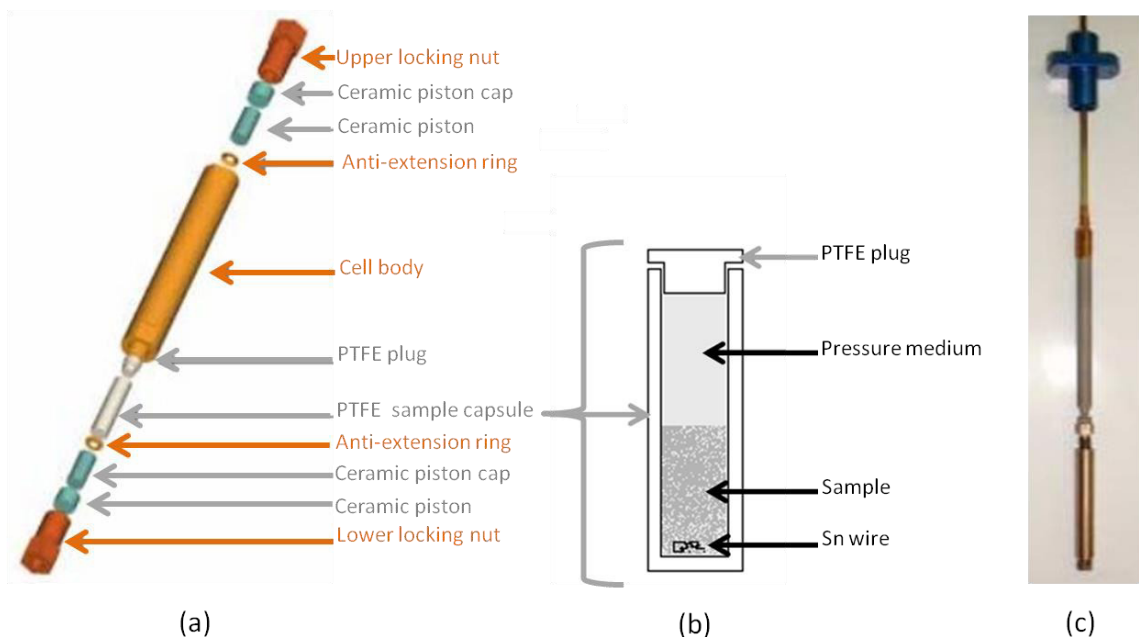
Figure 2.13 (a) easyLab Mcell 10 General Assembly drawing; (b) schematic diagram of the PTFE sample capsule; (c) cell body mounted on the MPMS high pressure sample rod [171].

A small coil of Sn wire (~5 mm long piece of 0.25 mm diameter) used as a manometer is placed inside the PTFE capsule before loading anything as the temperature dependence of the superconducting transition temperature of Sn at

71

different pressures is known accurately. The Sn superconducting T_c decreases with increasing pressure, according to the following function [171].

$$P = (5.041489 \times [T_c(0) - T_c(P)]^2) + (17.81287 \times [T_c(0) - T_c(P)]) \quad \text{Equation 2.46}$$

where P is the pressure in kbar, and T_c is in units of K. The estimated error in pressure determination is ~0.2-0.3 kbar.

Once the Sn wire has been inserted, the required amount of sample is loaded into the PTFE capsule inside an argon-filled glovebox. Typically 20-30 mg of sample should be sufficient for A_3C_{60} superconductors. Finally, pressure transmitting oil (Daphne oil) is dispensed into the PTFE cell using a syringe and dispenser to obtain hydrostatic pressures (see Figure 2.13 (b) for the assembly). The user must ensure that there are no air bubbles at this stage inside the PTFE capsule. The PTFE capsule is then closed using a PTFE plug.

Once the PTFE capsule has been prepared properly, it is positioned in the cell body. The cell is closed by tightening the upper locking nut, and then the height from the main body of the cell to the top of the upper locking nut is measured using a Vernier calliper. This value is then recorded onto the loading sheet which is created to inspect whether or not the cell is overtightened at subsequent pressurisations and compare the values with that of previous measurements as overtightening can permanently damage the high pressure cell. Finally, the assembled cell is ready to be pressurised with the hydraulic press (Mpress) ram. The cell is pressurised by pushing a tungsten carbide piston onto the ceramic pistons. In turn, the volume of the PTFE capsule, in which the sample and Sn wire are surrounded by the pressure transmitting medium, is reduced and hence the pressure increases.

Since there will be background contributions from the cell, a background measurement is carried out with no sample in the PTFE capsule but with the presence of the pressure medium. The background measurements are performed with ZFC and FC protocols over the exact temperature range of the forthcoming actual measurements and precisely in the same field. These raw data are then subtracted from the actual measurements using the Automated Background Subtraction (ABS) feature. Background measurements were collected using PTFE

capsules of two different lengths, to best emulate the background contribution of the cell at low and high pressures.

Furthermore, in order to centre the position of the cell inside the detection coils, a ferromagnetic nickel sphere is first centered because it can be difficult to centre the sample inside the cell under weak fields. Then the length of the rod with the attached high pressure cell can be accurately measured. In this way the sample height with small adjustments using the SQUID's software can be defined more precisely.

Chapter 3 Structural and magnetic studies of fcc-structured $K_xCs_{3-x}C_{60}$ ($0.12 \leq x \leq 2$) materials

3.1 Introduction

The previously reported studies on the discovery of superconductivity in fcc A_3C_{60} (A = K, Rb, Cs or a combination thereof), focusing on their novel structural and electronic features were summarised in section 1.2.4.

Martin McDonald and colleagues had pioneered the use of the liquid ammonia synthetic route to synthesise and characterise high-quality superconducting fcc $Rb_xCs_{3-x}C_{60}$ materials at the highest known lattice expansion covering the compositional range of $0 \leq x \leq 0.5$ [66]. They showed that high-quality overexpanded $Rb_xCs_{3-x}C_{60}$ materials could be synthetically accessed and displayed an anomalous trend in $T_c(V)$. This work was subsequently extended by Zadik and co-workers who probed in detail the nature of the magnetic and electronic properties of these materials. This was achieved by the preparation of high quality fcc-rich overexpanded $Rb_xCs_{3-x}C_{60}$ samples using a solid-state synthetic route (overcoming various issues of the liquid ammonia route such as low shielding fractions and inadequate stoichiometry control) and with x systematically varied between 0.25 and 2. Bulk superconductivity was observed for all fcc-rich $Rb_xCs_{3-x}C_{60}$ ($0.25 \leq x \leq 2$) samples. An important feature of this work was that the Mott insulator-metal transition was shifted to ambient pressure *via* the application of chemical pressure through substitution of Cs^+ in Cs_3C_{60} by the smaller Rb^+ cation. The study led to the construction of the global bandwidth-controlled electronic phase diagram in fullerides, extending from the strongly correlated antiferromagnetic Mott-Jahn-Teller insulator (MJTI) Cs_3C_{60} at large interfullerene separations to a conventional metal Rb_3C_{60} as the unit cell volume, V, becomes significantly smaller [28], [67].

3.1.1 Purpose of present study

The Mott insulator-to-metal transition in Cs_3C_{60} has been previously traversed through application of both hydrostatic and chemical pressure, which

reduce interfullerene separation [28], [67], [80]. By means of chemical pressure, the interfullerene spacing is controlled by the cation distribution at the fcc tetrahedral interstitial sites. Structural and magnetic characterisation of $Rb_xCs_{3-x}C_{60}$ ($0.25 \leq x \leq 2$) verified that the chemical pressure effect on the electronic properties of the most expanded fcc Cs_3C_{60} is comparable to that by application of hydrostatic pressure. Indeed, it was reported that pressurizing Rb_3C_{60} can reduce the lattice parameter to that of K_3C_{60} and lead to approximately the same T_c for both materials, suggesting that alkali ions themselves only act to alter the unit cell dimensions [41]. However, in Rb_3C_{60} both tetrahedral and octahedral interstitial sites are entirely occupied by Rb^+, while in fcc $A_xCs_{3-x}C_{60}$, the tetrahedral sites are occupied by both A^+ and Cs^+ (except $x = 3$, 2 and 0) cations in a disordered fashion. The disorder in size might influence the magnetic and structural properties of compositions. Indeed, some deviation in the variation of T_c with fcc unit cell volume was reported when comparing physical and chemical (*i.e.* K substitution) means of reducing the Rb_3C_{60} lattice parameter [172]. However, this cation specific effects have not been addressed in any detail.

This study aimed to shift the Mott insulator-metal transition to ambient pressure *via* the application of chemical pressure through substitution of Cs^+ in Cs_3C_{60} by the smaller K^+ cation. A wide compositional range of fcc $K_xCs_{3-x}C_{60}$ compositions are synthesised using solid-state synthetic routes. Compositions range from underexpanded K_2CsC_{60} through to overexpanded systems close to the Mott-metal insulator boundary. Samples are targeted to have high fcc phase fractions, good stoichiometry control and be highly crystalline, becoming bulk superconductors with high shielding fractions at low temperature. This study investigates the structural and electronic properties of fcc $K_xCs_{3-x}C_{60}$. Special attention is paid to the comparison with fcc $Rb_xCs_{3-x}C_{60}$ to investigate cation specific effects on the electronic properties of fcc $A_xCs_{3-x}C_{60}$.

Temperature- and pressure-dependent high-resolution synchrotron X-ray powder diffraction studies were undertaken to finely explore the structural evolution of these materials. Combination of structural and magnetic property results using different techniques allowed comparison of the response of the properties to the application of hydrostatic and chemical pressure.

3.2 Experimental methods

All samples in this study were synthesised by the candidate, with the exception of two samples (nominal composition, KCs_2C_{60} and $K_{0.25}Cs_{2.75}C_{60}$), prepared by project student V. Wong using the same preparative route. For nominal stoichiometries $K_xCs_{3-x}C_{60}$ (x = 0.12, 0.25, 0.35, 0.5, 0.75, 1 and 2), samples from the same batch were used in all measurements described in this chapter.

3.2.1 Preparation of the precursors, K_6C_{60} and Cs_6C_{60} and of the $K_xCs_{3-x}C_{60}$ ($0.12 \leq x \leq 2$) series by solid state routes

Due to the extreme air and moisture sensitivity of all samples synthesised in this work, all sample manipulations were carried out within the inert atmosphere of an argon-filled glove box (MBraun MB 200B) with low O_2/H_2O levels ($H_2O < 0.3$ p.p.m., $O_2 < 0.1$ p.p.m.). All apparatus used for the synthesis inside the glove box was thoroughly dried in an oven at ~85°C and pumped in the external chamber of the glove box three times (with the first pumping time of no less than 15 minutes) before being transferred inside.

Prior to synthesis, as-purchased pristine C_{60} (MER corporation, 99.9%) was purified by sublimation: 500-600 mg of C_{60} were ground with a mortar and pestle, loaded to the bottom of a 12 mm-diameter quartz ampoule with a separating striction using a funnel and then degassed for 3-4 hours in a dynamic vacuum of 10^{-4}-10^{-5} mbar. Sublimation was undertaken using a tube furnace by ramping (10°C/min) from ambient temperature to 550°C and dwelling there for 16 hrs under dynamic vacuum. Once sublimation was complete, the furnace was removed, the ampoule was sealed with a Young's tap and adaptor with Swagelok connector and transferred to the glove box. The sublimed material above the striction of the ampoule was then removed using a long spatula and stored in the glove box after grinding for later use.

For the synthesis of the K_6C_{60} and Cs_6C_{60} precursors, reaction mixtures of K ($\geq$99.95% Aldrich/Acros, used as supplied) and sublimed C_{60} were placed in a 5-mm diameter open tantalum cell in stoichiometric quantities. The open tantalum cell was then placed in a 12-mm diameter Pyrex glass ampoule, closed with a high-vacuum Swagelok fitting with J. Young tap, and removed from the glove box. The

ampoule was evacuated to ~1×10⁻⁴ mbar using a high-vacuum glass manifold setup with a Leybold vacuum PT70B turbo pump for 20 minutes, filled with a small He gas pressure (typically 350-450 mbar) and sealed. Thereafter, the sealed ampoule was placed vertically in a muffle furnace and heated to 250°C with a rate of 5°C/min, followed by 17 hrs annealing and cooling to room temperature (RT) with the same rate as heating. Inside the glove box, the product was ground, pelletized, and this time loaded into a tantalum cell with tightened screw ends which was then placed in a 15-mm Pyrex glass ampoule. After evacuation and sealing under He, the product was annealed for further period of 48+48 hrs at 300°C with one intermediate grinding.

For the synthesis of phase-pure Cs_6C_{60}, a vapour transport method was employed, with a ~2.2× excess amount of Cs. Sublimed C_{60} was first loaded into the bottom of a 12-mm diameter Pyrex ampoule with a striction, using a funnel. The excess Cs was loaded in a 7-mm diameter Pyrex capsule which was lowered in the glass ampoule down to where the striction is. After evacuation and sealing under He (~400 mbar), the sealed ampoule was placed in a 3-zone horizontal tube furnace in order to create a temperature gradient between Cs and C_{60} for vapour transport. The 'Cs zone' was ramped to 350°C from RT (2°C/min) followed by dwelling for 3 days. At the same time, the 'C_{60} zone' was ramped to 330°C (2°C/min), to allow vapour transport from the 'Cs zone' to 'C_{60} zone'. Once the annealing was complete, the temperature gradient was reversed before allowing the sample to cool down to room temperature, in order to condense away any un-intercalated Cs from the newly formed Cs_6C_{60}. The reaction mixture was then removed from the reaction vessel inside the glove box, ground, pelletized and placed in a tantalum cell with tightened screw ends which was then evacuated and sealed under He, and annealed at 350°C for another 3 days to improve the crystallinity.

The quality of all the products obtained after each intermediate grindings was checked by laboratory powder X-ray diffraction (XRPD). After confirmation that the precursors are phase-pure, they were stored in the glove box for later use. Several batches of precursors were synthesised to meet the required quantities for the synthesis of $K_xCs_{3-x}C_{60}$ materials.

$K_xCs_{3-x}C_{60}$ can be prepared by a direct synthetic route, where stoichiometric quantities of K, Cs and C_{60} are mixed and annealed to afford $K_xCs_{3−x}C_{60}$ directly. The alternative synthetic route, which was used in the present study was to employ as starting materials the appropriate A_6C_{60} (A = K, Cs) precursors. The advantage here over the direct synthesis method is that the A_6C_{60} compounds are free-flowing powders allowing accurate weighing of the reactant quantities and therefore better stoichiometry control of the target compositions, especially when small amounts of the individual reactants are needed.

Stoichiometric quantities of phase-pure free-flowing powders of K_6C_{60}, Cs_6C_{60} and sublimed C_{60} were mixed and ground thoroughly with a mortar and pestle; thereafter the ground mixture was pelletized using a 7-mm diameter pellet die set and placed in a tantalum cell with tightened screw ends. The following stoichiometric equation describes the ideal reaction, with an example shown for $x = 0.75$.

$$\frac{x}{6}K_6C_{60} + \frac{3-x}{6}Cs_6C_{60} + \frac{1}{2}C_{60} \rightarrow K_xCs_{3-x}C_{60} \qquad \text{Equation 3.1}$$

$$\frac{1}{8}K_6C_{60} + \frac{3}{8}Cs_6C_{60} + \frac{1}{2}C_{60} \rightarrow K_{0.75}Cs_{2.25}C_{60} \qquad \text{Equation 3.2}$$
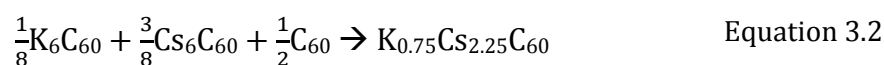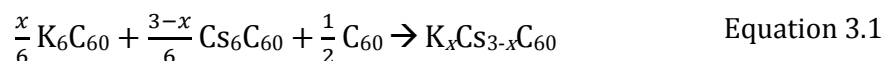
The tantalum cell was then placed in a 15-mm diameter Pyrex glass ampoule, closed with a high-vacuum Swagelok fitting with J. Young tap, and removed from the glove box. The ampoules were evacuated to $\sim 1 \times 10^{-4}$ mbar using the same high-vacuum glass manifold setup for 20 minutes, filled with a small He gas pressure (typically 350-400 mbar) and sealed. Finally, the sample was placed vertically in a muffle furnace and was annealed with the following procedure: ramp at 5°C/min from RT to 200°C, dwell for 3 hrs, ramp to 300°C, dwell for 18 hrs, ramp to 350 °C, dwell for 5 days, ramp at 5°C/min to RT. Inside the glove box, the sample (free-flowing black powder) was ground with a mortar and pestle, pelletized, and loaded back into the same tantalum cell which was then placed in a glass ampoule, followed by evacuation and sealing under He gas as before; thereafter the sealed glass ampoule was placed in a muffle furnace for further annealing at 430°C (ramp at 5°C/min from RT) for 5 days. The sample was annealed for 15-20 days, with 3 intermediate grindings and pelletisations as before to improve crystallinity.

Laboratory powder X-ray diffraction

Prior to synchrotron XRPD studies and SQUID measurements, the quality of all intermediate and final stage polycrystalline products was routinely checked by laboratory XRPD using a Bruker D8 ADVANCE with DAVINCI design powder X-ray diffractometer, configured with a Debye-Scherrer geometry and a copper source $CuK_{\alpha 1}$ = 1.5406 Å (see section 2.2.7 for details). Ambient temperature laboratory XRPD profiles of the two representative final stage precursors, K_6C_{60} and Cs_6C_{60}, and of the nominal '$K_{0.75}Cs_{2.25}C_{60}$' collected after each annealing stage are shown in Figure 3.1 and Figure 3.2, respectively. Polycrystalline products were filled in 0.5–mm diameter glass capillaries, sealed under Ar atmosphere, and their XRPD profiles shown in the figures recorded over a 2θ angular range of 5-50°, with a step size of 0.04°, and a scan rate of 0.5°/min. Sample purity and approximate compositions were established by preliminary Rietveld analysis of the laboratory XRPD data. This verified that the precursors were phase-pure and crystallised with a bcc structure (space group $Im\bar{3}$). Figure 3.2 visually confirms that the majority phase is fcc and the crystallinity of the polycrystalline products of nominal composition '$K_{0.75}Cs_{2.25}C_{60}$' improves after each intermediate annealing. Rietveld fits to synchrotron XRPD data collected at ambient temperature for phase-pure K_6C_{60} and Cs_6C_{60}, and for nominal-composition $K_{0.75}Cs_{2.25}C_{60}$ are shown in Figure 3.3, and in Appendix I in Figure A2, respectively.
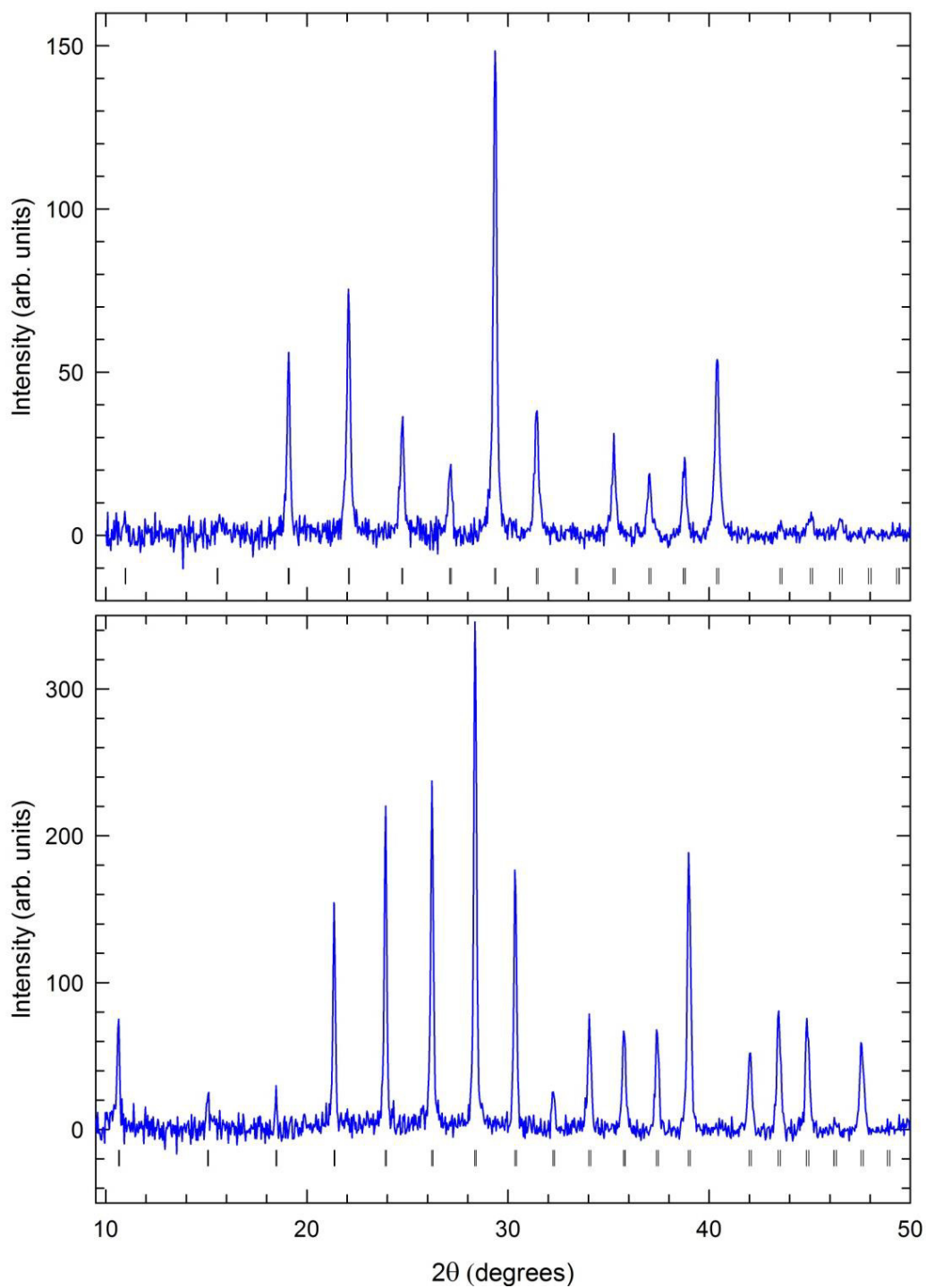
Figure 3.1 Representative laboratory X-ray powder diffraction profiles of phase-pure K_6C_{60} (upper panel) and Cs_6C_{60} (lower panel) at ambient temperature collected with a step size of 0.04°, and a scan rate of 0.5°/min ($\lambda = 1.5406$ Å). Black ticks mark the reflection positions of K_6C_{60} and Cs_6C_{60} with a body-centered-cubic structure ($Im\overline{3}$).
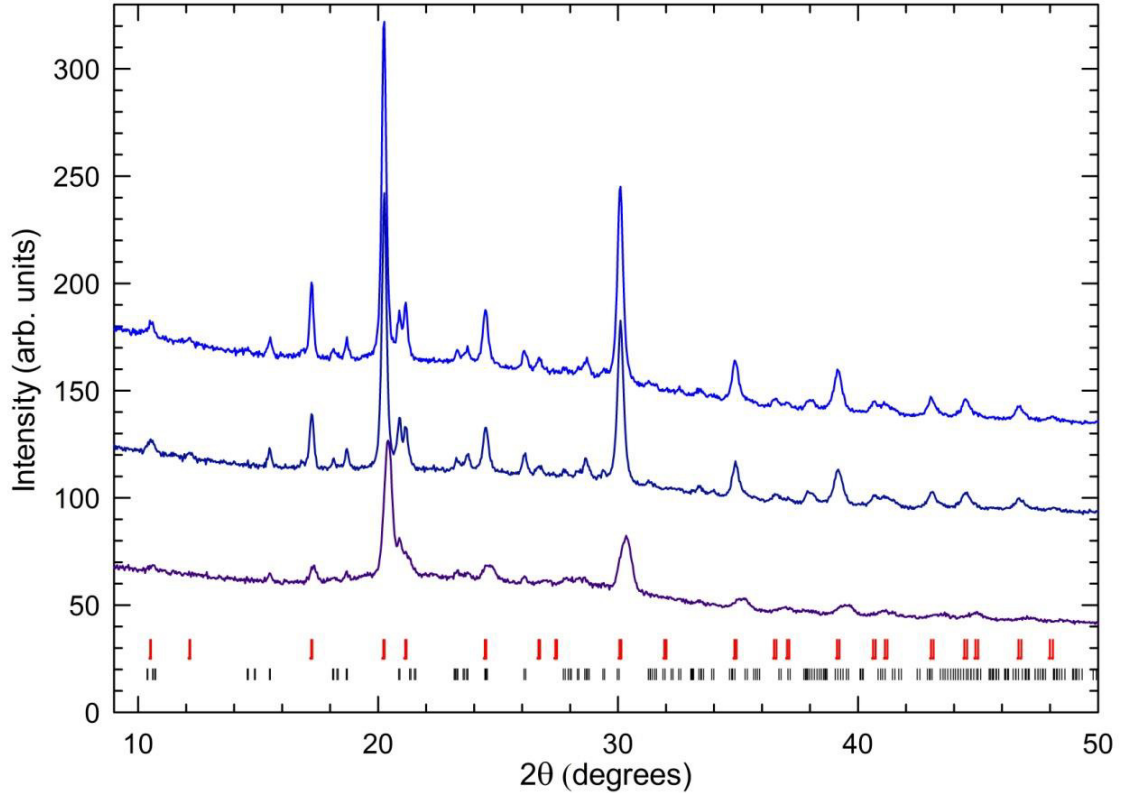
Figure 3.2 Laboratory X-ray powder diffraction profiles at different stages of the preparative procedure of nominal-composition 'K$_{0.75}$Cs$_{2.25}$C$_{60}$': from bottom-to-top data were collected after the first stage of annealing at 350°C for 5 days (bottom), after the second stage of annealing at 430°C for 5 days (middle) and finally after the final stage of annealing at 430°C for 5 days (top) at ambient temperature (λ = 1.5406 Å), with a step size of 0.04°, and a scan rate of 0.5°/min. Red and black ticks mark the reflection positions of co-existing fcc ($Fm\bar{3}m$) and body-centered-orthorhombic ($Immm$) Cs$_4$C$_{60}$ phases, respectively.

3.3 Synchrotron X-ray powder diffraction studies of K$_x$Cs$_{3-x}$C$_{60}$ (0.12 ≤ x ≤ 2)

In the following sections, structural characterisation with high-resolution synchrotron XRPD, employing Rietveld analysis, is described for the fcc K$_x$Cs$_{3-x}$C$_{60}$ series under ambient conditions, variable temperature and elevated pressures.

3.3.1 Experimental procedures

Ambient pressure high-resolution synchrotron XRPD data were collected at ambient temperature and as a function of temperature between 300 and 10 K with the diffractometer on beamline ID31 at the ESRF for samples of nominal composition K$_x$Cs$_{3-x}$C$_{60}$ (0.12 ≤ x ≤ 2), K$_6$C$_{60}$ and Cs$_6$C$_{60}$. The overall setup of the instrument and experimental procedures were outlined in Section 2.4.1. Samples

to be measured were filled in 0.5-mm diameter glass capillaries and sealed under ~300 mbar He. Typically two continuous scans over an angular range of $2\theta = 2\text{-}30°$ were collected at each temperature, with typically 2-3 extra scans over a range of $2\theta = 15\text{-}30°$ collected at the lowest and highest temperatures in order to improve the statistics and allow more precise determination of structural parameters. Data were binned with a step size of $0.002°$ or $0.003°$ in 2θ depending on the crystallinity of the sample. X-ray wavelengths of $\lambda \sim 0.4$ Å were used for data collections, with one exception: $\lambda = 0.354197$ Å was used for samples with nominal K-content of $x = 2$ and 1, for data collection at 300 K. Synchrotron XRPD data for sample with nominal K-content of $x = 1$ between 112 and 300 K were collected on beamline BL44B2 at the SPring-8 facility. The overall setup of the instrument and experimental procedures were outlined in Section 2.4.2. The sample was filled in a 0.3-mm diameter capillary and sealed under ~350 mbar pressure of He. Data were collected with a 5 minute exposure time and a step size of $0.002°$, with $\lambda = 0.81887$ Å.

High-resolution synchrotron XRPD data were also collected as a function of pressure at 7 K for samples of nominal composition $K_xCs_{3-x}C_{60}$ with $x = 0.25$, 0.75, and 1, typically at pressures between 0.2 and 10 GPa, with wavelengths of $\lambda = 0.41261$ Å for $x = 0.25$ and $\lambda = 0.41238$ Å for $x = 0.75$ and 1, on beamline BL10XU, SPring-8, Japan. The overall setup of the beamline, experimental and 2D image integration details were described in Section 2.5.2. Data were binned with step size of $0.01°$ in 2θ. The powdered samples were loaded in a helium-gas-driven membrane diamond anvil cell (MDAC), which was equipped with stainless steel gasket with a hole 100 μm deep and 200 μm in diameter. The MDAC diamond culet diameters were 500 μm. Helium gas in the MDAC was used as a pressure medium. The applied pressure was increased by controlling the He gas pressure to the membrane of the MDAC and was measured with the ruby fluorescence method. Images were collected using a flat image plate detector with 2 min exposure time.

3.3.2 Structural results at ambient temperature

The refinement procedure for Rietveld analysis of the synchrotron XRPD data collected under ambient pressure was as follows: a pseudo-Voigt profile function was used (continuous wavelength profile function '3' within GSAS); profile shape

coefficients *GU, GV, GW, LX, LY and L_{ij}* (*i, j* = 1-3) were allowed to refine for the majority crystallographic phases included in the analysis; low-angle peak asymmetry from axial divergence was modelled with coefficients *S/L* = 0.001, *H/L* = 0.0005 [173]; a Chebyschev polynomial function (~20 terms) was used to fit the background; the anomalous contributions to the X-ray form factors of all atoms, *f'* and *f"* corrections to *f*, were calculated using the program DISPANO for input into GSAS [174]; and a cylindrical absorption correction, given as μr/λ in GSAS [127], was applied for each sample. Consecutive cycles of improving profile shape coefficients in steps with intermediate refinements of zero point correction and background function were applied as well.

Precursors K_6C_{60} and Cs_6C_{60}

Representetive Rietveld refinements of the synchrotron XRPD data collected for K_6C_{60} and Cs_6C_{60} at room temperature are presented in Figure 3.3. These confirm that the K_6C_{60} and Cs_6C_{60} samples are phase-pure, crystallise with a body-centered-cubic structure (space group $Im\bar{3}$, and lattice constants, *a* = 11.3775(2) Å and *a* = 11.7887(2) Å, respectively). The literature lattice constants are as 11.39 Å [175] and 11.79 Å [176], respectively. Fractional atomic coordinates of K_6C_{60} and Cs_6C_{60} were adopted from [175] and [176] and were not refined. Only lattice parameters and isotropic thermal displacement parameters were refined together instrumental and profile parameters.
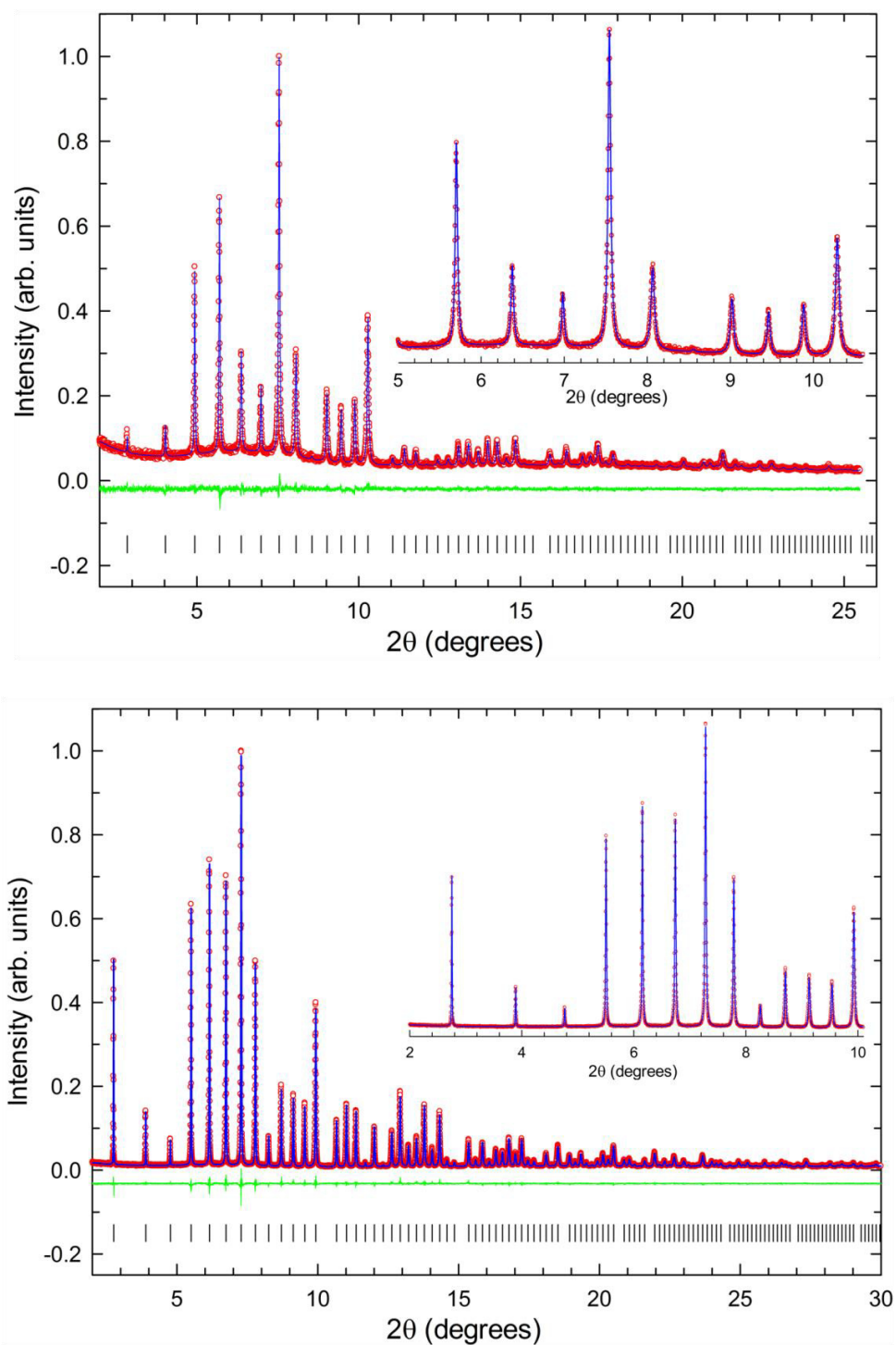
Figure 3.3 Rietveld fits to synchrotron XRPD data collected at ambient temperature for phase-pure K_6C_{60} (upper panel) and Cs_6C_{60} (lower panel) ($\lambda = 0.40006$ Å, step size = 0.002°). Red circles, blue line and green line represent the observed, calculated and difference profiles, respectively. Black ticks mark the reflection positions of K_6C_{60} and Cs_6C_{60} ($Im\bar{3}$). Both insets display expanded regions of the respective diffraction profiles. The weighted-profile and expected R-factors are $R_{wp} = 4.43\%$ and $R_{exp} = 4.18\%$ (K_6C_{60}) and $R_{wp} = 4.43\%$ and $R_{exp} = 3.58\%$ (Cs_6C_{60}).

$K_xCs_{3-x}C_{60}$ (0.12 ≤ x ≤ 2) materials

We now turn to the description of the model employed for the Rietveld analysis of the synchrotron XRPD data collected under ambient conditions for the series of $K_xCs_{3-x}C_{60}$ samples. Only $x = 2$ was successfully synthesised as single fcc phase; all other compositions contained additional minority components. Three crystallographic phases were included in the refinement: a majority fcc phase, and minority Cs_4C_{60} and CsC_{60} phases. XRPD profiles of samples with nominal composition $K_xCs_{3-x}C_{60}$ (0.12 ≤ x ≤ 2) under ambient conditions are shown in Figure 3.4.
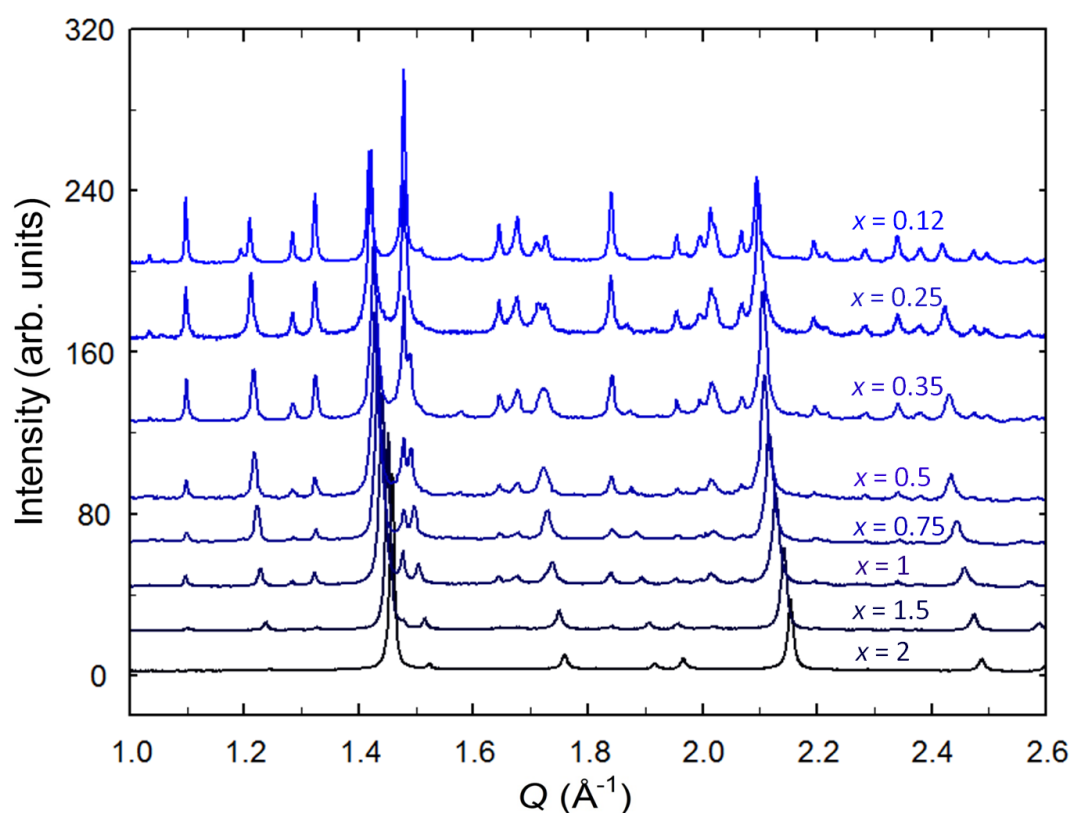
Figure 3.4 High-resolution XRPD profiles collected at ambient temperature for nominal $K_xCs_{3-x}C_{60}$ (0.12 ≤ x ≤ 2) samples.

For the majority fcc phase, the space group $Fm\overline{3}m$ (merohedrally disordered fcc model) was employed. As the O_h cavity (r = 2.06 Å) is significantly larger than the T_d (r = 1.12 Å) one, we expect that larger Cs^+ (r = 1.67 Å) ions would preferentially reside in the O_h site, while the smaller K^+ (r = 1.38 Å) would preferentially occupy the T_d cavity. A recent investigation tested different XRPD models of cation distribution in fcc $Rb_xCs_{3-x}C_{60}$ materials [66] and concluded that the O_h cavity is entirely occupied by Cs^+ and the T_d one is occupied by a disordered

Rb$^+$/Cs$^+$ mixture. Zadik *et al.* have also used the same cation distribution model for their extensive XRPD data analysis of Rb$_x$Cs$_{3-x}$C$_{60}$ materials [67], with one exception: for Rb$_2$CsC$_{60}$, full occupancy of the T_d and O_h cavities by Rb and Cs, respectively, was assumed in accordance with complementary ^{133}Cs and ^{87}Rb NMR experiments [177].

In the present work, the same cation disordered model was employed in accordance with these investigations. The O_h site was modelled as entirely occupied by Cs$^+$ while the T_d site as occupied by a disordered K$^+$/Cs$^+$ mixture. The total occupancy of the T_d site was fixed to 1.0 and the relative ratio of the two cations was allowed to refine. For K$_2$CsC$_{60}$, the T_d and O_h cavities were occupied by K and Cs, respectively. The validity of this approach has been confirmed by ^{133}Cs and ^{39}K NMR measurements on the same samples undertaken by our collaborators. NMR spectra of selected A$_x$Cs$_{3-x}$C$_{60}$ (a = K or Rb) compounds are presented in Appendix III Figure A7 and A8.

The fractional atomic coordinates for each crystallographic phase present were not allowed to refine. They were rescaled as the temperature varied to the refined lattice metrics thereby retaining the molecular shape unaltered. For the fcc phase, the fractional coordinates used were those obtained originally in Rb$_3$C$_{60}$ (with C$_{60}$ C-C bond distances of 1.42 Å) [175]. The Cs$_4$C$_{60}$ phase was modelled as body-centered-orthorhombic (bco) [28] (space group *Immm*) [178], and an orthorhombic [179] *Pmmn* model was employed for the minority CsC$_{60}$ phase. Thermal displacements of all atoms in the fcc phase were modelled as isotropic and allowed to refine under the condition that U_{iso} of the three inequivalent C atoms and U_{iso} of the K$^+$ and Cs$^+$ ions residing in the tetrahedral site were constrained to be equal to each other, respectively. Thermal displacements of Cs atoms in the bco phase were refined if the weight fraction of the phase was significant (>30%). The fcc phase structural parameters obtained from the refinements and two representative Rietveld fits to the XRPD data for samples with nominal K-content of x = 0.5 and 1 are shown in Table 3.1 and Figure 3.5, respectively.

Table 3.1 Refined structural parameters for fcc-structured $K_xCs_{3-x}C_{60}$ samples with nominal K-content of x = 0.5 and 1 (refined K-content of x = 0.64(1) and 1.28(1), respectively), from Rietveld analysis of synchrotron XRPD data collected at 300 K, with wavelengths of 0.39984 Å and 0.354197 Å, respectively. Site multiplicities are listed in column M. Values in parentheses are estimated errors from the least-squares fitting. The weighted-profile and expected R-factors are R_{wp} = 3.04% and R_{exp} = 2.21% (x = 0.5), and R_{wp} = 3.88% and R_{exp} = 2.82% (x = 1), respectively. The lattice constants are: a =14.6061(2) Å (x = 0.5) and 14.4611(1) Å (x = 1). The fractions of the co-existing phases for x = 0.5 are: fcc = 71.21(7)%, Cs_4C_{60} = 19.4(2)% and CsC_{60} = 9.2(3)%, and for x = 1 are fcc = 83.34(4)% and Cs_4C_{60} = 16.69(9)%.

x = 0.5	x/a	y/b	z/c	M	N	B_{iso} (Å^2)
K	0.25	0.25	0.25	8	0.319(5)	1.28(2)
Cs(1)	0.25	0.25	0.25	8	0.681(5)	1.28(2)
Cs(2)	0.5	0.5	0.5	4	1.0	5.43(4)
C(1)	0	0.04867	0.23605	96	0.5	0.53(4)
C(2)	0.20604	0.07869	0.09715	192	0.5	0.53(4)
C(3)	0.17583	0.15727	0.04867	192	0.5	0.53(4)
x = 1	x/a	y/b	z/c	M	N	B_{iso} (Å^2)
K	0.25	0.25	0.25	8	0.641(3)	1.11(2)
Cs(1)	0.25	0.25	0.25	8	0.359(3)	1.11(2)
Cs(2)	0.5	0.5	0.5	4	1.0	2.21(9)
C(1)	0	0.04916	0.23842	96	0.5	0.79(3)
C(2)	0.20812	0.07947	0.09812	192	0.5	0.79(3)
C(3)	0.17759	0.15885	0.04916	192	0.5	0.79(3)
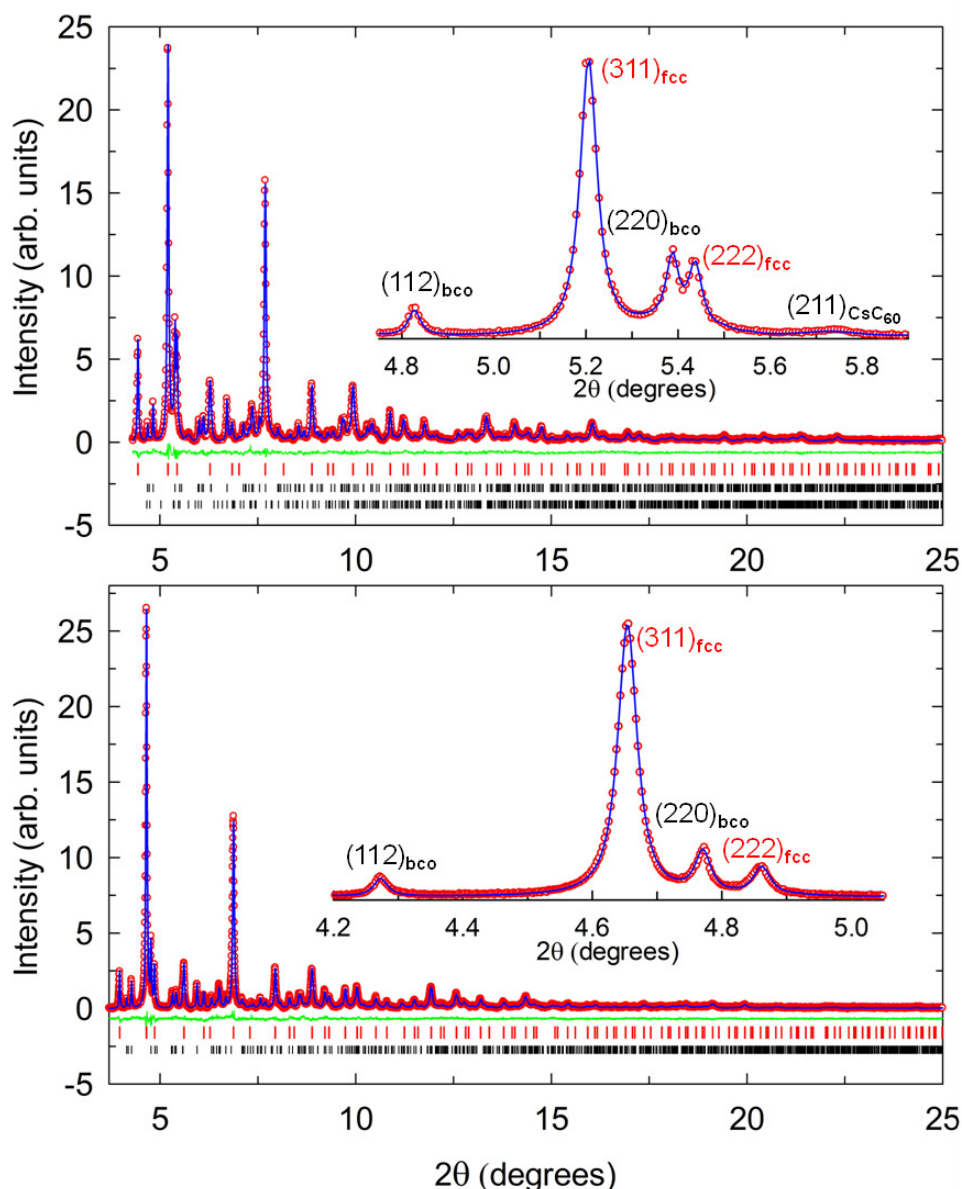
Figure 3.5 Rietveld fits to synchrotron XRPD data collected at 300 K, for fcc-rich nominal $K_{0.5}Cs_{2.5}C_{60}$ (upper panel, R_{wp} = 3.04% and R_{exp} = 2.21%, λ = 0.39984 Å), and KCs_2C_{60} (lower panel, R_{wp} = 3.88% and R_{exp} = 2.82%, λ = 0.354197 Å), phases. Red circles, blue lines and green lines represent the observed, calculated and difference profiles, respectively. Ticks mark the reflection positions, from top-to-bottom, of co-existing fcc (red ticks), body-centered-orthorhombic (bco) and CsC_{60} (observable in x = 0.5 only) phases. Both insets display expanded regions of the respective diffraction profiles; observed Bragg peaks are labelled by their (hkl) Miller indices.

Fractional site occupancy studies at 300 K

Refinement of the K^+/Cs^+ occupancy of the tetrahedral interstitial sites of the fcc structure revealed a deviation of the refined K-content from its nominal value. The reason can be traced to the incompatibility of the large Cs^+ cation size (r = 1.67 Å) with the size of the small tetrahedral hole (r = 1.12 Å) leading to a

tendency for reduced occupation of this site. Furthermore, because of the size mismatch between Cs^+ and K^+ cations, samples with nominal $x<0.5$ K-content show a greater tendency to disproportionate to the thermodynamically stable Cs_4C_{60} and CsC_{60} phases. The effect of size mismatch between the intercalants and the T_d site was previously experienced in the synthesis of $A_xCs_{3-x}C_{60}$, where A = Rb or K ($0.3 \leq x \leq 1$) [53], using a liquid ammonia route. It was found that attempts to increase the Cs content in $Rb_xCs_{3-x}C_{60}$ resulted in the absence of a concomitant increase in the unit cell size. This implied that beyond a certain limiting value, it was not possible to approach any closer the Cs-pure phase boundary. In the present study, even though there were clear discrepancies between nominal and actual values of the K content in the fcc phase, a systematic decrease of the unit cell volume was successfully observed with increasing x (Figure 3.7).

For the investigation of the stoichiometry of the fcc $K_xCs_{3-x}C_{60}$ phases, a series of test refinements of the high-statistics XRPD datasets was undertaken. As XRPD data were not collected at low temperatures for all samples, for consistency, the investigation was undertaken on datasets collected at 300 K. As a start, a test on the $K_{0.75}Cs_{2.25}C_{60}$ dataset was undertaken. Three different models were employed in the investigation: (I) the relative ratio of K:Cs in the T_d site (N_{T_d}) and U_{iso} of all atoms in the fcc phase were allowed to refine (the total occupancy of the T_d site was fixed at 1.0), (II) N_{T_d} was fixed at the nominal stoichiometry, K:Cs = 0.375:0.625 and U_{iso} was fixed at values obtained from (I), and finally (III) N_{T_d} was fixed at the nominal stoichiometry and all U_{iso} values were refined. Once the applicability of this strategy was confirmed, it was applied to all compositions in the series of samples.

Table 3.2 summarizes the resulting structural parameters of the models employed for nominal $K_{0.75}Cs_{2.25}C_{60}$. In the case of model (III), the thermal displacements of the carbon atoms refined to negative values, and those of the K and Cs atoms in the T_d site showed a pronounced increase. Model (I) gives the best fit to the data with reduced χ^2 and physically meaningful thermal displacements. To confirm that refined occupancy results in the best fit, we have examined the variation in the resulting χ^2 and B_{iso} by manually changing the relative ratio of K:Cs in the T_d site between the nominal and refined stoichiometry values for nominal

$K_{0.75}Cs_{2.25}C_{60.}$ Resulting refined parameters are presented in Figure 3.6. Reduced χ^2 goes to a minimum when the K^+ occupancy at T_d site is equal to the refined occupancy value of 0.435, then gradually increases with increasing occupancy. The variation of the fcc lattice constant, a with K^+ occupancy (between the refined and nominal occupancy values) at T_d site was also examined for the nominal $K_{0.75}Cs_{2.25}C_{60}$ and found no variation within error in a. This investigation was applied to all compositions in the series of samples, and the same trend was obtained for each sample. U_{iso} of all atoms in the fcc phase and the profile shape coefficients were kept fixed at values obtained from model (I), only the relative ratio of K:Cs distributed in the T_d site was manually changed for each test refinement.

Table 3.2 Refined structural parameters for fcc-structured phase with nominal composition $K_{0.75}Cs_{2.25}C_{60}$ for models (I), (II) and (III), from Rietveld analysis of synchrotron XRPD data collected at 300 K. Site multiplicities and fractional occupancies are listed in columns M and N, respectively. Values in parentheses are estimated errors from the least-squares fitting.

$K_{0.75}Cs_{2.25}C_{60}$		Model (I) χ^2=1.87, R_{wp}=3.6% $K_{0.87(1)}Cs_{2.13(1)}C_{60}$		Model (II) χ^2=2.14, R_{wp}=3.8% $K_{0.75}Cs_{2.25}C_{60}$		Model (III) χ^2=1.97, R_{wp}=3.7% $K_{0.75}Cs_{2.25}C_{60}$	
Atom	M	N	B_{iso} (Å^2)	N	B_{iso} (Å^2)	N	B_{iso} (Å^2)
K (T_d)	8	0.435(6)	1.09(1)	0.375	1.09(1)	0.375	1.56(3)
Cs (T_d)	8	0.565(6)	1.09(1)	0.625	1.09(1)	0.625	1.56(3)
Cs (O_h)	4	1.0	4.49(4)	1.0	4.49(4)	1.0	4.39(5)
C(1)	96	0.5	0.57(3)	0.5	0.57(3)	0.5	−0.04(4)
C(2)	192	0.5	0.57(3)	0.5	0.57(3)	0.5	−0.04(4)
C(3)	192	0.5	0.57(3)	0.5	0.57(3)	0.5	−0.04(4)
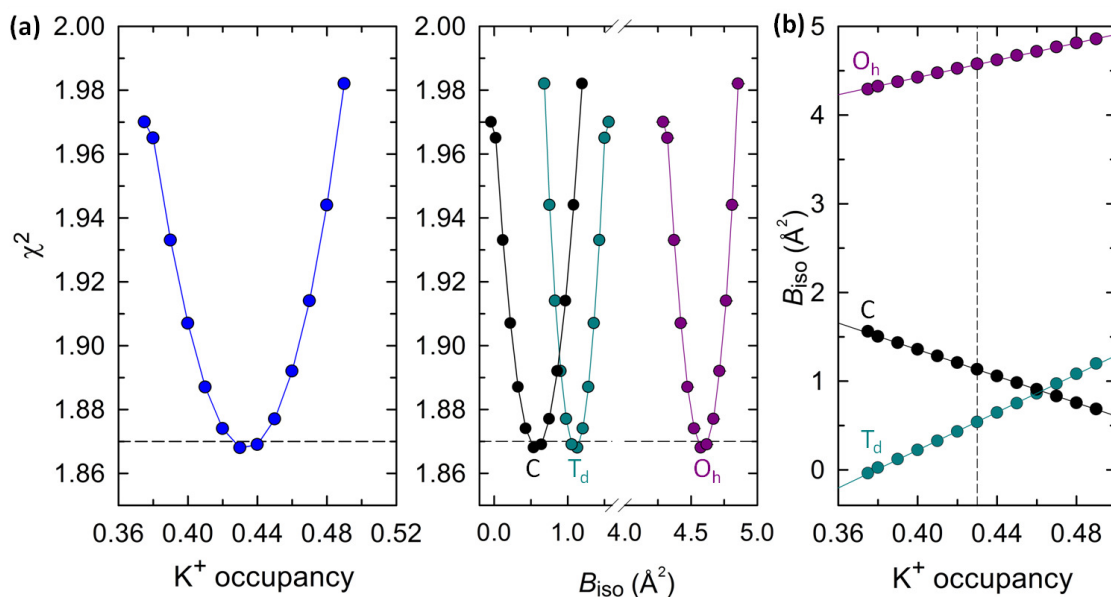
Figure 3.6 (a): Variation of χ^2 with K^+ occupancy of the T_d site and with B_{iso} for carbon (black), for atoms in the T_d site (dark green), and for Cs in the O_h site (dark pink). The solid lines are guides to the eye, and the dashed lines depict the minimum value of χ^2. (b): Evolution of B_{iso} of all atoms in fcc nominal $K_{0.75}Cs_{2.25}C_{60}$ phase with K^+ occupancy in the T_d site, with the same colour code used in (a). The solid line through the data points is a linear fit. Presented parameters obtained from Rietveld refinement to synchrotron XRPD data collected at 300 K for nominal $K_{0.75}Cs_{2.25}C_{60}$.

The final evolution of χ^2 with K content for all samples studied confirmed that χ^2 takes its minimum value when the K content is fixed at the refined value (Figure 3.7). The refined K content for each sample was found to correlate well with the fcc lattice parameter, a, at ambient temperature: Vegard's law is obeyed and a varies linearly with refined K content, x_K (Figure 3.7), with a slope of $da/dx_K = -0.234(3)$ Å. Although x_K is always larger than the nominal value for each sample, the variation of a with x_K confirms that control of the fcc lattice dimensions was successfully achieved. Zadik *et al.* have found smaller deviation of the refined x_{Rb} from the nominal Rb_x values. a was found to vary linearly with refined x_{Rb}, with smaller rate of $da/dx_{Rb} = -0.151(3)$ Å [67]. The refined fcc lattice parameters are tabulated together with the refined fcc phase fractions and K-content in Table 3.3. From now on, instead of nominal x, the refined x_K values will be used to label the samples.
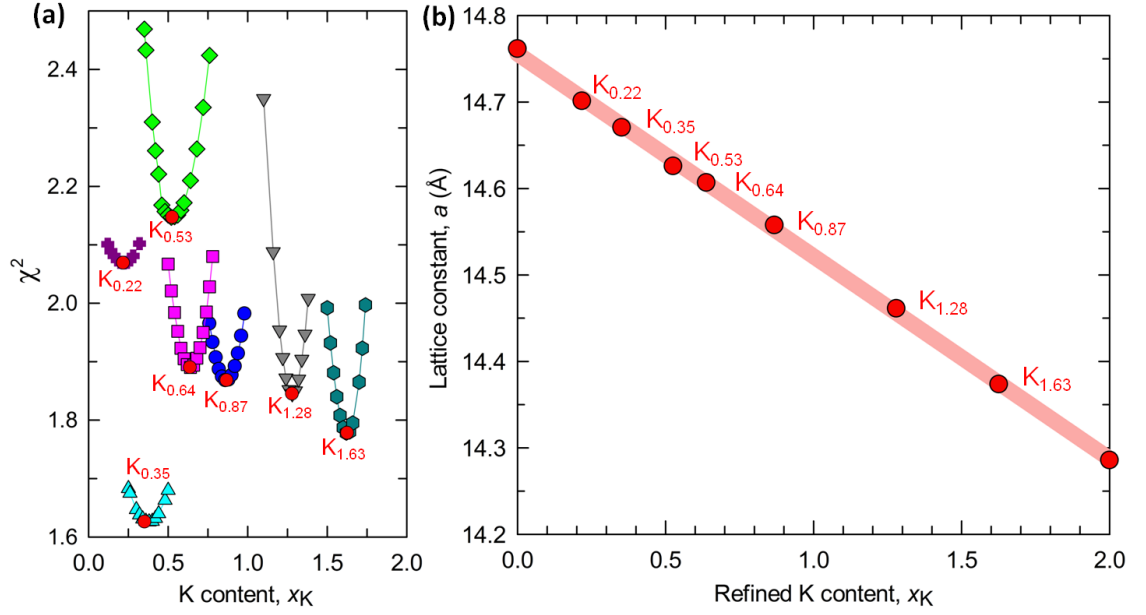
Figure 3.7 (a): Variation of χ^2 with K-content, x_K, for each sample in the series of $K_xCs_{3-x}C_{60}$; solid lines are guides to the eye, red circles represent the refined x_K for each sample at which χ^2 reduces to its minimum. (b): Variation of the ambient temperature fcc lattice constant of $K_xCs_{3-x}C_{60}$ ($0 \le x \le 2$) with refined x_K, from analysis of synchrotron XRPD data at 300 K. The $x = 0$ lattice constant is from ref.[28]; the solid line is a linear fit, yielding a value of $da/dx_K = -0.234(3)$ Å.

Table 3.3 The fcc lattice parameter and refined K-content for fcc $K_xCs_{3-x}C_{60}$ samples at 300 K. Values in parentheses are statistical errors from the least-squares fitting.

Nominal x	Refined x_K	X-ray λ (Å)	a_{fcc} (Å)	fcc phase (wt.%)	R_{wp} ; R_{exp}(%)
0.12	0.22(1)	0.39999	14.7011(2)	31.5(2)	4.90 ; 3.40
0.25	0.35(1)	0.39999	14.6736(2)	53.0(2)	5.34 ; 4.47
0.35	0.53(1)	0.39984	14.6262(5)	54.0(2)	4.11 ; 2.96
0.5	0.64(1)	0.39984	14.6061(2)	71.21(7)	3.04 ; 2.21
0.75	0.87(1)	0.39984	14.5576(2)	85.18(7)	3.55 ; 2.60
1	1.28(1)	0.35419	14.4611(1)	83.34(4)	3.88 ; 2.82
1.5	1.626(4)	0.39996	14.37345(8)	94.05(1)	4.55 ; 3.41
2	2	0.35419	14.28571(7)	100	3.76 ; 2.74

The fcc phase structural parameters obtained from the refinements and Rietveld fits to the 300 K XRPD data for $K_xCs_{3-x}C_{60}$ samples with K-content of $x_K = 0.22(1)$ and 0.53(1); 0.87(1); 1.626(4) and 2; and finally 0.35(1) are presented in Appendix I in Tables and Figures A1; A2; A3; and A4, respectively.

Table 3.4 The co-existing phase fractions for fcc-structured $K_xCs_{3-x}C_{60}$ samples at 300 K. Values in parentheses are statistical errors from the least-squares fitting.

x_K	fcc phase (wt. %)	Cs_4C_{60} (wt. %)	CsC_{60} (wt. %)
0.22(1)	31.5(2)	52.69(7)	14.9(2)
0.35(1)	53.0(2)	40.9(2)	5.7(3)
0.53(1)	54.0(2)	29.9(2)	16.1(3)
0.64(1)	71.21(7)	19.4(2)	9.2(3)
0.87(1)	85.18(7)	14.8(1)	-
1.28(1)	83.34(4)	16.69(9)	-
1.626(4)	94.05(1)	5.95(7)	-
2	100	-	-

Cation size variance in the fcc tetrahedral sites

Attfield *et al.* have reported that the superconducting T_c is highly sensitive to cation disorder in the series of $(L_{1-x}M_x)_2CuO_4$ superconductors, in which L^{3+} (La and Nd) and M^{2+} (Ca, Sr and Ba) cations are randomly distributed amongst the 'type A' lattice sites. In the same study they showed that T_c decreases linearly with increasing A-site disorder across the full range of samples with the same doping level and mean A-site radius [180]. This type of particular response of superconducting T_c to the cation disorder may be also present for the fcc $A_xCs_{3-x}C_{60}$ superconducting fullerides as a greater size mismatch between the substituted cations occupying the tetrahedral sites naturally leads to a greater cation disorder.

Cation disorder in the fcc tetrahedral interstitial sites was quantified by the variance in the distribution of the T_d site cation radii to investigate the effect of cation disorder on superconducting T_c. Attfield *et al.* studied several compositions in the series of $(L_{1-x}M_x)_2CuO_4$ superconductors and prepared the compositions with the same total doping level and mean A-site radius <r_A>, and quantified the cation disorder at the A-site by the cation size variance, σ^2, of A-site cation radii, and expressed as $\sigma^2 = \langle r_A^2 \rangle - \langle r_A \rangle^2$ [180]. In the same study, they reported that the superconducting temperature, T_c, should increase quadratically with <r_A> for superconductors containing a single CuO_2 layer, but only if there was no disorder,

and confirmed that the T_c is very sensitive to σ^2. Similar studies were undertaken on $(Ln_{1-x}M_x)MnO_3$ perovskites (Ln = rare earth, A = alkaline earth) and found that electronic and magnetic properties of these compounds are highly sensitive to the size disorder which results from the size mismatch between the substituted cations occupying the A-site [181]. Investigations into the effects of cation size disorder, which was again quantified by σ^2, on the electronic and magnetic properties of rare-earth cobaltates and manganates found that they can be rendered ferromagnetic and metallic from non-magnetic insulators by decreasing σ^2 while keeping $<r_A>$ constant [182], [183].

When we apply this expression for the series of $K_xCs_{3-x}C_{60}$ samples, where the T_d sites are randomly occupied by a disordered K^+/Cs^+ mixture (except $x = 2$) but with a fixed total occupancy of 1.0, the expression of the cation size variance at the T_d site, $\sigma^2_{r_{T_d}}$, can be written as follows:

$$\sigma^2_{r_{T_d}} = \sum x_A\, r_A^2 - \langle r_A \rangle^2 \qquad \text{Equation 3.3}$$

where x_A is the refined occupancy of the cation at the T_d site, with total occupancy at the T_d site is fixed at 1: $\sum x_A = 1$, r_A is the ionic radius (r_{K^+}= 1.38 and r_{Cs^+} = 1.67 Å) and $\langle r_A \rangle$ is the average ionic radius at the T_d site. Two representative calculation of $\sigma^2_{r_{T_d}}$ for the cation-disorder free K_2CsC_{60} and cation-disordered $K_{0.87}Cs_{2.13}C_{60}$ samples can be written as follows:

$$\sigma^2_{r_{T_d}} = [(1 \times 1.38^2) + (0 \times 1.67^2)] - [(1 \times 1.38) + (0 \times 1.67)]^2 = 0\ \text{Å}^2$$

$$\sigma^2_{r_{T_d}} = [(0.435 \times 1.38^2) + (0.565 \times 1.67^2)] - [(0.435 \times 1.38) + (0.565 \times 1.67)]^2$$

$$= 0.021(2)\ \text{Å}^2$$

where the relative cation occupancy ratio at the T_d sites for K_2CsC_{60} and $K_{0.87}Cs_{2.13}C_{60}$ are x_{K^+}: x_{Cs^+} = 1:0 and x_{K^+}: x_{Cs^+} = 0.435(6):0.565(6), respectively. The same study was then undertaken for the series of fcc $Rb_xCs_{3-x}C_{60}$ samples to compare the cation size variance in the case of K^+ and Rb^+ (r_{Rb^+}= 1.52 Å) substitution. The refined cation occupancies at the tetrahedral sites in this family were taken from ref. [67] (Table 3.5).

Table 3.5 Nominal and refined Rb-content for fcc-rich $Rb_xCs_{3-x}C_{60}$ samples [67].

Nominal x_{Rb}	Refined x_{Rb}
0.25	0.22(1)
0.35	0.33(2)
0.5	0.426(8)
0.75	0.73(1)
1	1.02(1)
1.5	1.64(1)
2	2

While the calculations of the average ionic radius and the cation size variance at the T_d site were carried out using the refined Rb-content, the nominal x_{Rb} values were used to label the $Rb_xCs_{3-x}C_{60}$ samples. The evolution of $\langle r_A \rangle$ for fcc $A_xCs_{3-x}C_{60}$ compositions (A is either K or Rb) with refined x_A at the T_d site is presented in Figure 3.8, and the variation of the cation size variance with refined x_A at the T_d site and with fcc lattice constant, a, is given in Figure 3.9. Due to the smaller ionic radius of K, $\langle r_A \rangle$ decreases at a significantly greater rate ($d\langle r_A \rangle/dx_A = -0.145$ Å and -0.075 Å, for x_K and x_{Rb}, respectively) compared to that in the Rb-substituted system.
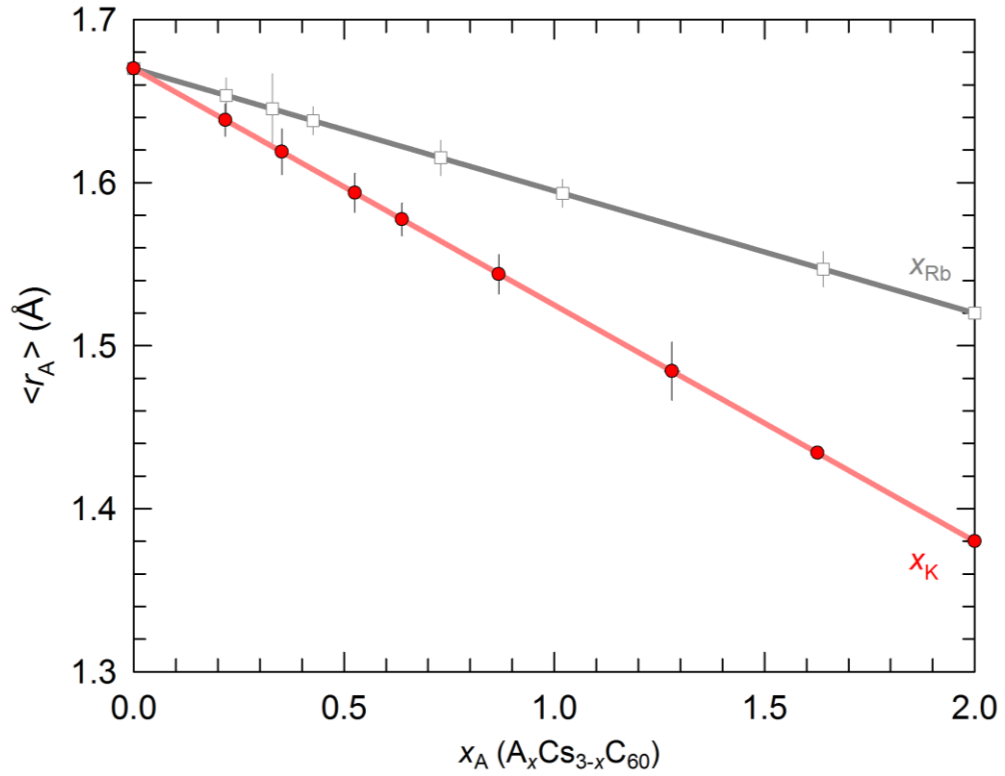
Figure 3.8 The variation of average tetrahedral site cation radius $\langle r_A \rangle$ with x_A for fcc $A_xCs_{3-x}C_{60}$ compositions where A is either K or Rb. Data for fcc $Rb_xCs_{3-x}C_{60}$ are from ref [67]. Statistical errors on $\langle r_A \rangle$ are calculated using the statistical errors of the refined site occupancies of K^+, Rb^+ and Cs^+ cations from Rietveld analysis.

The calculated variance, σ^2 gradually increases by replacing Cs^+ with K^+ or Rb^+ at the T_d interstitial sites of fcc Cs_3C_{60}, reaches a maximum, $(\sigma^2)_{max}$, for the optimally expanded $K_{0.87}Cs_{2.13}C_{60}$ ($a = 14.5576(2)$ Å) and $RbCs_2C_{60}$ (refined $x_{Rb} = 1.02(1)$, $a = 14.60211(5)$ Å). Beyond this point, with further increasing the amount of A^+ at the T_d site, σ^2 decreases with increasing x_{A^+}, producing a 'dome' shaped scaling of cation size variance with x_{A^+} and a. Whilst a dome-shaped scaling is observed for both fulleride families, at the same fcc lattice constant of ~14.60 Å, σ^2 for $K_{1.28}Cs_{1.72}C_{60}$ is $1.8(2) \times 10^{-2}$ Å^2 and $0.6(1) \times 10^{-2}$ Å^2 for nominal $RbCs_2C_{60}$. This reflects the smaller cation size disorder in the case of substitution by Rb^+. A 'dome'-shaped scaling of T_c with fcc unit cell constant, $T_c(a)$, in $Rb_xCs_{3-x}C_{60}$ system was observed [67], with nominal $RbCs_2C_{60}$ showing the maximum superconducting T_c at 32.9 K. The variation of T_c with σ^2 and a in both fulleride families will be discussed in sections 3.4.2 and 3.4.5.
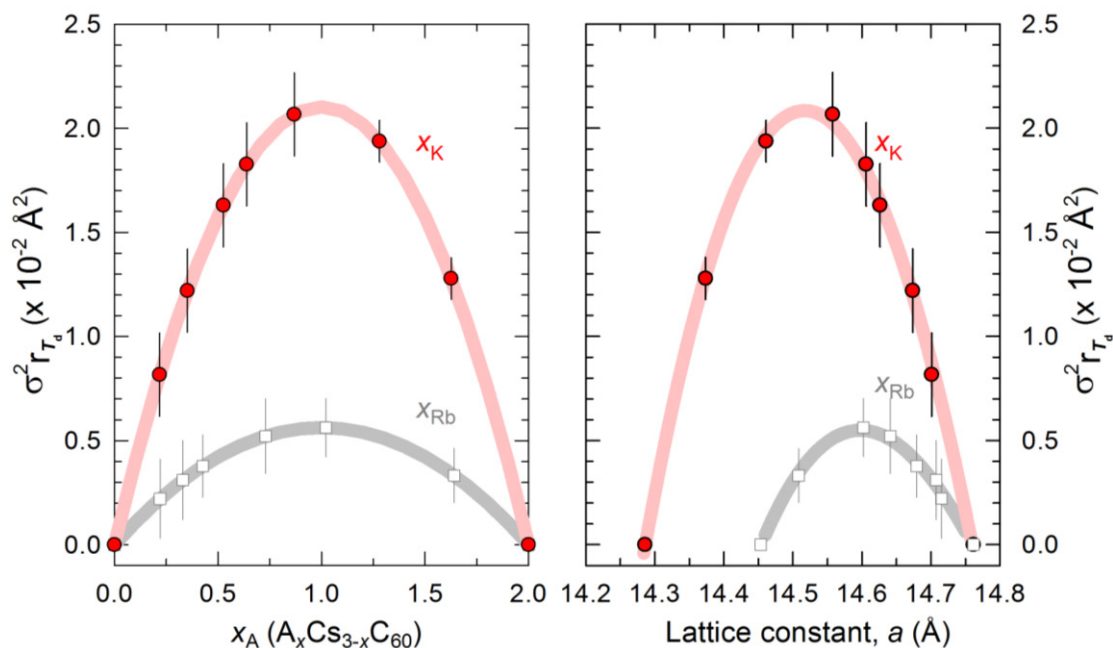
Figure 3.9 Variation of cation size variance at the T_d site with refined A^+ content and with fcc lattice constant of $A_xCs_{3-x}C_{60}$ where A^+ is either K^+ (red circles) or Rb^+ (open squares, from ref. [67]); data for $x = 0$ from ref. [28]. Solid lines through the data points in left panel are calculated using Equation 3.3 and in right panel are guides to the eye. Statistical errors on σ^2 are estimated using the statistical errors on refined site occupancies of K^+, Rb^+ and Cs^+ cations from Rietveld analysis. Statistical errors on lattice parameters are smaller than data point size.

3.3.3 Structural results at low temperatures

Rietveld analysis was undertaken for the high-resolution synchrotron XRPD data collected for $K_xCs_{3-x}C_{60}$ compositions with K-content of $x = 0.35$, 0.64, 0.87 and 1.28. All XRPD datasets except that of $x = 1.28$ were collected typically between 10 and 300 K, on beamline ID31, ESRF. Datasets for fcc $K_{1.28}Cs_{0.72}C_{60}$ were collected between 112 and 300 K on beamline BL44, SPring-8. As at ambient temperature, the same refinement model was employed. The fcc interstitial K^+/Cs^+ distribution was fixed to values found at ambient temperature. The relative phase fractions were also fixed to values refined from the 300 K datasets. The fcc phase structural parameters obtained from the refinements and two representative Rietveld fits to the XRPD data for samples with K-content of $x = 0.64$ and 0.87 are shown in Table 3.6 and Figure 3.10, respectively, and of $x = 0.35$ (Table and Figure A4) and 1.28 (Table and Figure A5) are presented in Appendix I.

Table 3.6 Refined structural parameters for fcc-structured $K_xCs_{3-x}C_{60}$ samples with K-content of $x = 0.64$ and 0.87 from Rietveld analysis of synchrotron XRPD data collected at 10 K with wavelength of 0.39984 Å. Site multiplicities are listed in column M. Values in parentheses are estimated errors from the least-squares fitting. The weighted-profile and expected R-factors for $x_K = 0.64$ and 0.87 are: $R_{wp} = 3.38\%$, $R_{exp} = 2.54\%$, and $R_{wp} = 3.62\%$, $R_{exp} = 2.89\%$, respectively. The lattice constants of $x_K = 0.64$ and 0.87 compositions at 10 K are 14.5040(1) Å and 14.4584(1) Å, respectively. Co-existing phase fractions fixed to values refined from the 300 K datasets: for $x_K = 0.64$ fcc, Cs_4C_{60}, and CsC_{60} phase fractions are 71.21%, 19.4%, and 9.2%, respectively. For $x_K = 0.87$ phase fractions of co-existing fcc and Cs_4C_{60} at 300 K are 85.18% and 14.8%, respectively.

$x = 0.64$	x/a	y/b	z/c	M	N	B_{iso} (Å²)
K	0.25	0.25	0.25	8	0.319	0.40(1)
Cs(1)	0.25	0.25	0.25	8	0.681	0.40(1)
Cs(2)	0.5	0.5	0.5	4	1.0	0.84(1)
C(1)	0	0.049014	0.237715	96	0.5	0.22(2)
C(2)	0.207491	0.079238	0.097830	192	0.5	0.22(2)
C(3)	0.177068	0.158377	0.049014	192	0.5	0.22(2)
$x = 0.87$	x/a	y/b	z/c	M	N	B_{iso} (Å²)
K	0.25	0.25	0.25	8	0.435	0.59(1)
Cs	0.5	0.5	0.5	4	0.565	0.59(1)
Cs(2)	0.5	0.5	0.5	4	1.0	1.11(1)
C(1)	0	0.045305	0.241300	96	0.5	0.33(2)
C(2)	0.209783	0.082731	0.094550	192	0.5	0.33(2)
C(3)	0.181221	0.157584	0.050230	192	0.5	0.33(2)

The temperature evolution of the fcc unit cell parameter for $x = 0.35$, 0.64, 0.87 and 1.28 (Figure 3.12), investigated with Rietveld analysis, has revealed that besides the shifts in peak positions due to the volume contraction upon cooling, no changes in relative peak width and intensities (Figure 3.11), and no phase transition to a structure with different crystal symmetry are apparent. However, for $x = 0.35$, 0.64 and 0.87, the variation of lattice metrics with temperature

appears non-monotonic. Upon cooling, an anomalous rapid shrinkage of the unit cell size is seen at a certain temperature. The onset temperature of this lattice decrease increases with decreasing unit cell size, through increasing K^+ content, and the transition extends over a broader temperature range. On the other hand, no anomalies are seen in unit cell volumes of fcc $K_{1.28}Cs_{1.72}C_{60}$ and Cs_3C_{60} [28] on cooling and typical thermal contraction upon cooling to low temperature is observed over the experimental temperature range.
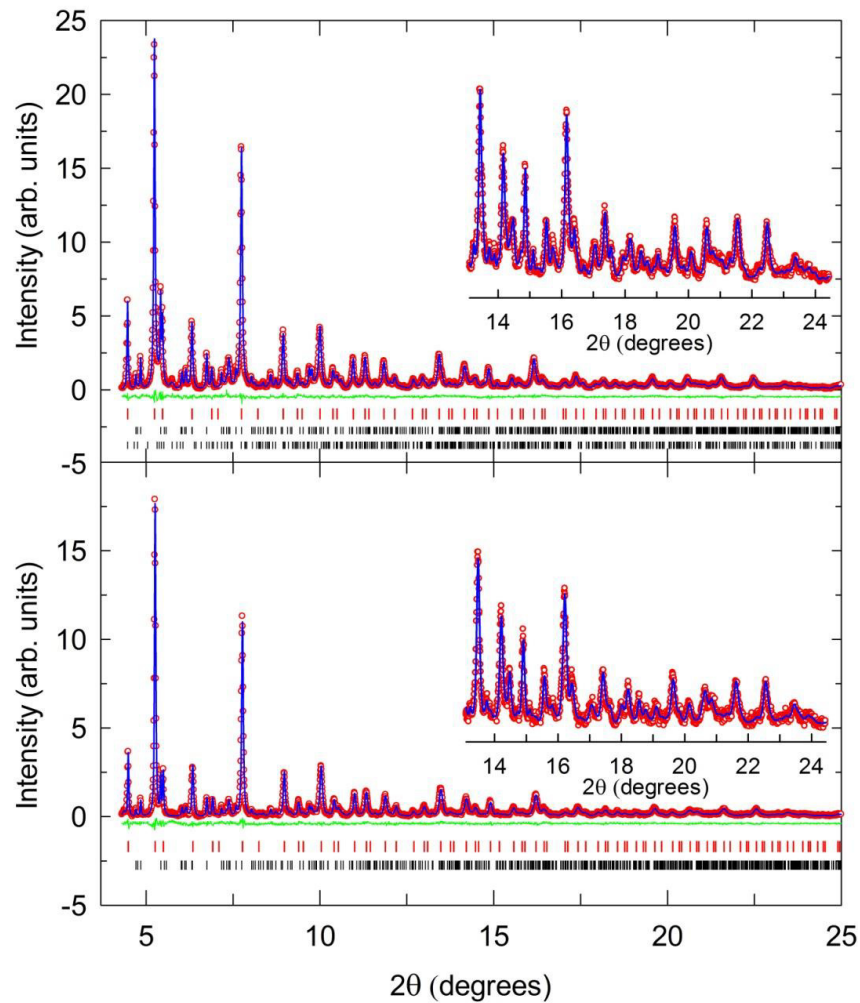
Figure 3.10 Rietveld fits to synchrotron XRPD data collected at 10 K for fcc-structured $K_xCs_{3-x}C_{60}$ samples with K-content of $x = 0.64$ (upper panel) and $x = 0.87$ (lower panel) with $\lambda = 0.39984$ Å. Red circles, blue lines and green lines represent the observed, calculated and difference profiles, respectively. Ticks mark the reflection positions, from top-to-bottom, of co-existing fcc (red ticks), body-centered-orthorhombic (bco) and CsC_{60} (observable in $x = 0.64$ only) phases. Both insets display expanded regions of the respective diffraction profiles at high Bragg angles.

To investigate whether or not the space group $Fm\bar{3}m$ is preserved to low temperatures or phase co-existence is present, we examined the temperature

evolution of the full-width-at-half-maximum (FWHM) for two relatively intense isolated fcc Bragg peaks: (311) and (220), from $x = 0.35$ and 0.64 which yield the most pronounced rapid shrinkage of the unit cell size on cooling. If any such issues were present, some peak broadening across the temperatures where the anomalies are seen would have been anticipated; however, there is little variation of the peak widths over the experimental temperature range and no changes at any specific temperatures are evident (Figure 3.11). In accordance with this, it can be concluded that it is an isosymmetric collapse of the unit cell volume as there is no symmetry-lowering transition and the space group $Fm\bar{3}m$ is preserved to low temperatures.
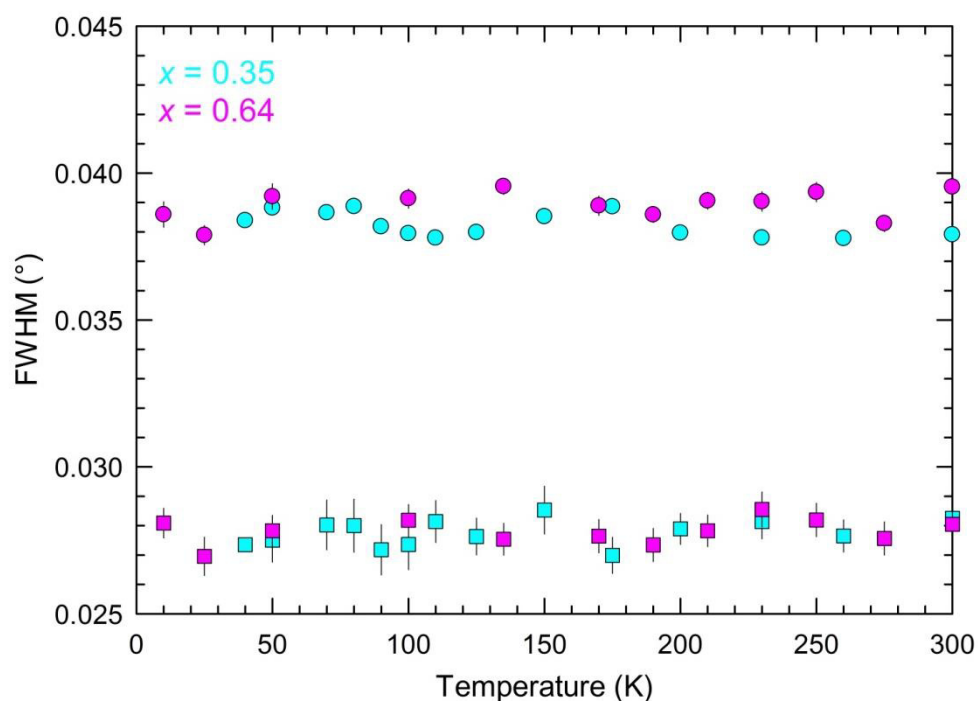
Figure 3.11 The temperature evolution of the full-width-at-half-maximum (FWHM) of the (311) (circles) and 220 (squares) Bragg peaks of fcc-structured $K_xCs_{3-x}C_{60}$ samples with $x = 0.35$ and 0.64.

The temperature dependence of the unit cell volume, $V(T)$ (Figure 3.12) was modelled using a Debye-Grüneisen model and employing Equation 2.37 to fit the $V(T)$ data above the anomaly onsets for the $x = 0.35$, 0.64 and 0.87 compositions (Section 2.3.6) [134]. The Debye temperature, Θ_D, of each sample was fixed to that obtained for fcc Cs_3C_{60} ($\Theta_D = 218$ K [28]). Comparable behaviour was observed for the $V(T)$ response in fcc $Rb_xCs_{3-x}C_{60}$ ($0.25 \leq x \leq 1.5$) [67] which also shows distinct anomalies at well-defined temperatures (Figure 3.12).
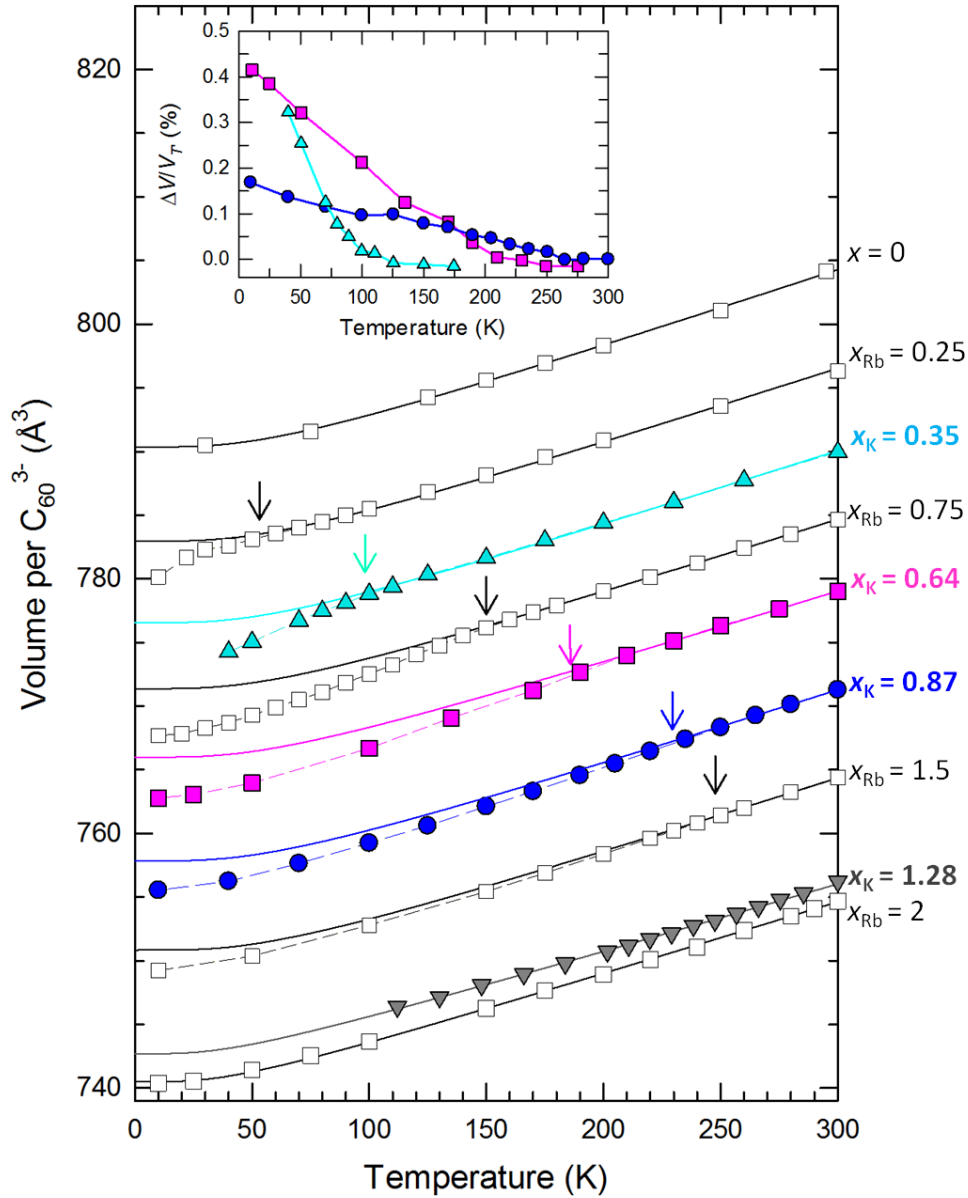
Figure 3.12 The temperature evolution of volume, V, occupied per C_{60}^{3-} anion for fcc-structured $K_xCs_{3-x}C_{60}$ samples with x_K = 0.35, 0.64, 0.87 and 1.28, for fcc-structured $Rb_xCs_{3-x}C_{60}$ samples with x_{Rb} = 0.25, 0.75, 1.5 and 2 [67], and for Cs_3C_{60} [28]. Arrows mark the onset temperatures of the change in lattice response, denoted T, where present. The solid lines through the data are Debye-Grüneisen fits for $T > T$ (or over all T for x = 0, x_K = 1.28 and x_{Rb} = 2). The dotted lines through the data at $T < T$ are guides to the eye. Inset: Temperature dependence of the normalised volume change, $\Delta V/V_T$ for x_K = 0.35, 0.64 and 0.87. Statistical errors in V per C_{60}^{3-} from Rietveld analysis are smaller than the data point size.

This isosymmetric collapse in unit cell volume was attributed to a metal-to-insulator (MI) crossover, evidenced by both the temperature dependence of the magnetic susceptibility and of the $1/^{13}T_1T$ (^{13}C spin-lattice relaxation rates divided by temperature) data [67]. It is consistent with a lower unit cell size for the metallic phase compared with the insulating phase, $\Delta V_{MI} = V_M - V_I < 0$ – according to

the virial theorem, a transition from localised to itinerant behaviour lowers the volume [184], [185]. In a similar way, we also attribute the collapse in unit cell volume on cooling to the occurrence of an insulator-to-metal crossover. This is also corroborated by SQUID magnetometry data discussed later in section 3.4.4. The Mott insulator-to-metal transition is of first order and ends at a critical point in the volume-temperature electronic phase diagram [186]. The absence of a phase co-existence in the XRPD (and complementary NMR) data implies that all samples in the present study lie above the critical temperature for the MIT.

The inset in Figure 3.12 shows the temperature dependence of the normalised volume change, $\Delta V/V_{T'}$, for $x = 0.35$, 0.64 and 0.87, where ΔV is the difference between volume per C_{60}^{3-} derived from the Debye-Grüneisen fits extrapolated below the onset temperatures of the change in lattice response, T' and that extracted from Rietveld analysis at given experimental temperatures below T'. $V_{T'}$ is the volume per C_{60}^{3-} at T'. $\Delta V/V_{T'}$ approaches the same value of $\sim 0.4\%$ for overexpanded $x = 0.35$ and 0.64, but the isosymmetric transition becomes smeared out at $x = 0.87$, and only a value of $\sim 0.17\%$ is reached at 10 K.

Derived parameters from the Debye-Grüneisen fits to the $V(T)$ data of both fcc $K_x Cs_{3-x} C_{60}$ and $Rb_x Cs_{3-x} C_{60}$ families and the variation of T' with volume, V, occupied per C_{60}^{3-} at T' are summarised in Table 3.7 and Figure 3.13, respectively. T' values of $x_K = 0.35$, 0.64 and 0.87 are in excellent agreement with those found for fcc $Rb_x Cs_{3-x} C_{60}$. The $V(T)$ data for the full temperature range were included for $K_{1.28}Cs_{1.72}C_{60}$ which shows no anomaly over the full temperature range; however, lack of low-temperature data points necessitated the use of a fixed value of Θ_D –this was fixed to 152 K which is the value for metallic Rb_2CsC_{60} [67] (Figure 3.12).

Table 3.7 Summary of resulting parameters from the Debye-Grüneisen fits to the $V(T)$ data of fcc $K_xCs_{3-x}C_{60}$, of fcc $Rb_xCs_{3-x}C_{60}$ [67], and of fcc Cs_3C_{60} [28]. T is the insulator-to-metal crossover temperature, defined as the first point of deviation, on cooling, between V from experiment and V calculated for the high-temperature insulating phase. The symbols '*' and '**' label the data from [28] and [67], respectively (in italics).

x_A	T range (K)	V_0 (Å³)	Θ_D (K)	I_V (Å³ K⁻¹)	T(K)	V/C_{60}^{3-} at T (Å³)
x = 0*	*30 – 295*	*3161.4(7)*	*218*	*0.246(7)*	*-*	*-*
x_{Rb} = 0.25**	*50 - 300*	*3131.8(3)*	*218*	*0.240(3)*	*50*	*783.126(8)*
x_K = 0.35	100 - 300	3106.2(3)	218	0.239(2)	100	778.82(6)
x_{Rb} = 0.75**	*160 – 300*	*3085.5(1)*	*218*	*0.235(7)*	*150*	*776.16(1)*
x_K = 0.64	210 – 300	3063.9(7)	218	0.231(4)	190	772.65(3)
x_K = 0.87	265 – 300	3031.4(6)	218	0.238(1)	235	767.39(3)
x_{Rb} = 1.5**	*280 – 516*	*3003.3(5)*	*218*	*0.2388(8)*	*260*	*762.01(5)*
x_K = 1.28	110 – 300	2973.8(2)	152	0.216(2)	-	-
x_{Rb} = 2**	*10 – 570*	*2962.0(3)*	*152(6)*	*0.2293(9)*	*-*	*-*
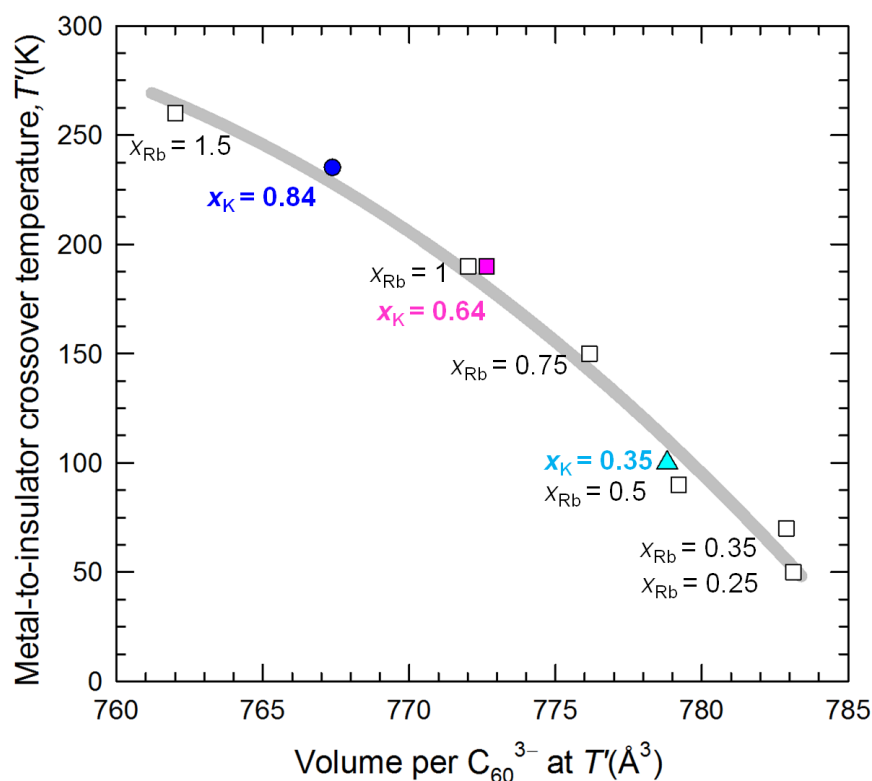
Figure 3.13 Variation of the metal-to-insulator crossover temperature (T) (from XRPD data) with volume, V, occupied per C_{60}^{3-} at T, for various fcc $K_xCs_{3-x}C_{60}$ and $Rb_xCs_{3-x}C_{60}$ samples. Data for $Rb_xCs_{3-x}C_{60}$ compounds are from ref. [67]. The solid line through the data points is guide to the eye.

3.3.4 Summary of structural results at ambient pressure

The investigation of XRPD data collected under ambient conditions for fcc-structured $K_xCs_{3-x}C_{60}$ has revealed that the unit cell size of fcc Cs_3C_{60} was successfully chemically pressurised through substitution of the smaller K^+ for the Cs^+ cation. V decreases linearly with increasing x down to the literature value reported for fcc K_2CsC_{60} [30], [41], indicative of good fcc phase stoichiometry control. Temperature evolution of the unite cell size for selected compounds to low temperatures shows that while the insulating $x = 0$ analogue exhibits a typical thermal contraction behaviour, decreasing the unit cell volume leads to well-defined volume changes upon cooling at well-defined temperatures. Moreover, the onset temperature of volume change increases with increasing x with no evidence for any lattice symmetry change upon cooling. Therefore, the transition was concluded to be isosymmetric in nature.

3.3.5 Structural results at high pressure at 7 K

In this section, Rietveld analysis results of high-resolution synchrotron XRPD data collected for fcc-structured $K_xCs_{3-x}C_{60}$ samples with K-content of $x = 0.35$, 0.87 and 1.28 at 7 K will be presented. In this section, the same structural model was employed to that used in the ambient pressure data analysis. There were, however, certain differences in the Rietveld model used: isotropic thermal displacement parameters of carbon, which were constrained to take the same value, were only allowed to refine at the lowest pressure (typically ~0.3 GPa) and then fixed at all other pressures. The fcc phase K^+/Cs^+ occupancies were fixed to those values found at 300 K (section 3.3.2) and were kept fixed at all other pressures. No absorption correction was employed, in contrast to the ambient pressure data analysis. The pressure evolution of the XRPD profiles for fcc-rich $K_{0.87}Cs_{2.13}C_{60}$ and $K_{1.28}Cs_{1.72}C_{60}$ is presented in Figure 3.14, and Rietveld fits to the XRPD data for the two compositions at low and high pressure are shown in Figure 3.15 and Figure 3.16. The corresponding structural parameters for the majority fcc phase for $K_{0.87}Cs_{2.13}C_{60}$, obtained from Rietveld refinement are listed in Table 3.8, and for $x = 0.35$ (Table and Figure A6) and 1.28 (Table A7) are presented in Appendix II together with the Rietveld fits (for $x = 0.35$) to the XRPD data.
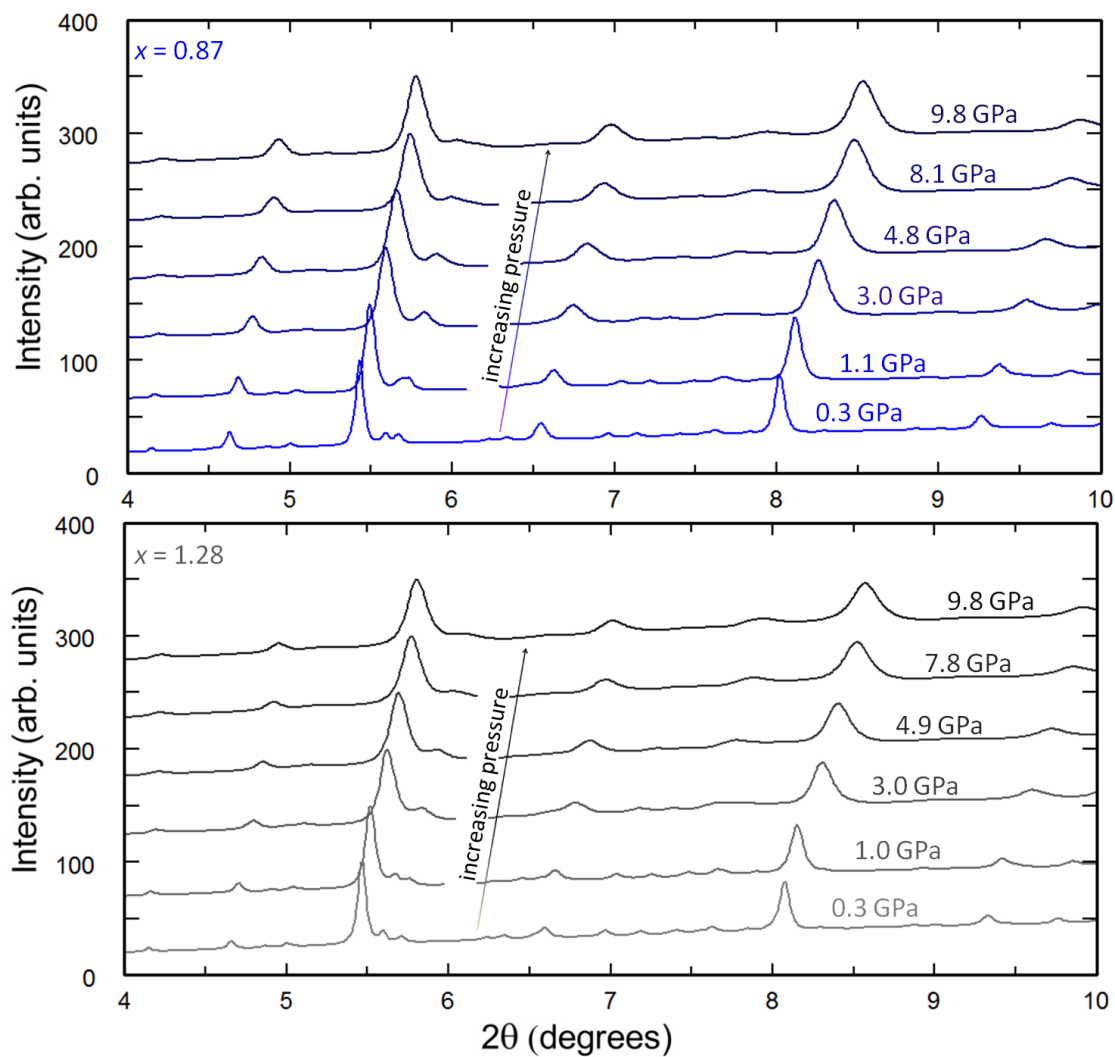
Figure 3.14 Pressure evolution of synchrotron XRPD profiles, collected at 7 K, for fcc-rich $K_{0.87}Cs_{2.13}C_{60}$ (upper panel) and $K_{1.28}Cs_{1.72}C_{60}$ (lower panel), with $\lambda = 0.41238$ Å. Intensities are normalized to the most intense peak and offset for clarity.
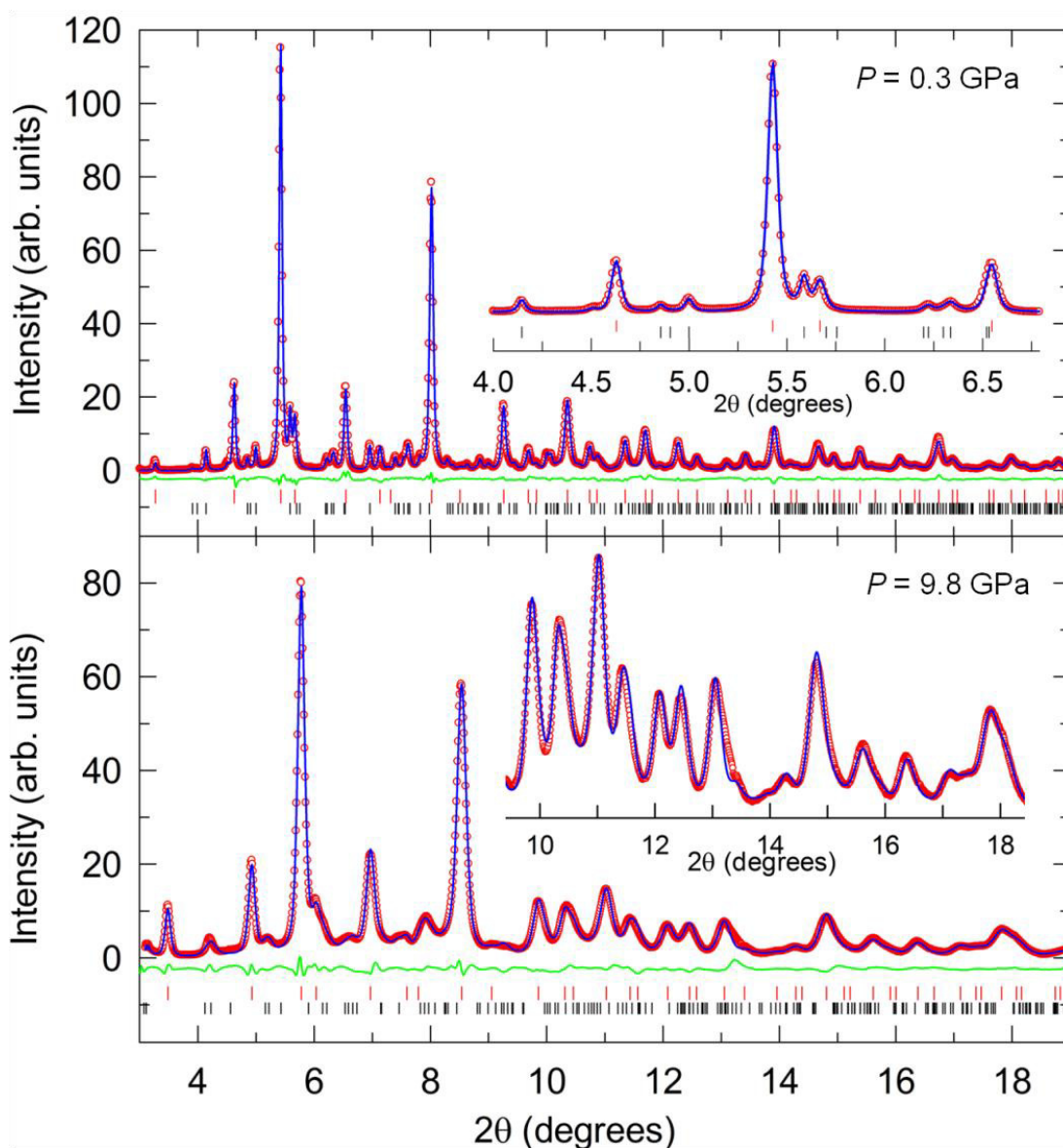
Figure 3.15 Rietveld fits to high-pressure synchrotron XRPD data collected at 7 K for fcc-rich $K_{0.87}Cs_{2.13}C_{60}$ at 0.3 GPa (upper panel) and 9.8 GPa (lower panel), with $\lambda = 0.41238$ Å . Red circles, blue lines and green lines represent the observed, calculated and difference profiles. Ticks mark the reflection positions of co-existing fcc (red ticks) and body-centered-orthorhombic (bco) phases. The insets display expanded regions of the respective diffraction profiles at low and high Bragg angles, respectively. The fitted background contribution has been subtracted for clarity.
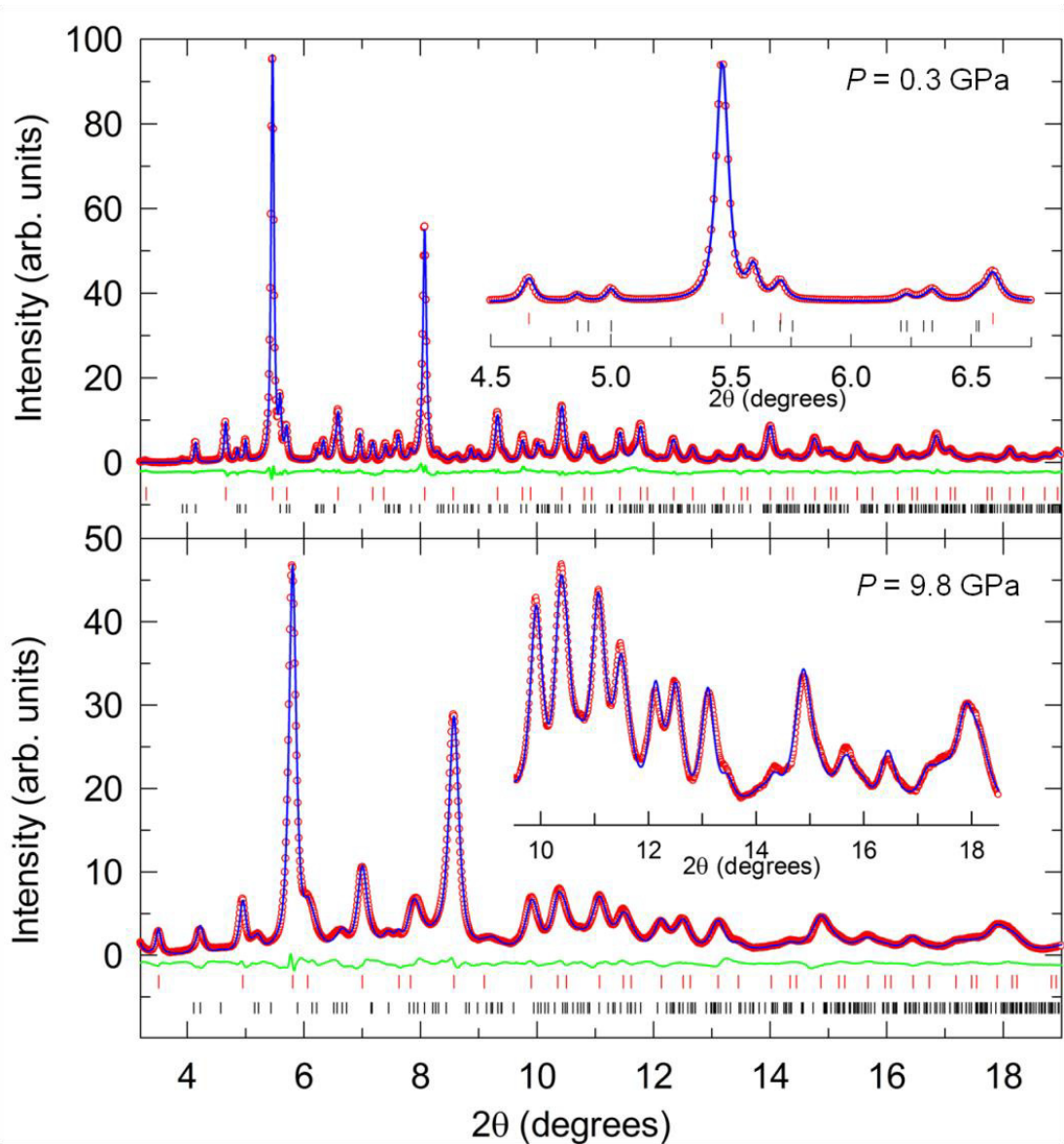
Figure 3.16 Rietveld fits to high-pressure synchrotron XRPD data collected at 7 K for fcc-rich $K_{1.28}Cs_{1.72}C_{60}$ at 0.3 GPa (upper panel) and 9.8 GPa (lower panel), with $\lambda = 0.41238$ Å . Red circles, blue lines and green lines represent the observed, calculated and difference profiles. Ticks mark the reflection positions of co-existing fcc (red ticks) and body-centered-orthorhombic (bco) phases. The insets display expanded regions of the respective diffraction profiles at low and high Bragg angles, respectively. The fitted background contribution has been subtracted for clarity.

Table 3.8 Structural parameters for the majority fcc phase of $K_{0.87}Cs_{2.13}C_{60}$ extracted from Rietveld analysis of synchrotron XRPD data collected at 7 K at 0.3 and 9.8 GPa ($\lambda = 0.41238$ Å). The fractional site occupancies, N of the tetrahedral site were fixed to values obtained from the analysis of 300 K high statistics data, as described earlier (Table 3.3). Values in parentheses are statistical errors from Rietveld refinement. The weighted-profile and expected R-factors are: $R_{wp} = 0.56\%$ and $R_{exp} = 0.39\%$ (at 0.3 GPa), and $R_{wp} = 0.67\%$ and $R_{exp} = 0.38\%$ (at 9.8 GPa). Refined fcc and bco phase fractions at 0.3 GPa are 84.02(5)% and 16.3(2)%, respectively.

$K_{0.87}Cs_{2.13}C_{60}$, $a_{7K, 0.3 GPa}$ = 14.4468(1) Å, fcc phase fraction: 84.02(5)%					
P = 0.3 GPa	x/a	y/b	z/c	N	B_{iso} (Å^2)
K	0.25	0.25	0.25	0.435	0.92(3)
Cs(1)	0.25	0.25	0.25	0.565	0.92(3)
Cs(2)	0.5	0.5	0.5	1.0	1.42(4)
C(1)	0	0.04921	0.23866	0.5	0.44(4)
C(2)	0.20831	0.07955	0.09822	0.5	0.44(4)
C(3)	0.17777	0.15900	0.04920	0.5	0.44(4)

$K_{0.87}Cs_{2.13}C_{60}$, $a_{7K, 9.8 GPa}$ = 13.5821(3) Å					
P = 9.8 GPa	x/a	y/b	z/c	N	B_{iso} (Å^2)
K	0.25	0.25	0.25	0.435	0.92
Cs(1)	0.25	0.25	0.25	0.565	0.92
Cs(2)	0.5	0.5	0.5	1.0	1.42
C(1)	0	0.05234	0.25385	0.5	0.44
C(2)	0.22158	0.08462	0.10448	0.5	0.44
C(3)	0.18909	0.16913	0.05234	0.5	0.44

The compressibility behaviour of the three compositions was investigated using the pressure dependence of the fcc unit cell volume data, $V(P)$, extracted from Rietveld analysis, followed by modelling the $V(P)$ data for each composition with the Murnaghan EoS (Equation 2.28). The $V(P)$ trends for each sample together with a least-squares fit to the Murnaghan EoS are presented in Figure 3.17 and the derived EoS fit parameters are tabulated in Table 3.9.
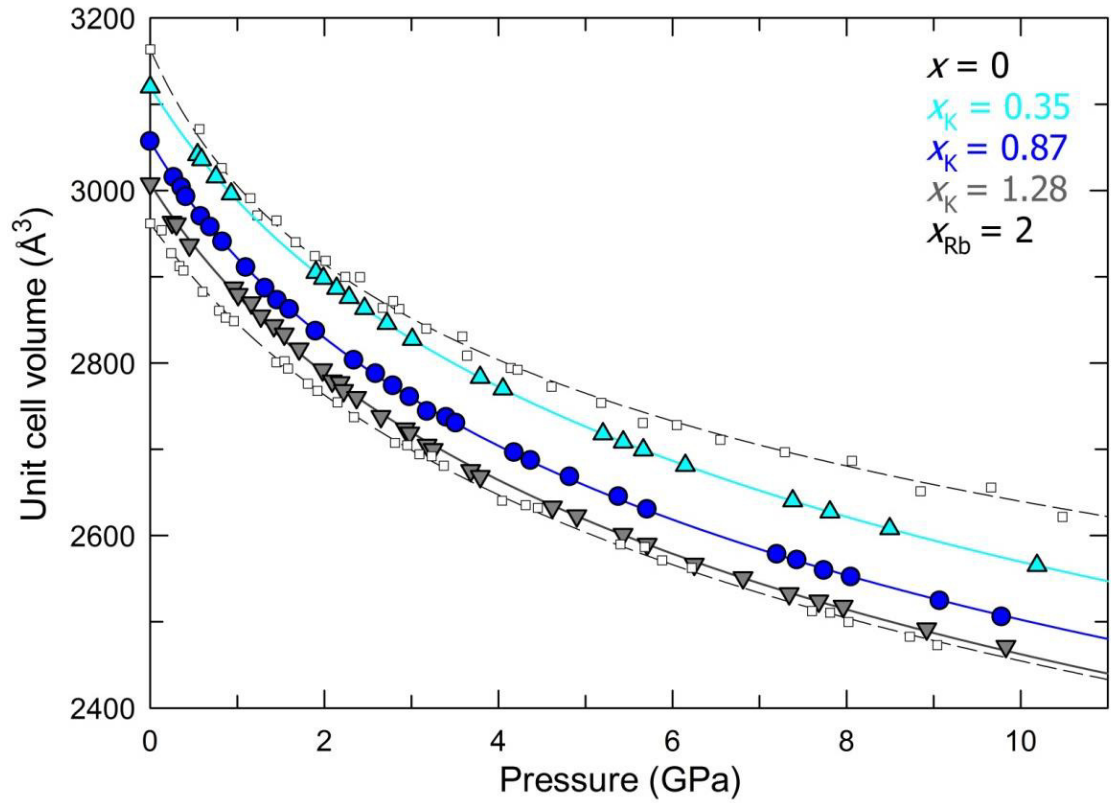
Figure 3.17 Pressure evolution of fcc unit cell volume at 7 K for $K_xCs_{3-x}C_{60}$; x_K = 0.35, 0.87 and 1.28. Data for fcc Cs_3C_{60} at 15 K (dashed line through squares) from ref. [28] and for Rb_2CsC_{60} at 7 K (dashed line through squares) from ref. [67] are also presented for comparison. The lines through the data points show results from least-squares fits to second-order Murnaghan EoS. Statistical errors in V from Rietveld analysis are smaller than the data point size.

Table 3.9 Derived parameters from the Murnaghan EoS fits to the 7 K $V(P)$ data for fcc $K_xCs_{3-x}C_{60}$ (x_K = 0.35, 0.87, 1.28), for fcc Rb_2CsC_{60} [67], and for fcc Cs_3C_{60} [28]. The literature data are labelled with the symbol '*' (in italics). Statistical errors from the least-squares fits are in parentheses.

x_A	K_0 (GPa)	K'_0	$\kappa = d\ln V/dP$ (GPa^{-1})	V_0 (Å^3)
*x = 0**	*13.7(3)*	*13.0(3)*	*0.073(2)*	*3163.6*
x_K = 0.35	19.0(1)	9.00(1)	0.0526(3)	3120(1)
x_K = 0.87	17.9(2)	8.94(9)	0.0559(6)	3057(1)
x_K = 1.28	18.7(6)	8.6(2)	0.053(2)	3008(3)
*x_{Rb} = 2**	*20.9(3)*	*8.8(2)*	*0.0479(7)*	*2961.9*

The present results are consistent with those from previously reported studies on the compressibility of fcc A_3C_{60} (A = K, Rb, Cs) [28], [67], [187], [188], *i.e.* an average volume compressibility of 0.041(3) GPa^{-1} for K_3C_{60} and Rb_3C_{60} [187]. The values of K_0, K'_0 found here experimentally are typical for fcc A_3C_{60}; K_0 = 14(1) GPa, K'_0 =10.0(3) reported for Rb_3C_{60} obtained from Murnaghan EoS at ambient temperature [188]. In conclusion, our $V(P)$ data presently available reveals that the series of fcc-structured $K_xCs_{3-x}C_{60}$ materials shows a smooth compressibility behaviour over the experimental pressure range (P < 11 GPa) with no evidence for any change in crystal symmetry.

3.4 Magnetic properties of $K_xCs_{3-x}C_{60}$ (0.12 ≤ x ≤ 2)

In the following sections, the investigation of the magnetic properties of fcc $K_xCs_{3-x}C_{60}$ (0.12 ≤ x ≤ 2) using the Magnetic Property Measurement System (MPMS XL) Superconducting Quantum Interference Device (SQUID) magnetometer will be presented. The overall setup of the SQUID and experimental procedures for different type of SQUID magnetisation measurements were outlined in Section 2.6.5.

3.4.1 Experimental methods

SQUID magnetisation measurements at ambient pressure were carried out on ~20-25 mg powder samples, loaded in thin-walled 5 mm-diameter Suprasil® quartz ampoules for SQUID measurements of air sensitive materials, evacuated to ~1×10^{-4} mbar using a glass high-vacuum manifold setup with a Leybold vacuum PT70B turbo pump for 20 minutes, filled with a small He gas pressure (typically ~400 mbar) and sealed.

Three different types of data collection were performed at ambient pressure for magnetic characterisation. The superconducting properties were investigated by low-field (10-20 Oe) magnetisation measurements as a function of temperature under both zero-field-cooled (ZFC) and field-cooled (FC) protocols. Temperature dependence of the magnetisation was investigated between 1.8 and 300 K under FC protocol at 3 and at 5 T. Finally, magnetisation measurements were undertaken at 295 and 5 K as a function of applied field between 0 and 5 T.

High-pressure SQUID magnetisation measurements were also carried out on ~20-25 mg samples of fcc $K_xCs_{3-x}C_{60}$ ($0.35 \leq x \leq 2$) as a function of temperature using an EasyLab MCell 10 high-pressure cell. The details about the assembly of the high-pressure cell and experimental setup are provided in Section 2.6.7. Data were collected at temperatures between 1.8 and 40 K, under magnetic fields of 20 Oe using a ZFC protocol, at pressures between ~0.3-10.5 kbar.

3.4.2 Ambient pressure, low-field magnetisation measurements

The temperature dependence of magnetisation, $M(T)$, for all $K_xCs_{3-x}C_{60}$ ($0.12 \leq x \leq 2$) samples, collected under a ZFC protocol, is shown in Figure 3.18. Figure 3.19 shows $M(T)$ data for selected samples collected under both ZFC and FC protocols.
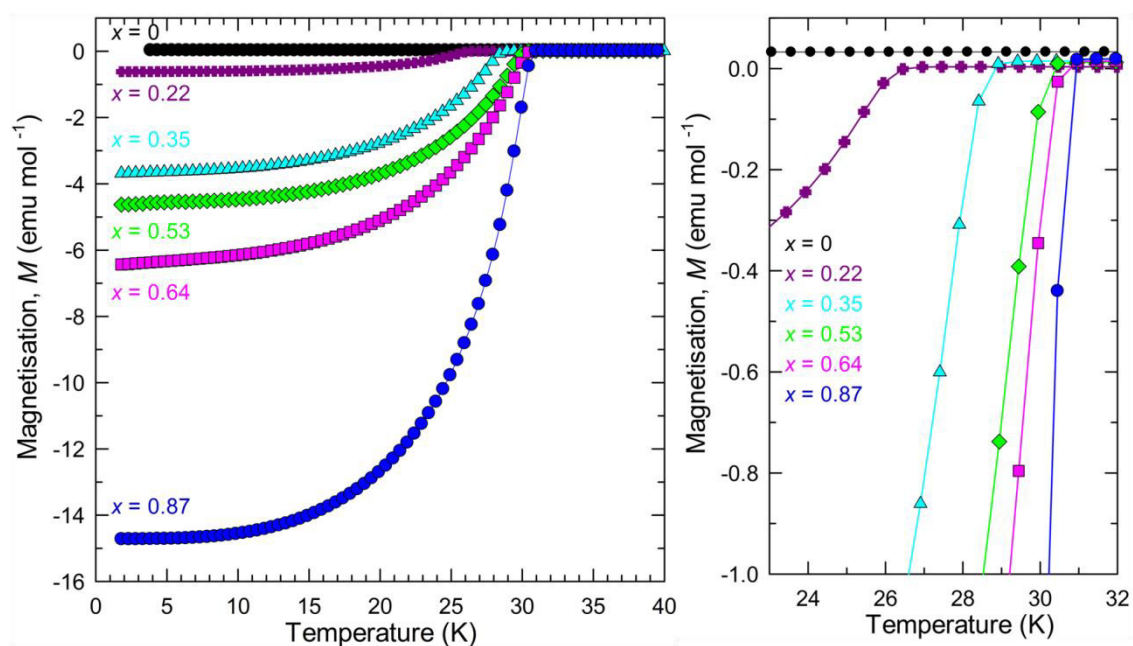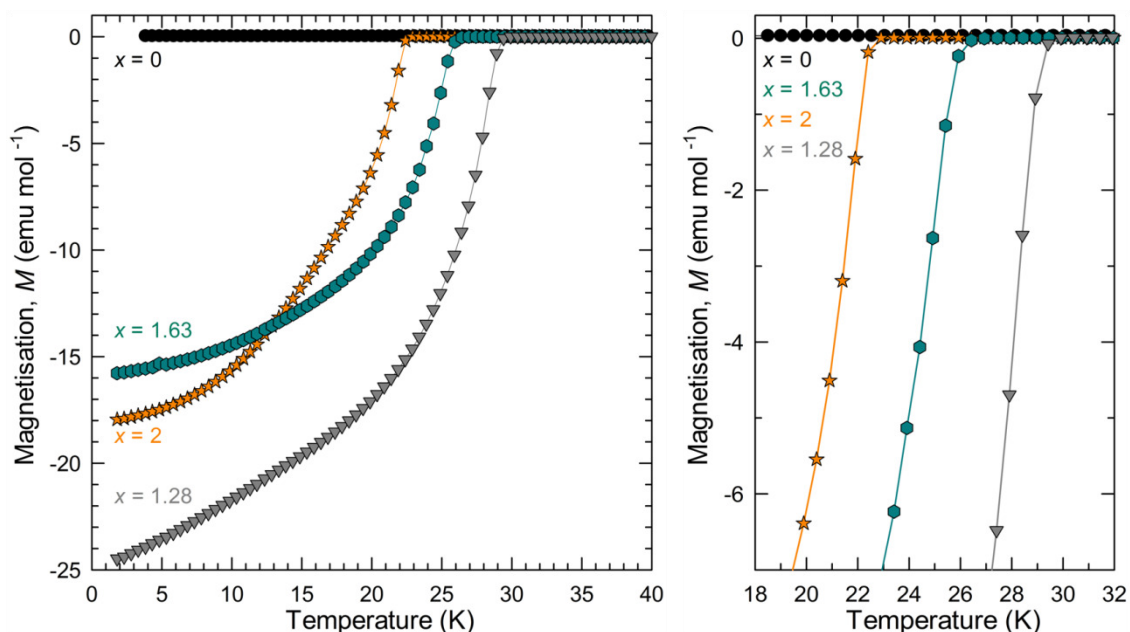
Figure 3.18 Temperature dependence of the ZFC magnetisation, M, of fcc $K_xCs_{3-x}C_{60}$ ($0.22 \leq x \leq 2$), divided by the applied magnetic field (20 Oe for $x = 0.35$ and 1.28, 10 Oe for other samples). Right panels display expanded regions of the respective $M(T)$ data around the temperatures where diamagnetic shielding starts; more expanded ($x \leq 0.87$) and less expanded ($1.28 \leq x \leq 2$) samples are shown in different panels for clarity.

Superconductivity is observed in the series of $K_xCs_{3-x}C_{60}$ ($0.22 \leq x \leq 2$) samples with onset superconducting transition temperatures T_c ranging from 22.8 to 30.6 K. The shielding fraction and superconducting T_c vary with K-content. The $M(T)$ data for K_2CsC_{60} shows a very tiny kink at $\sim$19 K which might correspond to superconducting T_c for K_3C_{60}, albeit no Bragg reflections from K_3C_{60} phase could be detected with synchrotron XRPD data. Shielding fractions were estimated from the ZFC data using Equation 2.45 (Table 3.10). The small magnitude of the FC magnetisation signal indicates that pinning in the samples is extremely strong, with little magnetic field expulsion. T_c values of fcc-structured $K_xCs_{3-x}C_{60}$ both at ambient and high pressures were derived from the first derivatives of ZFC and FC datasets with respect to temperature (Figure 3.20). The first points of deviations were chosen to represent T_c for each sample. These are tabulated in Table 3.10 together with the estimated shielding fractions and fcc phase fractions (extracted from Rietveld analysis). Estimated shielding fractions in the series of $K_xCs_{3-x}C_{60}$ samples range from 10% (for $x = 0.35$) to 52% (for $x = 2$). Dahlke *et al.* synthesised a series of fcc-rich $K_xCs_{3-x}C_{60}$ and $Rb_xCs_{3-x}C_{60}$ samples using a liquid ammonia solution technique and reported shielding fractions of 30-50% ($0.64 \leq x_K \leq 0.97$) and 25-60% ($0.32 \leq x_{Rb} \leq 1$) from ZFC magnetisation measurements [53]. Zadik *et*

al. reported estimated shielding fractions of 32-91% in the series of Rb$_x$Cs$_{3-x}$C$_{60}$ (0.35 ≤ x ≤ 2) samples [67].
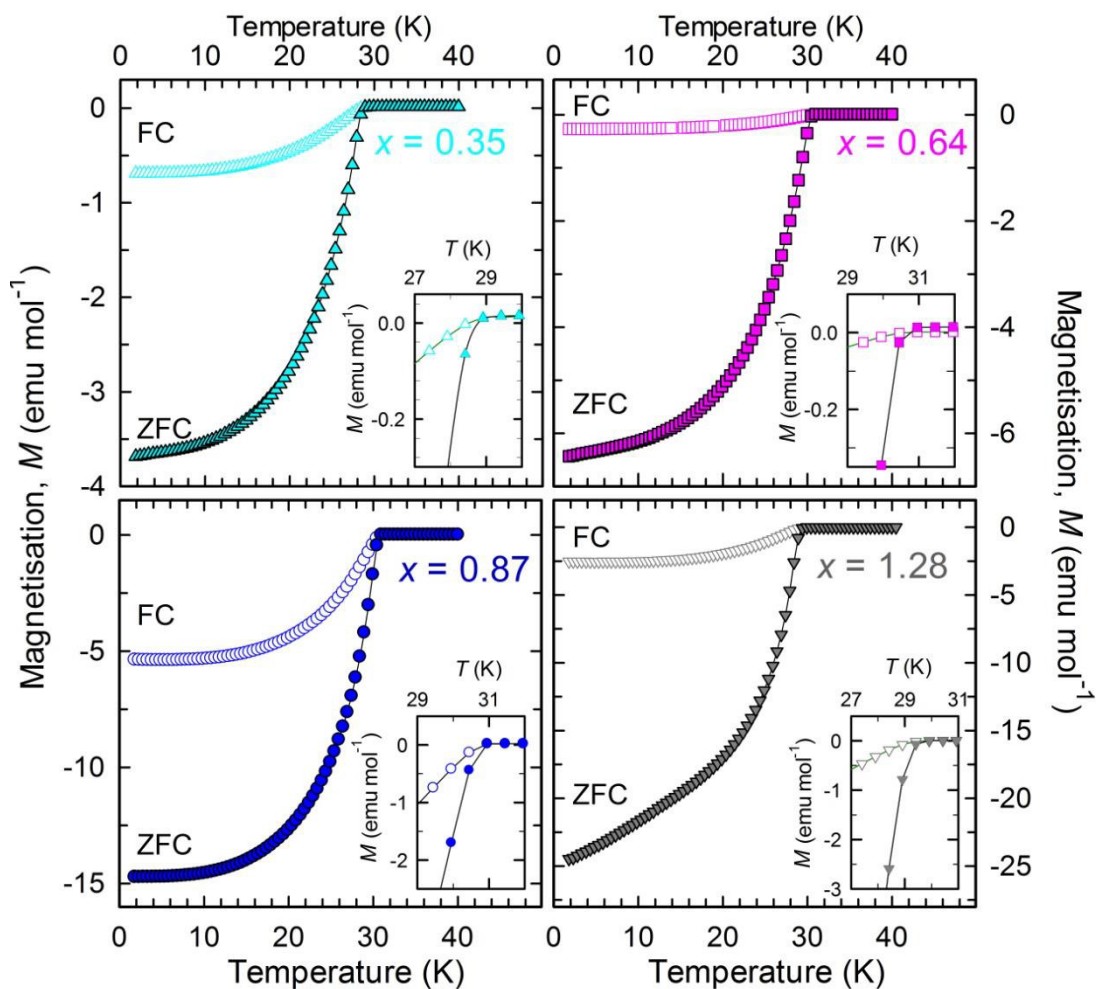
Figure 3.19 Temperature dependence of the magnetisation, *M*, under both ZFC and FC protocols, divided by the applied magnetic field (20 Oe for x = 0.35 and 1.28, 10 Oe for x = 0.87 and 0.64) for the series of compounds, K$_x$Cs$_{3-x}$C$_{60}$ (0.35 ≤ x ≤ 1.28). Insets show expanded regions of the respective *M*(*T*) data near the superconducting T_c.
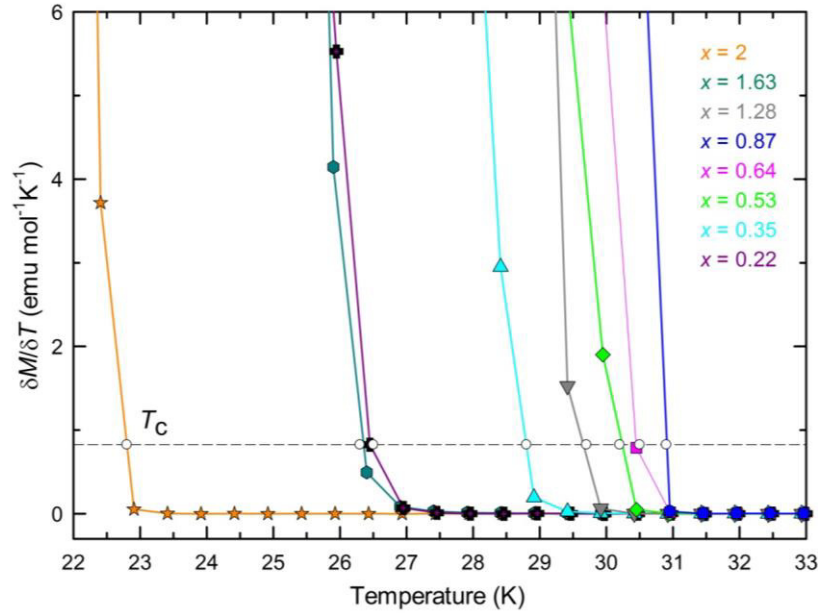
Figure 3.20 Temperature evolution of the first derivative of ZFC magnetisation dataset with respect to temperature for $K_xCs_{3-x}C_{60}$. The dashed line represents the T_c line at which the open black edged circles signify the corresponding T_c values for each sample (see Table 3.9 for details).

Table 3.10 Superconducting T_c and estimated shielding fractions (SF) at ambient pressure for $K_xCs_{3-x}C_{60}$ ($0.22 \leq x \leq 2$) samples. Applied magnetic field is 20 Oe for $x = 0.35$ and 1.28 and 10 Oe for other samples.

Refined x_K	T_c (K)	SF (%)	fcc phase (wt.%)	Refined x_K	T_c (K)	SF (%)	fcc phase (wt.%)
0.22(1)	26.5	16	31.5(2)	0.87(1)	30.9	40	85.18(7)
0.35(1)	28.8	10	53.0(2)	1.28(1)	29.7	33	83.27(4)
0.53(1)	30.2	13	54.0(2)	1.626(4)	26.3	44	94.05(1)
0.64(1)	30.5	17	71.21(7)	2	22.8	52	100

In contrast to the monotonic response of superconducting T_c to the volume contraction observed in the underexpanded A_3C_{60} superconductors, the variation of T_c with refined x_K, $T_c(x_K)$, (Figure 3.21) and with unit cell volume $T_c(V)$, is reminiscent of the pressure-induced $T_c(V)$ behaviour in both superconducting Cs_3C_{60} polymorphs [28] and of the $T_c(V)$ and $T_c(x_{Rb})$ behaviour in fcc-rich $Rb_xCs_{3-x}C_{60}$ ($0.25 \leq x \leq 2$) [67] (Figure 3.22) displaying a 'dome' shaped scaling of T_c with x_K and V.
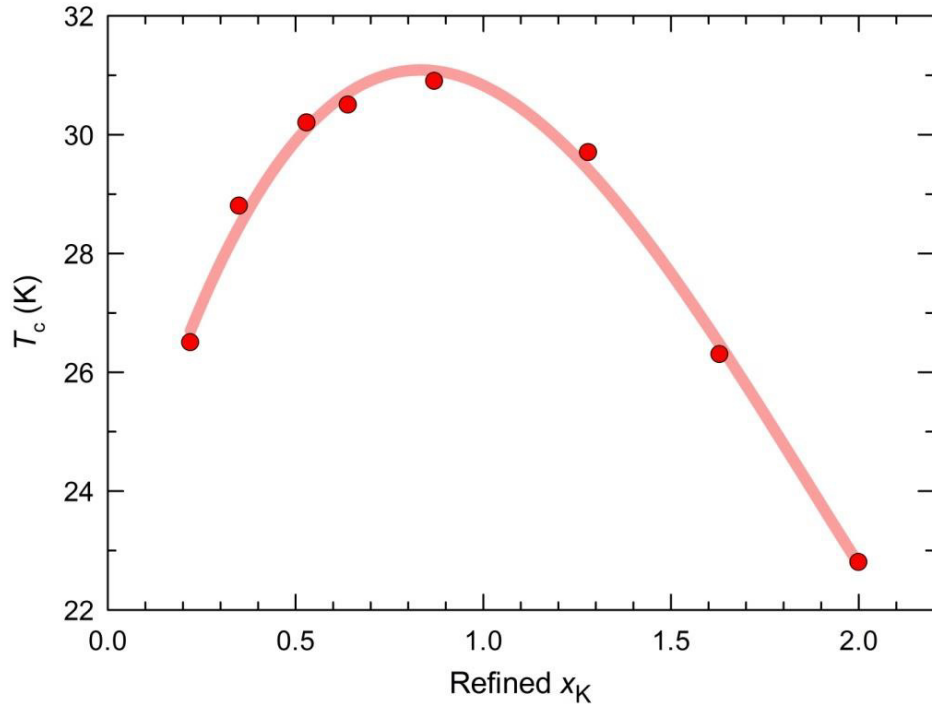
Figure 3.21 Variation of superconducting T_c with refined K-content, x_K, for $K_xCs_{3-x}C_{60}$ ($0.22 \leq x \leq 2$). The solid line is guide to the eye.

Unit cell volume for the series of $K_xCs_{3-x}C_{60}$ samples at T_c has been estimated through extrapolation of the volume determined from Rietveld analysis of datasets collected at low temperature. However, as low-temperature XRPD datasets were only available for x_K = 0.35, 0.64, 0.87 and 1.28, V at $T = T_c$ for the remaining compositions of x_K = 0.22, 0.53, 1.63 and 2 was estimated using the parameters obtained from the Debye-Grüneisen fits (Equation 2.37) to the available $V(T)$ data. As seen in Figure 3.22, the variation of T_c for fcc $K_xCs_{3-x}C_{60}$ mimics the $T_c(V)$ and $T_c(x)$ behaviour of $Rb_xCs_{3-x}C_{60}$ and fcc Cs_3C_{60}, forming distinct dome shapes; however, there is a significant suppression of T_c at a given V in the K-series despite the comparable unit cell volumes to those of the Rb-doped analogues and fcc Cs_3C_{60}. This can be tentatively attributed to the greater cation disorder in the fcc tetrahedral interstitial sites of the series of $K_xCs_{3-x}C_{60}$ samples than that of the $Rb_xCs_{3-x}C_{60}$ family. Attfield *et al.* reported that the superconducting T_c decreases linearly with increasing A-site disorder, quantified by σ^2, in three different A_2CuO_4 series, with fixed mean A-site radius $<r_A>$, and general formula of $(La_{0.925-f}Nd_fSr_{0.075-g-h}Ca_gBa_h)_2CuO_4$ [180].
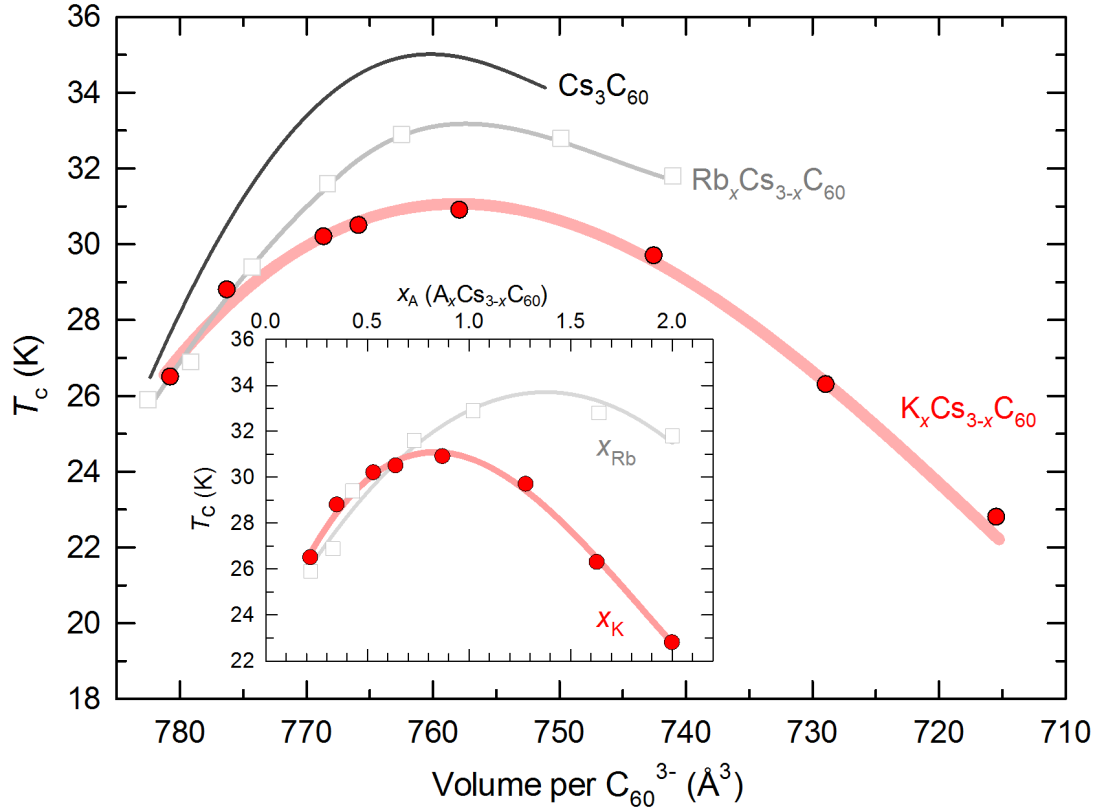
Figure 3.22 Variation of superconducting T_c with volume, V, occupied per C_{60}^{3-} anion at $T = T_c$ for $K_xCs_{3-x}C_{60}$ (0.22(1) $\leq x \leq$ 2), for $Rb_xCs_{3-x}C_{60}$ (0.22(1) $\leq x \leq$ 2) [67] at ambient pressure and for fcc Cs_3C_{60} at low temperature and under pressure [28]. Volumes per C_{60}^{3-} for $K_xCs_{3-x}C_{60}$ at T_c are estimated by extrapolation of the volumes determined from low-temperature structural data (Section 3.3.3). The inset shows the dependence of superconducting T_c on x_K (red circles) and x_{Rb} (open squares). Solid lines are guides to the eye.

For fcc $A_xCs_{3-x}C_{60}$, A is either K or Rb. σ^2 in the fcc tetrahedral interstitial sites gradually increases with x_A within the compositional range where superconducting T_c also increases with x_A. However, once reaching a maximum in σ^2, $(\sigma^2)_{max}$, with further increasing x_A, σ^2 rapidly decreases together with T_c, exhibiting a dome shaped scaling. Although a dome shaped scaling of σ^2, with x_A and fcc lattice constant is found in both families, $(\sigma^2)_{max}$ in the $Rb_xCs_{3-x}C_{60}$ family is significantly (~3.2 times) smaller than that in $K_xCs_{3-x}C_{60}$ (Section 3.3.2). $(\sigma^2)_{max}$ in the two families corresponds to $K_{0.87}Cs_{1.13}C_{60}$ with a T_c of 30.9 K and $RbCs_2C_{60}$ with a T_c of 32.9 K, which are the maximum superconducting T_c, $(T_c)_{max}$, found at ambient pressure, as seen in Table 3.11.

Table 3.11 Calculated cation size variance for the tetrahedral interstices of fcc $A_xCs_{3-x}C_{60}$ where A is either K or Rb, together with superconducting T_c and volume/C_{60} at $T = T_c$ for each sample. Data for $Rb_xCs_{3-x}C_{60}$ are from ref. [67]. Statistical errors in parentheses are calculated using the estimated errors on refined fractional occupancies of K^+, Rb^+ and Cs^+ cations in the tetrahedral sites of fcc $A_xCs_{3-x}C_{60}$ from Rietveld analysis. For the $x = 2$ compositions, full occupancy of the tetrahedral and octahedral sites by K or Rb and Cs were assumed in accordance with the results of the complementary NMR studies. The symbol '*' depicts the maximum values of cation size variance and T_c (in italics).

x_K	$\sigma^2_{r_{T_d}}$ (Å^2)	T_c (K)	V/C_{60}^{3-} (Å^3)	x_{Rb} nominal; refined	$\sigma^2_{r_{T_d}}$ (Å^2)	T_c (K)	V/C_{60}^{3-} (Å^3)
0	0	0	-	0; 0	0	0	-
0.22(1)	0.008(2)	26.5	780.9	0.25; 0.22(1)	0.002(2)	25.9	782.5
0.35(1)	0.012(2)	28.8	776.3	0.35; 0.33(2)	0.003(2)	26.9	779.1
0.53(1)	0.016(2)	30.2	768.6	0.5; 0.426(8)	0.004(2)	29.4	774.3
0.64(1)	0.018(2)	30.5	765.7	0.75; 0.73(1)	0.005(2)	31.6	768.3
*0.87(1)**	*0.021(2)*	*30.9*	*757.9*	*1; 1.02(1)**	*0.006(1)*	*32.9*	*762.5*
1.28 (1)	0.019(1)	29.7	742.5	1.5; 1.64(1)	0.004(1)	32.8	749.9
1.626(4)	0.013(1)	26.3	728.9	2; 2	0	31.8	741.0
2	0	22.8	715.6				

Compositions of fcc $K_xCs_{3-x}C_{60}$ and $Rb_xCs_{3-x}C_{60}$ with approximately the same fcc unit cell volume show different T_c. This behaviour might indicate that previous assumptions about the identical effect of chemical [41] and physical pressure [187] on the variation of T_c in fcc $A_xCs_{3-x}C_{60}$ superconductors is not valid for our work where the tetrahedral sites are occupied by a disordered mixture of K^+/Cs^+ (or Rb^+/Cs^+[67]). A study on Rb_3C_{60} reported that applying physical pressure to Rb_3C_{60} reduces the lattice parameter to that of K_3C_{60} and leads to approximately the same T_c for both materials [41]. In contrast, a later study reported some deviation in the variation of T_c with fcc unit cell volume when comparing physical and chemical (*i.e.* K substitution) means of reducing the Rb_3C_{60} lattice parameter [172]. In accordance with combined results of this work and the study reported by Zadik *et al.*, we tentatively propose that the effect of 'chemical' and 'physical' pressure on T_c differs in cases where a chemically-induced cation disorder is present (*i.e.* K, Rb, Cs substitution). This topic will be discussed further in section 3.5.

3.4.3 Ambient pressure, field-dependent magnetisation measurements

In order to determine the lower critical field, H_{c1}, the field-dependent magnetisation, $M(H)$, has been measured at 5 K for the most expanded fcc-rich composition, $K_{0.53}Cs_{2.47}C_{60}$, at applied fields between 0-2000 Oe. H_{c1} was estimated as the field at which a deviation from linear $M(H)$ behaviour is seen. Detailed information about alternative types of measurement methods employed for the estimation of H_{c1} can be found in a review study reported by Buntar and Weber [189].

Not many studies on the measurements of H_{c1} in overexpanded fcc $A_xCs_{3-x}C_{60}$ systems have been undertaken besides that by Zadik *et al.* [67]. Estimations of H_{c1} (0 K) are as follows: 55-81 Oe for $RbCs_2C_{60}$ [190], 75 Oe for $Rb_{0.32}Cs_{2.68}C_{60}$ [53], 120 Oe [191] for Rb_3C_{60} and 132 Oe for K_3C_{60} [192]. Zadik *et al*. estimated H_{c1} (5 K) for two fcc-rich $Rb_{0.35}Cs_{2.65}C_{60}$ and Rb_2CsC_{60} samples as 100-120 Oe and 120-140 Oe, respectively[67]. The temperature dependence of H_{c1} can be formulated as: $H_{c1}(T) = H_{c1}$ (0 K) $[1 - (T/T_c)^2]$ [191] which allows to estimate H_{c1} (0 K). Figure 3.23 shows the $M(H)$ curve for $K_{0.35}Cs_{2.65}C_{60}$ at 5 K together with a least squares linear fit to $M(H)$, at low fields between 0-160 Oe. The first deviation from linearity upon increasing the applied field is seen between 120-140 Oe, corresponds to an estimated value of 123-144 Oe for H_{c1} (0 K). To highlight the onset of deviation, $\Delta M = M_{calculated} - M_{exp}$ was also plotted as a function of applied field (Figure 3.24). $M_{calculated}$ is the magnetisation at each applied field calculated from the resulting linear fit parameters and M_{exp} is the measured magnetisation.
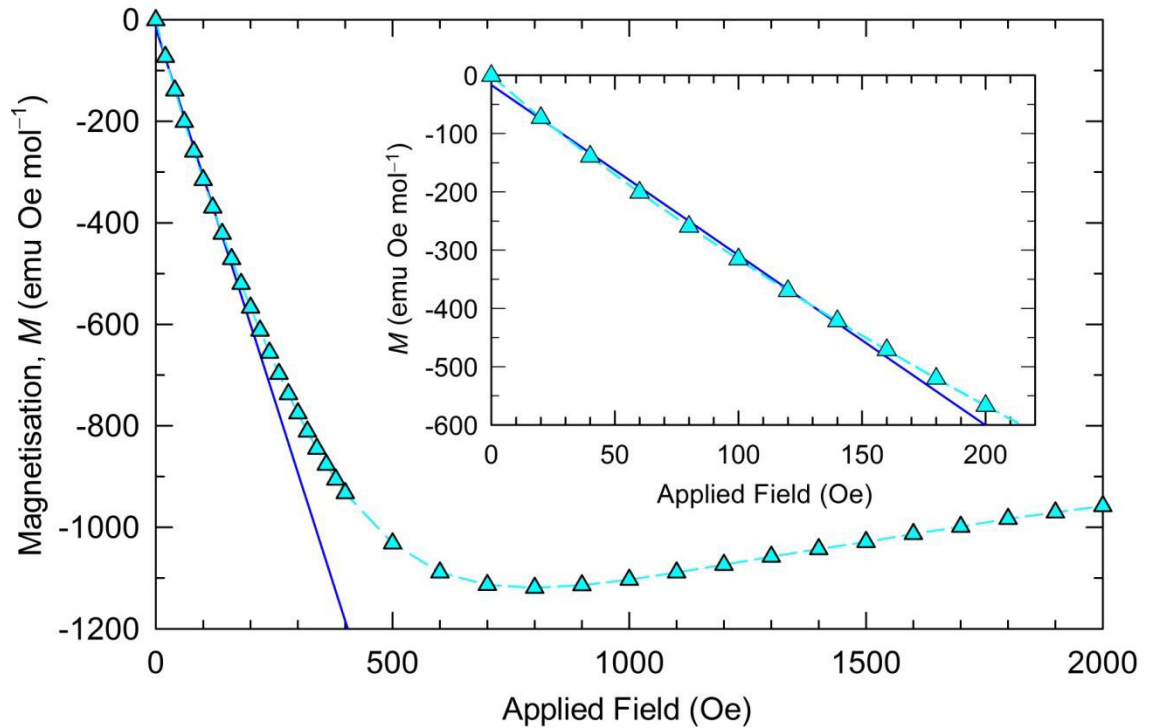
Figure 3.23 The field-dependence of magnetisation, $M(H)$, at 5 K for $K_{0.35}Cs_{2.65}C_{60}$ (fcc phase fraction 52.7(2)%). Dotted line is guide to the eye and the solid line through the data points is a linear fit to $M(H)$ at low fields (0-160 Oe).
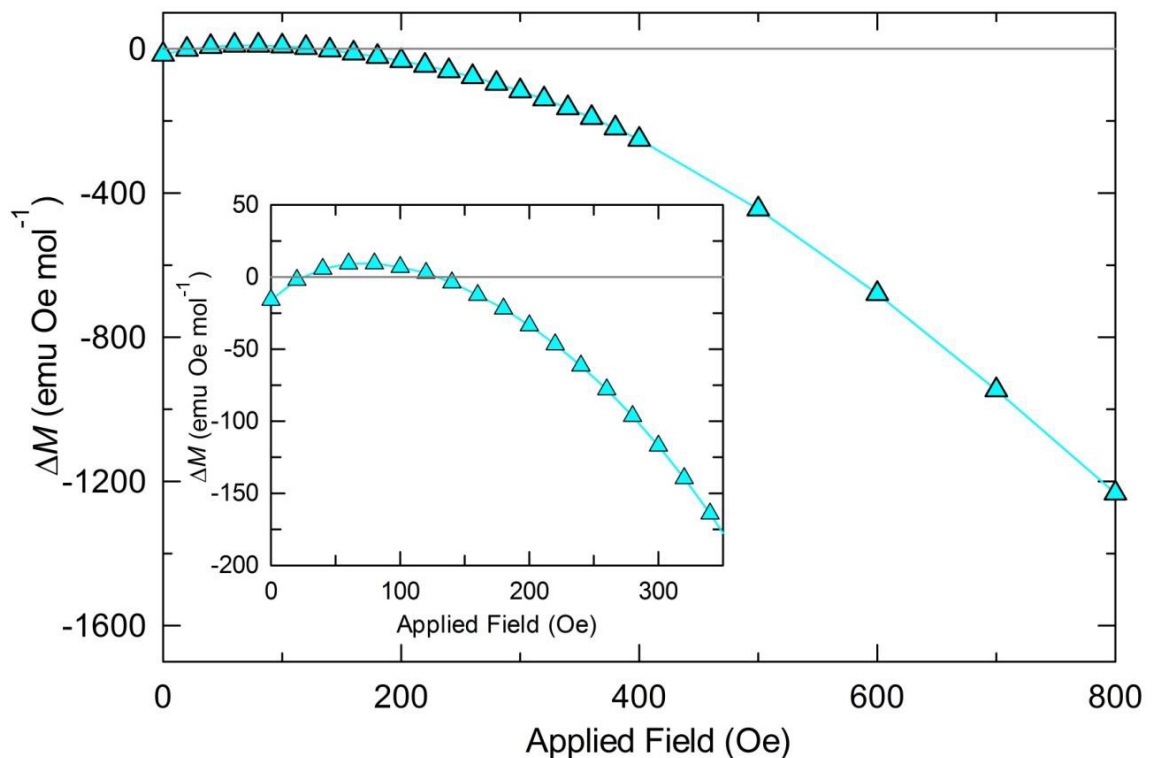
Figure 3.24 The variation of ΔM with applied field, H, at 5 K, for $K_{0.35}Cs_{2.65}C_{60}$ where $\Delta M = M_{calculated} - M_{exp}$, and $M_{calculated}$ is the magnetisation at each applied field calculated from the resulting linear fit parameters and M_{exp} is the measured magnetisation. Solid line (cyan) through data points is guide to the eye, and the horizontal gray line highlights the non-linearity below H_{c1}.

119

Our results are in excellent consistency with those reported for overexpanded fcc-rich $Rb_{0.35}Cs_{2.65}C_{60}$ (100-120 Oe [67]) and Rb_2CsC_{60} (120-140 Oe [67]. It should be noted that the fcc phase fraction of $K_{0.35}Cs_{2.65}C_{60}$ is 52.7(2)% (the remaining comprising coexisting CsC_{60} and Cs_4C_{60}) and no corrections for demagnetisation were applied, which might lead to deviation from the true lower critical field.

3.4.4 Ambient pressure, high-field magnetic susceptibility measurements

Magnetic measurements were performed under FC protocol both at 5 and 3 T to subtract out any ferromagnetic impurity contribution (χ_{FM}). Experimentally, ferromagnetic impurity contributions saturate at applied fields below 3 T, and 5 T was the highest available magnetic field for our instrument; therefore these fields were selected for the measurements. The $\chi(T)$ data were obtained from the difference of magnetisation values obtained at 5 and 3 T, and are hereafter termed $\chi(5T - 3T)$. The core diamagnetic susceptibilities, χ_{core}, of pristine C_{60} (-2.43×10^{-4} emu mol^{-1}) [193], K$^+$ and Cs$^+$ (-14.9×10^{-6} and -35.0×10^{-6} emu mol^{-1}, respectively) [194] were also subtracted [$\chi(5T - 3T) - \chi_{core}$]. The temperature dependence of the magnetic susceptibility, $\chi(T)$ for $K_xCs_{3-x}C_{60}$ ($0.22 \leq x \leq 0.87$) samples is shown in Figure 3.25.
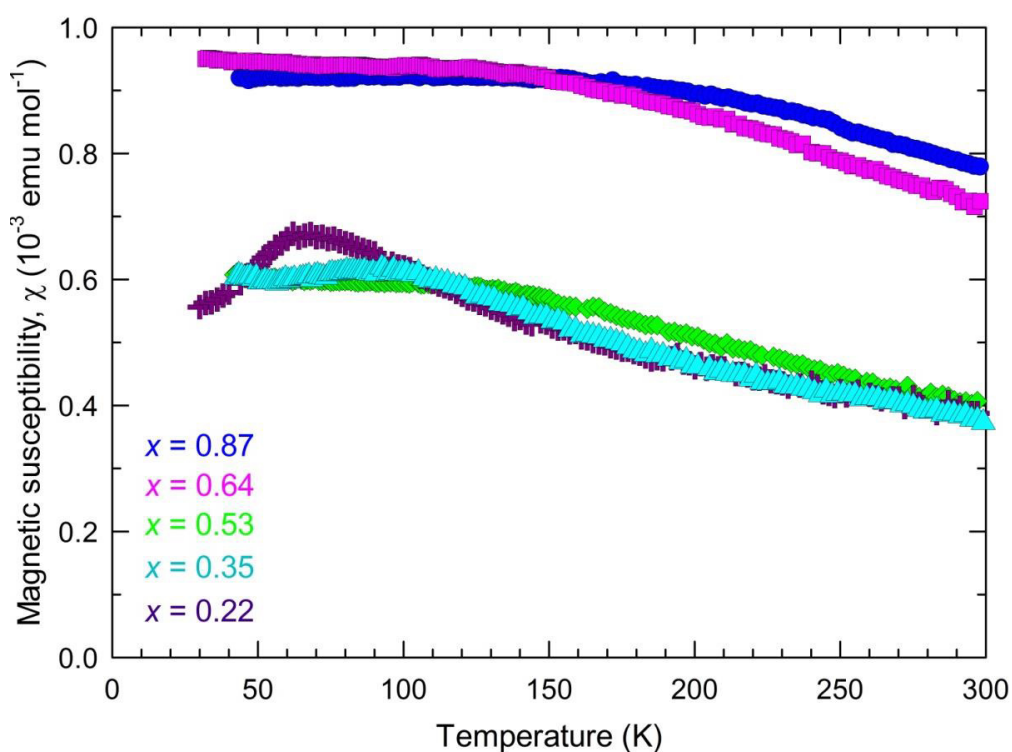
Figure 3.25 Temperature dependence of the magnetic susceptibility, $\chi(T)$, of $K_xCs_{3-x}C_{60}$ samples.

The $\chi(T)$ data for the most expanded $x = 0.22$ sample display a well-defined cusp on cooling, and in contrast to the higher temperature behaviour, below a certain temperature, χ gradually decreases with temperature. By increasing x up to 0.53, we find that the cusps broaden significantly while at the same time the maximum temperature at the cusp, T' also increases. The maxima of cusps for $x = 0.22$ and 0.35 occur at 68 and 97 K, respectively. This particular behaviour of $\chi(T)$ is reminiscent of the $V(T)$ trends; the onset temperature of the lattice changes increases and the transition becomes smeared out as K-content increases; these lattice changes were attributed to insulator-to-metal transitions (section 3.3.3). For $x = 0.35$, the lattice change was observed at ~100 K which coincides with the T' value of 97 K. However, $x = 0.53$, 0.64 and 0.87 do not display a cusp but do not exhibit a temperature-independent Pauli susceptibility term either; χ starts deviating from linearity on heating above ~126 K, ~150 K and ~180 K, respectively with increasing x. This behaviour is consistent with the $V(T)$ trends of $x = 0.64$ and 0.87 samples as the lattice transformations of these samples were also found to extend over a broader temperature range and not as prominent as that for $x = 0.35$.

The Curie-Weiss law function was fitted to the linear region of the inverse susceptibility, $[1/\chi(5T - 3T) - \chi_{core}]$, by least-squares fitting:

$$\chi(5T - 3T) - \chi_{core} = \frac{C}{T - \Theta} \qquad \text{Equation 3.4}$$

where C represents the Curie constant, T is the temperature, and Θ is the Weiss temperature. The refined parameters from the Curie-Weiss fits and two representative Curie-Weiss fits for $x_K = 0.22$ and 0.53 are presented in Table 3.12 and Figure 3.26, respectively. Due to small temperature range available for fitting in the linear high temperature region of the $x = 0.87$ sample, the Weiss temperature was fixed to that found for $x = 0.64$. The magnetic moments presented in Table 3.12, μ_{eff}, were calculated as follows:

$$\mu_{eff} = \mu_B\sqrt{8C} \qquad \text{Equation 3.5}$$

where μ_B is the Bohr magneton.

Table 3.12 Resulting parameters from Curie-Weiss fits to $K_xCs_{3-x}C_{60}$ ($0.22 \leq x \leq 0.87$) susceptibility data in the high temperature region. The Weiss temperature for $x = 0.87$ was fixed to that found for $x = 0.64$.

Refined x_K	T range (K)	C (emu K mol^{-1})	μ_{eff} (μ_B/C_{60}^{3-})	Θ (K)
0.22(1)	90-250	0.191(2)	1.236(6)	−220(3)
0.35(1)	150-250	0.197(2)	1.255(6)	−215 (4)
0.53(1)	200-300	0.183(3)	1.209(9)	−158(6)
0.64(1)	210-300	0.400(5)	1.79(1)	−257(6)
0.87(1)	230-300	0.4284(4)	1.8513(9)	−257
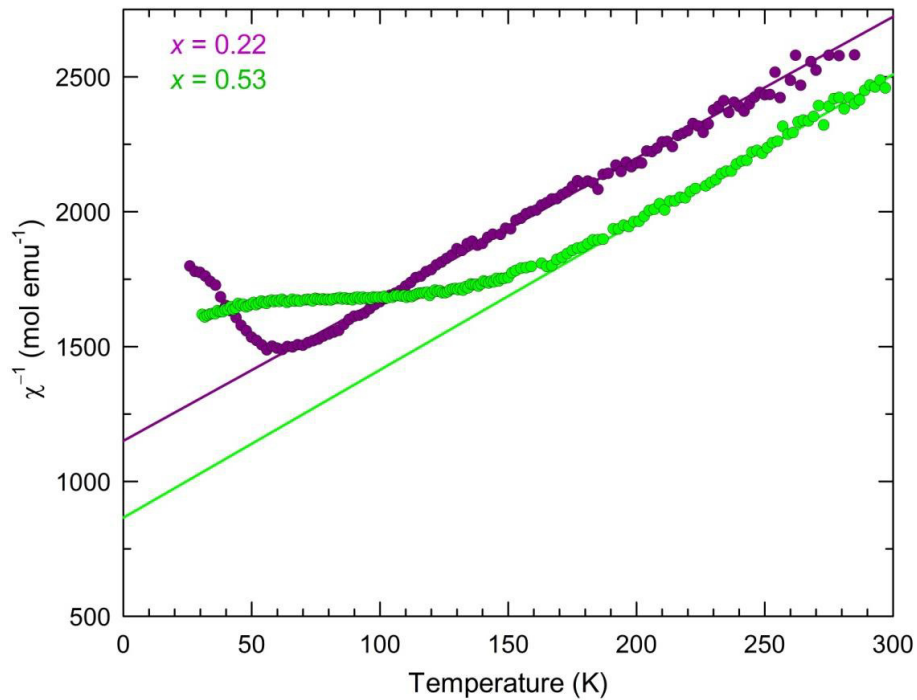
Figure 3.26 The temperature dependence of the inverse magnetic susceptibility, $\chi^{-1}(T)$, for x_K = 0.22 and 0.53. Solid lines through data points show fits of the Curie-Weiss law function to the linear regions (90 < T < 250 K and 200 < T < 300 K for x_K = 0.22 and 0.53, respectively) of the $\chi^{-1}(T)$ data.

Fits of the high temperature linear regions of the inverse susceptibility yielded large negative Weiss temperatures approximately between −158 K and −250 K and effective magnetic moments per C_{60}^{3-} ~1.2 μ_B for samples displaying cusps, and ~1.8 μ_B for less expanded x = 0.64 and 0.87 samples. For insulating fcc Cs_3C_{60} and A15 Cs_3C_{60} effective magnetic moments were estimated as 1.614(4)μ_B [28] and 1.32(1)μ_B [80] which are comparable to our results found for $K_xCs_{3-x}C_{60}$

samples, indicating a $S = \frac{1}{2}$ localized electron ground state with antiferromagnetic correlations in fcc $K_xCs_{3-x}C_{60}$ ($0.22 \leq x \leq 0.87$) samples. Zadik *et al.* also reported $\mu_{eff} \sim 1.6$-1.8 μ_B and negative Weiss temperatures between -95 and -160 K for fcc-rich overexpanded $Rb_xCs_{3-x}C_{60}$ ($0.25 \leq x \leq 1$) samples. However, their results are more consistent with the high temperature $\chi(T)$ behaviour of fcc Cs_3C_{60}; they found a striking overlap in the high temperature region of fcc Cs_3C_{60} and fcc $Rb_xCs_{3-x}C_{60}$ ($0.25 \leq x \leq 1$) samples, underlining the similarity between those materials. This can be tentatively attributed to the better sample quality with much higher fcc phase fraction compared to that of expanded $K_xCs_{3-x}C_{60}$ materials. As a test, a refinable temperature-independent term, χ_0, was also included in the Curie-Weiss fits using the following form: $\chi(5T - 3T) - \chi_{core} = \frac{C}{T - \Theta} + \chi_0$ to account for any temperature-independent contributions to the magnetic susceptibility from minor impurity phases, (*e.g.* non-magnetic insulators Cs_4C_{60} and CsC_{60}). However, refinement of χ_0 did not yield physically meaningful values and led to relatively large errors in C and Θ. Therefore, χ_0 was set to zero in the final Curie-Weiss fits.

In a Jahn-Teller distorted C_{60}^{3-} molecule, in contrast to Hund's rules, the ground state maximizes double occupancy of energy levels, and hence favours low-spin ($S = \frac{1}{2}$) rather than high-spin ($S = 3/2$) ground state. The C_{60}^{3-} anions in antiferromagnetic Mott insulating $NH_3K_3C_{60}$ were also found in a low-spin state and their high-spin state were found approximately 100 meV higher in energy [195]; in agreement with the previous assumptions of the energy between the low-spin ground state and the lowest high-spin excited state which was expected to be of the order of 0.1 eV [196], [197]. This low-spin state characterises the overexpanded fullerides as 'Mott-Jahn-Teller' insulators (MJTI) which are Mott insulators whose sites are in a JT stabilized low-spin state (inverted Hund's rule coupling) [198], like fcc Cs_3C_{60}. Therefore, the insulating state of the overexpanded $K_xCs_{3-x}C_{60}$ ($0.22 \leq x \leq 0.87$) samples at high temperatures may also be described as MJTI, with medium-strength JT coupling, low-spin ground state and strong antiferromagnetic correlations; this was also encountered in the overexpanded $Rb_xCs_{3-x}C_{60}$ ($0.35 \leq x \leq 1$) samples in insulating regime by Zadik *et al* [67].

We now turn to the temperature dependence of the magnetic susceptibility, $\chi(T)$ for $K_{1.63}Cs_{1.37}C_{60}$ (fcc phase fraction 94.05(1)%) and phase-pure K_2CsC_{60}

samples. The χ data were corrected as $\chi(5T - 3T) - \chi_{core}$, as was employed for the more expanded samples. The $\chi(T)$ data (Figure 3.27) reveal that upon further lattice contraction for $x \geq 1$, $\chi(T)$ comprises a single nearly temperature-independent Pauli spin susceptibility term, χ_P, in the experimental temperature range, consistent with a metallic ground state from which superconductivity emerges on cooling. The observed significant decrease in χ at high temperatures for $x = 0.87$ is no longer visible for $x = 1.63$ and 2 samples; however a small increase in χ_P is observed upon cooling in both compositions.
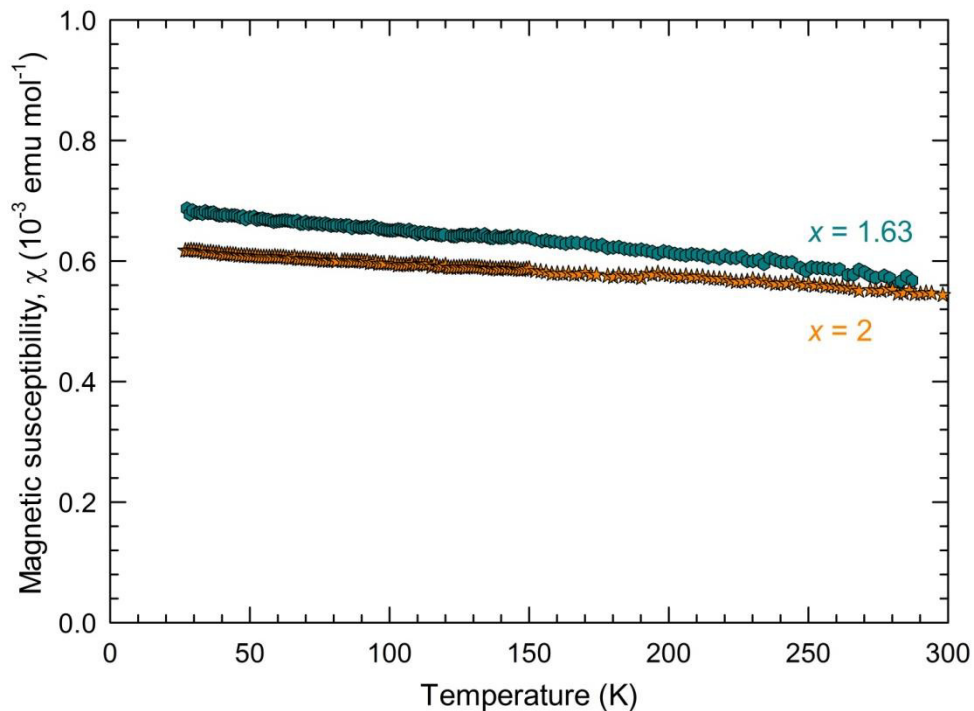
Figure 3.27 Temperature dependence of the magnetic susceptibility, $\chi(T)$, of fcc-rich $K_{1.63}Cs_{1.37}C_{60}$ and K_2CsC_{60} samples. The scale and range of both axes have been fixed, for comparative purposes, to those of the plot displaying analogous data for overexpanded $K_xCs_{3-x}C_{60}$ (Figure 3.25).

Previous SQUID magnetic susceptibility measurements of K_3C_{60} and Rb_3C_{60} discussed the reason for observing this small increase in the χ_P with decreasing temperature. This was attributed to the influence of ferro-like magnetic susceptibilities that remain even after correction by subtracting of values collected at different magnetic fields; such small ferromagnetic contributions would be enhanced at low temperatures [199]. On the other hand, in the same study of ref. [199], $\chi(T)$ for K_3C_{60} and Rb_3C_{60} obtained from EPR spectroscopy decreases with decreasing temperature. This was explained by the reduction of the $N_{\varepsilon F}$ values due to the thermal contraction upon decreasing temperature as for free non-

interacting electrons in a paramagnetic metal, in the absence of enhancement through spin fluctuations, χ_P is directly related to the 'bare' density of states at the Fermi level, $N_{\varepsilon F}$ as follows: $\chi_P = 2\mu_B^2 N_{\varepsilon F}$. Indeed, Bukhart *et al.* have calculated a decrease of 6 and 8% for Rb_3C_{60} and K_3C_{60}, respectively, due to thermal contraction upon cooling from ambient temperature to T_c [200]. However, in our susceptibility data no decrease is observed in χ upon cooing, indicating the decrease in $N_{\varepsilon F}$ was dominated by the effect of the ferro-like magnetic susceptibilities. The absence of ferro-like behaviour in EPR data was ascribed to strong electron spin-spin correlations of ferro spins, resulting in very short relaxation times which could not be observed in EPR, leading to enhancement of the effect of thermal contraction [199]. Field-dependent magnetisation measurements of these two underexpanded samples were performed at 295 K to extract the susceptibility from a least-squares fit of the linear, high field region of the $M(H)$ data where the ferromagnetic impurity contribution is fully saturated. Extracted Pauli susceptibility in the metallic regime was used for an estimation of $N_{\varepsilon F}$ for these samples.
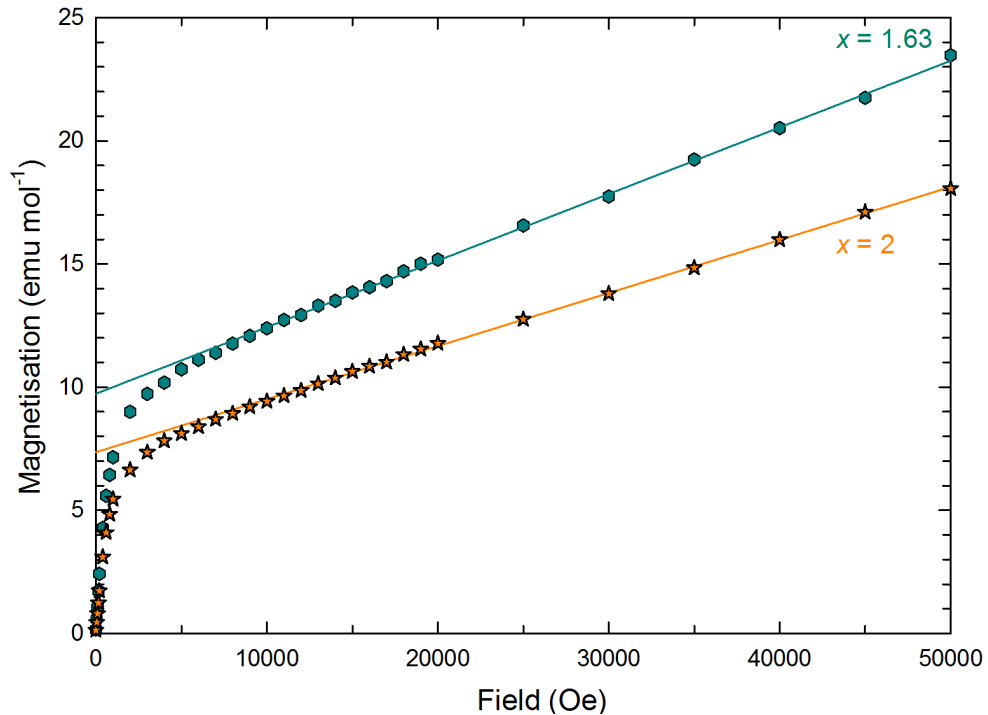
Figure 3.28 The field-dependence of magnetisation at 295 K for K_2CsC_{60} (22 mg) and $K_{1.63}Cs_{1.37}C_{60}$ (24 mg). The solid line through data points are least-squares fits over the field range $1\ T \leq H \leq 5\ T$, using the function $M = \chi H + M(0\ Oe)$. The refined parameters for $x = 2$ are: $\chi = 0.216(1)\times10^{-3}$ emu mol^{-1} (prior to correction for χ_{core}) and $M(0\ Oe) = 7.36(3)$ emu mol^{-1}, and for $x = 1.63$ are: $\chi = 0.270(3)\times10^{-3}$ emu mol^{-1} (prior to correction for χ_{core}) and $M(0\ Oe) = 9.73(7)$ emu mol^{-1}.

The values of χ_{core} are -0.308×10^{-3} and -0.315×10^{-3} emu mol^{-1}, for $x = 2$ and $x = 1.63$, respectively, and the subtracted value of $\chi_{295\ K} - \chi_{core}$ from $M(H)$ measurements for these samples are found as 0.53×10^{-3} and 0.59×10^{-3} emu mol^{-1}, respectively. Using the $\chi_P = 2\mu_B^2 N_{\varepsilon F}$ relation, $N_{\varepsilon F}(295\ K)$ for K$_2$CsC$_{60}$ is ~8.2 states eV^{-1} C$_{60}^{-1}$ and for K$_{1.63}$Cs$_{1.37}$C$_{60}$ is ~9.1 states eV^{-1} C$_{60}^{-1}$ which are in excellent agreement with those estimated from theoretical calculations of $N_{\varepsilon F}$ for K$_3$C$_{60,}$ Rb$_3$C$_{60}$ [201] and fcc Cs$_3$C$_{60}$ under pressure (~4 kbar) [79]: 7.2, 8.1 and ~10 states eV^{-1} C$_{60}^{-1}$, respectively. Typically, theoretical estimates of $N_{\varepsilon F}$ for A$_3$C$_{60}$ fullerides give values between ~7 and 10 eV^{-1} C$_{60}^{-1}$. However, $N_{\varepsilon F}$ values estimated for K$_3$C$_{60}$ (14 eV^{-1} C$_{60}^{-1}$) and Rb$_3$C$_{60}$ (19 eV^{-1} C$_{60}^{-1}$) [202] from magnetic susceptibility measurements at ambient temperature are considerably higher in magnitude than the present results in this study.

3.4.5 High pressure, low-field magnetisation measurements

In this section, investigation of the superconducting response of fcc-structured K$_x$Cs$_{3-x}$C$_{60}$ ($0.35 \leq x \leq 2$) samples to both chemical and external hydrostatic pressure is discussed. Magnetisation measurements as a function of temperature, $M(T)$, have been performed under ZFC protocol with applied pressure up to ~10.3 kbar. Figure 3.29 collects the $M(T)$ data for K$_x$Cs$_{3-x}$C$_{60}$ ($0.35 \leq x \leq 2$) samples. The variation of superconducting T_c and estimated shielding fraction with pressure are presented in Figure 3.30 and Figure 3.31, respectively. The $M(T)$ data for K$_2$CsC$_{60}$ again show a very tiny kink at ~19 K at pressures up to 4 kbar, consistent with that observed at ambient pressure, corresponding to superconducting T_c for K$_3$C$_{60}$; however, this is suppressed at higher pressures.

For the most expanded fcc-rich sample, K$_{0.35}$Cs$_{2.65}$C$_{60}$, T_c initially increases with increasing pressure, with a large positive initial pressure coefficient of $(\mathrm{d}T_c/\mathrm{d}P)_{P=0} = +1.5(2)$ K kbar^{-1}; however, this rate of increase rapidly decreases with increasing K-content. It approaches zero for $x = 0.87$, which displays the maximum T_c at ambient pressure in this series of samples. It finally becomes negative over the full pressure range for the $x = 1.28$ and 2 samples, which exhibit a strongly negative pressure dependence ($-0.88(1)$ and $-0.99(3)$ K kbar^{-1}, respectively), comparable to those reported for K$_3$C$_{60}$ (-0.78 K kbar^{-1}) [203] and Rb$_3$C$_{60}$ (-0.97 K kbar^{-1}) [191]. Non-linear pressure dependence of T_c, $T_c(P)$, of

more expanded $0.35 \leq x \leq 0.87$ samples produces superconductivity $T_c(P)$ domes; the behaviour is reminiscent of that observed for both fcc and A15 Cs_3C_{60} [28], and fcc-rich series of $Rb_xCs_{3-x}C_{60}$ ($0.35 \leq x \leq 2$) samples [67] (Figure 3.32).
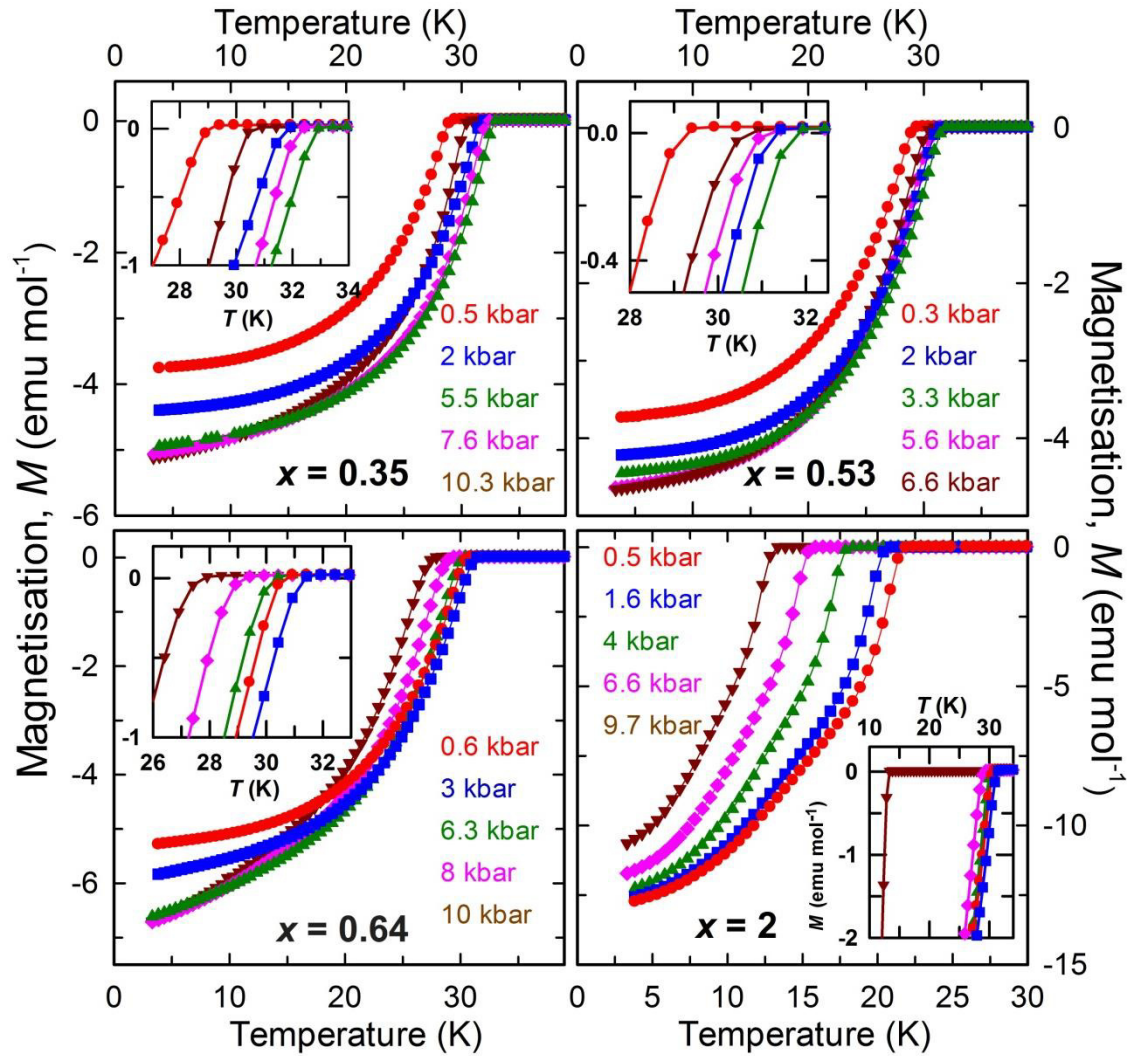
Figure 3.29 Temperature dependence of magnetisation, $M(T)$, (20 Oe, ZFC protocol) for fcc $K_xCs_{3-x}C_{60}$ ($0.35 \leq x \leq 2$), at selected pressures. The insets show expanded regions of the respective data near superconducting T_c.
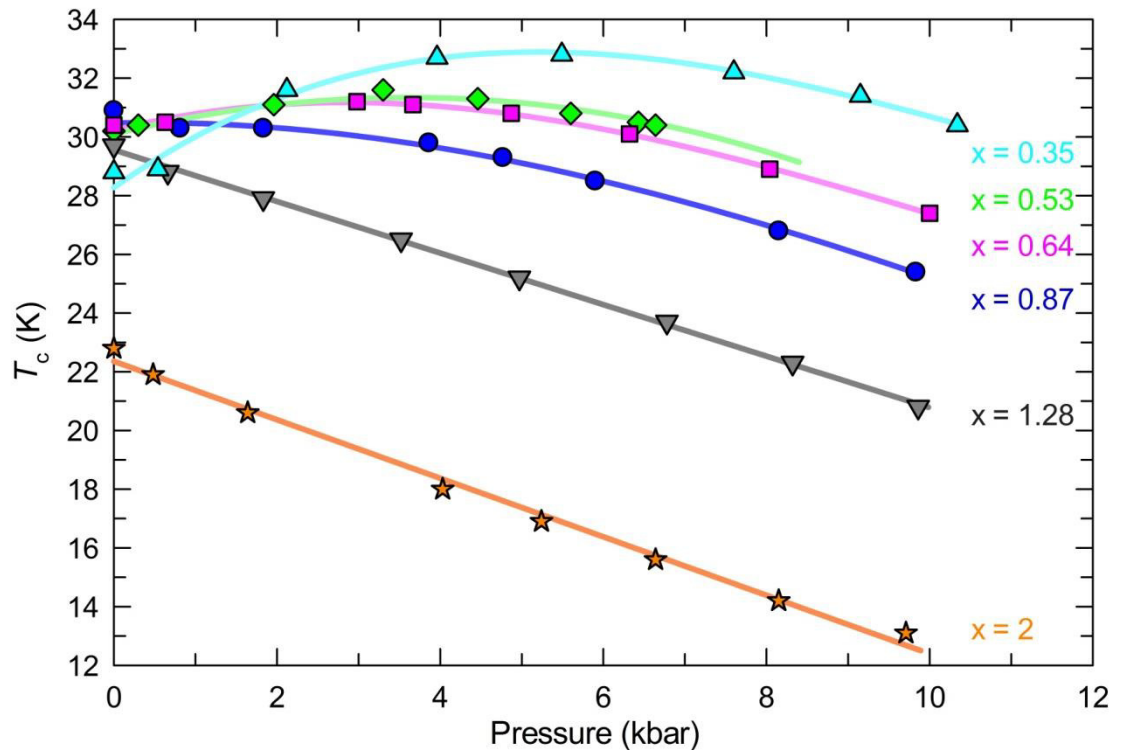
Figure 3.30 The variation of superconducting T_c with pressure for fcc-structured $K_xCs_{3-x}C_{60}$ ($0.35 \le x \le 2$), from magnetisation measurements with applied fields of 20 Oe and under ZFC protocols. The solid lines through data points are guides to the eye except those through the data points of $x = 1.28$ and 2; they represent linear fit results, yielding $dT_c/dP = -0.88(1)$ K kbar^{-1} and $-0.99(3)$ K kbar^{-1}, respectively.
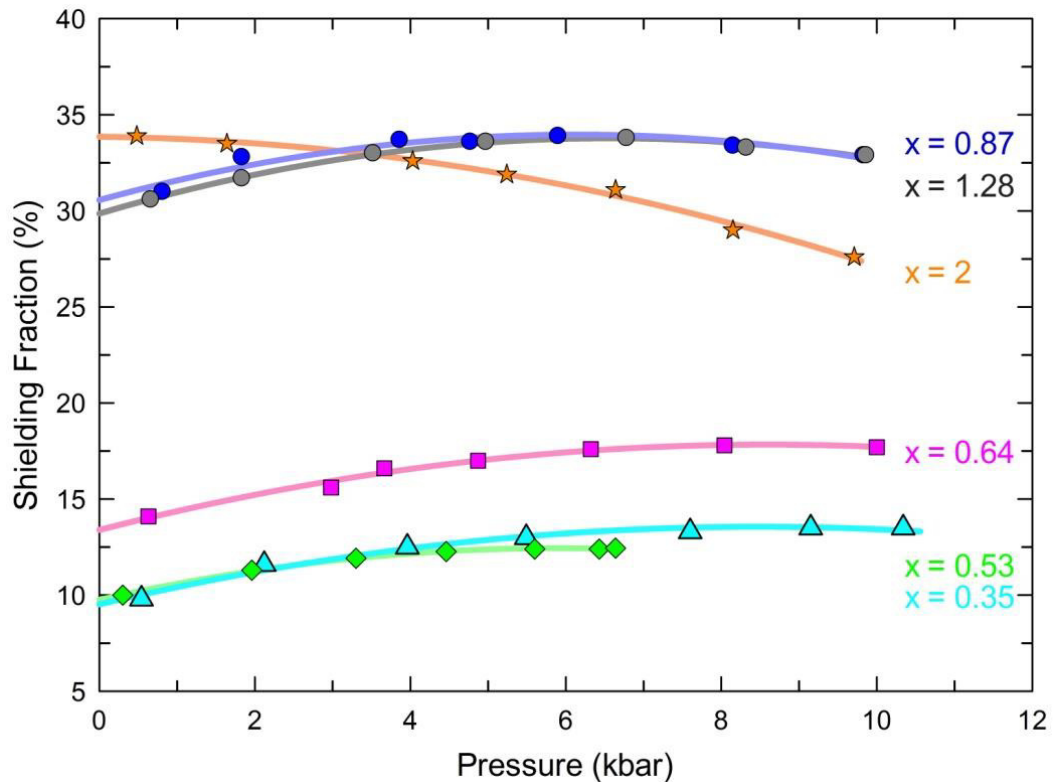
Figure 3.31 Pressure evolution of shielding fraction at 4 K, estimated from ZFC measurements under 20 Oe applied field for $K_xCs_{3-x}C_{60}$ ($0.35 \le x \le 2$). The solid lines are guides to the eye.

The variation of the superconducting T_c of $K_xCs_{3-x}C_{60}$ ($0.35 \leq x \leq 2$) with unit cell volume, V, at low temperature was extracted using the combination of 7 K $V(P)$ compressibility data described in section 3.3.5 and the $T_c(P)$ data (Figure 3.30). V at a particular P was estimated from the Murnaghan EoS fits. However, as the low-temperature $V(P)$ compressibility data were only available for $x_K = 0.35$, 0.87 and 1.28, V of the remaining $x_K = 0.53$, 0.64 and 2 compositions at a particular P was estimated from Murnaghan EoS (Equation 2.28) using derived parameters from the Murnaghan EoS fits to the 7 K $V(P)$ data for $x_K = 0.35$, 0.87, 1.28, respectively. Extracted $T_c(V)$ trends for each sample are presented in Figure 3.32.
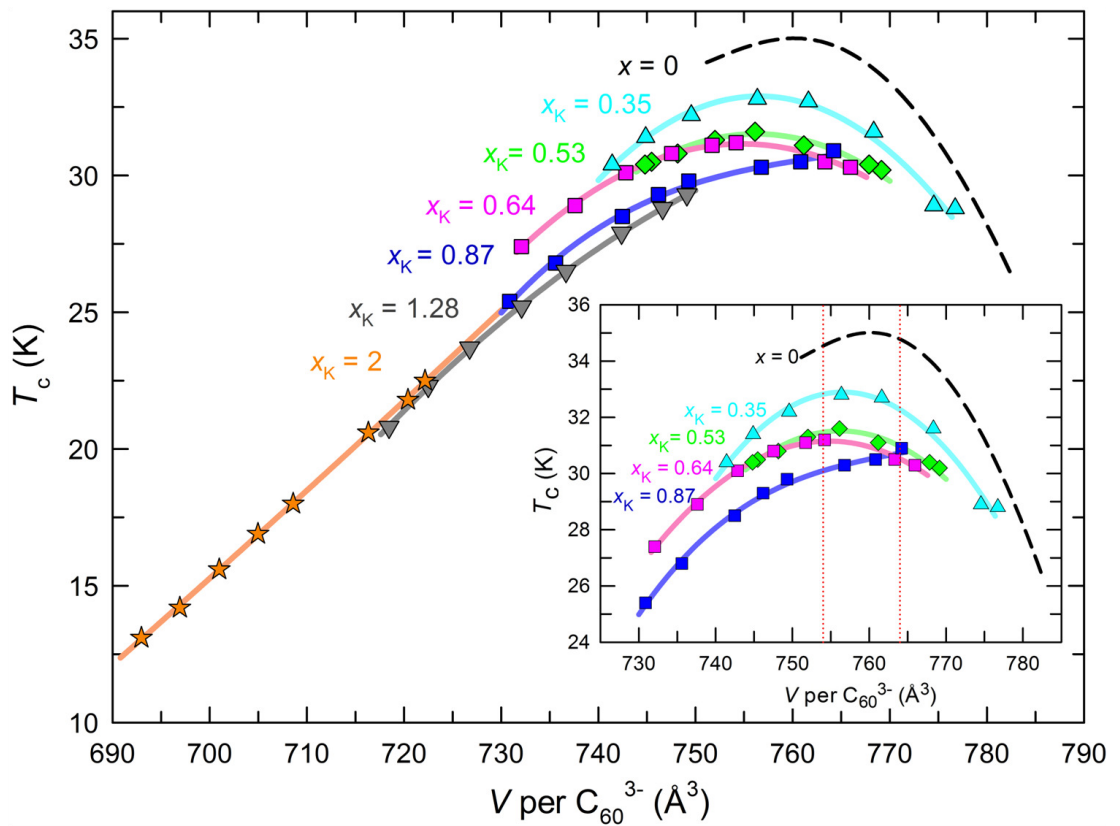
Figure 3.32 The variation of superconducting T_c with volume, V, occupied per C_{60}^{3-} anion at low temperature for fcc $K_xCs_{3-x}C_{60}$ ($0.35 \leq x \leq 2$), and for fcc Cs_3C_{60} ([28]), presented with black dashed line. Solid lines through x_K data points are guides to the eye. The inset shows expanded view of $T_c(V)$ data for samples which show a 'dome' shaped $T_c(V)$ scaling. Dotted lines in red colour depict the volume range where individual superconductivity domes peak.

Application of hydrostatic pressure to fcc Cs_3C_{60} and overexpanded $K_xCs_{3-x}C_{60}$ samples ($x = 0.35$, 0.53, 0.64) has yielded similar $T_c(V)$ trends; however, there is a striking observation on the response of T_c to the K-content. The maximum T_c, $T_{c(max)}$, for each composition of the $K_xCs_{3-x}C_{60}$ series is significantly smaller than the

$T_{c(max)}$ of 35 K for fcc Cs_3C_{60}, even if the $T_{c(max)}$ of individual x_K samples has been observed around the same value of V (Table 3.13).

3.4.6 Summary of magnetic measurement results at ambient and high pressures

Superconductivity in fcc structured $K_xCs_{3-x}C_{60}$ ($0.22 \leq x \leq 2$) samples has been confirmed by low-field magnetisation measurements at ambient pressure. The chemical pressure has been found to have a non-monotonic effect on superconducting T_c, producing a dome-shaped scaling of T_c with K-content; T_c initially increases with K content from 26.5 K in $K_{0.22}Cs_{2.78}C_{60}$ to 30.9 K in $K_{0.87}Cs_{2.13}C_{60}$ then decreases to 22.8 K in underexpanded K_2CsC_{60}, analogous to the response of fcc Cs_3C_{60} upon the application of hydrostatic pressure [28].

The $dT_c(dP)$ trends of $K_xCs_{3-x}C_{60}$ ($0.35 \leq x \leq 2$) have been studied by low-field magnetisation measurements at high pressure. While underexpanded $x = 1.28$ and 2 samples display large negative $dT_c/(dP)$, more expanded samples ($0.35 \leq x \leq 0.87$) show a dome-shaped scaling of T_c with pressure. Temperature-dependent high field magnetic susceptibility measurements have shown that the most expanded $x = 0.22$ and 0.35 samples display well-defined cusps in $\chi(T)$, which are attributed to insulator-to-metal crossover. Underexpanded $x = 1.63$ and 2 samples show a temperature-independent $\chi(T)$ behaviour, implying Pauli metallic behaviour over the experimental temperature range, with an estimated $N_{\varepsilon F}$ of ~9.1 and 8.2 states eV^{-1} C_{60}^{-1}, respectively, in their metallic regime. Remaining $x = 0.53$, 0.64 and 0.87 samples display neither a temperature-independent Pauli susceptibility term nor distinct cusps but show a deviation from their linear $\chi(T)$ behaviour at high temperatures. This behaviour coincides well with that observed in the $V(T)$ trends of $x = 0.64$ and 0.87, in which the lattice anomaly has been found to extend over a broad temperature range.

Finally, experimentally obtained critical temperatures of the $K_xCs_{3-x}C_{60}$ system (magnetic characterisation: T_{max} from $\chi(T)$ and superconducting T_c, structural characterisation: T' (XRPD)) have been combined and included in a global electronic phase diagram of A_3C_{60} fullerides (Figure 3.33). The series of $K_xCs_{3-x}C_{60}$ compositions tracks the superconductivity 'dome' of the A_3C_{60}

superconductors, extending from close to the Mott boundary, over the maximum of the dome and well into the underexpanded regime. K_2CsC_{60} connects the merohedrally disordered underexpanded fcc A_3C_{60} (space group $Fm\bar{3}m$) superconductors to orientationally ordered primitive cubic superconducting fullerides Na_2AC_{60} (A = Rb, Cs).
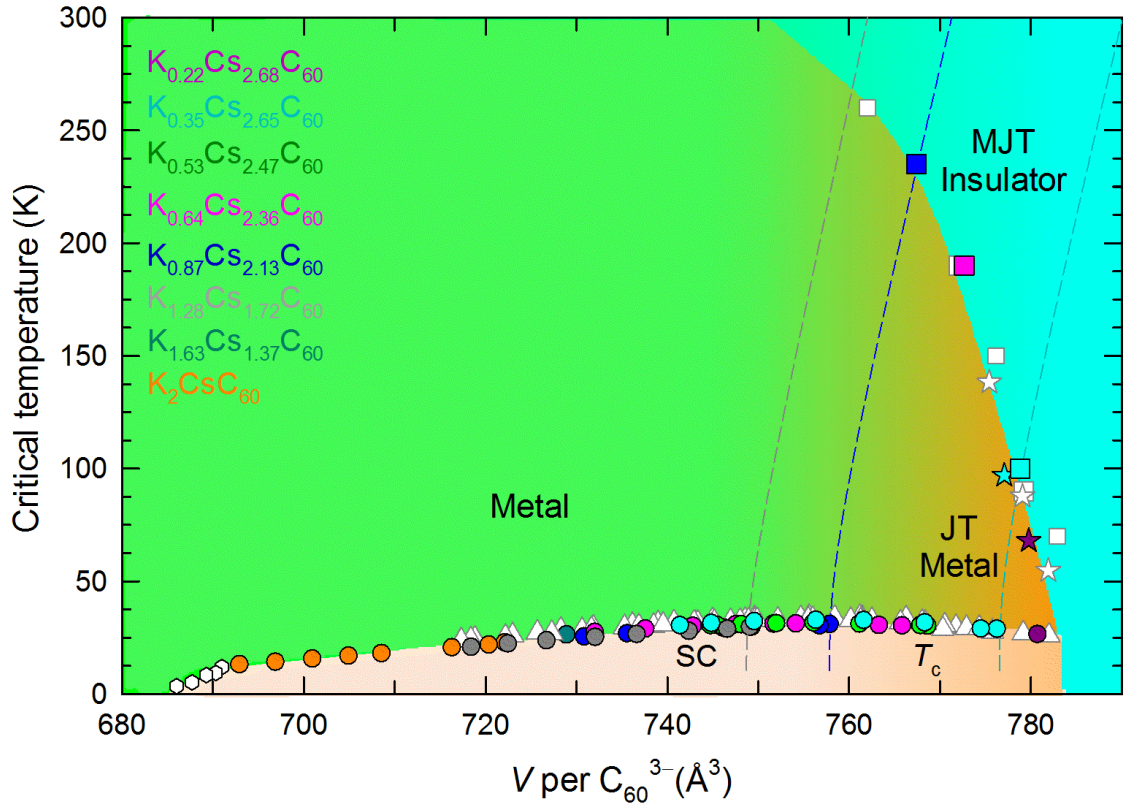
Figure 3.33 Global electronic phase diagram for A_3C_{60}, showing the evolution of T_c as a function of volume, V, occupied per C_{60}^{3-} anion and the MJTI-to-JTM crossover temperature, T' as a function of V (XRPD: squares; $\chi(T)$: stars). Open triangles, squares and stars are for the fcc $Rb_xCs_{3-x}C_{60}$ system ($0.35 \leq x \leq 2$) [67]. Open hexagons correspond to the ambient pressure T_c of simple cubic fullerides with $Pa\bar{3}$ symmetry [28]. 'MJT' abbreviates Mott-Jahn-Teller. Within the metallic (superconducting) regime, gradient shading from orange to green schematically illustrates the JTM to conventional metal crossover. Gray, blue and cyan dashed lines mark experimental $V(T)$ tracks for $K_xCs_{3-x}C_{60}$ compositions with K-content of $x_K = 1.28$, 0.87 and 0.35, respectively.

The insulating and superconducting states of overexpanded fcc A_3C_{60} fullerides are connected by an anomalous metallic state, labelled as 'JT metal', where both localized JT-active and itinerant electrons coexist, as revealed by IR and NMR spectroscopy studies of $Rb_xCs_{3-x}C_{60}$ [67]. Unconventional superconductivity in overexpanded A_3C_{60} fullerides emerges from the JTMs upon cooling, while conventional superconductivity is encountered when the JT effect fades away at small interfullerene separations [67]. These results signify the importance of

molecular electronic structure in producing the unconventional superconductivity in fcc A_3C_{60} fullerides. The findings in the present work are in excellent agreement with those of ref. [67] and confirm the remarkable difference in electronic response between fullerides close to and far away from the Mott insulator boundary. They are not consistent with the BCS phenomenology implying the importance of strong electron-electron interactions.

3.5 Discussion

An interesting characteristic of Mott insulators is that an external stimulus such as physical or chemical pressure may provoke Mott insulator-to-metal transitions *via* the enhancement of the bandwidth, W; this is one of the clear manifestations of strong electron correlations in condensed matter. For instance, the low-spin Mott-insulating phase was transformed to the neighbouring metallic phase in fcc Cs_3C_{60} upon pressurisation, followed by a transition to a superconducting state on cooling which reveals that this class of material belongs to the correlated electron systems [28].

The significance of the discovery of a MJTI-to-metal transition in molecular superconductors, without symmetry breaking, has been recently amplified by the experimentally [67] and theoretically [204] produced electronic phase diagram of fcc $Rb_xCs_{3-x}C_{60}$ materials in which conventional phonon-mediated superconductivity and unconventional Mott physics meet, leading to a rich electronic phase diagram as a function of volume per C_{60}^{3-}; this is strikingly similar to that of cuprates where high temperature superconductivity emerges from a Mott insulating state, with a 'dome' shaped scaling of the T_c, *via* doping insulating CuO_2 layers with holes (doping control).

A pressure-induced Mott insulator-to-metal transition was also reported in organic 2D κ-(BEDT-TTF)$_2X$ based materials where BEDT-TTF is bis(ethylenedithio)tetrathiafulvalene and X stands for various anions. This organic superconducting family exhibits similar behaviour to high-T_c copper oxides. Whilst the Mott transition is induced by hydrostatic pressure in this organic family, it is induced by carrier doping in the high-T_c cuprates, but in both cases superconductivity emerges in the marginal metallic phase near the

antiferromagnetic insulating state [205]. As tuning parameter to control the bandwidth, the use of hydrostatic pressure and temperature is more preferable rather than alloying techniques as it allows the fine alteration of experimental conditions and eliminates any effect from impurities which could influence the transition.

In this study, the MJTI Cs_3C_{60} was first subjected to chemical pressure *via* K substitution to control *W*. This led to the destruction of the MJTI state and the emergence of a metallic phase upon cooling without symmetry breaking, reminiscent of the cooling-induced insulator-to-metal transitions observed in the fcc $Rb_xCs_{3-x}C_{60}$ analogues [67]. There are however certain differences between the two cation-substituted systems due to the greater size mismatch between the substituted cations. The alkali atoms have been hitherto considered to act as rigid spectators only to expand the lattice and cation specific effect on the electronic properties of the fcc A_3C_{60} compounds have not been addressed in any detail. The differences between various systems have been attributed solely to the volume dependence of the density-of-states at the Fermi level, $N_{\varepsilon(F)}$.

Here we recall that in rare-earth manganates of the type $(Ln_{1-x}A_x)MnO_3$ (Ln = rare earth, A = alkaline earth) are key examples of cooling-induced insulator-to-metal transition, in which the effect of size mismatch between the doped cations on the magnetic properties can be clearly exemplified [182], [206]. The effect of size mismatch in rare-earth manganates, with a general formula of $La_{0.7-x}Ln_xBa_{0.3}MnO_3$ (Ln = Pr, Nd, Gd or Dy) was investigated by Kundu *et al* [182]. They quantified the effect of doped cation size through calculation of cation size variance, σ^2, which range from 0.001 to 0.030 $Å^2$, and have revealed that when σ^2 is close to 0.020 $Å^2$, an insulator-to-metal transition occurs on cooling, with transition temperature decreasing with increasing σ^2, while keeping $<r_A>$ constant.

In this study, the effect of doped cation size has been visualised by the variation of superconducting T_c with volume per C_{60}^{3-} for individual K- and Rb-substituted fcc-structured $A_xCs_{3-x}C_{60}$ materials (Figure 3.34). The T_c response of individual x_K and x_{Rb} samples, where $x \leq 1$, is similar to that of $x = 0$, displaying a dome-shaped dependence of T_c on interfullerene separation. However, whilst the maximum T_c for each composition of the $Rb_xCs_{3-x}C_{60}$ ($0.35 \leq x \leq 1$) system is

slightly smaller than the $T_{c(max.)}$ of 35 K for fcc Cs_3C_{60}, it becomes significantly smaller for fcc $K_xCs_{3-x}C_{60}$ (0.35 ≤ x ≤ 0.87), even if the $T_{c(max)}$ of individual x_K and x_{Rb} samples has been observed around the same value of V.
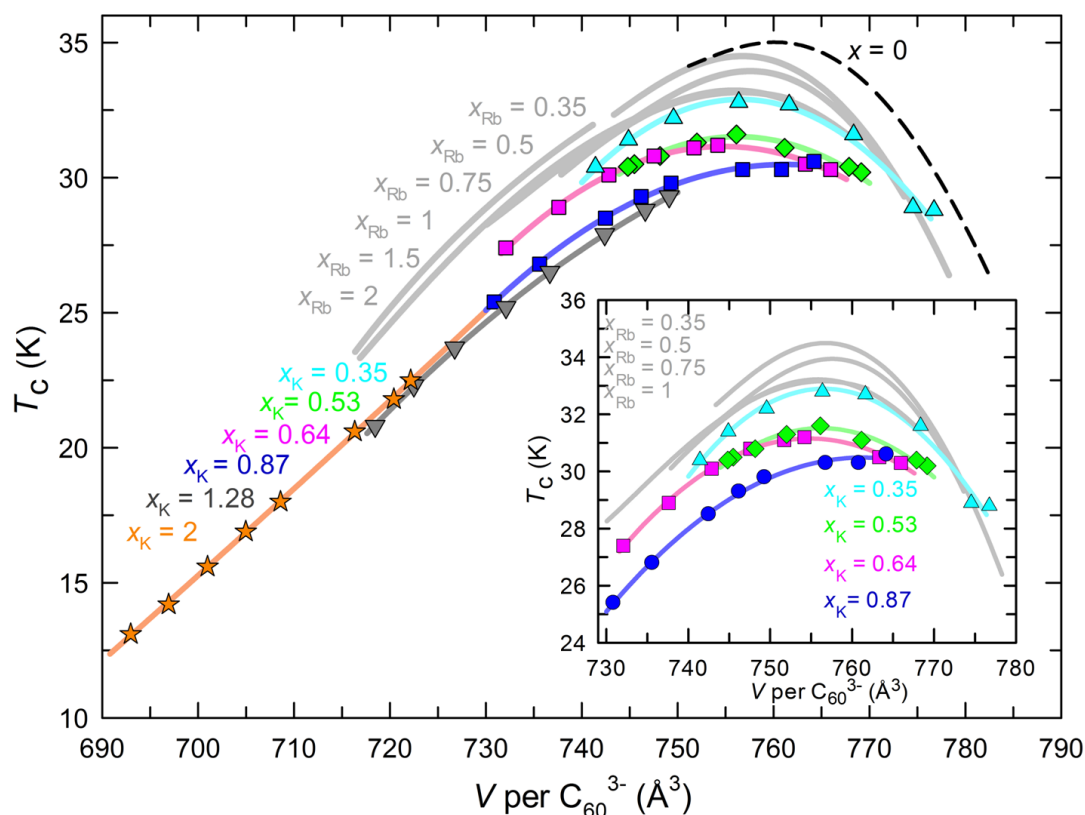
Figure 3.34 The variation of superconducting T_c with volume, V, occupied per C_{60}^{3-} anion at low temperature for fcc $K_xCs_{3-x}C_{60}$ (0.35 ≤ x ≤ 2), for fcc $Rb_xCs_{3-x}C_{60}$ (0.35 ≤ x ≤ 2) ([67]) (presented as gray solid lines) and for fcc Cs_3C_{60}[28] (presented as a black dashed line). Solid lines through x_K data points are guides to the eye. The inset shows expanded view of T_c (V per C_{60}^{3-}) data for samples which show a 'dome' shaped scaling.

The variation of the $T_{c(max)}$ with cation size variance in the fcc T_d sites for the compositional ranges where the $T_{c(max)}$ in a superconducting dome can be ascertained for both $K_xCs_{3-x}C_{60}$ and $Rb_xCs_{3-x}C_{60}$ systems is presented in Figure 3.35 and listed in Table 3.13. $T_{c(max)}$ decreases by ~4 K, with an increase of σ^2 by 0.021 Å², from fcc Cs_3C_{60} to the least expanded sample of $K_xCs_{3-x}C_{60}$ that produces a superconductivity dome (x_K = 0.87), but it only decreases by ~1.8 K, with an increase of σ^2 by 0.006 Å², for the $Rb_xCs_{3-x}C_{60}$ system. In fcc Cs_3C_{60}, it has been assumed that there are no tetrahedral cation vacancies (σ^2 = 0 Å²), which results in an homogenous distribution of 8 Cs^+ cations in the tetrahedral sites that surround C_{60}^{3-} anions; however by substitution of smaller K^+ or Rb^+ cations, C_{60}^{3-} anions will be surrounded by tetrahedral interstitial sites which are occupied by a disordered

mixture of K^+/ Cs^+ or Rb^+/Cs. Greater size mismatch between Cs^+ and K^+ cations in the T_d site has yielded a bigger detrimental effect on $T_{c(max)}$ (Figure 3.35).

Table 3.13 List of cation size variance in the fcc tetrahedral interstitial sites of $K_xCs_{3-x}C_{60}$ ($0.35 \leq x \leq 0.87$) and $Rb_xCs_{3-x}C_{60}$ ($0.35 \leq x \leq 1$) which are the compositional ranges where the maximum T_c in a superconducting 'dome' can be ascertained in Figure 3.32 for both superconducting families, together with volume, V, per C_{60}^{3-} where $T_{c(max)}$ for each composition is observed.

x_K	$\sigma^2_{r_{T_d}}$ (Å^2)	$T_{c(max)}$ (K)	V_{max} (Å^3)	x_{Rb} nominal; refined	$\sigma^2_{r_{T_d}}$ (Å^2)	$T_{c(max)}$ (K)	V_{max} (Å^3)
0	0	35	760	0; 0	0	35	760
0.35(1)	0.012(2)	32.8	756	0.35;0.33(2)	0.003(2)	34.3	756
0.53(1)	0.016(2)	31.6	756	0.5; 0.426(8)	0.004(2)	33.9	758
0.64(1)	0.018(2)	31.2	754	0.75; 0.73(1)	0.005 (2)	33.3	756
0.87(1)	0.021(2)	30.9	764	1; 1.02(1)	0.006(1)	33.2	756
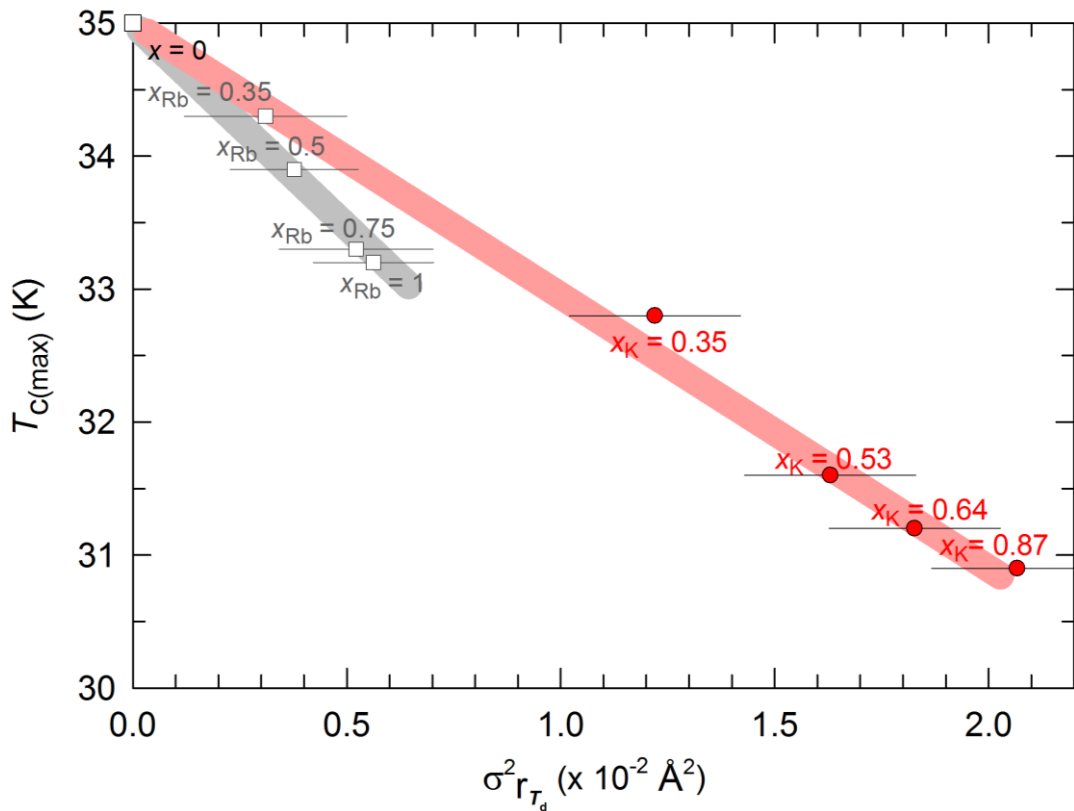
Figure 3.35 Variation of the maximum T_c, $T_{c(max)}$, extracted from the $T_c(V)$ trends of fcc $K_xCs_{3-x}C_{60}$ ($0.35 \leq x \leq 0.87$), of fcc $Rb_xCs_{3-x}C_{60}$ ($0.35 \leq x \leq 1$) ([67]) and of fcc Cs_3C_{60}([28]) with cation size variance in the fcc tetrahedral interstitial sites. Statistical errors on cation size variance were estimated using the refined site occupancy of cations from Rietveld refinements. The solid lines through data points for the K- and Rb- substituted systems are linear fits, yielding $d\sigma^2_{r_{T_d}}/dT_{c(max)} = -201(5)$ K/Å^2 and $-306(18)$ K/Å^2, respectively.

The $T_{c(max)}$ decreases quasi-linearly with increasing cation size variance. This scaling is similar to that found for the series of A_2CuO_4 superconductors, prepared with fixed mean A-site radius $<r_A>$, and general formula of $(La_{0.925-f}Nd_fSr_{0.075-g-h}Ca_gBa_h)_2CuO_4$ [181]. These results indicate that in addition to the fcc unit cell volume, the superconducting T_c is very sensitive to lattice strains, and hence the influence of the substituted cations on the electronic properties cannot be neglected, consistent with previously reported studies of the cation size disorder effect on the structural and magnetic properties of non-fulleride materials [180], [182], [183].

3.6 Conclusion

In this study, using a solid-state synthetic route, fcc-structured $K_xCs_{3-x}C_{60}$ ($0.22 \leq x \leq 2$) samples have been synthesised. Structural and magnetic characterisations of these samples have been undertaken under variable temperature and pressure. All samples have been found to be fcc-rich (except the most expanded $x = 0.22$) and to exhibit superconducting transition at critical temperatures varying between 22.8 and 30.9 K, with a dome-shaped scaling of T_c with x and with unit cell volume. This contrasts with the well-established conventional $N_{\varepsilon(F)}$ dependence of T_c in the less expanded fcc A_3C_{60} systems.

Combination of high pressure structural and magnetization data allowed us to track the dependence of T_c with unit cell volume, V, at low temperature. The fcc-structured $K_xCs_{3-x}C_{60}$ compositions follow the universal superconductivity 'dome' of the A_3C_{60} fullerides. Resulting dependence of T_c on V in $K_xCs_{3-x}C_{60}$ system has been compared to that of $Rb_xCs_{3-x}C_{60}$ and found that doped cations themselves do not only act to expand the lattice but also influence the molecular electronic properties *via* the size mismatch between the Cs^+ and A^+ cations. In the overexpanded regime of the $K_xCs_{3-x}C_{60}$ ($0.22 \leq x \leq 0.87$) system, insulator-to-metal crossover driven by temperature- and substitution-induced volume contraction effects has been experimentally observed at ambient pressure, evidenced by a unit cell volume collapse and by a cusp in the magnetic susceptibility; however, the susceptibility cusps and correlated lattice collapses are not as clear as those observed in the overexpanded $Rb_xCs_{3-x}C_{60}$ ($0.25 \leq x \leq 1$) materials. The onset insulator-to-metal crossover temperatures, T' well above superconducting T_c for

samples x_K = 0.35, 0.64 and 0.87, evidenced by T-dependent structural XRPD data and for samples x_K = 0.22 and 0.35, evidenced by T-dependent magnetic susceptibility data, similar to that of overexpanded $Rb_xCs_{3-x}C_{60}$ materials in character, follow the same Mott insulator-metal boundary on the global fcc A_3C_{60} electronic phase diagram [67]. T' has been tuned (bandwidth control) through application of chemical pressure *via* adjusting the K^+/Cs^+ dopant ratio. The present results of this study have revealed that, even though fcc-structured $K_xCs_{3-x}C_{60}$ and $Rb_xCs_{3-x}C_{60}$ materials exhibit comparable structural and electronic properties, cation specific effects are also of importance and should be taken into account in the description of the electronic properties of $A_xCs_{3-x}C_{60}$ fullerides.

Chapter 4 LF-μSR studies of Rb_2CsC_{60} and $Rb_{0.5}Cs_{2.5}C_{60}$

4.1 Introduction

For many years, observation of a Hebel-Slichter coherence peak in underexpanded Rb_3C_{60}, K_3C_{60} and Na_2CsC_{60} by Longitudinal Field Muon Spin Relaxation (LF-μSR) measurements [74] and its absence in unconventional superconductors such as the high-T_c oxides [207], [208], had been taken as clear evidence of electron-phonon driven BCS-type superconductivity in fcc A_3C_{60} fullerides. According to BCS theory, the attractive interaction between electrons in the superconducting state needed to overcome the Coulomb repulsion is mediated by phonons; conversely, strong enough repulsion tends to localize the electrons on atomic sites, leading to a Mott insulator (MI) in which strong electron correlations are responsible for the suppression of the metallic state. The experimental observation of a MI phase next to the superconducting phase in Cs_3C_{60} has changed the perspective that superconductivity in A_3C_{60} fullerides is driven only by electron-phonon coupling as the same strong correlations responsible for the Mott state are likely to influence also the superconducting state. The relevance of strong electron-electron interactions in the expanded A_3C_{60} fullerides has become apparent upon the discovery that the superconducting state borders a strongly correlated antiferromagnetic MI state and on approaching the MI boundary the superconducting T_c shows a 'dome'-shaped dependence on interfullerene separation [28], [67], reminiscent of the phase diagrams of many unconventional superconductors.

Furthermore, the importance of cooperation between the electron correlations and the electron-phonon interactions to reach high-T_c s-wave superconductivity in overexpanded A_3C_{60} superconductors has become increasingly clear upon the discovery of the molecular electronic structure control of superconductivity in this system [67], [204]. Following the experimental discovery that the two extremes (conventional and unconventional superconducting states) of the electronic phase diagram of the fcc A_3C_{60} fullerides

are connected by 'Jahn-Teller' metals (JTM) where localized electrons on the fullerene molecules coexist with metallicity [67], a quantitative theoretical description of the superconducting mechanism in A_3C_{60} system has been very recently reported by Nomura *et al* [204]. Their theoretical study has revealed that the s-wave superconductivity is driven from unusual multiorbital interactions that are caused by Jahn-Teller phonons, and strong electronic correlations arising from a subtle competition between Hund's coupling and Jahn-Teller phonons play a crucial role, leading to an important difference from conventional phonon-driven superconductivity [204].

4.1.1 Purpose of present study

In metals, the Korringa mechanism is the expected spin-lattice relaxation mechanism in which $1/T_1 T$ ($1/T_1$ being the nuclear spin-relaxation rate) is temperature independent, and nuclear relaxation arises primarily from energy exchanges with electrons at the top of the Fermi distribution. Therefore, the relaxation rate in normal metals and superconductors are expected to be significantly different [209].

The Hebel-Slichter coherence peak is seen as an enhancement of temperature dependence of $1/T_1 T$ on cooling just below T_c and is explained by the divergent density of states at the superconducting gap edges in BCS theory [209], [210]. Following the initial observation of the peak in Rb_3C_{60} by LF-μSR [73], NMR and further LF-μSR measurements of other fullerides (*e.g.* Rb_3C_{60}, K_3C_{60}, Na_2CsC_{60} and Rb_2CsC_{60}) confirmed the presence of the coherence peak but with a smaller magnitude than expected and a strong field-induced suppression [74], [210].

At the time, due to there being insufficient amount of high quality fcc-rich A_3C_{60} superconducting fullerides, with ambient pressure unit cell volumes spanning the 'dome' region of the $T_c(V)$ phase diagram (see Figure 1.5) and approaching the Mott-insulator-metal boundary, temperature response of $1/T_1 T$ of these systems remained unresolved. Recent synthetic efforts, using solid-state synthesis protocols, on the optimization of highly expanded fcc-rich A_3C_{60} fullerides spanning the superconductivity dome at ambient pressures in the $Rb_xCs_{3-x}C_{60}$ solid solution series have resulted in the availability of very large

masses of high quality samples (>1 g, an order of magnitude larger than previously available for these challenging materials). Large batch samples of fcc-rich $Rb_xCs_{3-x}C_{60}$ ($x = 2$ and 0.5) materials used in this study were synthesised in our laboratory by Dr. Ruth Zadik, according to a previously reported protocol [67] and were well-characterized by members of Prassides laboratory (Raman measurements by Dr. Ruth Zadik, SQUID magnetization measurements by Dr. Ross Colman, and X-ray powder diffraction by the candidate).

This study aimed to extract signatures of the importance of correlated behaviour in superconducting fcc-rich Rb_2CsC_{60} and $Rb_{0.5}Cs_{2.5}C_{60}$ fullerides with measurements of the temperature dependence of the LF-μSR rate of endohedrally-formed muonium (Mu@C_{60}; see section 2.3.3 for details). With this aim, we have searched for the existence of the Hebel-Slichter coherence peak for both compositions and extracted the superconducting gap magnitude from the low-temperature activated behaviour of $1/T_1$ in the superconducting state.

4.2 Experimental procedures

LF-μSR experiments were performed using the HiFi spectrometer at ISIS, UK. The overall setup of the spectrometer was summarised in Section 2.4.3. Due to the extreme air- and moisture-sensitivity of the samples, all sample manipulations were carried out within the inert atmosphere of a helium glove box (H_2O < 0.1 ppm and O_2 ~4 ppm). Samples (~1.1 g of each) were first placed in a silver sheet (thickness: 0.05 mm) which was then carefully folded and sealed within an air-tight flat plate aluminium sample holder (Figure 4.1), with screw-able titanium upper closing ring and closing sheet (thickness: 0.05 mm).

Samples inside the air-tight sample holder were placed in a helium-flow cryostat for temperature dependent measurements. Cooling from ambient temperature to 50 K, well above the superconducting T_c of the compounds, were undertaken under a small field (~100 G) perpendicular (transverse field, 'TF') to the initial muon polarisation. Once temperature stabilisation was achieved, TF measurements were carried out to determine the detector calibration factor. Once the data collection had been completed at small fields, a longitudinal field of 2.5 T was applied for the LF-μSR experiments undertaken on warming from 10 to 50 K, at a rate of ~90 million events per hour (Mev hr^{-1}). All muon relaxation spectra were analysed using the WiMDA programme suite [168].
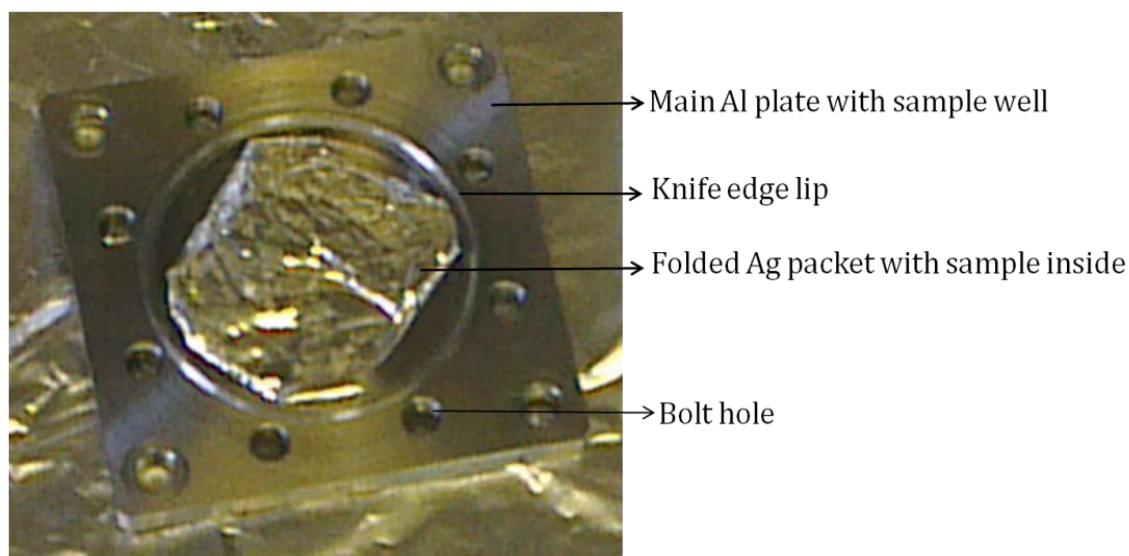
Figure 4.1 Air-tight aluminium sample holder with sample inside a folded Ag packet.

4.2.1 Determination of the detector calibration factor, α

Before analysing the muon data, it is essential to determine the detector calibration factor, α which is dependent on detector efficiencies and sample, and has to be determined for each individual experiment. This has been typically undertaken by applying TF to the initial muon polarisation which then rotates about the applied field, pointing first towards the forward detector and then towards the backward detector such that the signal oscillates symmetrically about the time axis. In this study, α of the individual experiments of Rb_2CsC_{60} and $Rb_{0.5}Cs_{2.5}C_{60}$ compounds were determined for forward and backward detector pairing by analysis of the TF data collected under fields of 90 and 100 G, and at temperatures of 50 K and 35 K, respectively. At HiFi spectrometer there are 64 detectors, and the '*grouping*' window within the software WiMDA allows to group all data in detectors 1 to 32 (a group of detectors referred to forward, F) and in detectors 33 to 64 (a group of detectors referred to backward, B) together.

4.2.2 Other correction parameters included in the analysis

In addition to the α correction, the *grouping* window within WiMDA provides several correction parameters such as *deadtime correction*, *background correction*, *binning type*, t_0, t_{good} *offset*, and *bunch factor*. Since ISIS produces a pulsed muon beam, a *deadtime* calibration has to be recorded. After a positron has been counted by a detector, there is a small interval before it is able to detect another count. Especially at high data collection rates, there is a high probability that a positron will arrive within this interval and not be recorded. At HiFi, a silver sample is used to determine *deadtime* values for each detector and they are recorded into a *deadtime* data file which is stored in the NeXus file internally. '*auto load*' option, being the option in this work, in WiMDA allows this internally stored *deadtime* correction data to be employed in the analysis [211].

When the middle of the muon pulse has reached the sample, the timing for the muon response in the sample starts; however, the *good data* region is not obtained until the entire muon pulse arrives at the sample. This time is known as t_{good}. The time at which the centre of the pulse reaches the sample is defined as t_0. The difference between t_{good} and t_0 is defined as the t_{good} *offset*. t_0 and t_{good} *offset* are

loaded from the NeXus file having been already determined locally [211]. Non-muon-related continuous background signal such as cosmic rays, electronic noise can be subtracted from the total positron count. WiMDA provides several options for background correction; the '*auto*' option, being the option in this work, corrects for the background count by fitting the data to a muon decay plus background and then subtracting the background signal [212].

Series of time values for positron events are grouped in amounts of time that are a fixed length of time, referring to '*bins*'. The *'fixed'* option was selected for *binning type* for the analysis in this work. While the *binning type* is fixed during the analysis, *bunch factor* can be varied by averaging several values from different adjacent bins. The bunching creates a time average by increasing the bunch factor to specify the length of time that the average is to be taken over. Large bunch factors reduce the statistical errors which makes easier to visually check the quality of fitting. If the relaxation is rapid, smaller bunch factor should be used [212]. In this work, bunch factor of 1 was used for the analysis of the LF-μSR data.

4.2.3 Analysis

After summarising correction parameters under *grouping* window, we now turn to '*analyse*' window which contains the fitting functions and parameters such as *group to fit*, *time range*, *asymmetry*, and *relaxation components. Group to fit* allows different groups to be selected and fitted. '*FB asym'* and '*F, B'* options under *group to fit* were selected for the current LF-μSR and TF-μSR (for α determination) data analysis, respectively. '*FB asym'* fits the plots of the forward/backward asymmetry and '*F, B'* displays and fits the counts detected by the forward and backward channels [212]. Time range of 0-10 μs was used for fittings of the LF-μSR data. *Asymmetry* parameter is the product of an initial asymmetry, baseline asymmetry and relaxing asymmetry. The initial asymmetry refers to the total asymmetry at time = 0, the baseline asymmetry modifies the α value to allow accurate balancing of the forward and backward detector sets in a forward/backward grouping. Once the baseline asymmetry is determined, it should be fixed during fitting of the LF datasets. Relaxing asymmetry is the difference between the initial and baseline asymmetries; $A_{initial} - A_{baseline} = A_{relaxing}$. Due to there being such constraint, not all the asymmetries can be allowed to vary

simultaneously; therefore, which asymmetry parameter will be dependent on the other fitted asymmetry parameter should be selected using the *dependent asymmetry* box in the *analyse* window [212]. For the analysis of the current LF-µSR data, the initial asymmetry was selected as the dependent asymmetry.

The *analysis* window in WiMDA allows µSR data to be fitted with up to six relaxation components. Each relaxation component is a product of an 'oscillation' and a 'relaxation' term, and standard oscillation and relaxation functions are provided in WiMDA [212]. As summarised previously in Section 2.3.3, the LF-µSR technique involves measuring the time dependence of the muon decay asymmetry. In this study, the time dependence of the asymmetry, $A(t)$, was fitted using a model with one component and exponential relaxation, using the following single Lorentzian relaxation function allowing the $1/T_1$ longitudinal muon spin relaxation rate to be extracted [213]:

$$A(t) = A_{relax}e^{(-\lambda t)} + A_{baseline}$$

Equation 4.1

where λ represents the $1/T_1$ muon spin relaxation rate in MHz at time t. Oscillation function was not applied in the current analysis.

The following procedure was applied for the extraction of the $1/T_1$ from the LF- µSR datasets:

1.   The time dependence of the muon decay asymmetry at each temperature was fitted allowing all three variables ($A_{relaxing}$, $A_{baseline}$, and λ) in the relaxation function to vary independently and simultaneously.

2.   The baseline was defined using the high temperature data where $A_{baseline}$ exhibits almost temperature-independent behaviour and the relaxation is fast.

3.   The time dependence of the muon decay asymmetry at each temperature was fitted with a fixed-baseline while refining $A_{relaxing}$ and λ; thereafter the magnitude of the relaxing component was defined using the low-temperature data where $A_{relaxing}$ was assumed to be temperature-independent and the relaxation is slow.

4.   Finally, the baseline and relaxing component were fixed to that obtained at [2] and [3], and only λ was allowed to refine.

4.3   Rb$_2$CsC$_{60}$

The quality of Rb$_2$CsC$_{60}$ was checked by laboratory X-ray powder diffraction at ambient temperature (Figure 4.2). After confirmation that the sample is phase-pure and the fcc lattice parameter, a = 14.4440(2) Å, is in agreement with the previously reported value (a = 14.45169(9) Å [67]), temperature dependent magnetisation measurements, $M(T)$, were performed under both ZFC and FC protocols at applied fields of 10 Oe and 2.5 T to define the superconducting T_c.
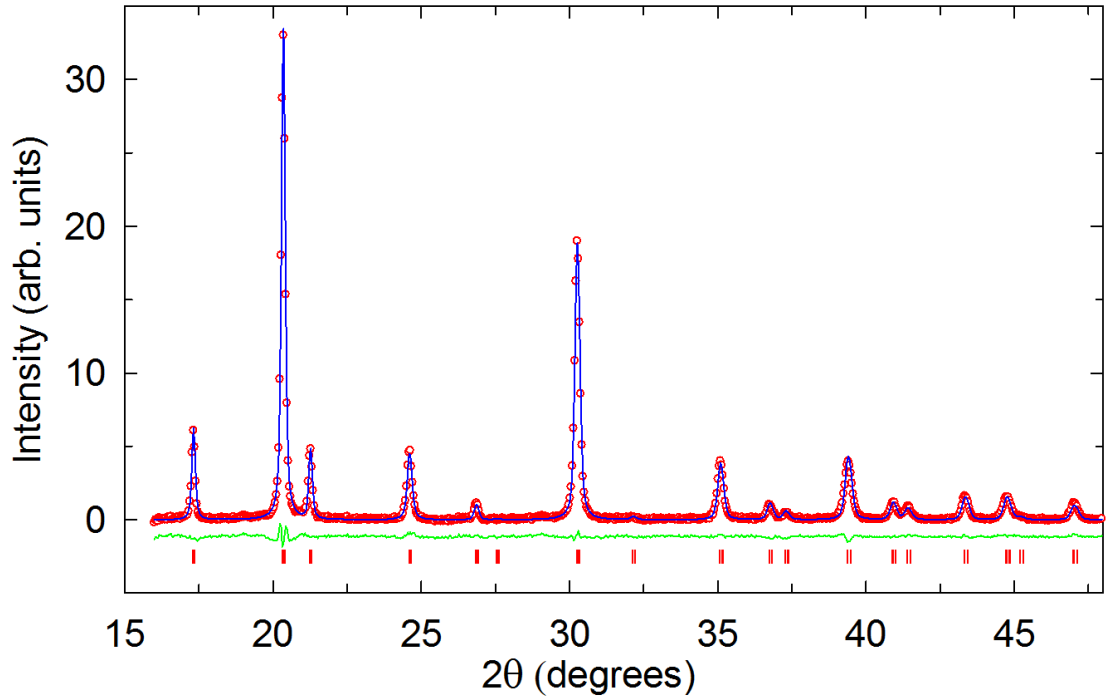
Figure 4.2 Rietveld fit to laboratory XRPD data collected for phase-pure Rb$_2$CsC$_{60}$ at ambient temperature (λ = 1.5406 Å, R_{wp} = 3.02% and R_{exp} = 1.88%). Red circles, blue lines and green lines represent the observed, calculated and difference profiles, respectively. Red ticks mark the reflection positions of fcc phase.

Figure 4.3 shows the corresponding ZFC and FC $M(T)$ data. The inset in Figure 4.3 (b) demonstrates that T_c varies little with increasing the applied field to the range of values employed in the LF-μSR measurements. The difference between the first deviation points of the two ZFC datasets is ~0.5 K or less. Here T_c is defined as 32.5 and 32 K at fields of 10 Oe and 2.5 T, respectively. Shielding fraction is estimated as 95% at a field of 10 Oe. As a longitudinal field of 2.5 T was applied for the LF-μSR experiments, T_c of 32 K is used in the subsequent treatment and analysis of the datasets.
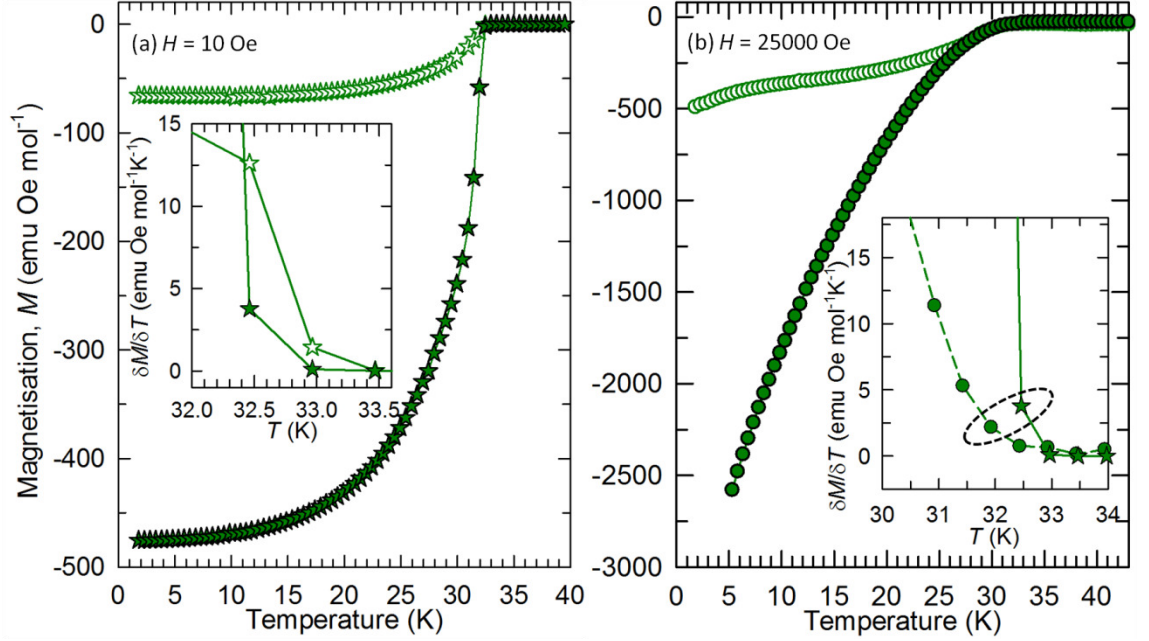
Figure 4.3 Temperature dependence of the ZFC and FC magnetisation, $M(T)$, of fcc Rb_2CsC_{60} measured at fields of (a): 10 Oe (solid stars: ZFC $M(T)$, open stars: FC $M(T)$), and of (b): 25000 Oe (solid circles: ZFC $M(T)$, open circles: FC $M(T)$). Insets in (a) and (b) show the temperature evolution of the first derivatives of the ZFC and FC magnetisation, and of the ZFC magnetisation datasets (measured at fields of 10 Oe: solid stars, and of 25000 Oe: solid circles) with respect to temperature, respectively. Lines through data points are guides to the eye. Dotted black edged circle in (b) depicts the difference between the first deviation points of the two ZFC datasets.

4.3.1 Determination of α

Prior to analysis of the LF-μSR datasets, the TF-90 G data were analysed to determine the detector calibration factor, α; this was undertaken by fitting the counts detected by the forwards and backwards channels *via* selecting the '*F, B*' option under *group to fit*. The time evolution of the muon spin polarisation, $P\mu(t)$ (Figure 4.4) can be described by the following function:

$$P_\mu(t) \propto exp(-\frac{1}{2}\sigma^2 t^2)\,cos(\omega_\mu t + \varphi_\mu) \qquad \text{Equation 4.2}$$

Here σ measures the width of the local field distribution at the muon site and $\omega_\mu = \gamma_\mu B_\mu$ is the muon precession frequency and φ_μ its phase, and γ_μ is the muon gyromagnetic ratio.

The fits yielded an α value of 1.1992(9) and $A_{relaxing}$ = 18.87(6)%. The average count between the two forward and backward channels ('*NO*' in WiMDA) and the background count for the forward ($BG(F)$) and backward ($BG(B)$) channels were refined to 26423(10), 0.014(66), and −0.144(66), respectively. The α correction of

146

1.1992(9) was employed in the analysis of the LF datasets. Once the parameter α had been determined, analysis of the LF runs was started following the analysis procedure given in Section 4.2.3.
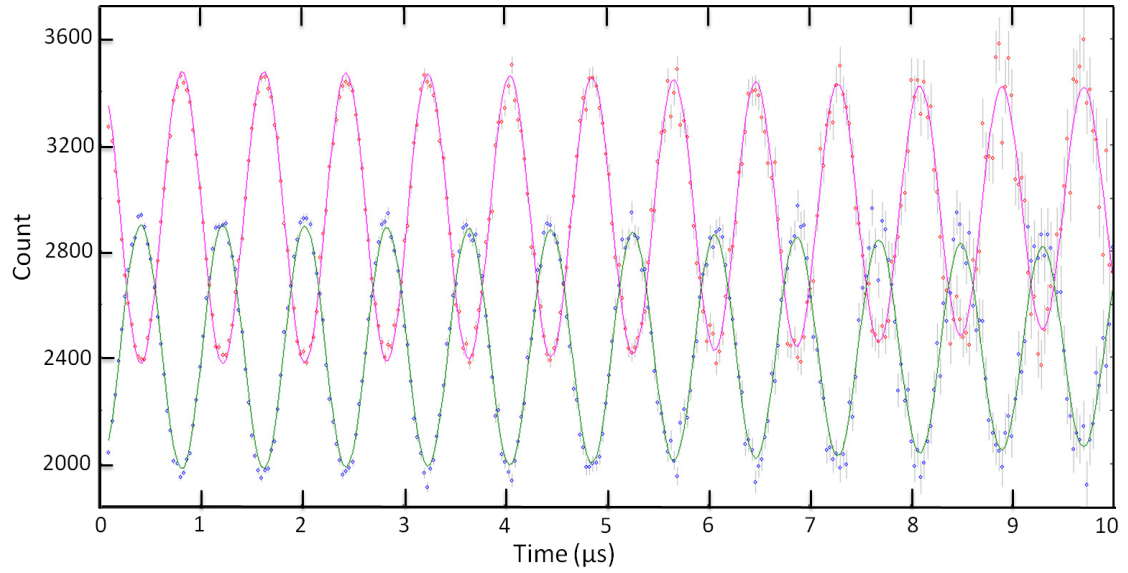
Figure 4.4 Time dependence of the counts detected by the forward and backward channels, from TF-90 measurements of Rb_2CsC_{60} at 50 K, together with final fits represented with pink and green solid lines for the forward and backward channels, respectively.

4.3.2 LF-µSR data analysis

Step 1: The time dependence of the asymmetry was fitted allowing $A_{baseline}$, $A_{relaxing}$, and λ to vary independently and simultaneously with increasing temperature.
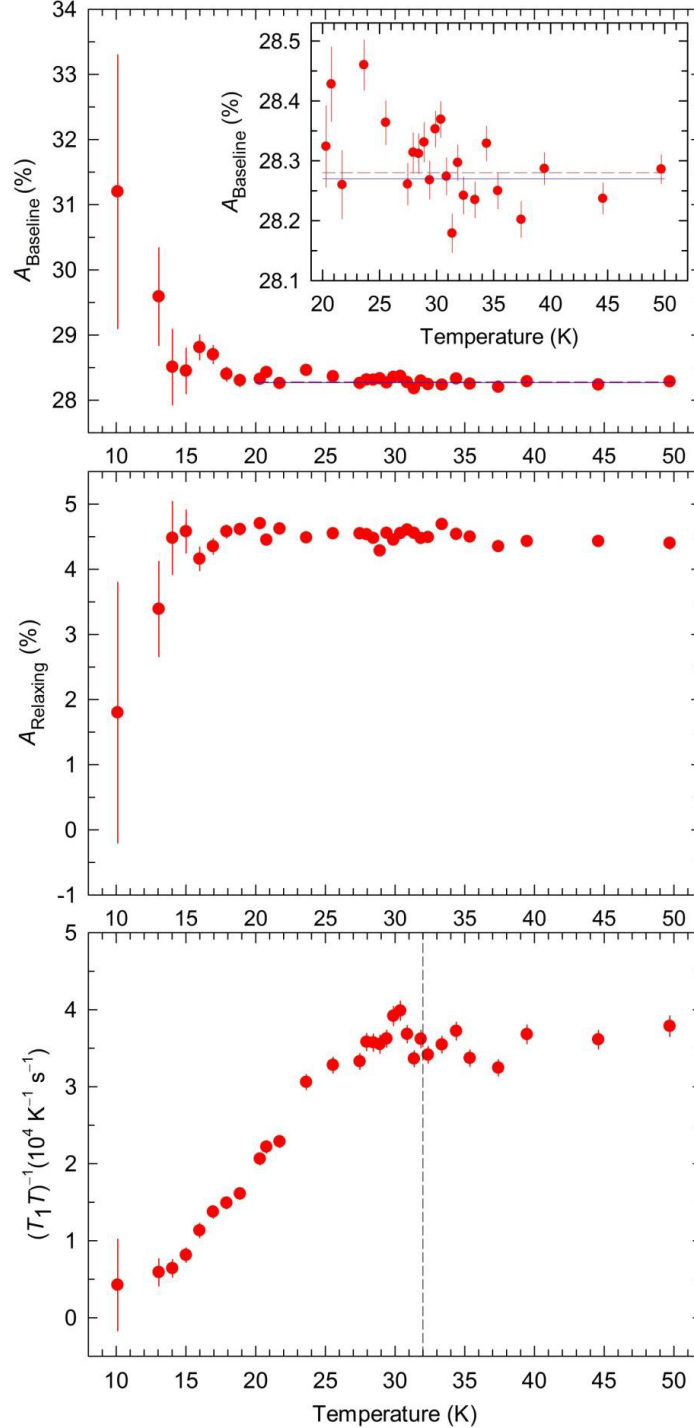
Figure 4.5 From top-to-bottom: temperature dependence of the refined $A_{baseline}$, $A_{relaxing}$, and spin-relaxation rate of Mu@C_{60} divided by temperature, $(T_1 T)^{-1}$, in fcc Rb_2CsC_{60} in a longitudinal applied field of 2.5 T. The inset in top panel displays an expanded region of the respective plot; pink and blue lines represent the average $A_{baseline}$, $<A_{baseline}>$, values of 28.28(5)% and 28.27(5)%, respectively. Dashed line in bottom panel signifies the superconducting T_c of 32 K for Rb_2CsC_{60}.

Step 2: $A_{baseline}$ was defined using the high temperature data, where relaxation is fast, assuming $A_{baseline}$ is temperature-independent.

As seen in Figure 4.5, $A_{baseline}$ at high temperatures between 20 and 50 K, where the relaxation is high, is quite robust, exhibits almost temperature-independent behaviour. Therefore, an average of $A_{baseline}$, $<A_{baseline}>$, could be taken over different temperature ranges to fix the $A_{baseline}$ at an appropriate average value for fitting the time dependence of the asymmetry, $A(t)$, while refining the $A_{relaxing}$ and spin-relaxation rate, $1/T_1$. $<A_{baseline}>$ in the temperature ranges of $25\,K \leq T \leq 50\,K$, $30\,K \leq T \leq 50\,K$ and $40\,K \leq T \leq 50\,K$ were found as 28.28(5), 28.27(5) and 28.27(2)%, respectively.

When all the three variables were allowed to refine simultaneously, even though resulting temperature dependence of the relaxation rate $(T_1 T)^{-1}$ exhibits almost temperature-independent behaviour in the normal state between 50 K and the superconducting T_c of 32 K, data points are significantly scattered at this point (Figure 4.4). Fixing $A_{baseline}$ should minimise this scatter leading to a smoother temperature dependence of $(T_1 T)^{-1}$; therefore for the next step of the analysis, the $A_{baseline}$ was fixed at 28.27%, assuming $A_{baseline}$ is temperature-independent, and only the $A_{relaxing}$ and $1/T_1$ were allowed to refine.

The asymmetric decay of muons gives different counts at the forward and backward counters. Figure 4.6 shows the fit results of the time dependence of asymmetric decay of muons at selected temperatures while refining all the three variables in the relaxation function (Equation 4.1). At low temperatures below 22 K, there is a very slow relaxation of the muon spin compared to the relaxation at high temperature; the change in the counting rate of the F and B detectors with time is relatively small in magnitude. Especially at 10 K, the ratio between the F and B counters stays almost constant and does not change much with time. Conversely, there is a significant change in the counting rate of the F and B detectors at 22 and 50 K implying a fast relaxation of the muon spin. $A(t)$ data also verifies that there is only one relaxation component and no sign from a sample and/or sample holder dependent residual relaxation. If there was more than one relaxing component, a peculiar deviation in the $A(t)$ data would have been expected, displaying different relaxation behaviour differing with rate.
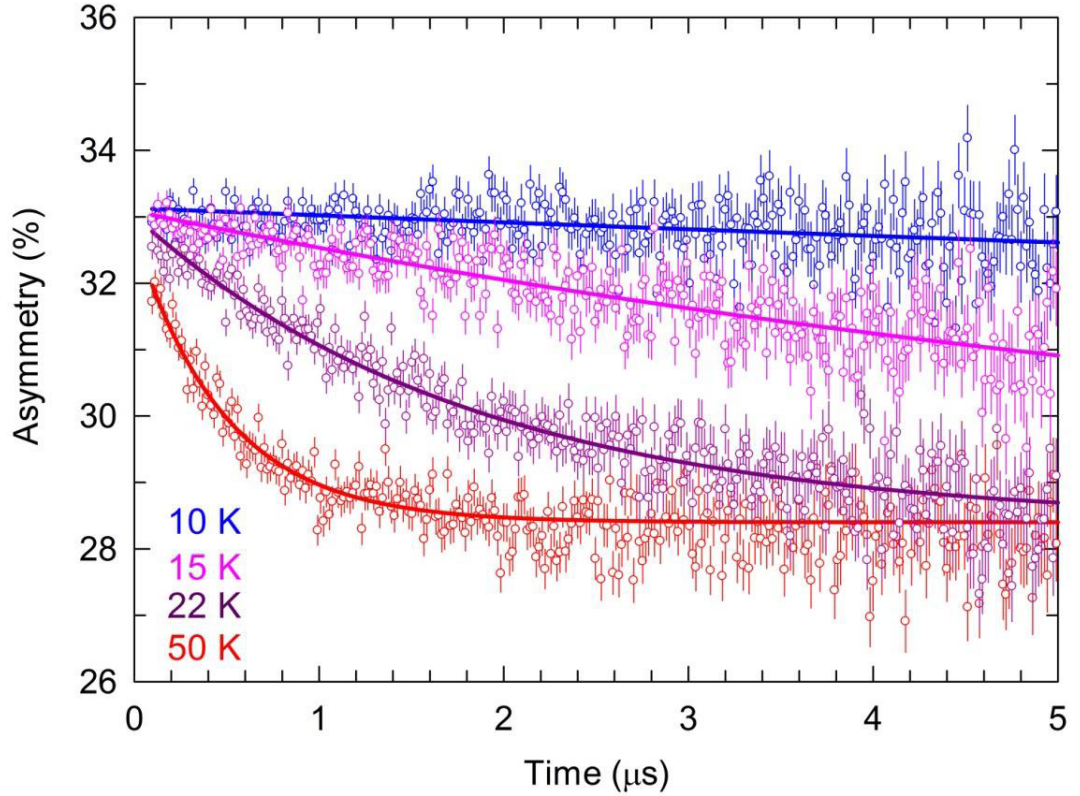
Figure 4.6 The time dependence of the muon decay asymmetry, A(t), measured by LF-μSR in fcc Rb_2CsC_{60} at a field of 2.5 T at selected temperatures. A(t) were fitted using the Lorentzian relaxation function (Equation 4.1) in which $A_{baseline}$, $A_{relaxing}$ and λ are simultaneously refined ; solid lines show the fit results at selected temperatures. LF-μSR spectra were bunched with a factor of 1, and the fits were performed in the time range of 0-10 μs; however only 0-5 μs region is shown for visual clarity.

Step 3: The time dependence of the muon decay asymmetry was fitted with a fixed-baseline value of 28.27% with refined $A_{relaxing}$ and $1/T_1$; thereafter the magnitude of the relaxing component was defined using the low-temperature data where $A_{relaxing}$ was assumed to be temperature-independent.

The plot of $(T_1T)^{-1}$ *vs* T is now less scattered all over the experimental temperature range compared to the case where all the three variables were allowed to refine, as seen in Figure 4.7 (b). Temperature dependence of the extracted $A_{relaxing}$ is also less scattered varying between ~4.2% and 4.8% (Figure 4.7 (a)), compared to the top panel of Figure 4.6. So far, we only fixed the baseline asymmetry which in turn improved the scattered behaviour of the $(T_1T)^{-1}$ *vs* T plot.
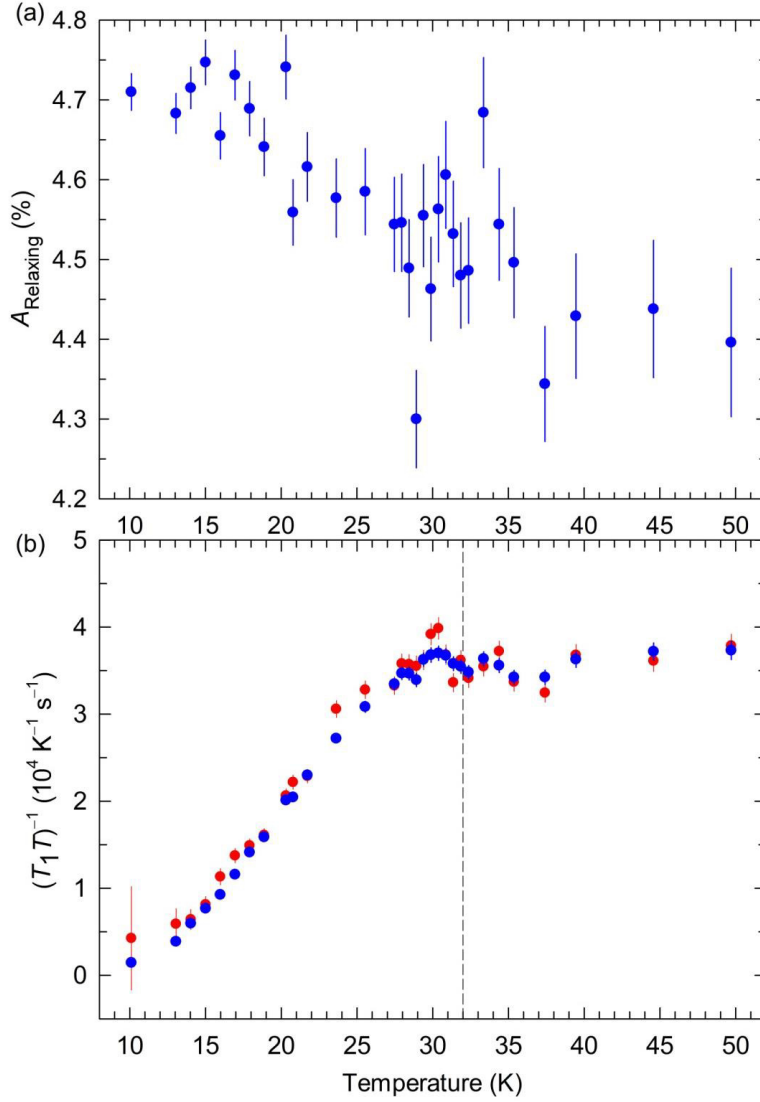
Figure 4.7 (a): Temperature dependence of the A_{relaxing} and (b): of the spin-relaxation rate of Mu@C$_{60}$ divided by temperature, $(T_1T)^{-1}$, in fcc Rb$_2$CsC$_{60}$ in a longitudinal applied field of 2.5 T. Data are obtained from the fits using Lorentzian relaxation function in which A_{baseline}, A_{relaxing}, λ are refined; represented with red circles and A_{baseline} fixed, A_{relaxing} and λ are refined; represented with blue circles. Dashed black line signifies the superconducting T_c of 32 K for Rb$_2$CsC$_{60}$.

We should now define a value to fix the A_{relaxing} together with A_{baseline} in the relaxation function; this was undertaken by taking several average values of A_{relaxing} over different temperature ranges between 10 and 50 K (see Table 4.1 for details). When A_{baseline} is already fixed, it is expected that the lowest temperature point (A_{relaxing} at 10 K = 4.71(2)%), which yields the lowest relaxation rate, will give the most accurate value of A_{relaxing} as this essentially defines A_{initial}, and is most easily defined when the change in the counting rate of the F and B detectors with time is relatively small in magnitude, in other words, when the spectra is flattest, such that the 10 K spectra shown in Figure 4.6.

Table 4.1 Average values of A_{relaxing} taken over different temperatures ranges.

Temperature (K)	A_{relaxing} (%)
$10 \leq T \leq 15$	4.71(2)
$10 \leq T \leq 20$	4.70(3)
$10 \leq T \leq 25$	4.67(3)
$10 \leq T \leq 50$	4.57(12)
29	minimum A_{relaxing} = 4.30

The time dependence of the muon decay asymmetry that were fitted at selected temperatures with A_{baseline} fixed at 28.27% and with various fixed A_{relaxing} values as tabulated in Table 4.1 is shown in Figure 4.8(a).
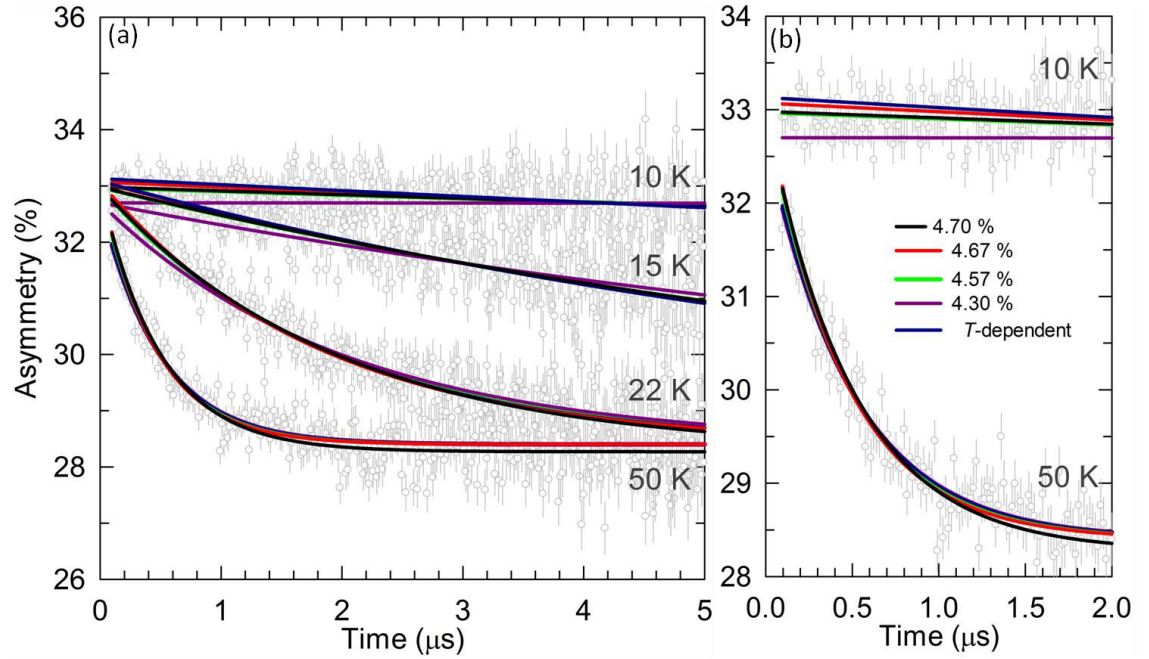
Figure 4.8 (a): The time dependence of the muon decay asymmetry, A(t), measured by LF-μSR in fcc Rb_2CsC_{60} at a field of 2.5 T at selected temperatures; from top-to bottom: 10, 15, 22 and 50 K. A(t) data were fitted using the Lorentzian relaxation function in which A_{baseline} was fixed at 28.27%, A_{relaxing} were fixed at values of 4.70, 4.67, 4.57 and 4.30%; resulting fits are presented with black, red, green, and purple solid lines, respectively. Dark blue solid line is the fit in which A_{relaxing} is refined together with λ. (b) is the expanded view of (a); for visual clarity only 10 and 50 K spectra are shown together with fits. LF-μSR spectra were bunched with a factor of 1, and the fits were performed in the time range of 0-10 μs.

The minimum A_{relaxing} value of 4.30%, visually, did not result in a good fit between 0 and 3 μs at low temperatures; however, the other A_{relaxing}s led to similar trend (Figure 4.8(b)). At low temperatures (≤ 22 K), the larger A_{relaxing}s definitely fit the A(t) data better. At high temperatures, the differences in the chosen A_{relaxing}

did not make a significant difference to the visual quality of the fit. Extracted relaxation rate from various fittings led to following $(T_1T)^{-1}$ *vs T* plot in Figure 4.9.

Whilst the change in the magnitude of $A_{relaxing}$ clearly changes the extracted relaxation rate, the general trends are still present; a small enhancement of temperature dependence of $1/T_1 T$ on cooling just below T_c is clearly observed. Also, the small level of scatter is still apparent consistent between the various fittings. Clearly it is important to choose the most appropriate $A_{relaxing}$ for extraction of the superconducting gap magnitude from the low-temperature activated behaviour of $1/T_1$ in the superconducting state and determining coherence peak damping. Fixed $A_{relaxing}$ of 4.70% led to the most consistently low value of χ^2. The temperature dependent $A_{relaxing}$ also resulted in consistently low value of χ^2 compared to others but there is not a significant enough improvement over the fixed values.
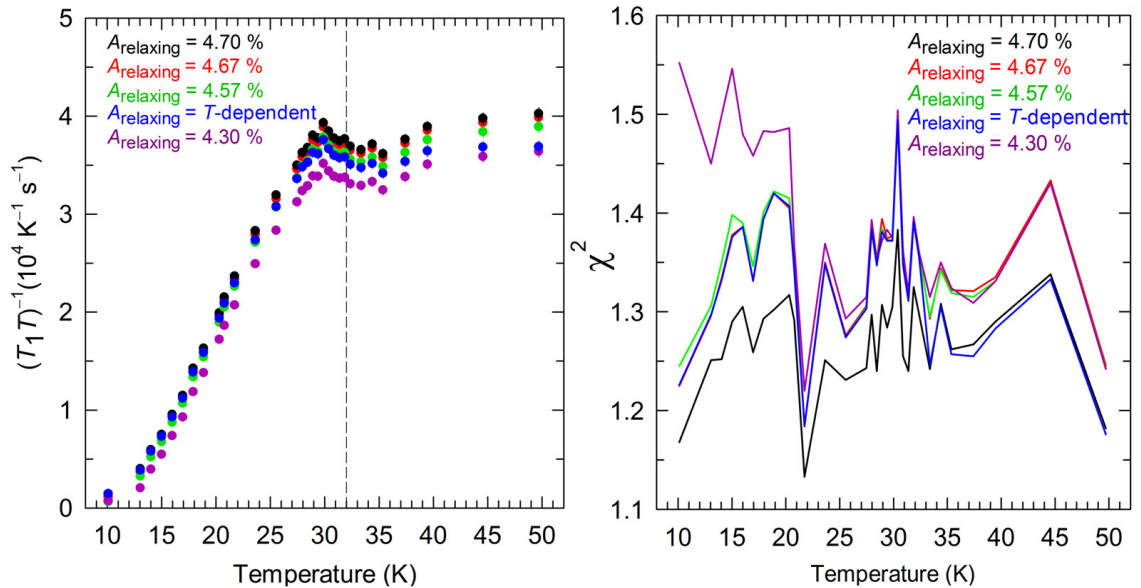
Figure 4.9 Left panel: Temperature dependence of the spin-relaxation rates of Mu@C$_{60}$ divided by temperature, $(T_1T)^{-1}$, in fcc Rb$_2$CsC$_{60}$ in a longitudinal applied field of 2.5 T. Black, red, green and purple circles represent the data extracted from the fits using Lorentzian relaxation function in which $A_{baseline}$ fixed at 28.27% and $A_{relaxing}$ fixed at values of 4.70, 4.67, 4.57 and 4.30%, respectively. Dark blue circles represent the data extracted from the fits in which $A_{relaxing}$ is refined together with λ. Dashed line signifies the superconducting T_c of 32 K for Rb$_2$CsC$_{60}$. Right panel: Variation of the goodness of the fits, χ^2, with temperature for various fixed $A_{relaxing}$s.

Figure 4.10 shows the plot of $(T_1T)_N/ T_1T$ *vs T* where spin-relaxation rate was normalised to the rate in the normal state just above the superconducting T_c, for various fixed $A_{relaxing}$s. The normal state relaxation rate was determined at 33.4 K

as 0.0366(5) MHz K^{-1}. When the $(T_1 T)^{-1}$ spin-relaxation rate was normalised to just above the T_c, a small Hebel-Slichter coherence peak appeared almost identical size and shape for various $A_{relaxing}$s (Figure 4.10).
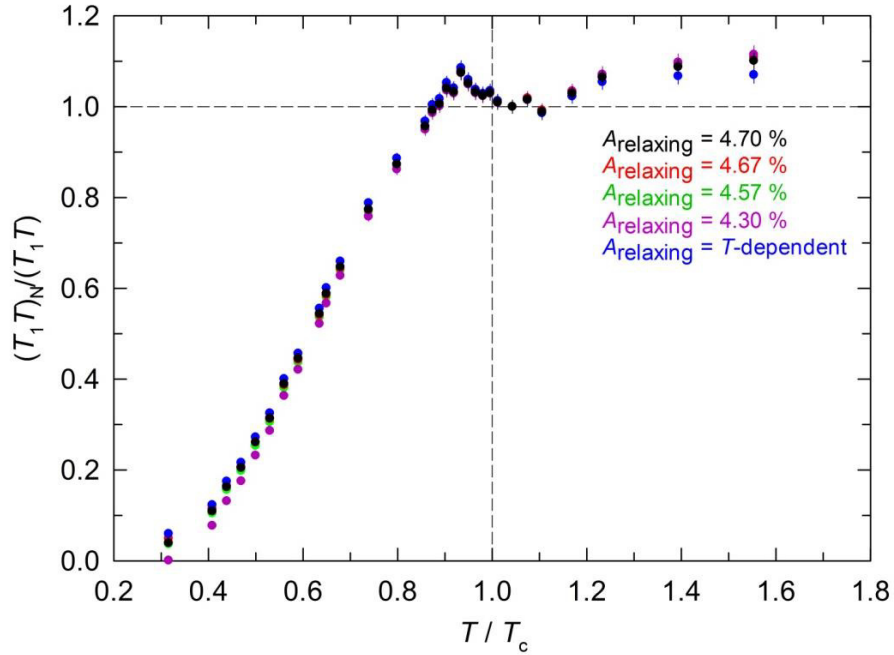
Figure 4.10 Temperature dependence of the spin-relaxation rates of Mu@C$_{60}$ in fcc Rb$_2$CsC$_{60}$ in a longitudinal applied field of 2.5 T, extracted for various fixed $A_{relaxing}$s. $(T_1 T)^{-1}$ is normalised to the rate in the normal state; divided by the rate of 0.0366 MHz K^{-1}.

We have already verified that $A_{relaxing}$ of 4.70% led to the most consistently low value of χ^2 amongst other $A_{relaxing}$s and altering $A_{relaxing}$ clearly changed the extracted relaxation rate; however the general trends are present with an enhancement of temperature dependence of $1/T_1 T$ on cooling just below the superconducting T_c of 32 K. For further comparison between various $A_{relaxing}$s, we have estimated the superconducting gap magnitude $2\Delta/k_B T_c$ (see Section 1.2.3 for details) from the low-temperature activated behaviour of $1/T_1$ for various $A_{relaxing}$s. In the superconducting state, the superconducting gap (activated energy), Δ, could be estimated from Arrhenius law; $1/T_1 \propto \exp(-\Delta/k_B T)$. While Arrhenius law accounts for the majority of the low-temperature dependence, it is not the complete dependence; a perfect Arrhenius behaviour is only seen if the density of states is gapped, Δ, and this Δ gives rise to Arrhenius law. Figure 4.11 shows the plot of $\ln(1/T_1)$ *vs* $1/T$ for various $A_{relaxing}$s together with linear fits to the low-temperature data in the temperature range 10 K < T < 24 K. The gradient of the linear fits gives the ratio of $-\Delta/k_B$ and in turn the relevant dimensionless parameter $2\Delta/k_B T_c$ (Table 4.2).
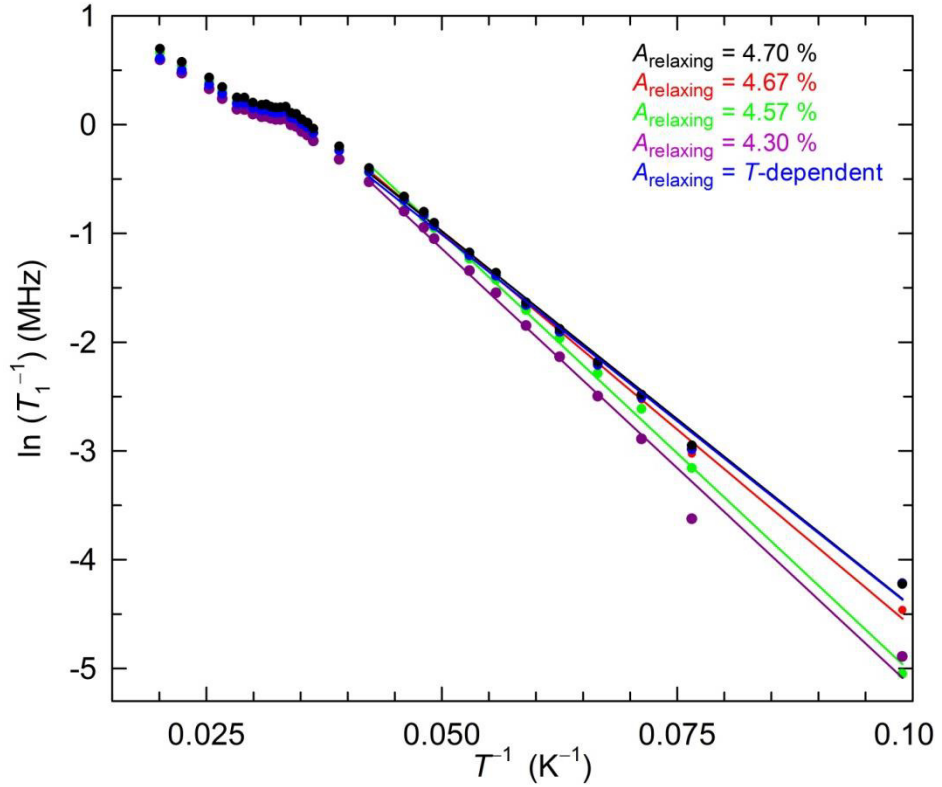
Figure 4.11 ln($1/T_1$) *vs* $1/T$ plot for various A_{relaxing}s. Lines through data points are linear fits to the low-temperature data in the temperature range 0.042 K < T^{-1} < 0.1 K, yielding values of $-\Delta/k_B$ = 69(1), 73(1), 81(1), 81(2) and 69(1) for various A_{relaxing}s.

Table 4.2 Estimated $2\Delta/k_B T_c$ for various A_{relaxing}s.

A_{relaxing} (%)	$-\Delta/k_B$	$2\Delta/k_B T_c$
4.70	69(1)	4.31(6)
4.67	73(1)	4.56(6)
4.57	81(1)	5.06(6)
4.30	81(2)	5.1(1)
T-dependent	69(1)	4.31(6)

Estimated $2\Delta/k_B T_c$ values for various A_{relaxing}s from the $1/T_1 \propto \exp(-\Delta/k_B T)$ variation for 0.042 K < T^{-1} < 0.1 K signify that values of $2\Delta/k_B T_c$ for any A_{relaxing} values are significantly larger than the value of $2\Delta/k_B T_c$ = 3.52 expected in the weak-coupling limit of BCS theory. While A_{relaxing} of 4.70% and *T*-dependent A_{relaxing} led to the identical estimation of $2\Delta/k_B T_c$, smaller A_{relaxing}s resulted in very large values. With the knowledge that fixing A_{relaxing} at 4.70% led to the best fits of the time dependence of the muon decay asymmetry over the experimental temperature range and resulted in $2\Delta/k_B T_c$ = 4.31(6) which is in excellent

agreement with 4.31(9) reported for fcc Rb_2CsC_{60}, determined from the temperature dependence of the ^{87}Rb spin-lattice relaxation rate [67], from now on, only $1/T_1$ extracted from the fits with fixed $A_{relaxing}$ at 4.70% will be used for extraction of $2\Delta/k_BT_c$ and for the final determination of the coherence peak for Rb_2CsC_{60}. Final Arrhenius plot of $1/T_1$ ($A_{relaxing}$ = 4.70%) is shown in Figure 4.12, displaying $1/T_1 \propto \exp(-\Delta/k_BT)$ variation for $1.35 < T_c/T < 3.17$, and the final fits to the LF spectra at selected temperatures with fixed $A_{baseline}$ at 28.27% and $A_{relaxing}$ at 4.70% are shown in Figure 4.13.
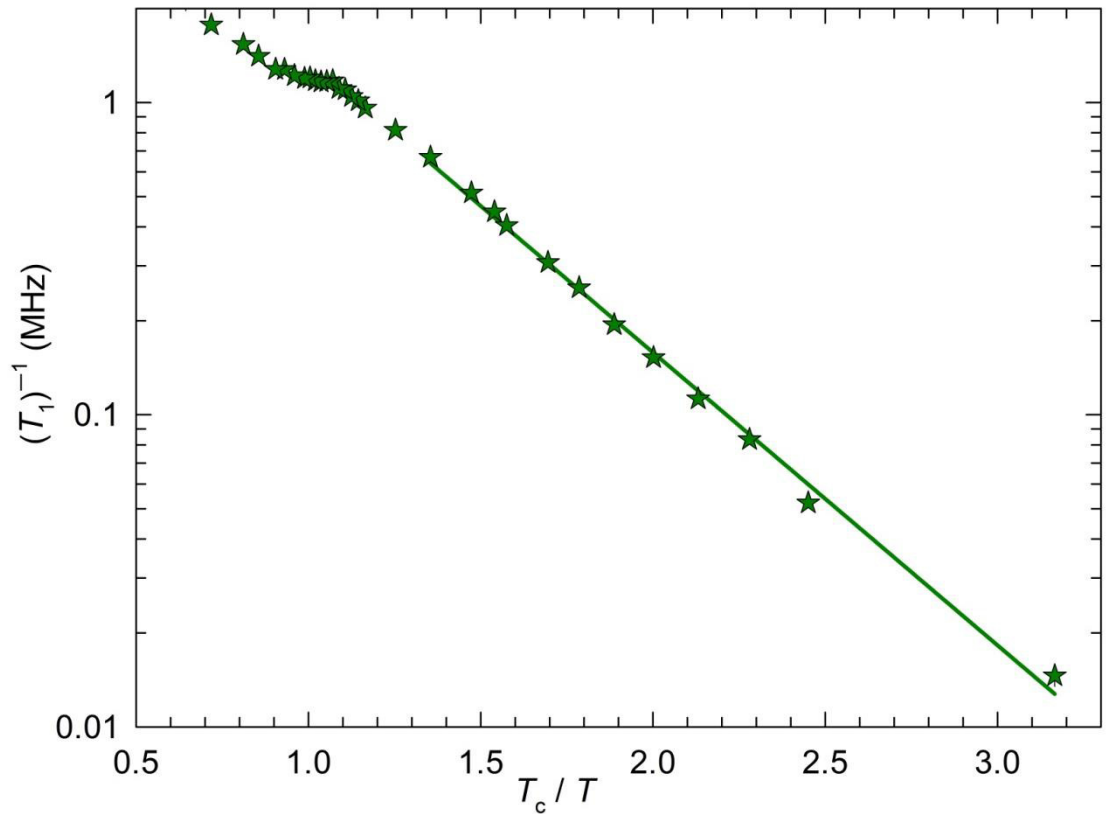
Figure 4.12 Arrhenius plot for the spin-relaxation rate of Mu@C_{60} in fcc Rb_2CsC_{60} in a longitudinal field of 2.5 T. Solid line through data points is fit to the equation, $1/T_1 \propto \exp(-\Delta/k_BT)$, in the low-temperature region, $1.35 < T_c/T < 3.17$.
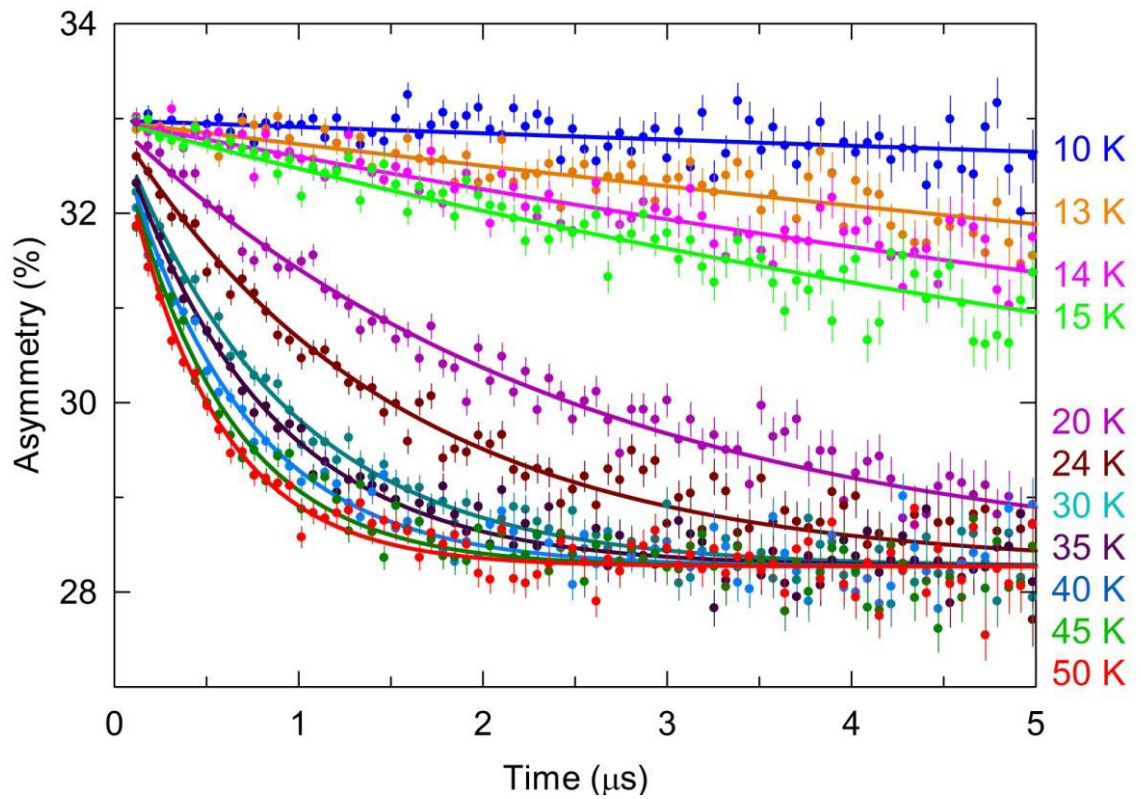
Figure 4.13 The time dependence of the muon decay asymmetry, A(t), measured by LF-μSR in fcc Rb_2CsC_{60} at a field of 2.5 T at selected temperatures. A(t) data were fitted using the Lorentzian relaxation function in which $A_{baseline}$ and $A_{relaxing}$ were fixed at 28.27% and 4.70%, respectively; resulting fits are presented with solid lines. For visual quality, LF-μSR spectra were bunched with a factor of 4, and only 0-5 μs region is shown.

4.4   Rb$_{0.5}$Cs$_{2.5}$C$_{60}$

Laboratory XRPD profile was collected at ambient temperature to reveal the quality of Rb$_{0.5}$Cs$_{2.5}$C$_{60}$. Rietveld fit to the XRPD data is shown in Figure 4.14. Three crystallographic phases were included in the refinement: a majority fcc phase, and minority Cs$_4$C$_{60}$ and CsC$_{60}$ phases. The weight fractions of these phases were found as 77.3(1)%, 16.2(2)% and 6.5(3)%, respectively. The refined fcc lattice constant is a = 14.6583(5) Å, consistent with previously reported value at ambient temperature: a = 14.6549(2) Å [67].
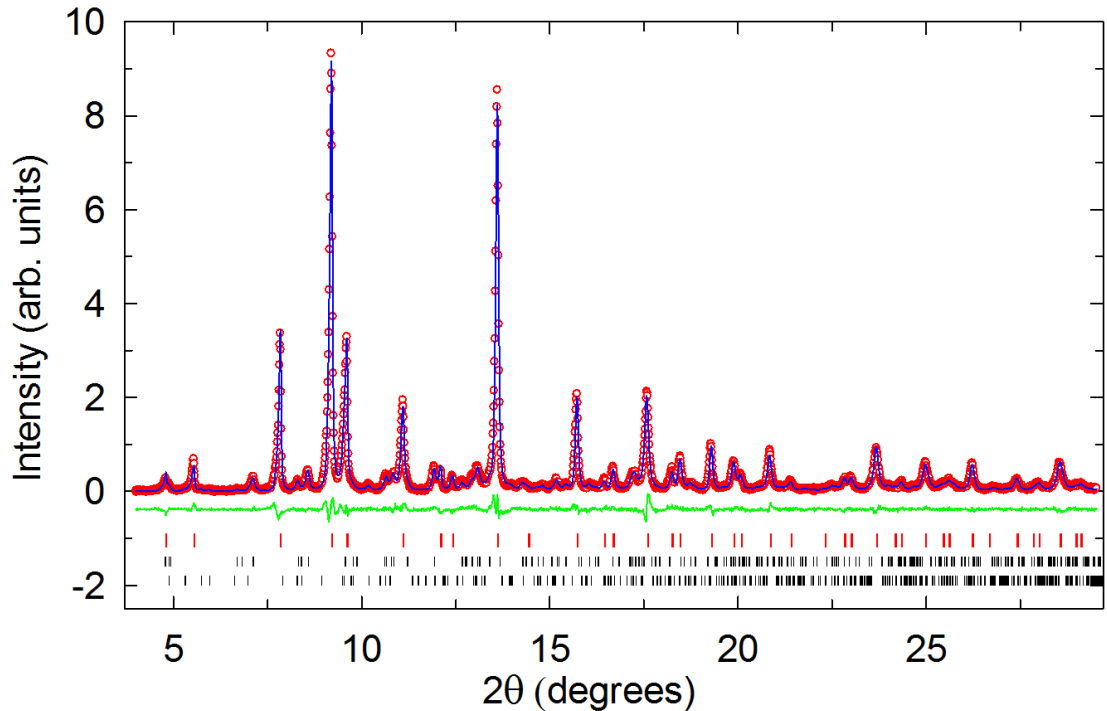
Figure 4.14 Rietveld fit to laboratory XRPD data collected at ambient temperature, for fcc-rich Rb$_{0.5}$Cs$_{2.5}$C$_{60}$ (λ = 0.7093 Å, R_{wp} = 7.48% and R_{exp} = 4.64%). Red circles, blue lines and green lines represent the observed, calculated and difference profiles, respectively. Ticks mark the reflection positions, from top-to-bottom, of co-existing fcc (red ticks), Cs$_4$C$_{60}$ and CsC$_{60}$ phases.

Prior to magnetisation measurements of the fcc-rich Rb$_{0.5}$Cs$_{2.5}$C$_{60}$ at a field of 2.5 T, $M(T)$ data were first collected at an applied field of 10 Oe under both ZFC and FC protocols. The temperature onset of the downturn in the ZFC magnetisation measured at a field of 2.5 T is consistent with that measured at 10 Oe, as for Rb$_2$CsC$_{60}$. As seen in the inset of Figure 4.15 (b), the difference between the first points of deviations of the two ZFC datasets is ~0.2 K or less. The superconducting T_c of this sample is defined as 30.4 K at an applied field of 2.5 T. Shielding fraction at a field of 10 Oe is estimated as 63%.
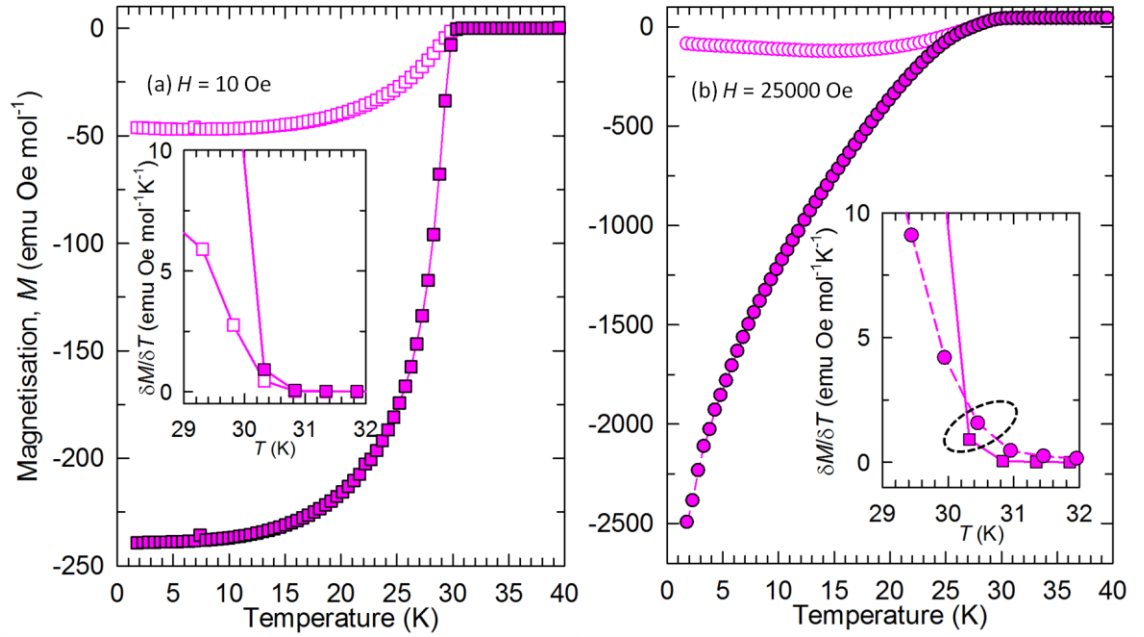
Figure 4.15 Temperature dependence of the ZFC and FC magnetisation, $M(T)$, of fcc $Rb_{0.5}Cs_{2.5}C_{60}$ measured at fields of (a): 10 Oe (solid squares: ZFC $M(T)$, open squares: FC $M(T)$), and of (b): 25000 Oe (solid circles: ZFC $M(T)$, open circles: FC $M(T)$). Insets in (a) and (b) show the temperature evolution of the first derivatives of the ZFC and FC magnetisation, and of the ZFC magnetisation datasets (measured at fields of 10 Oe: solid squares, and of 25000 Oe: solid circles) with respect to temperature, respectively. Lines through data points are guides to the eye. Dotted black edged circle in (b) depicts the difference between the first deviation points of the two ZFC datasets.

4.4.1 Determination of α

The detector calibration factor, α, was determined using the same method as employed for Rb_2CsC_{60} described in Section 4.3.1. Prior to LF runs, TF-100 G spectra were measured at 35 K. The final fits to the symmetrically oscillated counts about the time axis detected by the F-B channels yielded an α value of 1.117(1) and $A_{relaxing}$ = 17.69(7)%, which are comparable to that found from TF-90 G measurements of Rb_2CsC_{60}. The α value of 1.117(1) was employed in the analysis of LF-μSR datasets, using the same analysis procedure as employed for Rb_2CsC_{60} (see section 4.2.3 for details).

4.4.2 LF-μSR data analysis

Firstly, the time dependence of the asymmetry was fitted allowing $A_{baseline}$, $A_{relaxing}$, and λ (T_1^{-1}) to vary independently and simultaneously with increasing temperature. Temperature variation of the refined $A_{baseline}$ is shown in Figure 4.16 (a). At high temperatures between 20 and 50 K, $A_{baseline}$ exhibits almost

temperature-independent behaviour; $<A_{\text{baseline}}>$ in the temperature ranges of $20\,\text{K} \le T \le 50\,\text{K}$, $26\,\text{K} \le T \le 35\,\text{K}$ and $30\,\text{K} \le T \le 50\,\text{K}$ were found as 31.39(5), 31.39(7) and 31.41(4)%, respectively.

For the second step of the analysis, $A(t)$ data were fitted with fixed A_{baseline} at 31.39% allowing A_{relaxing} and T_1^{-1} to vary simultaneously. Temperature evolution of the refined A_{relaxing} and T_1^{-1} (blue circles) are shown in Figure 4.16 (b) and (c) respectively. Refined A_{relaxing}s are now significantly less scattered and exhibit almost temperature-independent behaviour at temperatures below 25 K. However, temperature dependence of the relaxation rate $(T_1T)^{-1}$ above the superconducting T_c in the normal state, where Korringa behaviour is expected, is still scattered; fixing A_{relaxing} reduced this scattering. $<A_{\text{relaxing}}>$ in the temperature ranges of $5\,\text{K} \le T \le 15\,\text{K}$, $5\,\text{K} \le T \le 20\,\text{K}$ and $5\,\text{K} \le T \le 40\,\text{K}$ were found as 2.42(3), 2.39(6) and 2.29(11)%, respectively. Finally, $A(t)$ data were fitted with fixed A_{baseline} at 31.39% and A_{relaxing} at 2.39%, and only T_1^{-1} was allowed to refine. Final temperature variation of the $(T_1T)^{-1}$ is shown in Figure 4.16 (c) (pink circles).
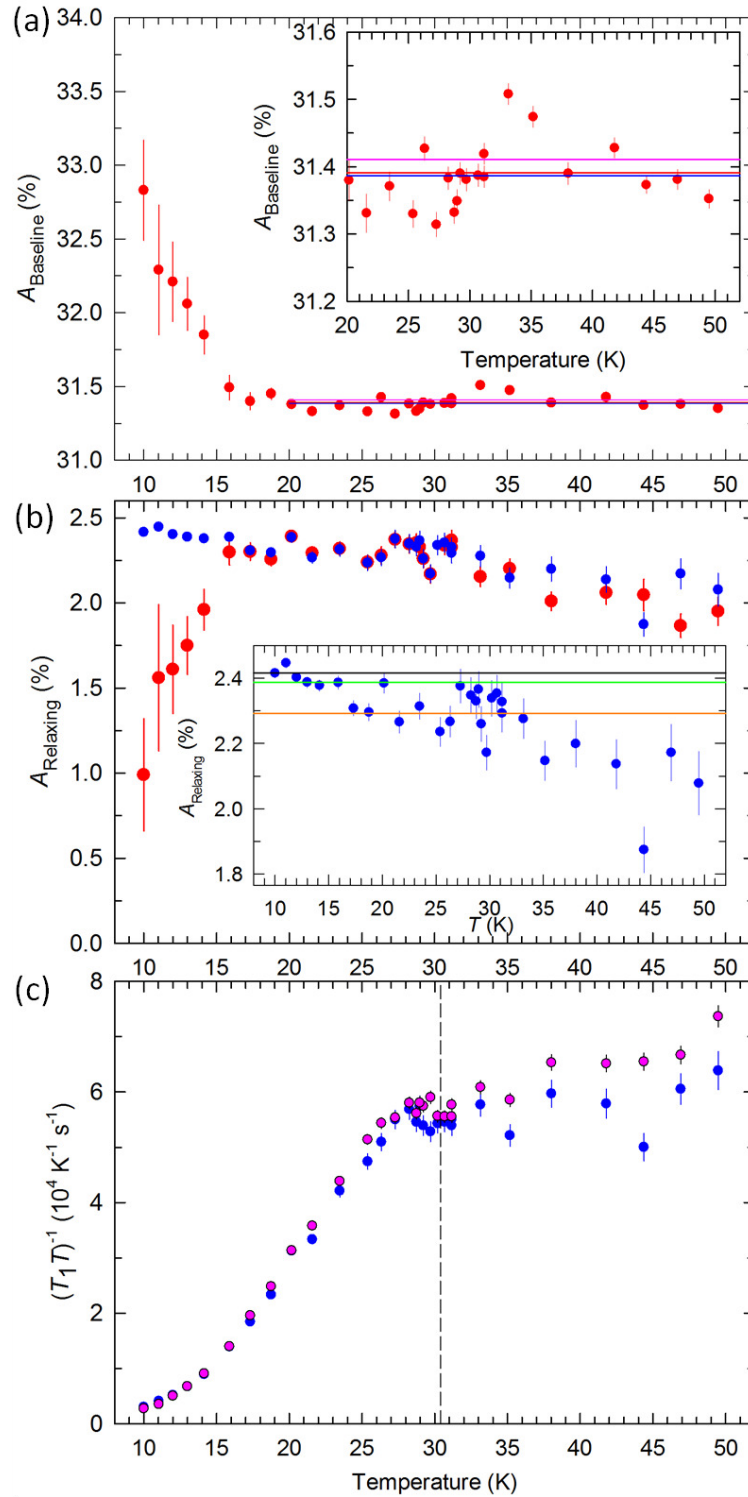
Figure 4.16 (a) Temperature dependence of the $A_{baseline}$; inset displays an expanded region of the respective plot; blue, red and pink solid lines represent <$A_{baseline}$> values of 31.39(5), 31.39(7) and 31.41(4)%, respectively. (b) and (c) display the temperature variation of the $A_{relaxing}$ and spin-relaxation rate of Mu@C_{60} divided by temperature, $(T_1 T)^{-1}$, in $Rb_{0.5}Cs_{2.5}C_{60}$ in a longitudinal applied field of 2.5 T: Data are obtained from the fits using Lorentzian relaxation function in which $A_{baseline}$, $A_{relaxing}$, λ are refined (red circles); $A_{relaxing}$ and λ refined (blue circles), and finally only λ is refined (pink circles). Inset in (b) displays an expanded region of the respective plot; black, green and orange solid lines signify the <$A_{relaxing}$> values of 2.42(3), 2.39(6) and 2.29(11)%, respectively. Dashed line in (c) signifies the superconducting T_c of 30.4 K for $Rb_{0.5}Cs_{2.5}C_{60}$.

The magnitude of the scattering is now considerably reduced, displaying almost temperature-independent behaviour within error in the normal state. The final fits to the LF spectra at selected temperatures with fixed $A_{baseline}$ at 31.39% and $A_{relaxing}$ at 2.39% are shown in Figure 4.17. At low temperatures below 20 K, relaxation is very slow compared to the relaxation at high temperature and the change in the counting rate of the F and B detectors with time is relatively small in magnitude. The major change in the counting rate of the F and B detectors at high temperatures above 20 K is apparent implying a fast relaxation of the muon spin.
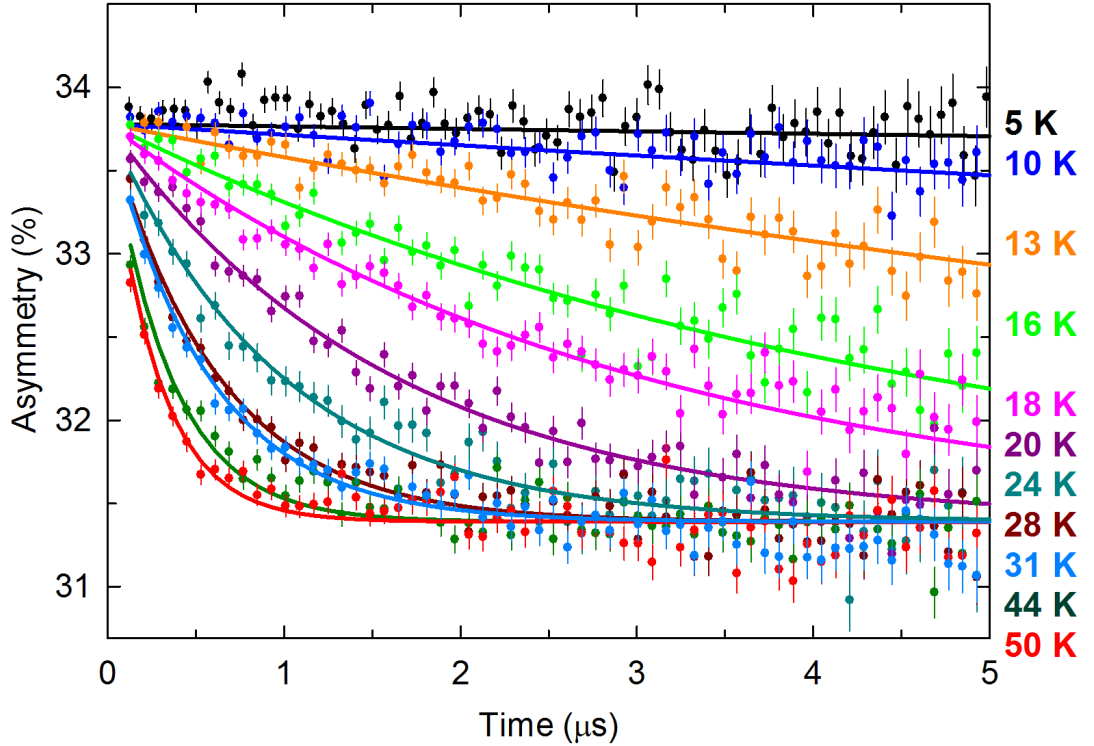
Figure 4.17 The time dependence of the muon decay asymmetry, A(t), measured by LF-μSR in fcc $Rb_{0.5}Cs_{2.5}C_{60}$ at a field of 2.5 T at selected temperatures. A(t) data were fitted using the Lorentzian relaxation function in which $A_{baseline}$ and $A_{relaxing}$ were fixed at 31.39% and 2.39%, respectively; resulting fits are presented with solid lines. For visual quality, LF-μSR spectra were bunched with a factor of 5, and only 0-5 μs region is shown.

Temperature dependence of the spin-relaxation rate of Mu@C_{60} in $Rb_{0.5}Cs_{2.5}C_{60}$ did not display an enhancement on cooling below the superconducting T_c such that seen in the $(T_1T)^{-1}$ vs T plot given for Rb_2CsC_{60} in Figure 4.9. For an accurate comparison of the temperature evolution of $(T_1T)^{-1}$ in $Rb_{0.5}Cs_{2.5}C_{60}$ and Rb_2CsC_{60}, $(T_1T)^{-1}$ for $Rb_{0.5}Cs_{2.5}C_{60}$ was normalised to the rate in the normal state just above the T_c of 30.4 K, as was done for Rb_2CsC_{60}. The normal state relaxation rate, $(T_1T)_N$, was determined as 0.057 MHz K^{-1} which is the

average value of $(T_1T)^{-1}$, $<(T_1T)^{-1}>$, over temperature ranges of 29.2 K $\leq T \leq$ 31.2 K and 30.2 K $\leq T \leq$ 35.2 K where $<(T_1T)^{-1}>$ were found as 0.057(1) MHz K^{-1} and 0.057(2) MHz K^{-1}, respectively.

While a small Hebel-Slichter coherence peak was clearly observed in Rb_2CsC_{60} as an enhancement of $(T_1T)_N/T_1T$ below T_c, we suggest that there might be a suppression of the enhancement in $Rb_{0.5}Cs_{2.5}C_{60}$ (Figure 4.18). In addition, $2\Delta/k_BT_c$ value for $Rb_{0.5}Cs_{2.5}C_{60}$ from the $1/T_1 \propto \exp(-\Delta/k_BT)$ variation for $1.29 < T_c/T < 2.76$ is estimated as 4.53(9) which is larger than that was estimated for Rb_2CsC_{60}; $2\Delta/k_BT_c = 4.31(6)$. Figure 4.19 displays an overplot of the Arrhenius plots for $1/T_1$ of Mu@C_{60} in $Rb_{0.5}Cs_{2.5}C_{60}$ and Rb_2CsC_{60} together with fits to the Arrhenius law function.
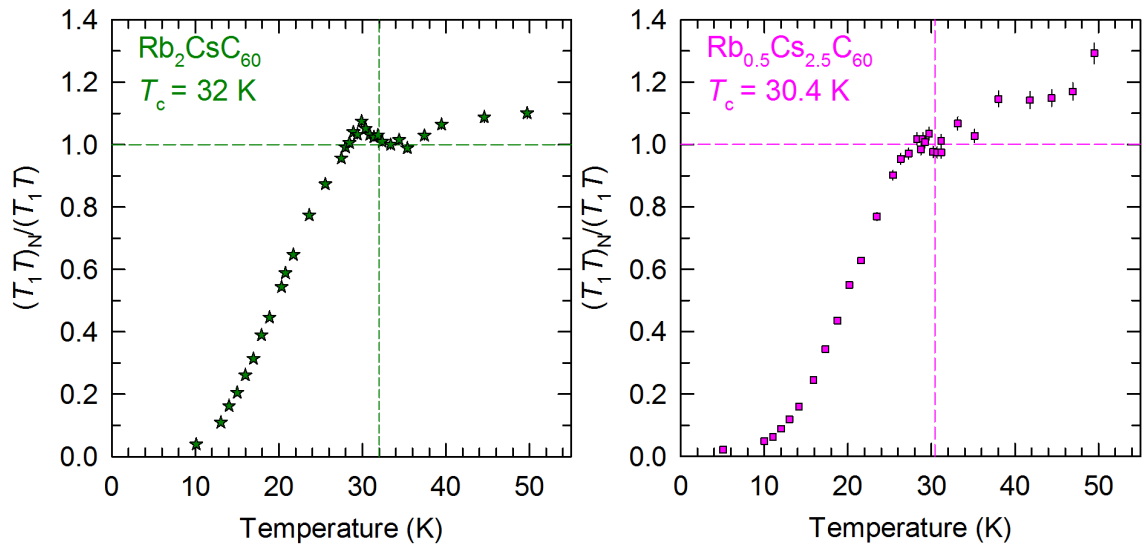
Figure 4.18 Temperature dependence of the spin-relaxation rate of Mu@C_{60} in fcc Rb_2CsC_{60} (left panel) and $Rb_{0.5}Cs_{2.5}C_{60}$ (right panel); $(T_1T)^{-1}$ in Rb_2CsC_{60} and $Rb_{0.5}Cs_{2.5}C_{60}$ are normalised to the rate of 0.037 at 33.4 K and to the average normal state rate of 0.057 MHz K^{-1}, respectively.
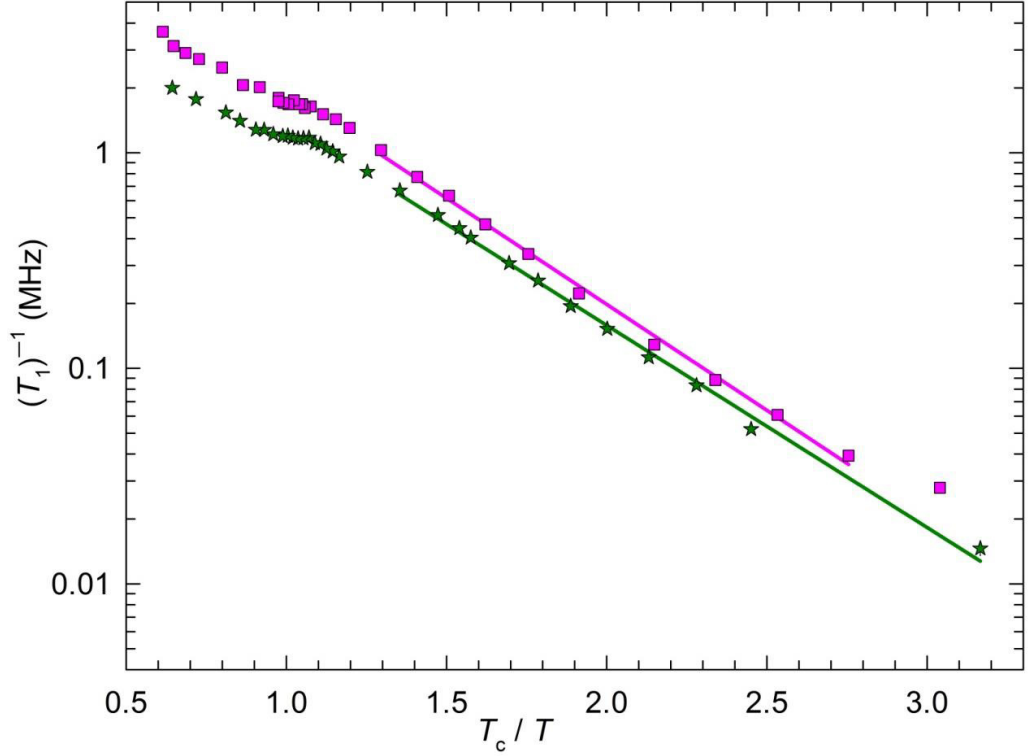
Figure 4.19 Arrhenius plots for the spin-relaxation rate of Mu@C$_{60}$ in fcc Rb$_{0.5}$Cs$_{2.5}$C$_{60}$ and Rb$_2$CsC$_{60}$ in a longitudinal applied field of 2.5 T. Solid lines through the data points of Rb$_2$CsC$_{60}$ and Rb$_{0.5}$Cs$_{2.5}$C$_{60}$ are fits to the equation, $1/T_1 \propto \exp(-\Delta/k_BT)$ variation for $1.35 < T_c/T < 3.17$ and $1.29 < T_c/T < 2.76$, respectively.

4.5 Discussion

The Hebel-Slichter (HS) coherence peak in the family of A$_3$C$_{60}$ fullerides has been previously observed in underexpanded K$_3$C$_{60}$, Rb$_3$C$_{60}$, Na$_2$CsC$_{60}$ [73], [74] and Rb$_2$CsC$_{60}$ [210] fullerides which are far from the MIT boundary and the effect of the JT active electrons in those is absent [67]. For many years, the existence of the HS peak and the isotropic Δ (s-wave) in K$_3$C$_{60}$ and Rb$_3$C$_{60}$, with $2\Delta/k_BT_c$ value in agreement with the prediction of the weak-coupling BCS limit, have been regarded as a result of electron-phonon driven BCS-type superconductivity in the weak-coupling limit in the family of fcc A$_3$C$_{60}$ fullerides. However, the relevance of strong electron-electron interactions in the overexpanded A$_3$C$_{60}$ fullerides results in the failure of the applicability of the BCS formalism (see section 1.2.4 for details).

At the time when the strength of the magnetic field was not known to be an important parameter for the HS peak, Tycko *et al.* used a magnetic field of 9 T for measurements of ^{13}C spin-lattice relaxation rate $(1/^{13}T_1)$ in K$_3$C$_{60}$ and Rb$_3$C$_{60}$ fullerides. Their $1/^{13}T_1$ *vs* T data displayed a monotonic drop-off in $1/^{13}T_1T$ as

temperature is lowered below T_c [214]. This is an unusual behaviour for conventional BCS-type superconductors as the absence of the HS peak could imply remarkable strong coupling effects, quantified by electron-phonon constant λ: sufficiently strong coupling could smear out the HS peak entirely. Several reported mechanisms could explain the reduced peak magnitude, such as temperature dependent pair-breaking [215] through *e.g.* inelastic-scattering from phonons [216], [217], gap anisotropy [218], quasi-particle lifetime broadening [219], or the effects of Coulomb interaction between conduction electrons [220]. Strong-coupling calculations of Akis *et al.* based on numerical solutions of the Eliashberg equations as a function of superconducting coupling strength, λ, indicated that as the coupling strength is increased, the HS peak is speedily suppressed and is finally completely smeared out; therefore, observation of an enhancement in $1/T_1$ may not always imply conventional BCS-type superconductivity, and its absence is not limited to the high-T_c oxide superconductors [217].

Soon after the report of Tycko *et al.* [214], Kiefl *et al.* performed µSR experiments on Rb_3C_{60} at a magnetic field of 1.5 T and they clearly observed the coherence peak (Figure 4.20, left panel) [73]. Shortly afterwards, Stenger *et al.* reported magnetic field suppression of the HS peak in Rb_2CsC_{60}; while the HS peak was clearly observable as an enhancement of $1/^{13}T_1$ on cooling below T_c for fields of 3 and 1.5 T, it was almost completely suppressed at fields greater than approximately 7 T [210].

In the present study, given the available data analysis, we suggest that the HS coherence peak may be suppressed in $Rb_{0.5}Cs_{0.5}C_{60}$ at a magnetic field of 2.5 T (Figure 4.20, right panel). Nonetheless, this has to be confirmed by modelling the temperature dependence of $1/T_1T$ using the Hebel-Slichter theory formulation. In accordance with the field dependent ^{13}C NMR measurements of Rb_2CsC_{60} [210], it is quite unlikely that this is a field-dependent suppression as the suppression of the HS peak in Rb_2CsC_{60} takes place at fields ~5 T which is significantly greater than our experimental magnetic field of 2.5 T. Furthermore, a small enhancement in $1/T_1T$ on cooling below the superconducting T_c of Rb_2CsC_{60} could be taken as evidence that the field of 2.5 T is relatively small in magnitude to eliminate the usual BCS $1/T_1T$ enhancement below T_c.
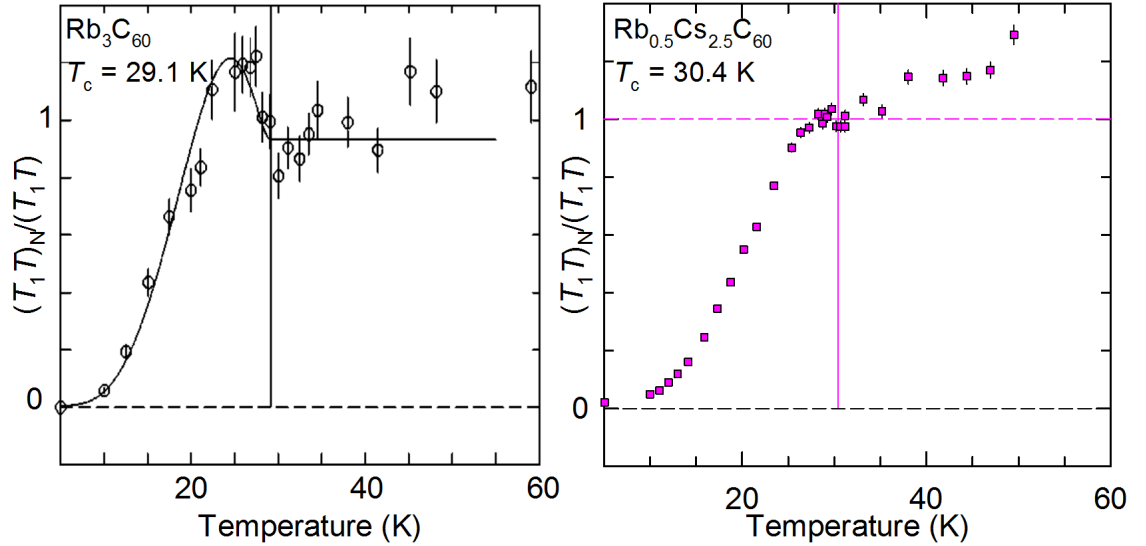
Figure 4.20 Temperature dependence of the spin-relaxation rate of Mu@C_{60} in fcc Rb_3C_{60} [73] and $Rb_{0.5}Cs_{2.5}C_{60}$, in magnetic fields of 1.5 and 2.5 T, respectively. $1/T_1$ are normalised to the rates in the normal state just above T_c. Black solid line through data points is the fit to the Hebel-Slichter function. Solid vertical lines mark the superconducting T_c.

Kiefl *et al.* reported $2\Delta/k_BT_c = 3.6(3)$ in Rb_3C_{60}, in agreement with the prediction of the weak-coupling BCS limit, from the measurements of the muon spin-relaxation rate at a field of 1.5 T. They fitted the temperature dependence of $1/T_1T$ to the Hebel-Slichter function with a broadened BCS density of states [73]. MacFarlane *et al.* have also found that $2\Delta/k_BT_c$ in K_3C_{60} and Rb_3C_{60} lie between 3.2 and 4, using the same method *via* fitting $1/T_1T$ *vs* T data to the Hebel-Slichter function [74]. Temperature dependence of the relaxation rates in conventional underexpanded Rb_3C_{60} and K_3C_{60} fullerides clearly showed Korringa behaviour in the normal state above the superconducting T_c and a small strongly field-dependent HS coherence peak just below the superconducting T_c [73], [221]. Optical reflectivity measurements on phase-pure K_3C_{60} and Rb_3C_{60} led to 3.6 and 2.98 for $2\Delta/k_BT_c$ [222], respectively, which are consistent with the BCS weak-coupling limit; however, the HS coherence peak in $1/T_1$ which is a characteristic feature of the conventional superconductors [209], was not observed. In contrast, early measurements of Δ in Rb_3C_{60} by tunnelling spectroscopy using a scanning tunnelling microscope gave significantly large gap corresponding to $2\Delta/k_BT_c = 5.2$ which had been taken as evidence for strong coupling in Rb_3C_{60} [71].

In sharp contrast to the non-monotonic scaling of superconducting T_c with pressure in MJTI Cs_3C_{60}, a comprehensive NMR study of fcc Cs_3C_{60} has revealed that, upon pressurization, $2\Delta/k_BT_c$ decreases monotonically from 5.3(2) (at 1.7

166

kbar) to BCS weak-coupling value of 3.52 at 7.8 kbar [70]. However, application of hydrostatic pressure in fcc Cs_3C_{60} leads to a 'dome'-shaped dependence of T_c: T_c initially increases ($T_c = 25.6$ K at ~ 1.3 kbar), reaches a maximum of 35 K at ~ 7 kbar, and then starts decreasing at higher pressures [28]. In ref. [70], $2\Delta/k_BT_c$ was estimated from the $1/^{13}T_1 \propto \exp(-\Delta/k_BT)$ variation for $1.25 < T_c/T$ ($1/^{13}T_1$ being the ^{13}C spin-lattice relaxation rate) [70]. However, no enhancement of $1/^{13}T_1$ just below T_c that would mark the presence of the Hebel-Slichter coherence peak was observed within the overall experimental pressure range [70]. NMR results on the A15 Cs_3C_{60} polymorph also showed a comparable volume dependence of the superconducting gap: $2\Delta/k_BT_c$ increases regularly with lattice expansion upon approaching the Mott transition, implying a lattice-independent superconductivity mechanism in both A15 and fcc Cs_3C_{60} polymorphs [75].

Zadik *et al.* performed ^{13}C, ^{133}Cs, and ^{87}Rb NMR experiments for measurements of spin-lattice relaxation rate, $1/T_1$, in fcc $Rb_xCs_{3-x}C_{60}$ ($0.35 \leq x \leq 3$) materials [67], and reported $2\Delta/k_BT_c = 3.6(1)$ in underexpanded conventional metal Rb_3C_{60}. In agreement with earlier work [70], they found that $2\Delta/k_BT_c$ increases upon lattice expansion to 4.31(9) for Rb_2CsC_{60}, to 4.9(1) for optimally expanded $RbCs_2C_{60}$ and then further to 5.6(2) for overexpanded $Rb_{0.35}Cs_{2.65}C_{60}$.

In the present study, in agreement with previous work [67] and [70], we found that the superconducting gap does not correlate with T_c in the overexpanded regime: the gap increases monotonically with interfullerene separation as the Mott boundary is approached, in contrast to the 'dome'-shaped scaling of T_c with V. $2\Delta/k_BT_c$ obtained from the $1/T_1$ muon spin-relaxation rate increases with increasing V, reaching 4.53(9) for overexpanded superconductor $Rb_{0.5}Cs_{2.5}C_{60}$ emerging from JTM upon cooling (see Figure 1.5 for details) [67]. Figure 4.21 illustrates the evolution of $2\Delta/k_BT_c$ and T_c as a function of V at low temperature for fcc A_3C_{60} fullerides.
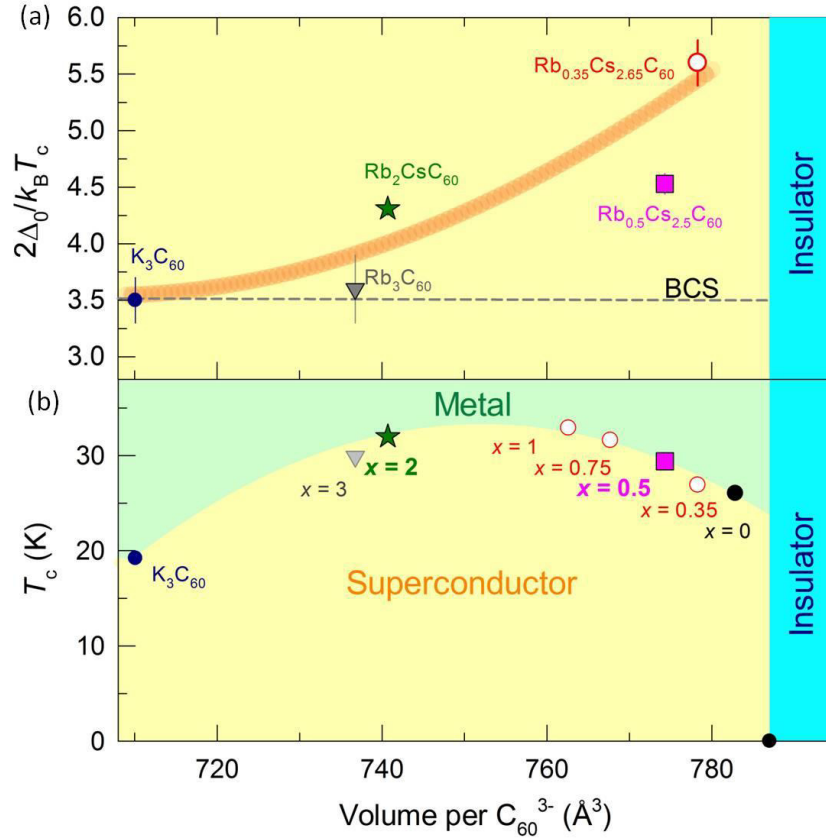
Figure 4.21 (a): The volume per C_{60}^{3-}, V, dependence of the superconducting gap divided by T_c, $2\Delta/k_B T_c$, at low temperature, obtained from the $1/T_1$ spin-relaxation rate of Mu@C_{60}; represented with solid symbols (data for K_3C_{60} and Rb_3C_{60} are from ref. [74] and [73]), and from the ^{87}Rb spin-lattice relaxation rate data, $1/^{87}T_1$ represented with open circle; from ref. [67]), in the superconducting state. The solid line is a guide to the eye and the dashed line marks the gap value $2\Delta/k_B T_c = 3.52$. (b): Evolution of T_c as a function of V at low temperature for fcc $Rb_xCs_{3-x}C_{60}$ ($0 \leq x \leq 3$) fullerides; black circles from ref. [28] and the other data points are from ref. [67].

In overexpanded fcc $Rb_{0.5}Cs_{2.5}C_{60}$, both suppression of the HS peak and the gap magnitude higher than the BCS weak-coupling value of 3.52 could be taken as evidence for a remarkable increase in the coupling strength as the system approaches the metal/superconductor–Mott insulator boundary. The weak-coupling limit of BCS theory requires the involvement of high-frequency intramolecular phonons ($\omega_{ph} = \sim 1000$-1600 cm^{-1}) in the superconducting pairing mechanism [25], [41], [59]. On the other hand, in principle, the superconducting gap values far higher than predicted for the BCS weak-coupling limit could be obtained for strong electron-phonon coupling but this requires the involvement of the low-frequency intermolecular phonons ($\omega_{ph} = \sim 100$ cm^{-1}) [68] in the pairing interaction [69]. This in turn necessities the occurrence of a switch-over from the involvement of the high to that of the low-frequency intermolecular phonons and

that the high- and low- frequency phonons would be active in different parts of the A_3C_{60} electronic phase diagram. However, this seems not applicable due to the regular presence of the high-frequency phonon modes and there being no obvious changes in the crystal and electronic structures [70]. As a result, conventional BCS-like explanation for the pairing mechanism in the overexpanded A_3C_{60} superconducting materials cannot be valid.

Zadik *et al.* reported that unconventional superconductivity in overexpanded $Rb_xCs_{3-x}C_{60}$ ($0.35 \leq x \leq 1$) compositions emerges from the JT metallic state on cooling where dynamically JT distorted $C_{60}{}^{3-}$ ions coexist with itinerant electrons [67] (see Section 1.2.4 and Figure 1.5 for details). However, the localised features gradually fade away with decreasing interfullerene separation; the molecular JT distortion is no longer apparent and a conventional metal, from which conventional superconductivity emerges upon cooling, is encountered in Rb_2CsC_{60} [67]. Hypothetically assuming, local heterogeneities in JTMs could broaden the singularity in the BCS density of states and thus reduce the amplitude of the HS peak, although the s-wave nature of the superconducting gap is retained right across the entire V range in the family of fcc A_3C_{60} superconductors.

Dynamical mean-field theory (DMFT) solutions of Capone *et al.* confirmed that superconductivity in a Hubbard model of fullerides, in which all important electron correlations occur within the molecular site, shares many of the properties that are attributed to high-T_c cuprates (*i.e.* emergence of superconductivity from the antiferromagnetic Mott insulating phase, 'dome'-like scaling of T_c), besides s-wave symmetry rather than d-wave in fcc A_3C_{60} fullerides [81]. In fact, both high-T_c s-wave superconductivity and a regular increase in $2\Delta/k_BT_c$ with increasing V upon approaching the MI boundary in the family of A_3C_{60} fullerides differ from the strongly correlated high-T_c cuprates where pairing of electrons takes place in a *d*-wave symmetry with superconducting gap values in the strong coupling regime [81], [223]. In high-T_c cuprates and also in pnictides in the underdoped regime, which is closer to the antiferromagnetic phase (AFM), the superconducting gap and T_c correlate. Initially, the gap size increases with increasing doping level and reaches a maximum, varying in a similar manner to T_c. Beyond this point, for greater doping levels, the gap size and T_c remain invariant

[224], [225]. However, NMR results on the A15 [75] and fcc Cs_3C_{60} polymorphs [70], and the results in the present study indicate that, in the overexpanded regime, the superconducting gap does not correlate with T_c. This contrasting variation of Δ and T_c from the underdoped cuprates and pnictides which are in proximity to the AFM state can provide important clues for the understanding of the interplay between antiferromagnetic fluctuations and superconductivity in those.

Although, in the present work, a suppression of the HS coherence peak and large coupling strength have been revealed in $Rb_{0.5}Cs_{2.5}C_{60}$, more realistic models rather than using a simple Arrhenius law must be employed for a precise estimation of Δ - such models are discussed in refs. [73] and [221] in detail. For instance, the temperature dependence of $1/T_1T$ can be modelled using the Hebel-Slichter theory formulation with a broadened BCS density of states. Our results are expected to stimulate the development of improved theoretical descriptions of the A_3C_{60} system, and further advancing our understanding of the origins and mechanism of superconductivity in other strongly-correlated high-T_c superconductors.

4.6 Conclusion

In conclusion, we have observed the spin-relaxation of $Mu@C_{60}$ in underexpanded Rb_2CsC_{60} and overexpanded $Rb_{0.5}Cs_{2.5}C_{60}$ compounds in which the temperature dependence of the relaxation rates exhibits Korringa behaviour above T_c and strong activated behaviour in the superconducting state. A small HS coherence peak was observed as an enhancement of the temperature dependence of $1/T_1T$ on cooling just below T_c in Rb_2CsC_{60} in which superconductivity emerges from a conventional metallic state (JT effect is absent [67]) upon cooling. On the other hand, for $Rb_{0.5}Cs_{2.5}C_{60}$, the available data suggested that the coherence peak might be suppressed, implying strong coupling effects in the overexpanded A_3C_{60} fullerides in which the molecular JT distortions continue to survive yielding unconventional metallic behaviour (*i.e.* JTM) in proximity to the MIT boundary [67]. The temperature dependence of the $1/T_1T$ in both compounds followed an activated behaviour with an s-wave superconducting gap, Δ, as described by the Arrhenius law. The superconducting gap was estimated from the low-temperature

behaviour of the $1/T_1$: underexpanded Rb_2CsC_{60} and overexpanded $Rb_{0.5}Cs_{2.5}C_{60}$ displayed significantly large ratios of superconducting gaps to T_c, $2\Delta/k_BT_c$, as 4.31(6)and 4.78(7), respectively, increasing with interfullerene separation [67], [70], [75] in contrast to the 'dome'-shaped dependence of T_c [67]. Although the s-wave symmetry is preserved, the coupling strength increases to anomalously large values, with $2\Delta/k_BT_c$ ratio approaching 5, for overexpanded superconductor emerging from JTMs upon cooling. This behaviour set the A_3C_{60} fullerides out as a remarkable class of strongly-correlated superconductors in which the boundary with the JTM directly affects superconductivity [67]. While the s-wave superconductors emerging from the underexpanded conventional metals display the HS coherence peak and $2\Delta/k_BT_c$ values characteristic of weak-coupling BCS superconductors, the ones forming from a strongly-correlated antiferromagnetic Mott-Jahn-Teller insulator Cs_3C_{60} display $2\Delta/k_BT_c$ ratio characteristic of unconventional non-BSC type high-T_c superconductors. These results indicate that the absence of the HS peak is not limited to high-T_c d-wave unconventional superconductors and a material can exhibit s-wave superconducting phase with high-T_c, which profits from strong correlations.

Chapter 5 Valence order - disorder transitions in alkali sesquioxide Cs$_4$O$_6$

5.1 Introduction

The previously reported studies on the structural and magnetic properties of the alkali sesquioxides, A$_4$O$_6$ (A = Rb, Cs) and their conflicting properties were summarised in section 1.3.1. One main controversial issue has arisen, due to the differing results of the crystallographic and spectroscopic studies. X-ray diffraction and elastic neutron scattering studies have hitherto revealed that A$_4$O$_6$ is isostructural to cubic Pu$_2$C$_3$ with the space group $I\bar{4}3d$, where all oxygen atoms are located on one and the same Wyckoff position, and no reduction of symmetry or ordering of the differently-sized indistinguishable dioxygen anions takes place down to 5 K [93]–[95]. Controversially, spectroscopy has provided unambiguous evidence for two localized valence states of dioxygen [95], [100]. However, no experimental crystallographic evidence had hitherto been found for the presence of two localized valence states of dioxygen in sesquioxides.

Arčon *et al.* have reported large differences in the temperature evolution of the electron paramagnetic resonance (EPR) and ^{133}Cs NMR spectra of Cs$_4$O$_6$ measured under different cooling protocols, indicating that the electronic properties of Cs$_4$O$_6$ depend on the cooling protocol employed. As a result they proposed that the adopted structure might differ depending on the thermal treatment [106]. However, the temperature evolution of the structure was unknown. As the magnetic and molecular orderings are strongly coupled to one other, the theoretical calculations and experimental studies undertaken so far have led to conflicting results. For instance, electronic structure calculations using the local spin-density approximation have proposed half-metallic ferromagnetism in Rb$_4$O$_6$ [101], while experimental studies have proposed that it is a magnetically-frustrated insulator [102]. Such a frustrated state was also supported by the magnetisation measurements of Cs$_4$O$_6$ [100].

The present study aimed to investigate the structural properties of Cs$_4$O$_6$ and resolve the conflicting electronic properties reported in the literature. For a

detailed structural investigation, first, the temperature response of Cs_4O_6 was studied with high-resolution neutron powder diffraction at ambient pressure. With the knowledge that the electronic properties are depended on the cooling protocol applied, different cooling procedures were followed for the study of the temperature response of the structure of Cs_4O_6. Once access to the adopted structures at low temperatures was achieved, high-resolution synchrotron X-ray diffraction investigations were undertaken, at variable temperatures and upon applying hydrostatic pressure.

All the different batches of Cs_4O_6 used in this study were synthesised by A. Sans according to a previously reported protocol [100] by a solid-state reaction of CsO_2 and Cs_2O in a molar ratio of 4:1, in a glass tube sealed under argon, annealing at 473 K for 24 hrs. Annealing was repeated with intermediate grindings. As sesquioxides are extremely air- and moisture-sensitive, all reactions were carried out under an inert atmosphere. Samples of Cs_4O_6 used in this study were found to contain a small fraction of superoxide, CsO_2, impurity phase, clearly evident in the diffraction profiles shown in the following sections.

5.2 Temperature-induced valence order-disorder transitions

In the following sections, structural characterisation with neutron time-of-flight (tof) powder diffraction, employing Rietveld analysis, is described for the sesquioxide Cs_4O_6, under both ambient conditions and at variable temperatures. Firstly, a summary of experimental procedures is provided.

5.2.1 Experimental procedures

Neutron tof powder diffraction experiments were carried out using the GEM tof diffractometer at ISIS, UK. The overall setup of the GEM diffractometer was outlined in Section 2.5.3. Due to the extreme air- and moisture-sensitivity of Cs_4O_6, all sample manipulations were carried out within the inert atmosphere of an argon glove-box (H_2O and O_2 < 0.1 ppm). A 1 g sample of Cs_4O_6 was held within a tightly sealed (indium-seal) 6 mm-diameter vanadium sample can. The height of the sample in the can was ~20 mm. A vanadium can is used as the sample holder as V has a very low coherent scattering length, $b = -0.38$ fm, leading to no significant Bragg reflections from the thin walls of the container, resulting in a flat

background. The same sample in the same vanadium can was used for all neutron tof powder diffraction data collections presented in this section. Temperature control was achieved using a helium continuous flow cryostat in the temperature range of 1.5 – 320 K. Due to the strong thermal hysteretic effects in the structural properties, the cooling and measurement protocols were closely monitored.

The main strategy of the data collection was to measure discrete tof diffraction patterns continuously whilst warming or cooling. The continuous collections were saved in 5-minute intervals, which corresponded to a temperature change, $\Delta T \approx 1$ K and to ≈ 12.5 µAmp of proton current. These discrete patterns were then summed in appropriate blocks. For instance, 10-minute blocks correspond to $\Delta T \approx 2$ K and give high enough statistics to confidently refine structural parameters, whilst achieving good resolution. All collected tof diffraction datasets presented in this chapter were summed in 10-minute blocks ($\Delta T \approx 2$ K). In addition to the continuous data collection, sets of high-statistics data at selected temperatures, such as 1.8, 10 and 320 K were obtained in order to search for the presence of magnetic scattering, as well as to allow higher-quality structural determination through Rietveld analysis.

Processing of the tof powder diffraction raw data and the absorption corrections were undertaken using the software MANTID [166]. Once the datasets were processed and summed into the desired blocks, Rietveld analysis was undertaken on the processed neutron tof diffraction datasets using the GSAS software suite.

5.2.2 Cs_4O_6 at 320 K

A high-statistics neutron tof diffraction pattern (≈ 351.2 µAmp) was collected at 320 K for a detailed structural characterisation of the high-temperature phase of Cs_4O_6. Rietveld analysis of the data was undertaken, employing the previously-reported Pu_2C_3 structure [93] with a cubic space group, $I\bar{4}3d$ (no: 220) where all oxygen atoms are located on the same Wyckoff position *24d* [95] to model the majority phase.

A description of the refinement method now follows. An alternative form of the Ikeda-Carpenter profile function was used (tof profile function '2' in GSAS) to

model the peak shape. Only the profile shape coefficients sig−1, sig−2, gam−1 and gam−2 of the function '2' were allowed to refine, but only if the refinement could converge. This function with the same refined profile shape coefficients has been employed for all neutron tof diffraction datasets analysed in this chapter. A Chebyschev polynomial function was used to model the background (background function '1' in GSAS), with different number of terms ranging from 12 to 24 for different banks of detectors. While banks 2, 3, 4, 5 and 6, at solid angles of 17.98°, 34.96°, 63.62°, 91.3° and 154.3°, respectively, were included in the analysis, bank-1 was excluded as it did not have a sufficient number of Bragg peaks. The same banks of detectors were included for all Rietveld analysis of the datasets collected at variable temperatures.

Whilst the diffractometer constant DIFC and ZERO were fixed as given in the instrument parameter file, DIFA for all banks, except backscattering bank-6, was refined periodically, but only if the refinement could converge. It was assumed that the diffractometer constants of bank-6 are best determined by the GEM calibration and do not need to be refined, but are fixed as given in the instrument parameter file. This method employed for the diffractometer constants was used for all Rietveld analysis of the neutron tof datasets collected at variable temperatures.

For high-statistics datasets, the caesium and oxygen thermal displacement parameters were modelled as isotropic and anisotropic, respectively, and refined freely; however, for low-statistics (≈12.5 μAmp) datasets, thermal displacements were modelled as only isotropic and refined freely. Fractional atomic coordinates in major crystallographic phases included in the model were always allowed to refine freely without introducing any restraints. The lattice parameters of all crystallographic phases included in the model were always refined as well.

Refined structural parameters of cubic Cs_4O_6 are given in Table 5.1. The lattice constant and unit cell volume are: $a = 9.8678(7)$ Å and $V = 960.9(2)$ Å^3, respectively, in agreement with the previously-reported lattice parameter at 300 K: $a = 9.84583(11)$ Å [100]. The occupancies of the Cs and O(1) were kept fixed at 1. Even if the occupancies were allowed to refine freely, they converged to 1.023(5) and 0.991(4) for Cs and O(1), respectively. To ensure the consistency of the refinement procedure at different temperatures, the occupancies were not

refined and were fixed at 1 for all refinement models that were employed for the analysis of all datasets. Refinement of the oxygen coordinates gave an O–O bond length of 1.271(3) Å, considerably lower than those in Rb_4O_6 (1.317(9) Å at 300 K [94] and 1.363(1) Å at 5 K [95]), superoxide O_2^- (1.34(3) Å) [226] and peroxide O_2^{2-} (1.541(6) Å) [227] units. However, it is longer than that in caesium superoxide, CsO_2 (1.187 Å [228] and 1.189 Å [97]).

Figure 5.1 shows the adopted cubic structure of Cs_4O_6 at 320 K, in which the thermal displacements of the atoms are also illustrated. The largest amplitudes (U_{22}) of the anisotropic thermal displacement factors of adjacent oxygen atoms are in a direction perpendicular to the O–O bonds and orient orthogonally to each other. Such an anomaly in the orientations of the thermal displacements of the oxygen atoms has been previously revealed in Rb_4O_6 by single crystal X-ray diffraction data collected at 295 and 213 K [94], and at 100 K [229] and by neutron powder diffraction data collected at 5 K [95]. This unphysical thermal motion might indicate that the assumed structural model corresponds to an average structure and at low temperatures the alignment of the oxygen dumbbells may tilt away from their original symmetry-defined orientations. This tilting might lead to a different crystal structure where oxygen species are disordered over different crystallographic sites.

Table 5.1 Refined structural parameters of cubic Cs_4O_6 ($I\bar{4}3d$) at 320 K from Rietveld analysis of the neutron tof diffraction data. Estimated errors in the last digits are given in parentheses. The total weighted-profile and expected R-factors are R_{wp} = 2.17% and R_{exp} = 2.69%, respectively. The fractions of the co-existing Cs_4O_6 and CsO_2 phases are 95.09(2)% and 4.9(3)%, respectively.

Atom	Wyckoff site	x/a	y/b	z/c
Cs	*16c*	0.94626(11)	0.94626(11)	0.94626(11)
O(1)	*24d*	0.56061(16)	0	0.75

Debye-Waller (thermal) displacement factors (Å²)						
	U_{iso}	U_{11}	U_{22}	U_{33}	U_{12}	U_{13}	U_{23}
Cs	0.0531(8)	-	-	-	-	-	-
O(1)	-	0.0629(17)	0.1255(18)	0.0457(14)	0	0	0.0092(11)
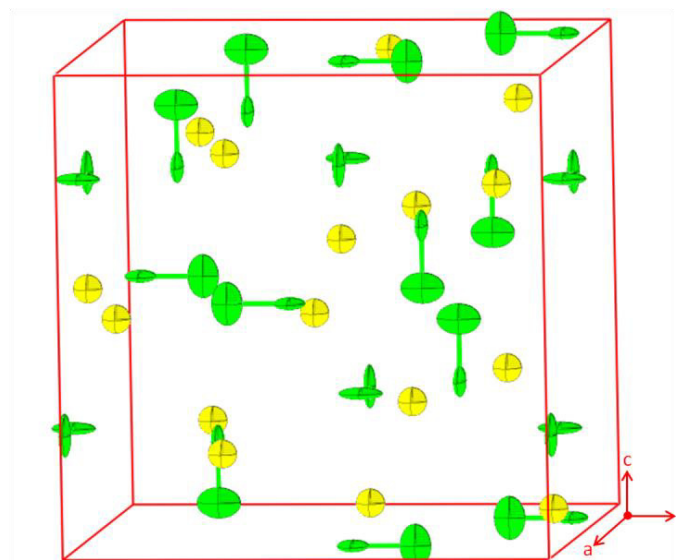
Figure 5.1 Cubic $I\bar{4}3d$ Cs_4O_6 structure at 320 K. Cs^+ and $O^{(4/3)-}$ ions are depicted in yellow and green, respectively. The oxygen dumbbells are oriented parallel to the crystallographic axes. Thermal displacement ellipsoids of the caesium and oxygen atoms are drawn at the 90% probability level.

The single crystallographic position of oxygen reflects the presence of symmetry-equivalent valency-delocalised $(O–O)^{(4/3)-}$ dumbbells (Figure 5.1), implying charge disorder with a general formula $Cs_4(O_2^{(4/3)-})_3$. The final Rietveld fits to the 320 K Cs_4O_6 neutron tof diffraction data collected at different banks of detectors are shown in Figure 5.2. The observed data were satisfactorily modelled by including caesium superoxide, CsO_2 as a second crystallographic phase. Although CsO_2 has been reported to adopt a tetragonal structure (space group $I4/mmm$) at room temperature [12], we found that its contribution at 320 K (Figure 5.3) is best modelled by its high-temperature cubic phase (fraction: 4.9(3) wt.%; space group $Fm\bar{3}m$). In the literature, CsO_2 was reported to be cubic at 473 K [11]. The fractional atomic coordinates and thermal displacement parameters of CsO_2 were kept fixed to literature values [228] but its lattice parameters were allowed to refine; this applies to all other Rietveld analysis in which the CsO_2 impurity phase was included in the model. The contribution of CsO_2 can be clearly seen in Figure 5.3, where only the Rietveld refinement of the diffraction pattern collected at bank-4 is shown over a restricted Q range.
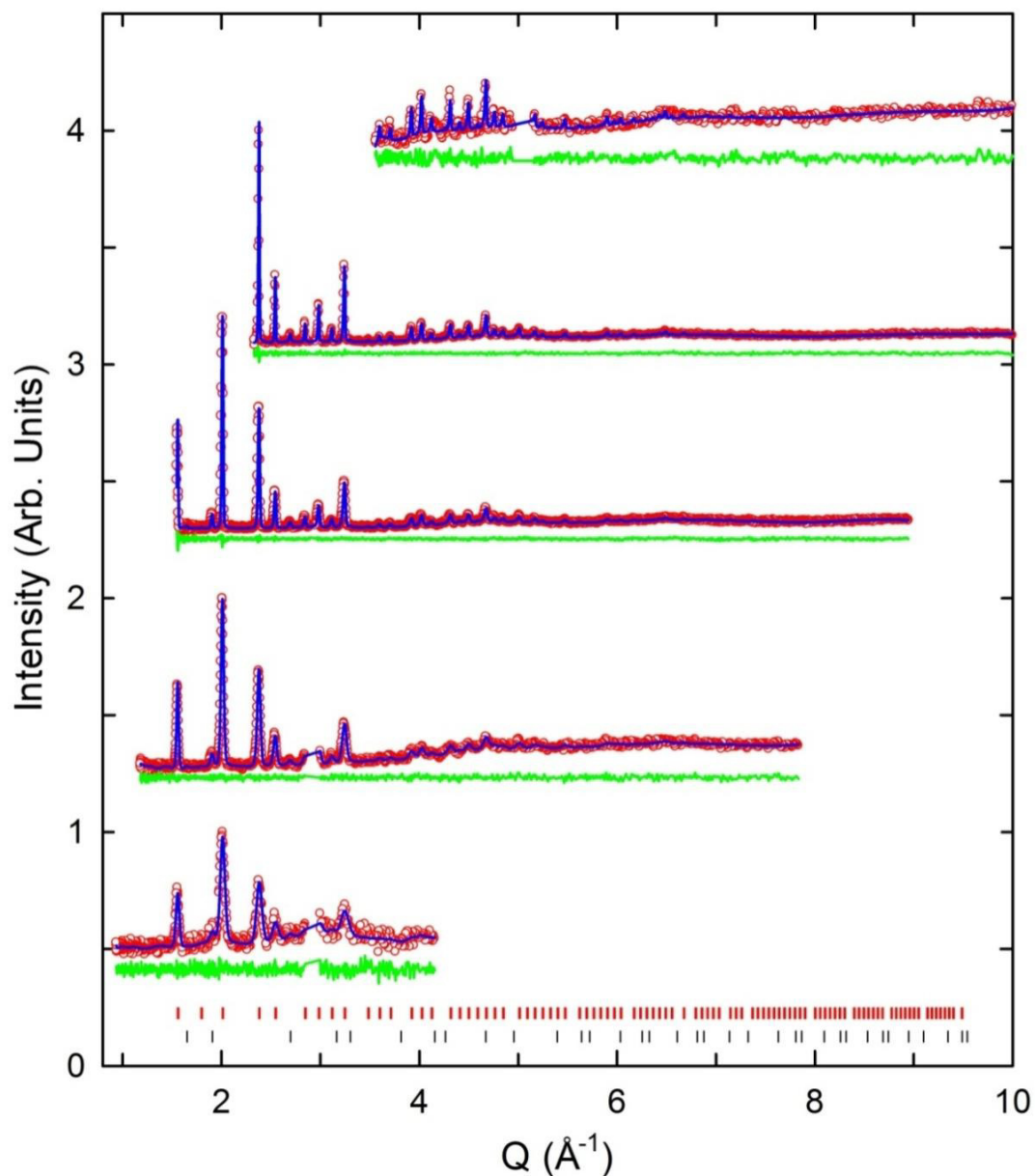
Figure 5.2 Final observed (red circles) and calculated (blue solid lines) tof neutron diffraction patterns at 320 K. Green lines represent the difference profiles. Data from bottom-to-top represent the following GEM detector banks (listed with their solid angles): bank-2 at 17.98°, bank-3 at 34.96°, bank-4 at 63.62°, bank-5 at 91.3° and bank-6 at 154.4°, respectively. The red and black tick marks show the reflection positions of the cubic Cs_4O_6 and 4.9(3)% impurity CsO_2 phase. Vanadium peaks from the sample holder at 2.9 Å^{-1} in all banks and a spurious contribution from the cryostat at 5.1 Å^{-1} in the 154.3° bank were excluded from the fitting. The total weighted-profile and expected R-factors are R_{wp} = 2.17% and R_{exp} = 2.69%, respectively.
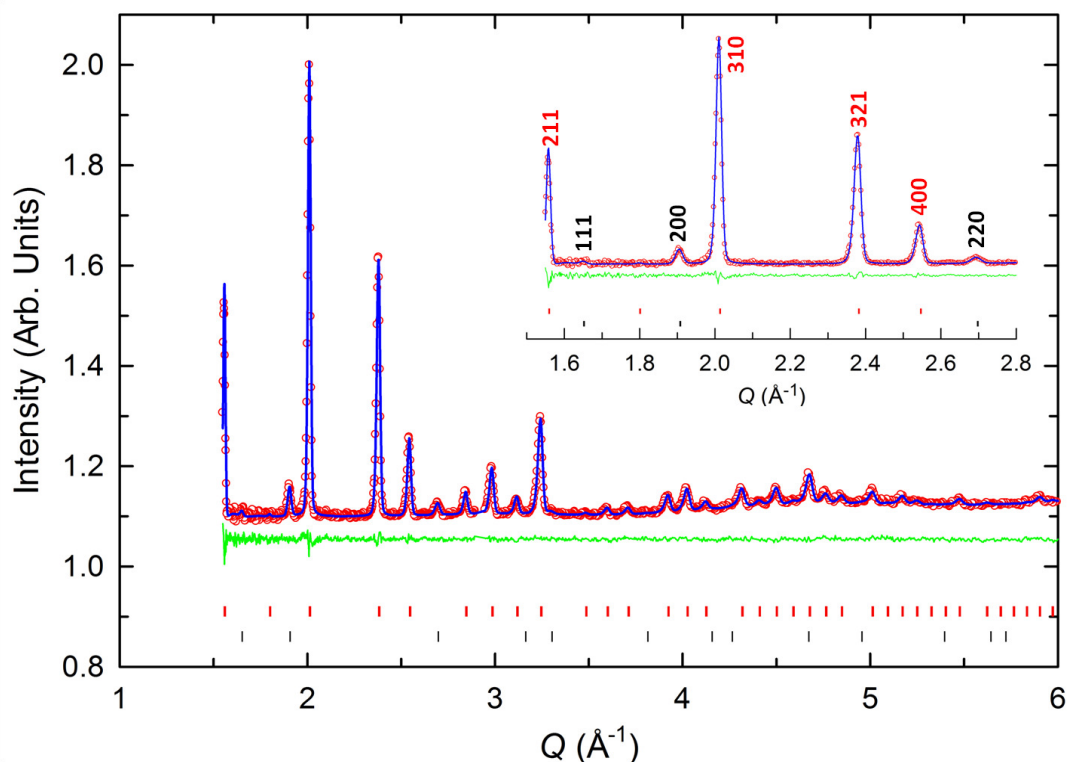
Figure 5.3 Final observed (red circles) and calculated (blue solid line) neutron tof diffraction patterns collected at bank-4 at 320 K. Red and black tick marks show the reflection positions of Cs_4O_6 and impurity CsO_2, respectively. The fractions of the co-existing Cs_4O_6 and CsO_2 phases are 95.09(2)% and 4.9(3)%, respectively. The inset displays an expanded region in Q and clearly shows the reflections of the CsO_2 phase; observed Bragg peaks are labelled by their (*hkl*) Miller indices with the same colours as the tickmarks. The weighted-profile and expected R-factors for bank-4 are R_{wp} = 2.46% and R_{exp} = 3.04%, respectively.

The refined lattice constant and unit cell volume of CsO_2 at 320 K were found to be a = 6.5870(7) Å and V = 285.80(9) Å³, consistent with previously reported values at 473 K: a = 6.62(1) Å and V = 290.12 Å³ [228]. In addition to the reflections arising from the sample, some contributions from the vanadium can and cryostat were also observed. We were able to identify the origin of the spurious peaks, thanks to data collection on the empty cryostat and the vanadium can. These extra peaks were excluded from the Rietveld analysis. Once the crystal structure of Cs_4O_6 at 320 K was confirmed to be cubic, as reported previously in the literature, we employed two different cooling protocols, rapid cooling and ultra-slow cooling, to investigate the low temperature structure.

5.2.3 Rapid cooling of Cs_4O_6

Rapid cooling of the sample was achieved *via* direct deep-quenching from 320 K into a bath of liquid nitrogen (77 K). To ensure reproducibility, the sample

was first warmed to 320 K in a tube furnace and allowed to equilibrate there for 30 minutes before cooling. After equilibration at 320 K, the sample was quenched into the liquid nitrogen bath and left there for 5 minutes for temperature equilibration. The sample was then transferred into the pre-cooled cryostat at 77 K. A helium-filled bag was used during quenching and transferring to prevent the condensation of moisture onto the sample or stick. The steps of the quenching procedure are illustrated in Figure 5.4.

He in

sample stick

sample in
vanadium can

77 K

1. Tube furnace   2. He bag   3. Deep-quench   4. Cryostat
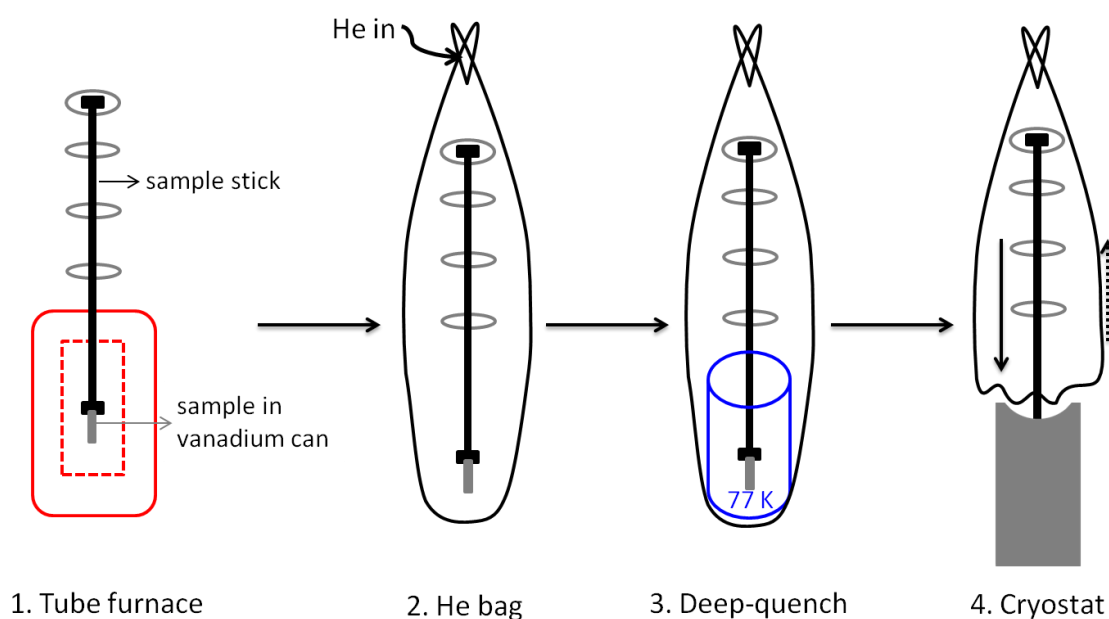
Figure 5.4 Schematic view of the rapid cooling experiment *via* direct deep-quenching.

Once the sample was transferred into the cryostat, cooling was immediately initiated directly to 10 K. After temperature equilibration at 10 K, a high-statistics dataset was collected for 2 hrs ($\approx$300 µAmp). The sample was then cooled down to 1.8 K, where another long 2-hr scan was recorded in order to search for the existence of magnetic scattering as a cusp in the low-temperature magnetic susceptibility was observed below 8 K with separation between zero-field-cooled and field-cooled measurement protocols, possibly implying long-range antiferromagnetic order [100], [102].

Low-temperature structure of Cs_4O_6 after rapid cooling

Rietveld analysis of the high-statistics tof neutron diffraction data collected at 10 and 1.8 K after rapid cooling was undertaken. The analysis revealed that the cubic structure of Cs_4O_6 survived through the rapid deep-quench cooling and the

system remained valency-disordered. The observation of a single symmetry-distinct oxygen species is consistent with two possible scenarios: either valency-delocalisation or valency-localisation accompanied by random static disorder.

The same space group, $I\bar{4}3d$ was employed to model the majority Cs_4O_6 phase. A small fraction (4.3(7) wt.%) of the impurity CsO_2 phase (space group $Fm\bar{3}m$) was again detected at low temperature. A general description of the analysis of the tof datasets was summarised in section 5.2.2. There were, however, certain differences in the Rietveld model used: the background was modelled using two different functions. A series of test refinements was performed employing different background functions for different banks of detectors. After qualitative and quantitative (by comparison of χ^2 and R_{wp}) examination of the test refinements, a Chebyschev polynomial function (function '1' in GSAS) was chosen for banks 2 and 6, and function '4' (in GSAS), which is designed to account for background contributions that increase with Q, was employed for banks 3, 4 and 5. The backgrounds of all banks were allowed to refine.

Figure 5.5 compares the final fits to the high-statistics data collected at 10 K after rapid cooling and at 320 K before cooling. No symmetry change is apparent. Table 5.2 summarizes the refined parameters from the Rietveld analysis of the datasets collected at 1.8, 10 and 320 K. An intramolecular O–O bond length of 1.3076(19) Å is derived at 10 K, shorter than that reported in Rb_4O_6 at 5 K (1.363(1) Å) [95]. The observation of an apparent increase in bond length on cooling (*cf.* 1.271(3) Å at 320 K), where thermal motion of the molecule is significantly reduced, suggests that the high-temperature refined bond length is artificially contracted due to the large librational motion of the oxygen dumbbells. Librational molecular motion provides a plausible explanation for unusually short bond lengths at high temperatures. Large librational motion of the diatomic molecule has been previously found to result in the observation [95] of an artificially contracted O_2 bond in diffraction studies [230]. The large amplitude librations of oxygen dumbbells in cubic Cs_4O_6 have been observed by EPR experiments, and it was revealed that librations freeze out on cooling on the EPR time scale [106]. Furthermore, the large anisotropic thermal displacements at high temperature might contribute to this artificial contraction as well. The thermal

displacements of oxygen at low temperatures again show anisotropy, with a shape similar to the high temperature case, albeit expectedly smaller, suggesting a significant reduction in librational motion.
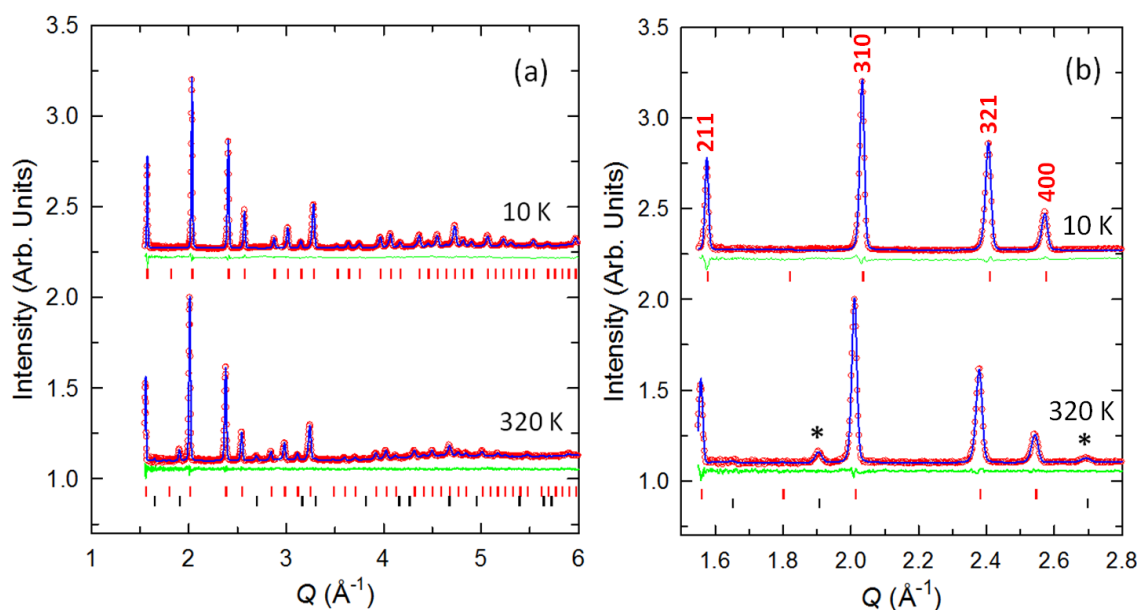
Figure 5.5 Calculated (blue lines) and observed (red circles) neutron tof powder diffraction patterns from bank-4 at 10 K after rapid cooling (upper pattern) and at 320 K before cooling (lower pattern). Red and black tickmarks show the cubic Cs_4O_6 and CsO_2 reflection positions, respectively. Panel (b) displays expanded regions of the respective diffraction profiles in (a); observed Bragg peaks are labelled by their (*hkl*) Miller indices. Asterisks represent the reflection positions of CsO_2 at 320 K, which is not detectable at bank-4 at 10 K. The refined fractions of the co-existing Cs_4O_6 and CsO_2 phases are 95.09(2)% and 4.9(3)% at 320 K, and 95.72(2)% and 4.3(7) % at 10 K, respectively. The total weighted-profile and expected R-factors are R_{wp} = 2.17% and R_{exp} = 2.69% (at 320 K), R_{wp} = 2.85% and R_{exp} = 2.08% (at 10 K), respectively.

To search for the presence of magnetic scattering appearing below 10 K, diffraction patterns collected at 1.8 and 10 K were overplotted (Figure 5.6). There are signs neither of magnetic Bragg diffraction peaks developing nor of a significant change in the diffuse scattering. The diffraction patterns collected at banks 1 and 2 which give access to the lowest Bragg reflection positions were carefully examined, and only reflections from the cubic structure of unchanged relative intensity were found to be present.
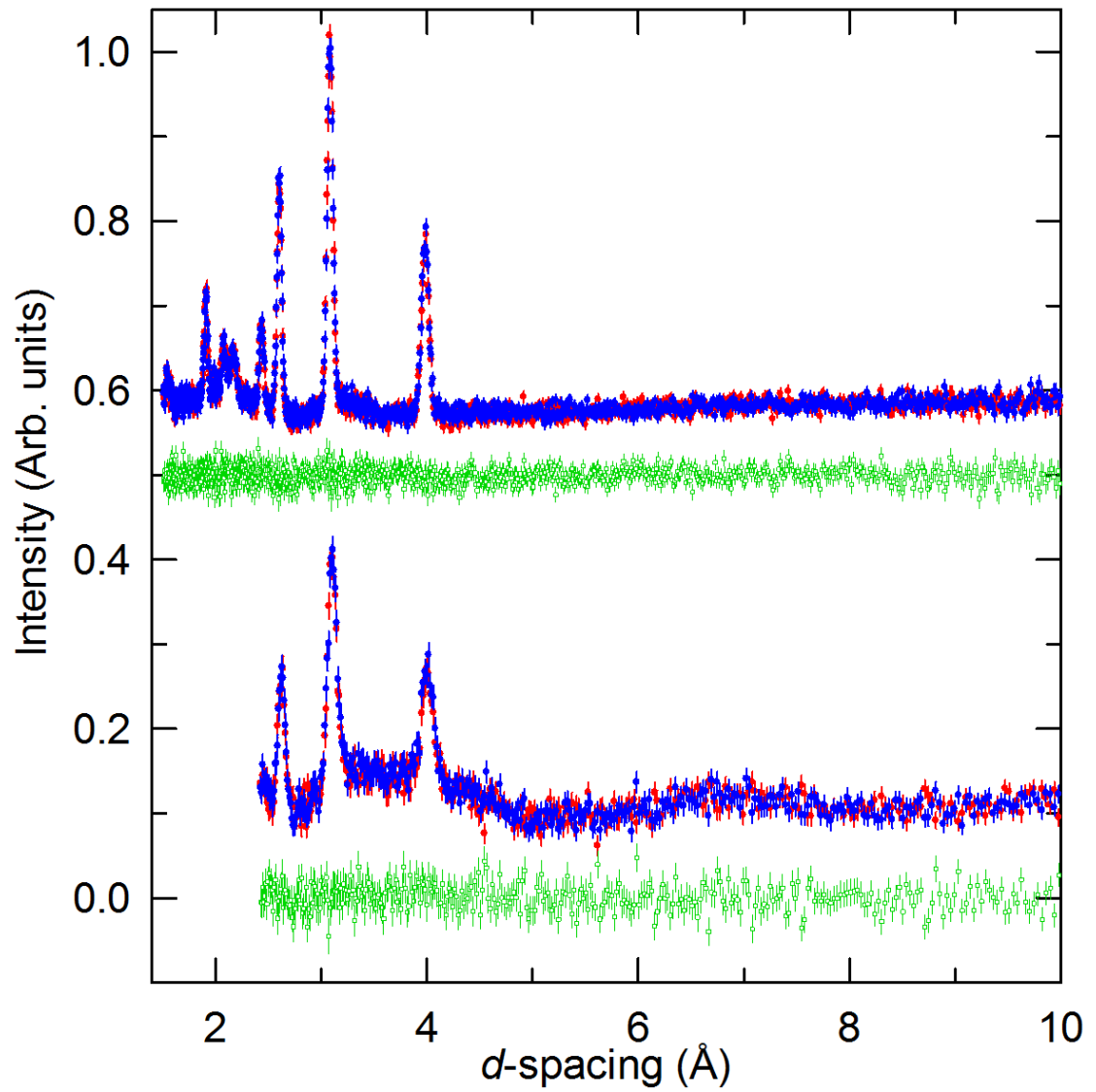
Figure 5.6 Observed neutron tof diffraction patterns collected at bank-1 (lower pattern) and bank-2 (upper pattern) at 10 K (red circles) and 1.8 K (blue circles). Green squares represent the difference profiles between the 10 and 1.8 K datasets.

Table 5.2 Refined structural parameters for the cubic Cs_4O_6 phase from the Rietveld fits to tof neutron diffraction data collected at 1.8 and 10 K after rapid cooling and at 320 K before cooling. Values in parentheses are estimated errors from the least-squares fitting. The fractions of the co-existing Cs_4O_6 and CsO_2 phases are 95.09(2)% and 4.9(3)% at 320 K, and 95.72(2)% and 4.3(7)% at 10 K, respectively; the relative phase fractions at 1.8 K were fixed to the values obtained at 10 K

	Temperature	1.8 K	10 K	320 K
	Space group	$I\bar{4}3d$	$I\bar{4}3d$	$I\bar{4}3d$
	a (Å)	9.75752(19)	9.7576(2)	9.8678(7)
	V (Å³)	929.01(6)	929.03(5)	960.9(2)
Cs	x/a	0.94639(6)	0.94633(7)	0.94626(11)
	U_{iso} (Å²)	0.0207(3)	0.0208(3)	0.0531(8)
O(1)	x/a	0.55804(11)	0.55808(11)	0.56061(16)
	y/b	0	0	0
	z/c	0.75	0.75	0.75
	U_{11}	0.0341(7)	0.0329(8)	0.0629(17)
	U_{22} (Å²)	0.0659(8)	0.0650(9)	0.1255(18)
	U_{33}	0.0094(5)	0.0088(6)	0.0457(14)
	U_{12}, U_{13}, U_{23} (Å²)	0, 0, 0.0045(5)	0, 0, 0.0037(6)	0, 0, 0.0092(11)
	O—O (Å)	1.3061(18)	1.3076(19)	1.271(3)
	R_{wp} (%)	2.33	2.85	2.17
	R_{exp} (%)	1.68	2.08	2.69

Temperature response of rapidly-cooled Cs_4O_6 on warming

Once the high-statistics datasets at 1.8 and 10 K had been collected after rapid cooling, a continuous data collection procedure was initiated whilst warming towards 320 K at a rate of 8.8 K h⁻¹. No significant changes in the pattern were observed on warming up to 170 K other than a continuous peak shifting due to lattice expansion. However, on warming above 170 K, a new set of diffraction

peaks emerged signifying the appearance of a new phase. The new reflections grew in intensity, at the expense of those of the cubic phase, up to ~220 K (Figure 5.7).
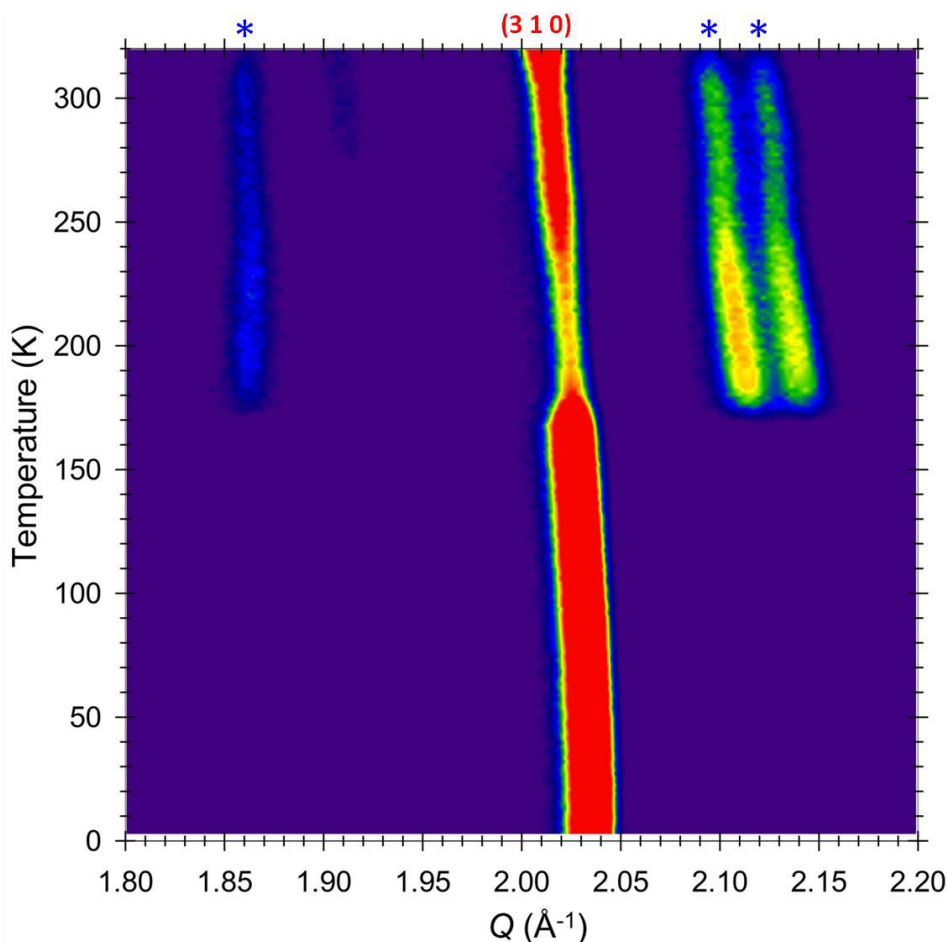
Figure 5.7 Temperature response of the diffraction pattern of Cs_4O_6 in the vicinity of the cubic (310) Bragg reflection on warming at a rate of 8.8 K h^{-1} after rapid cooling to base temperature. Only the bank-4 data are shown in the plot. The new peaks, which appear at ~1.86, 2.13 and 2.15 Å^{-1} above 170 K are labelled with asterisks.

Unexpectedly, heating past 220 K led to a reduction in intensity of the new peaks with recovery of intensity of the cubic phase reflections. At 320 K, this intermediate-temperature phase almost entirely disappears, with only the cubic phase surviving. The new peaks that appear above 170 K can be indexed to a tetragonal cell with space group $I\bar{4}2d$ (no. 122). Our tof powder neutron diffraction studies can now address the fundamental questions related to the mixed valence behaviour of Cs_4O_6. Rietveld analysis of all diffraction profiles collected on warming was then undertaken. The phase which emerges above 170 K was best modelled using a tetragonal unit cell (space group $I\bar{4}2d$) in which the orientation of the oxygen dumbbells originally pointing along the cubic a and b crystallographic axes changes drastically. Therefore 2/3 of the dioxygen units are now found to be

directed at an angle to the tetragonal c axis. The remaining 1/3 of dioxygen units are still oriented parallel to the c axis (Figure 5.8).
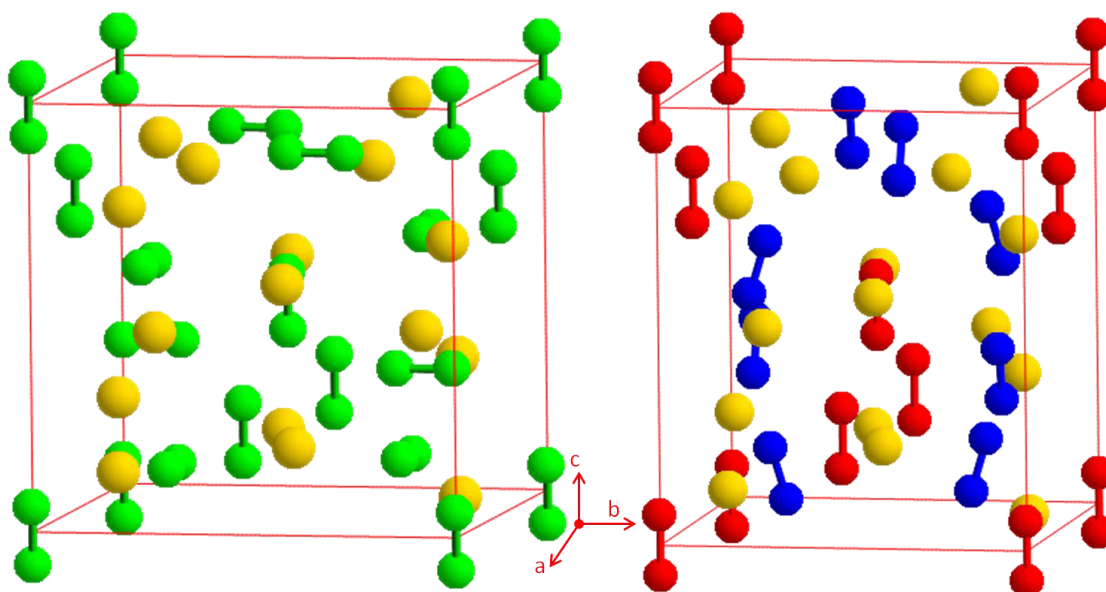
Figure 5.8 Cubic (space group $I\bar{4}3d$, displayed with an origin shift of (-1/2,-1/4,-1/8) for clarity) and tetragonal (space group $I\bar{4}2d$) structures of Cs_4O_6. In the cubic structure, all oxygen dumbbells (green) are symmetry equivalent and oriented parallel to the three crystallographic axes. In the tetragonal structure, there are two distinct Wyckoff sites where peroxide, O_2^{2-} (red) and superoxide, O_2^{-} anions (blue) reside: the O_2^{-} anions in the tetragonal phase are reoriented to align along the c-axis. Caesium ions are shown in yellow in both structures. Note the tilted orientation of the O_2^{-} anions in the tetragonal structure, away from the crystallographic c axis.

The reorientation of the molecular units and their near-alignment along c results in elongation of the c axis and contraction of the ab basal plane dimensions. In $I\bar{4}2d$, splitting of the oxygens into two different crystallographically sites with occupancy ratio of 2:1 allows the distinction between O_2^{-} and O_2^{2-} anions. Indeed, two clearly different sets of bond distances emerge from the refinements at 1.48(2) Å (8c site) and 1.27(2) Å (16e site) (at 200 K). This is consistent with the occurrence of charge ordering, and the molecular formula of the compound can be written as $(Cs^+)_4(O_2^-)_2(O_2^{2-})$. The observed bond distances are in good agreement with those known from the literature, namely 1.541(6) Å in O_2^{2-}[227], and 1.34(3) Å in O_2^- [226].

Given the very large number of datasets collected and processed on warming, *i.e.* 198, sequential Rietveld refinements were performed to finely probe the structural evolution of Cs_4O_6 on warming. Nevertheless, in order to confirm the reliability of the results of the sequential refinements, single dataset refinements

were also undertaken at selected temperatures. The analysed datasets were divided into two parts: part-I (1.8 K ≤ T < 170 K) and part-II: (170 K ≤ T ≤ 320 K). The part-I datasets were modelled with a two-phase model incorporating the cubic Cs_4O_6 (space group $I\bar{4}3d$) majority phase and the CsO_2 (space group $Fm\bar{3}m$) impurity phase. Sequential refinements of part-I were initiated with the dataset collected at 1.8 K. The crucial stage in sequential refinement procedures is to obtain the best possible refinement model to start with, with the most appropriate profile shape coefficients and background functions with reasonable number of terms for different banks.

The profile shape coefficients and diffractometer constants of the starting refinement of part-I were obtained from the analysis of the high-statistics data collected at 10 K after rapid cooling. The background was modelled differently from that of the high-statistics 10 K data (≈ 300 µAmp) analysis due to the low-statistics (≈ 12.5 µAmp) of the subsequent datasets. A series of test refinements was undertaken in order to test modelling of the background and eventually background function 4 was employed for all banks except for bank-6, whose background was modelled using a Chebyschev polynomial function (function '1' in GSAS). Both functions were allowed to refine. The lattice parameters, fractional atomic coordinates, and profile shape coefficients for the major phase and the phase fractions of both phases were refined. The caesium and oxygen thermal displacement parameters in the major phase were modelled as isotropic and refined freely, although the oxygen thermal displacements were modelled as anisotropic in analysis of the high-statistics datasets. Solely for reasons of low data statistics, oxygen thermal displacements in the major phase were modelled as isotropic for all sequential Rietveld refinement procedures. All sequential refinements reported in this chapter were performed on datasets summed in 10 minute blocks (ΔT ≈ 2 K), corresponding to ≈ 12.5 µAmps of proton current.

Once a stable refinement had been obtained and the reliability of the model had been quantitatively verified (R_{wp} = 5.5% and R_{exp} = 5.97%), sequential refinements of the part-I datasets were undertaken using this model as a starting refinement (on data collected at 1.8 K). During the run of sequential refinements of part-I, the lattice parameters, fractional atomic coordinates and thermal

displacement parameters for the cubic Cs_4O_6 phase were refined. The phase fraction of the impurity CsO_2 phase was fixed to 4.3 wt.% that was found at 10 K. The profile shape coefficients of all phases included in the model were always fixed during the run of sequential refinements to those obtained from the starting refinement.

We now turn to part-II. The starting refinement of part-II datasets was performed on the data collected at 170 K. The refinement procedure described for the analysis of the part-I data was employed but with certain differences in the model. Three crystallographic phases were now included: cubic and tetragonal Cs_4O_6 (majority phases), and an impurity CsO_2 phase. After obtaining a stable starting refinement, the run of sequential refinements was started in which the lattice parameters, phase fractions, fractional atomic coordinates and thermal displacement parameters for the cubic and tetragonal Cs_4O_6 phase were refined. The phase fraction of the impurity CsO_2 phase was again fixed to 3.9 wt%.

Finally, the structural evolution of rapidly-cooled Cs_4O_6 was investigated by sequential Rietveld analysis between 1.8 and 320 K on warming. Initial visual examination of the temperature evolution of the bank-4 tof diffraction profiles is shown in Figure 5.9 to highlight the significant changes on warming after rapid cooling. Once the sample reached 320 K, it was held there for 2 hours to allow full recovery of cubic Cs_4O_6; eventually, the tetragonal Cs_4O_6 phase entirely transformed, leaving only the cubic structure together with the impurity phase. Apart from the complex phase conversion between the cubic and tetragonal phases and the d-spacing shift of the Bragg peaks due to the thermal contraction, no other structural anomalies were evident.

The temperature dependence of the phase fractions obtained from the Rietveld analysis is shown in Figure 5.10. Between 170 and 200 K, the tetragonal phase fraction rose at the expense of that of the cubic phase. At 200 K, a maximum tetragonal phase fraction of 72.0(4) wt.% was observed, before conversion back to the cubic phase on further heating was initiated. The tetragonal-to-cubic conversion then almost entirely stops as is apparent from the plateau observed in the temperature range of 270 – 300 K.
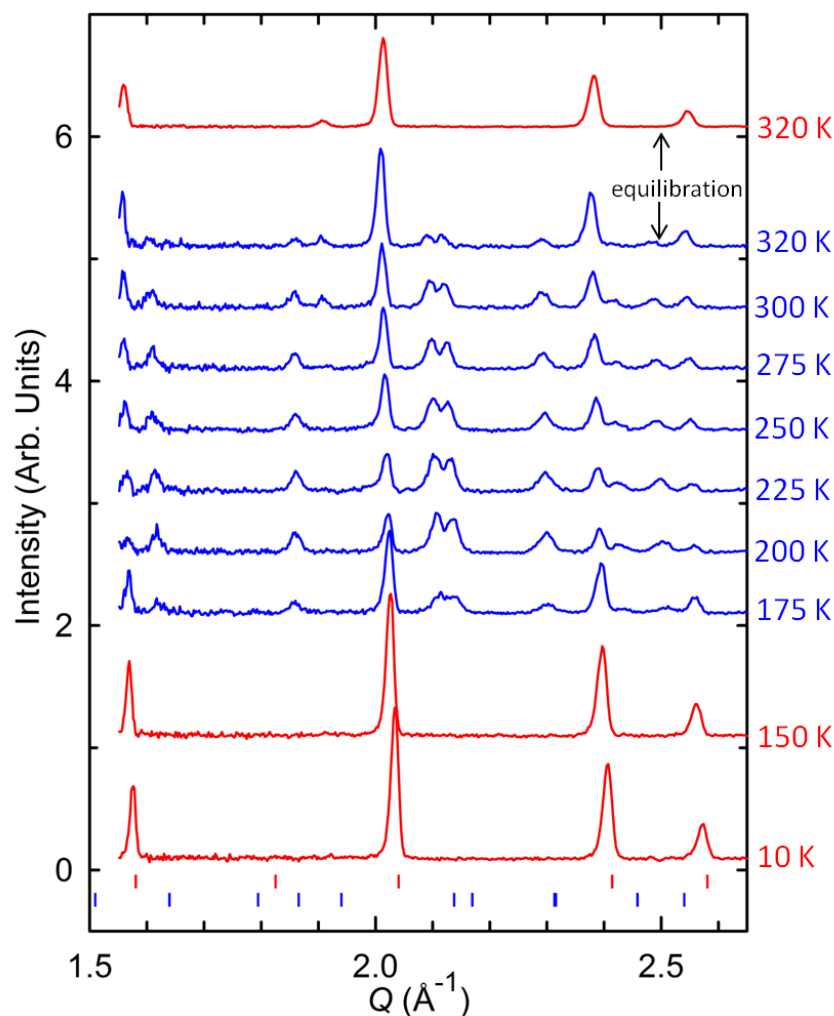
Figure 5.9 Neutron tof powder diffraction patterns at selected temperatures collected at bank-4 on warming. Red and blue tickmarks represent the reflection positions of cubic and tetragonal Cs_4O_6, respectively.

On approaching 320 K, the rate of tetragonal-to-cubic conversion again rapidly increased, leading to fast reduction of the intensity of the tetragonal phase peaks. A complete tetragonal-to-cubic transformation was finally achieved after holding the sample at 320 K for 2 hours. A detailed examination of the refined structural parameters of the cubic and tetragonal phases was undertaken for the rapid cooling state; these results will be presented together with those from the ultra-slow cooling experiment in section 5.2.5.
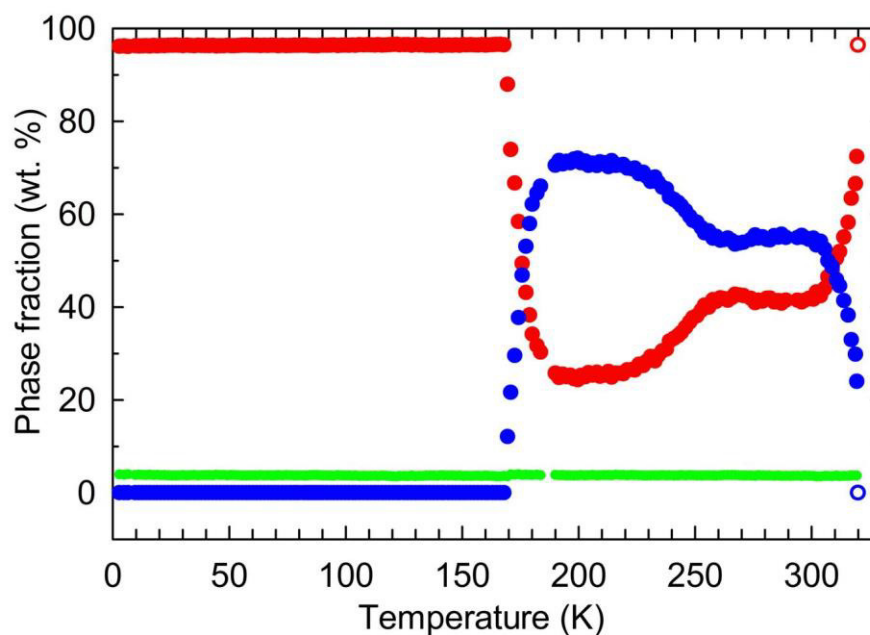
Figure 5.10 Evolution of the phase fractions on warming after rapid cooling. Red, blue and green circles represent the cubic Cs_4O_6, tetragonal Cs_4O_6 and impurity CsO_2 phases, respectively. Open circles denote the result obtained after holding the sample at 320 K for 2 hrs.

5.2.4   Ultra-slow cooling protocol of Cs_4O_6

With the knowledge that slow cooling of Cs_4O_6 leads to a transition to a low-symmetry structure, the sample was then very slowly cooled from 320 to 50 K at a rate of 1.68 K h^{-1}, to investigate the effects of thermal history and in an attempt to isolate this newly-observed structure at low temperatures. Once the sample had reached 50 K, it was held there for 4 days. While the sample was at 50 K in the cryostat, it was inserted into the GEM diffractometer, and then an initial diffraction pattern was collected to check whether or not the sample survived during this ultra-slow cooling treatment, which took 11 days in total. After the slow cooling, inspection of the initial diffraction pattern revealed a significantly different result compared to rapid cooling. The tetragonal Cs_4O_6 phase is now clearly evident at 50 K together with some untransformed cubic Cs_4O_6. Once the sample quality was confirmed, it was then cooled down to 10 K at a rate of 0.44 K min^{-1} and a high-statistics dataset ($\approx$ 351.6 μAmps) was collected . Following this, the sample was further cooled to 1.8 K.

190

Low temperature structure of Cs_4O_6 after ultra-slow cooling

Rietveld analysis of the high-statistics data collected at 10 K after ultra-slow cooling was first undertaken. Three crystallographic phases were included in the model as necessitated by visual inspection: cubic and tetragonal Cs_4O_6 (major phases) and minority CsO_2 (space group $Fm\bar{3}m$) phase. The background was again modelled using two different functions: a Chebyschev polynomial function for banks 2, 3, 5 and 6, and function 4 for bank-4. (See sections 5.2.2 and 5.2.3 for the refinement method).

The 10 K thermal displacement parameters of the oxygen atoms in the tetragonal phase and its structure are presented in Table 5.3 and Figure 5.11, respectively. The unphysical orientations of the tensor elements are once again present with a shape similar to that of cubic Cs_4O_6 (Figure 5.1). Especially, the thermal ellipsoids on the oxygen atoms located at the *16e* Wyckoff site (O_2^- ions) are significantly flattened compared to those of the oxygen atoms at the *8c* site (O_2^{2-} ions).

Concurrently with our work, single crystal X-ray diffraction studies of the rubidium analogue, Rb_4O_6 have also identified an isostructural tetragonal phase at 100 K and revealed a pronounced anisotropic thermal motion of the oxygen atoms generated by the space group $I\bar{4}2d$ [229]. Due to these seemingly unphysical thermal displacements, the possibility of a further symmetry reduction to the $I\bar{4}$ space group was discussed. In $I\bar{4}$, a further splitting of the atomic positions is allowed, while the O_2^- ions are still tilted with respect to the c axis, as for $I\bar{4}2d$. Nonetheless, refinement of the tetragonal structure in $I\bar{4}$ still showed strong anisotropic thermal displacements of the oxygen atoms in the directions perpendicular to the O–O bonds, but with smaller amplitudes than in the $I\bar{4}2d$ case. In the present study, any attempts to refine the structure using our neutron tof powder diffraction data in this lower symmetry tetragonal space group were unsuccessful. Whilst given the quality of the data, we cannot entirely rule out the possibility that the true space group is $I\bar{4}$, we find no evidence of breaking the ($00l : l = 4n$) reflection condition of the $I\bar{4}2d$ space group.

Table 5.3 Oxygen thermal displacement parameters in tetragonal Cs_4O_6 after ultra-slow cooling to 10 K. The fractions of the co-existing cubic and tetragonal Cs_4O_6 and CsO_2 phases are 23.2(2)%, 72.7(1)% and 4.1(2)%, respectively (R_{wp} = 3%, R_{exp} = 2.29%).

U_{iso} (Å^2)	O(1) - Wyckoff site *8c*	O(2) - Wyckoff site *16e*
U_{11}, U_{22}, U_{33}	0.0115(13), 0.0051(16), 0.0147(16)	0.0453(16), 0.0111(15), 0.0166(11)
$U_{12}\ U_{13}\ U_{23}$	0.0123(14), 0, 0	0.0048(13), -0.0064(14), 0.0058(12)
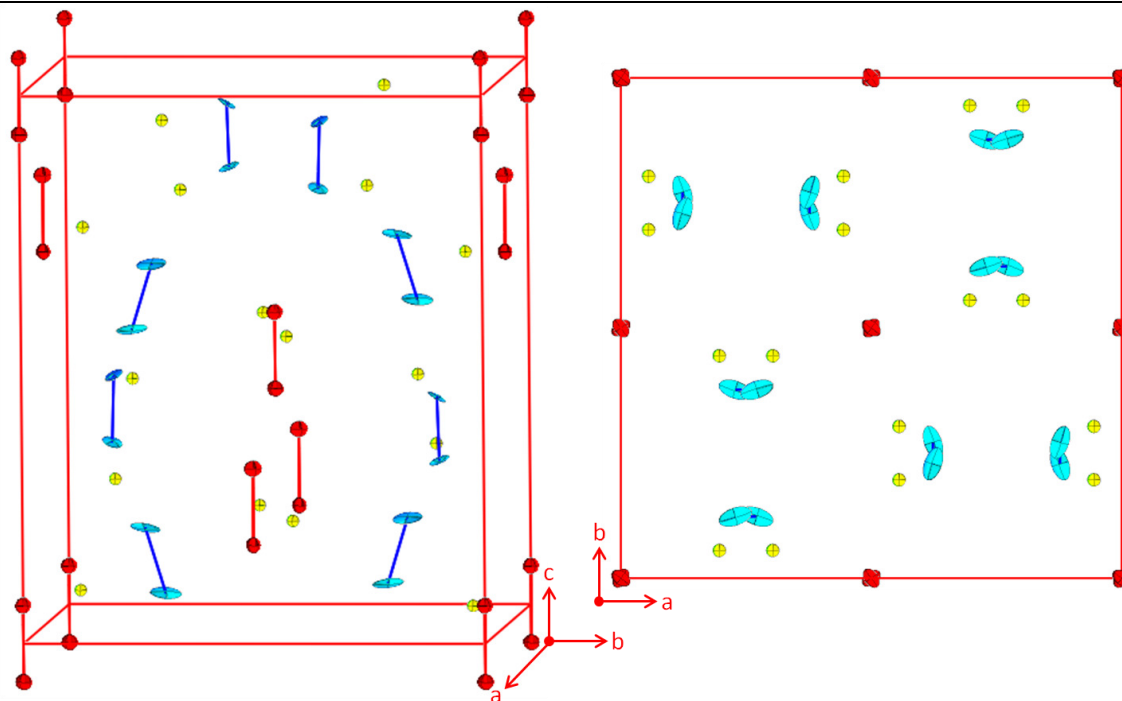
Figure 5.11 Tetragonal $I\bar{4}2d$ Cs_4O_6 structure at 10 K. Cs^+, O_2^{2-} and O_2^- ions are represented with yellow, red and blue colour, respectively. Thermal displacement ellipsoids of the caesium and oxygen atoms are drawn at the 90% probability level.

Refined temperature- and cooling-protocol-dependent structural parameters of the cubic and tetragonal phases and Rietveld fits to the 10 K data collected after rapid and ultra-slow cooling are presented in Table 5.4 and Figure 5.12, respectively. Refinement of the fractional coordinates of the oxygen atoms in the tetragonal phase at 10 K gave intramolecular bond lengths O(1)–O(1): 1.528(6) Å for O_2^{2-} and O(2)–O(2): 1.345(4) Å for O_2^-, which are in excellent agreement with values previously reported for O_2^{2-} (1.541(6) Å, [227]) and for O_2^- (1.34(3) Å, [226]).

Table 5.4 Temperature- and cooling-protocol-dependent structural parameters for Cs_4O_6. In the tetragonal phase $\bar{4}$, the O_2^- anions are reoriented to align with the c-axis.

Temperature		320 K	10 K after rapid cooling	10 K after slow cooling	
Symmetry		Cubic	Cubic	Cubic	Tetragonal
Space group		$I\bar{4}3d$	$I\bar{4}3d$	$I\bar{4}3d$	$I\bar{4}2d$
a (Å)		9.8678(7)	9.7576(2)	9.7382(2)	9.1587(2)
c (Å)		-	-	-	10.8656(5)
V (Å³)		960.9(2)	929.03(5)	923.51(6)	911.43(5)
	Wyckoff site	*16c*	*16c*	*16c*	*16e*
	x/a	0.94626(11)	0.94639(6)	0.9460(2)	0.30341(18)
Cs	y/b	-	-	-	0.0555(2)
	z/c	-	-	-	0.04741(18)
	U_{iso} (Å²)	0.0531(8)	0.0207(3)	0.0241(12)	0.0071(4)
	Wyckoff site	*24d*	*24d*	*24d*	*8c*
	x/a	0.56061(16)	0.55804(11)	0.5590(5)	0
O(1)	y/b	0	0	0	0
	z/c	0.75	0.75	0.75	0.0703(3)
	O(1)—O(1) (Å)	1.271(3)	1.3076(19)	1.3069(10)	1.528(6)
	Wyckoff site	-	-	-	*16e*
	x/a	-	-	-	0.3776(3)
O(2)	y/b	-	-	-	0.7705(2)
	z/c	-	-	-	0.18441(18)
	O(2)—O(2) (Å)	-	-	-	1.345(4)
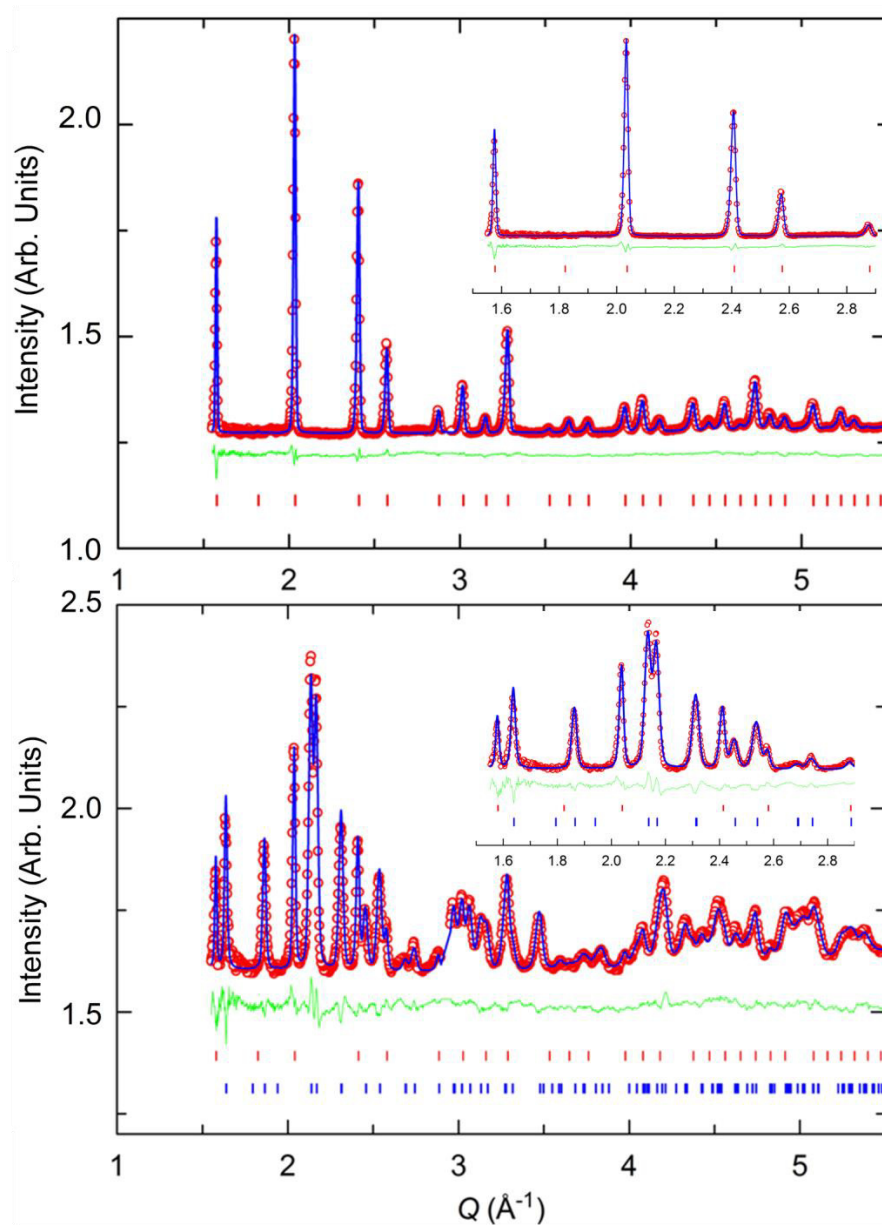
Figure 5.12 Final observed (red circles) and calculated (blue solid lines) tof neutron diffraction profiles at 10 K after rapid cooling (upper panel) and at 10 K after ultra-slow cooling (lower panel). Only the data collected from bank-4 are shown. Green lines represent the difference profiles. The red and blue tick marks show reflection positions of cubic and tetragonal Cs_4O_6, respectively. Contributions from the vanadium sample holder at Q = 2.85 - 2.95 Å^{-1} are excluded from the analysis. Both insets display expanded regions of the respective diffraction profiles. Reflection positions of CsO_2 are not detectable at bank-4 at 10 K.

Temperature response of ultra-slow cooled Cs_4O_6 on warming and cooling

We now turn to the structural response of Cs_4O_6 whilst warming to 320 K at a rate of 8.8 K h^{-1} from the ultra-slow cooled state. Again, a complex structural behaviour was seen on warming above 170 K (Figure 5.13) comparable to that of the rapidly-cooled state to heating (Figure 5.7).
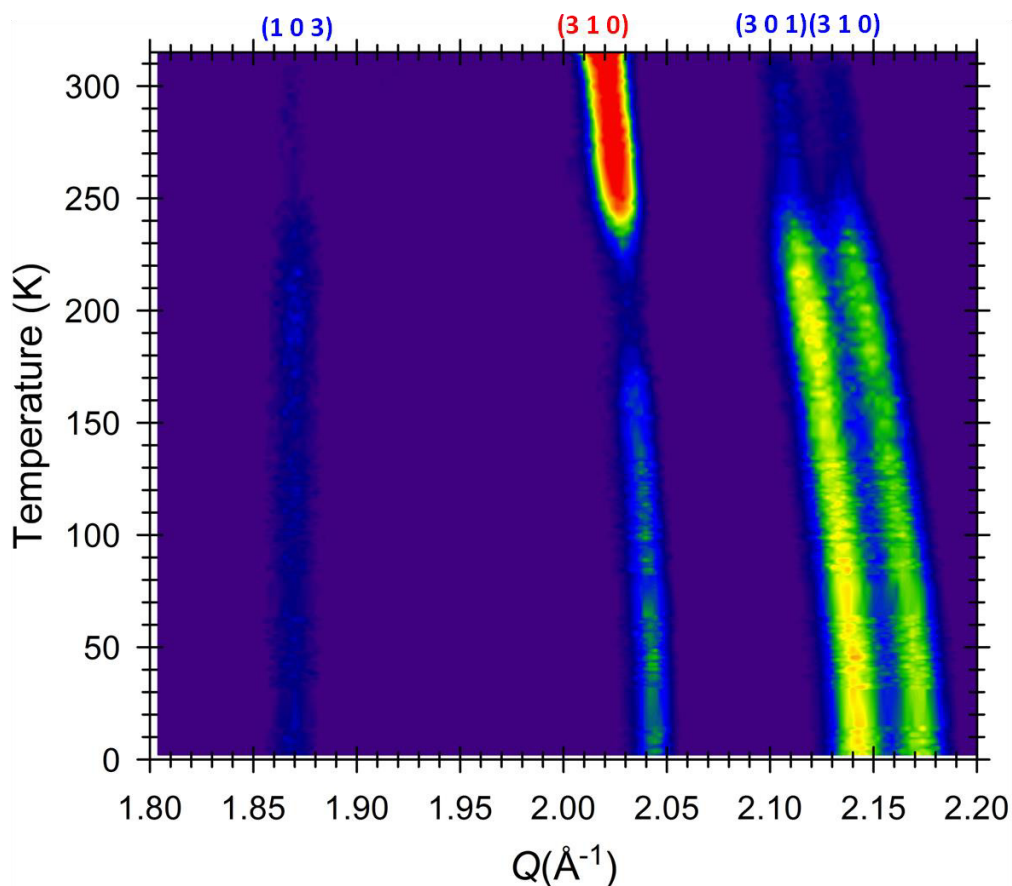
Figure 5.13 Temperature response of the diffraction pattern of Cs_4O_6 in the vicinity of the cubic (310) Bragg reflection on warming to 320 K at a rate of 8.8 K h^{-1} after ultra-slow cooling to low temperature. Only the bank-4 data are shown in the plot. All observed peaks are labelled with their corresponding Miller indices (red: cubic, blue: tetragonal).

Initially, the relative fractions of the tetragonal and cubic Cs_4O_6 phases remained unchanged on warming to 170 K. Between 170 and 200 K, the weight fraction of the cubic phase started to decrease. On further heating, conversion back to the cubic phase was re-eastablished at the expense of the tetragonal phase. Finally, at 320 K, the tetragonal-to-cubic conversion was almost entirely complete. Once the sample had reached 320 K, it was held there for 2 hours to achieve complete conversion back to the cubic phase. Once full conversion back was confirmed, the sample was cooled down to 140 K at a rate of 12 K h^{-1}. Solely for reasons of time restriction, no cooling below 140 K was possible. We found that cubic Cs_4O_6 is robust down to 200 K. However, below this temperature, new peaks consistent with the emergence of the tetragonal phase appear (Figure 5.14).
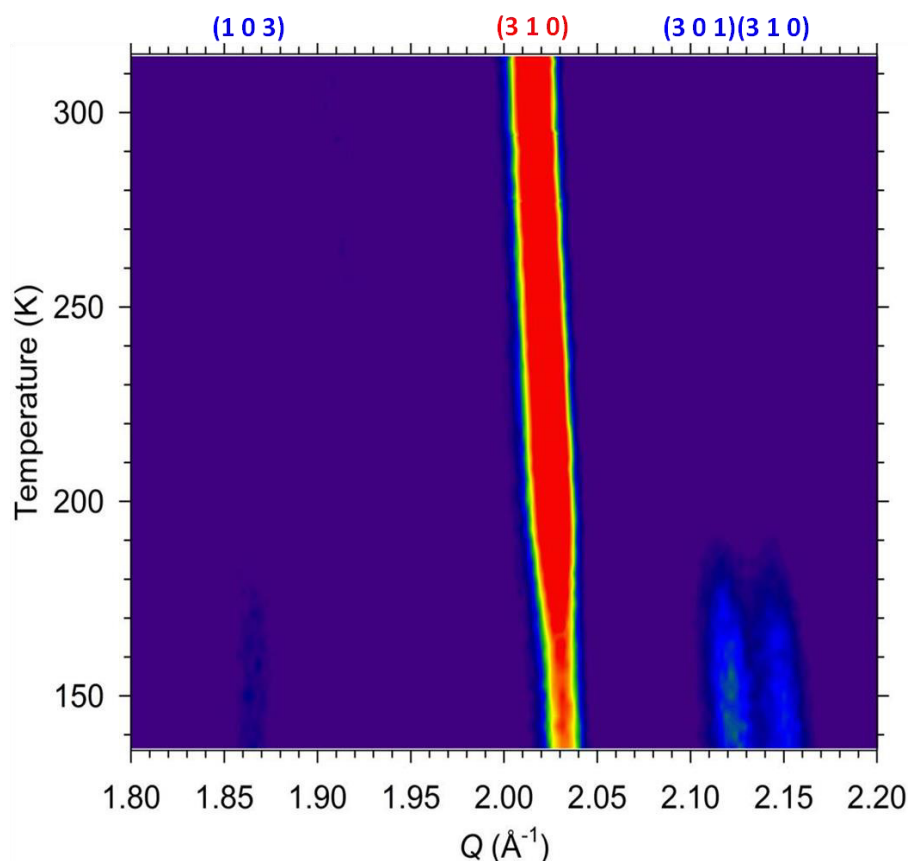
Figure 5.14 Temperature response of the diffraction pattern of Cs_4O_6 in the vicinity of the cubic (310) Bragg reflection on cooling at a rate of 12 K h^{-1} from 320 K. Only the bank-4 data are shown in the plot. All observed peaks are labelled with their corresponding Miller indices (red: cubic, blue: tetragonal).

Sequential Rietveld analysis of the datasets collected on warming and cooling was undertaken. The starting refinement of the datasets collected on warming was performed for the 1.8 K data. The structural model employed was comparable to that used for the 10 K data after ultra-slow cooling with certain differences: both caesium and oxygen thermal displacement parameters in the major phases were modelled as isotropic, solely for reasons of data quality. While the phase fractions and profile shape coefficients for the major phases were allowed to refine if the refinement could converge, they were fixed for the impurity CsO_2 phase to those obtained from the analysis of the high-statistics data collected at 10 K. Once a stable refinement had been obtained, sequential refinements on warming were initiated using this starting refinement. During the run of sequential refinements, the lattice parameters, background, fractional coordinates, phase fractions and thermal displacement parameters of the major phases were refined. The profile

shape coefficients and scale factor of the impurity phase were kept fixed as obtained in the starting refinement.

The run of sequential refinements of datasets collected on cooling was started with the dataset collected at 320 K. Since the tetragonal phase emerged on cooling below 200 K, in the temperature range between 320 K and 200 K, two crystallographic phases (cubic Cs_4O_6 and the impurity CsO_2 phase) were included in the model. The tetragonal phase was then also included for datasets collected below 200 K. A Chebyschev polynomial function was used to model the background for all banks of detectors. This time there was no need of including function '4' (in GSAS) as the background contributions did not increase with Q, displaying a little varying contribution over the experimental Q range. During the run of sequential refinements, the same parameters were refined as with the datasets collected on warming.

5.2.5 Structural results at ambient pressure

Here we discuss the results of the ambient-pressure neutron tof diffraction investigations of Cs_4O_6 in more detail. We especially focus on the complex structural evolution as revealed by the temperature response of structural parameters such as unit cell volume, torsion angles, O−O bond lengths and thermal displacement parameters.

The temperature dependence of the unit cell volume, $V(T)$, of cubic and tetragonal Cs_4O_6 (Figure 5.15) was modelled using a Debye-Grüneisen model such as that proposed by Sayetat *et al*. (described in Section 2.3.6) [134]. The function in Equation 2.37 was used to fit the $V(T)$ data. This Debye-Grüneisen model describes well the $V(T)$ data of the cubic structure over the whole temperature range. The tetragonal unit cell, however, shows a distinct deviation from the expected behaviour above ∼250 K; therefore only the $V(T)$ data of the tetragonal structure collected at temperatures below the volume anomaly were included in the fit. Derived parameters from the Debye-Grüneisen fits are shown in Table 5.5. The Debye temperature, Θ_D, found for the tetragonal structure is lower than that of cubic Cs_4O_6 while the thermal expansivities are essentially identical.

Table 5.5 Resulting parameters from the Debye-Grüneisen fits to the $V(T)$ data of. Statistical errors given in parentheses are from least-squares fitting.

Symmetry	Fitted T range (K)	V_0 (Å³)	Θ_D (K)	I_V (Å³ K⁻¹)
Cubic	3 - 320	929.67(6)	270(4)	0.1399(8)
Tetragonal	2 - 250	911.55(6)	183(4)	0.1440(9)

Due to the elongation of the c axis and contraction of the ab basal plane dimensions, the cubic-to-tetragonal phase transition should be accompanied by a drastic collapse in the unit cell size. Indeed, a 1.894(8)% contraction at 10 K is observed experimentally. At 10 K, the unit cell volumes of the cubic and tetragonal phases are 929.03(5) Å³ and 911.43(5) Å³.
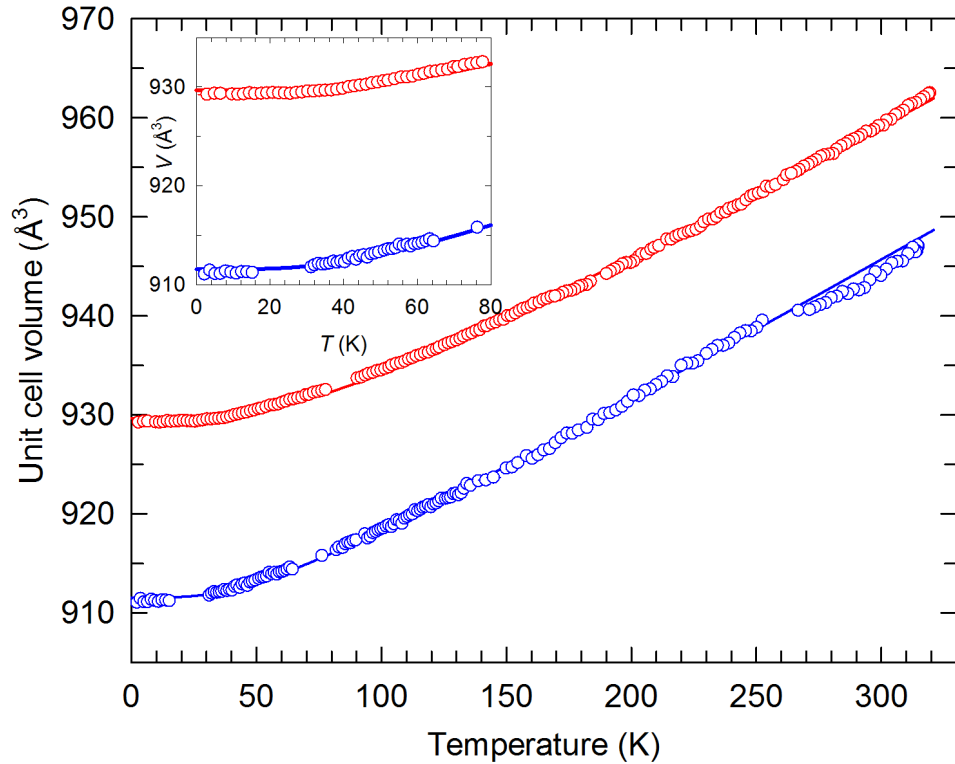
Figure 5.15 Thermal expansivity of cubic (red) and tetragonal (blue) Cs_4O_6, extracted from data collected on warming from rapid-cooled and ultra-slow-cooled states, respectively. The gaps between the data points are due to data collection interruption due to beam loss. The inset shows an expanded view of the low-temperature region. Solid lines through data points display the results of Debye-Grüneisen fits.

The anisotropic thermal expansivity of the tetragonal phase is highlighted in Figure 5.16, which shows the temperature dependence of the lattice parameters, with an evident expansion of the tetragonal a lattice parameter and a contraction along c. The anomalous behaviour above ~250 K is again clearly apparent. The

anomaly in the expansivity, concomitant with a reduction in the tetragonal-to-cubic phase conversion rate above 250 K, is evidence for a change in the tetragonal structure.
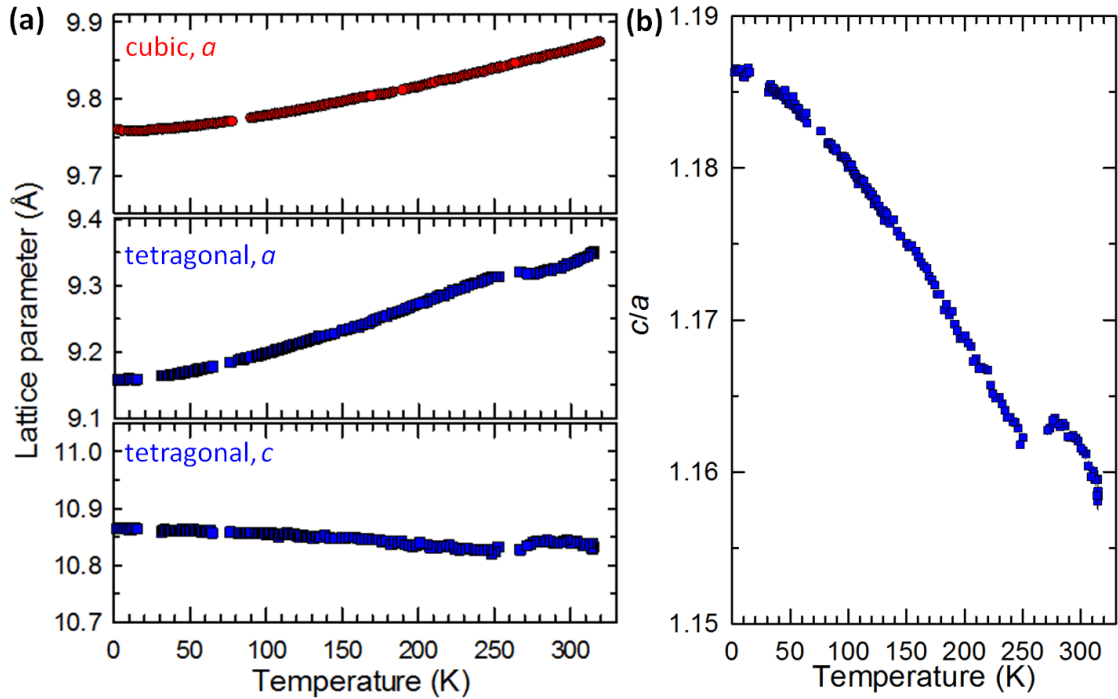
Figure 5.16 (a): Evolution of the lattice parameters of cubic and tetragonal Cs_4O_6 with temperature, extracted from data collected on warming from rapid-cooled and ultra-slow-cooled states, respectively. (b): Temperature dependence of the tetragonal distortion, c/a. The gaps between the data points are due to data collection interruption due to beam loss.

We now examine the evolution of the phase fractions after different cooling protocols were applied (Figure 5.17). Initially, the relative tetragonal and cubic phase fractions remained virtually unchanged on warming up to 170 K from the rapid- and ultra-slow-cooled states. A fast reduction in the intensity of the Bragg reflections of the cubic phase was then seen between 170 and 200 K. At ~201 K, maximum weight fractions of the tetragonal phase of 72.0(4) and 82.5(4) wt.% were observed for the rapid and ultra-slow cooling protocols, respectively. On further heating, the tetragonal phase started to convert back to cubic; however, this conversion showed non-monotonic behaviour for both cooling protocols. Between 270 and 300 K, the fractions of both the tetragonal and cubic phases remained invariant, then on approaching 320 K, the conversion rapidly increased, leading to a fast reduction of the tetragonal phase fraction (decreasing to 19.1(4) and 24.0(4) wt.% at 320 K for the ultra-slow and rapid cooling protocols,

respectively). Finally, a complete conversion back to the cubic phase was achieved by holding the sample at 320 K for 2 hours.
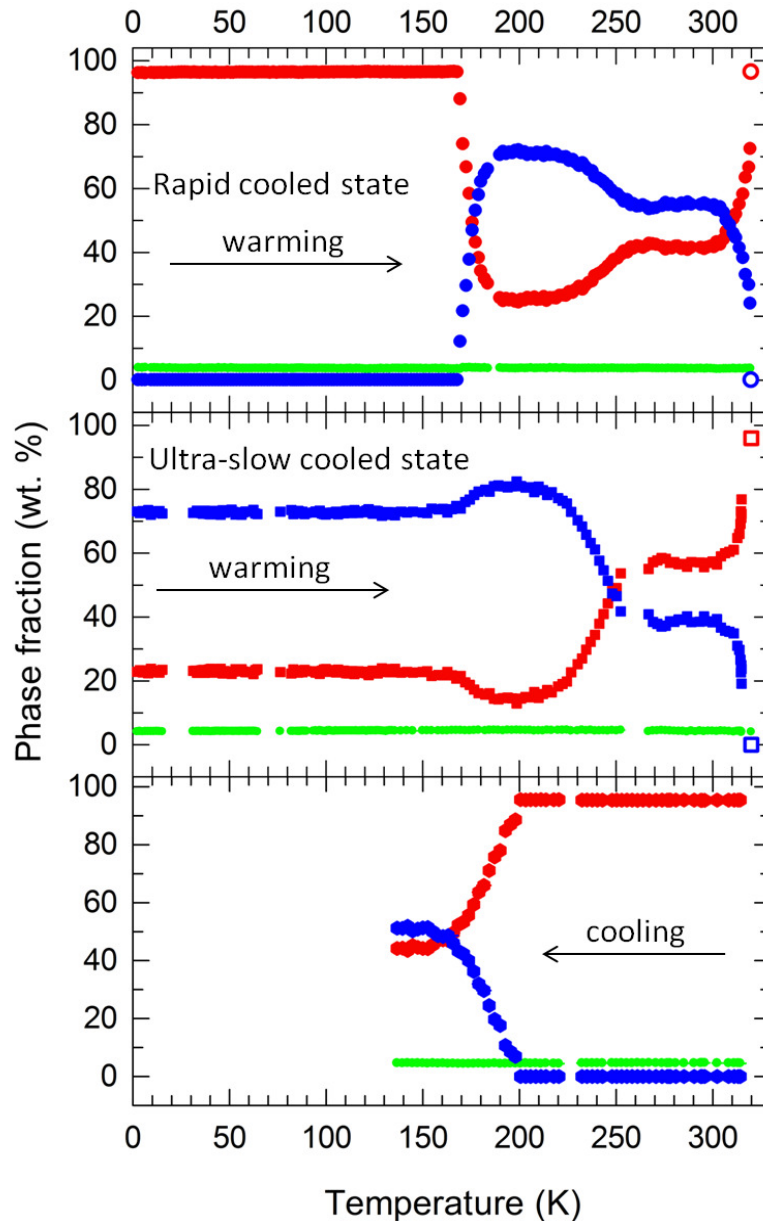
Figure 5.17 From top to bottom: temperature evolution of the phase fractions of cubic (red) and tetragonal (blue) Cs_4O_6 and impurity CsO_2 (green) on heating after rapid and ultra-slow cooling, and on cooling from high temperature.

The cubic Cs_4O_6 phase was stable on cooling from 320 to 200 K, where the maximum tetragonal phase fractions were observed on heating. Between 200 and 150 K, the cubic-to-tetragonal conversion occurred, but below 150 K, this conversion did not continue anymore; it appears that the phase fractions of the two phases no longer change on cooling below 140 K. These observations: phase-coexistence over a broad temperature range and large thermal hysteresis in the

course of a characteristic sluggish cubic-to-tetragonal phase transformation are consistent with a first-order transition between the two phases.

Since the transition from cubic to tetragonal structure is a result of the charge ordering and the two phases differ in the orientation of the O_2^- ions, the reasons behind the puzzling observations described so far could be related to the dependence of the orientation of the O_2^- ions on temperature. We now therefore examine the temperature dependence of the torsion (dihedral) angles defined by four atoms; two atoms from the O_2^- molecules (2/3 of the oxygen dumbbells) and two from the O_2^{2-} molecules (1/3 of the oxygen dumbbells) in the tetragonal $I\bar{4}2d$ cell. Since the O_2^{2-} molecules are oriented parallel to the c–axis, the temperature response of the O_2^- – O_2^{2-} torsion angles reflects the change in the tilting of the O_2^- anions from the crystallographic c axis. Figure 5.18 shows the tetragonal Cs_4O_6 crystal structure at 10 K, together with a representative view of the torsion angles of the O_2^- units. However, the reduced intensity of the Bragg reflections of the tetragonal phase on warming above 200 K makes definitive analysis of the temperature-dependent structural details difficult.

There are two distinct torsion angles between the O_2^- and O_2^{2-} anions and the temperature response of the two angles were found to be identical. As seen in Figure 5.18, the torsion angles between the O_2^- and O_2^{2-} anions are 14.62(3)° and 13.88(3)° at 10 K. The O_2^- anions exhibit varying degrees of reorientational behaviour on warming above 150 K, where the complex competition in stability of the cubic and tetragonal phases appears (Figure 5.19). In the case of the rapid-cooled state, at temperatures between 170 and 200 K, where the tetragonal phase fraction increases rapidly, the tilt angle between the two oxygen dumbbells also increases rapidly. On further heating above 260 K, where a plateau in the plot of wt.% $vs.$ T exists, the tilt angles start decreasing after reaching a maximum of 18.35(5)° at 254 K; finally, the tilting decreases significantly to 9.55(13)° at 317 K, concomitant with the fast reduction in the phase fraction of the tetragonal Cs_4O_6.
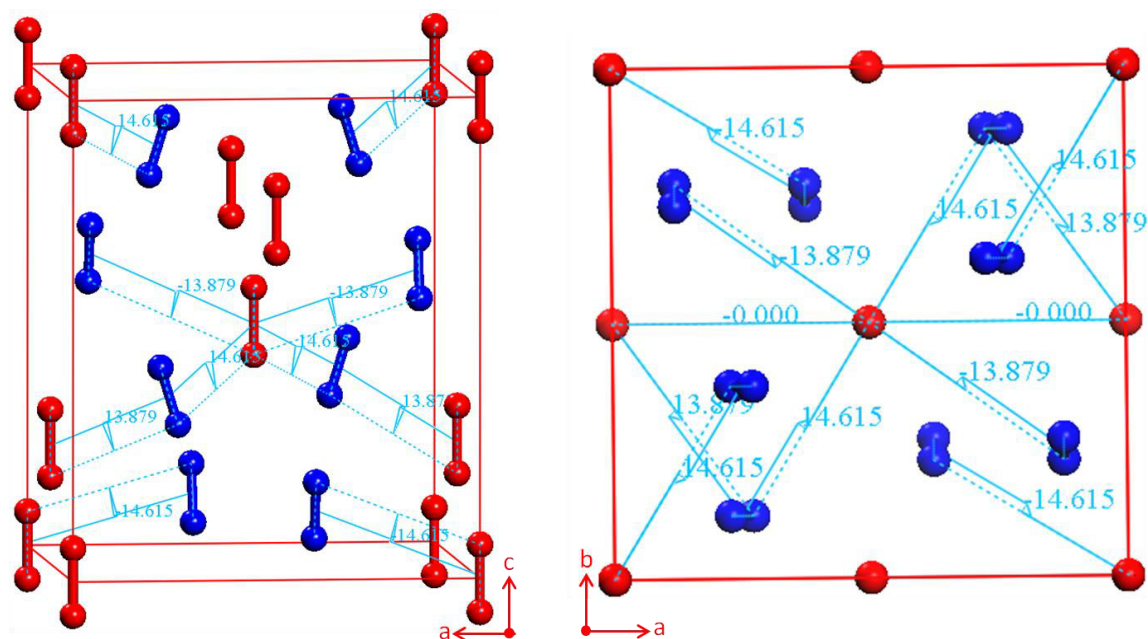
Figure 5.18 Tetragonal ($I\bar{4}2d$) Cs_4O_6 structure with the unit cell shown in red. Structural parameters to build the unit cell were taken from the results of the Rietveld analysis of the tof neutron diffraction data at 10 K after ultra-slow cooling. O_2^{2-} and O_2^- are shown in red and blue, respectively. The O_2^{2-} anions orient along the c-axis but with a tilt off the axis. Representative views of the torsion angles between the O_2^{2-} and O_2^- anions are shown in turquoise.

Similar anomalies in the torsion angles on heating were observed in the case of the ultra-slow-cooled state; at temperatures above 200 K, a systematic pronounced change was seen. At 269 K, the torsion angle reached 17.09(5)°, then decreased to 13.89(10)° at 304 K. On cooling, the torsion angles increased rapidly as soon as the tetragonal phase started growing in intensity from 200 to 150 K. When the tilting between the oxygen dumbbells decreased, O_2^- anions tended to orient parallel to the crystallographic c axis. Certainly, the transformation between the high-temperature cubic and low-temperature tetragonal phases involves large amplitude reorientations of the oxygen dumbbells and is non-monotonic. For instance, the variation in the degree of mobility of the O_2^- anions with temperature is more pronounced for the rapid-cooled state compared to the ultra-slow-cooled state.
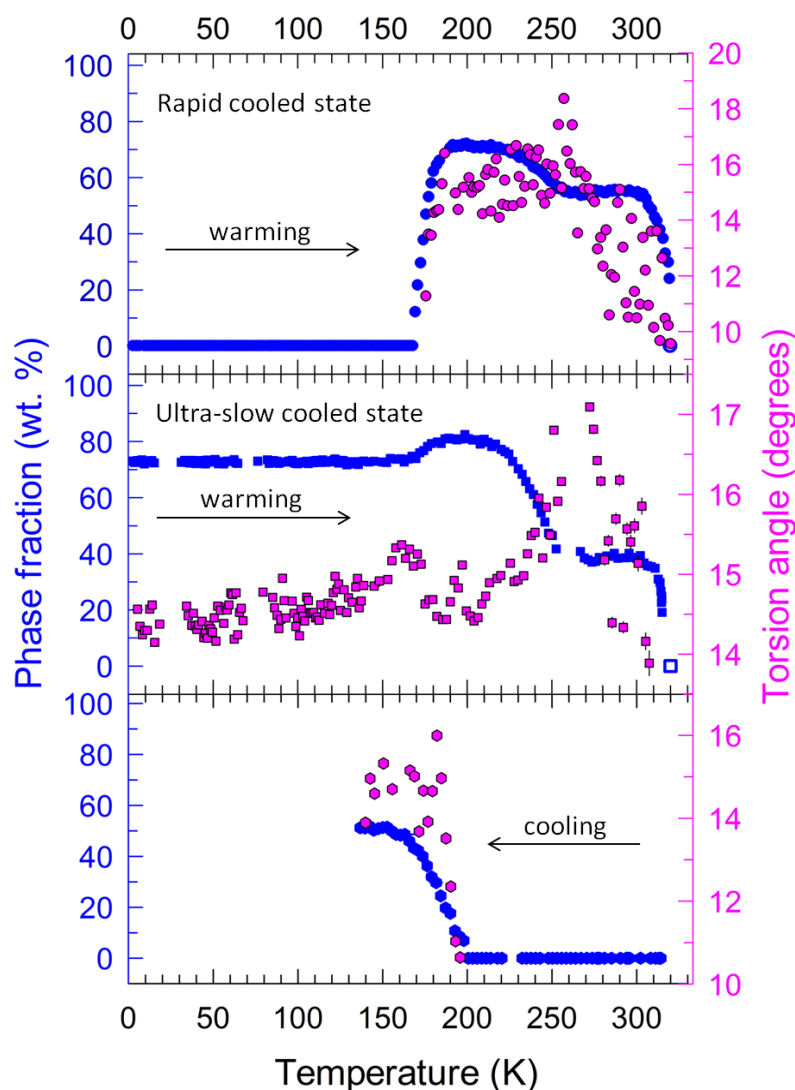
Figure 5.19 From top to bottom: temperature evolution of the phase fraction of the tetragonal Cs_4O_6 phase (left axis) and of the torsion angles between the O_2^{2-} and O_2^- anions (right axis) on warming after rapid cooling and ultra-slow cooling, and on cooling, respectively. Estimated errors are smaller than the data points.

The variation of the intramolecular O−O bond lengths and isotropic thermal displacements of oxygen and caesium in the tetragonal and cubic Cs_4O_6 phases with temperature was also investigated. The resulting refined bond lengths confirm the existence of different oxygen species with different charges over the experimental temperature range. The temperature responses of the two sets of bond lengths at the 16e (occupied by O_2^-) and 8c (occupied by O_2^{2-}) Wyckoff sites in the tetragonal $I\bar{4}2d$ unit cell, and that of the one distinct bond length at the 24d Wyckoff site in the cubic $I\bar{4}3d$ unit cell, are shown in panels (a): and (b) of Figure 5.20, respectively. The O−O bond length for the O_2^{2-} anion (depicted in red) shows a small increase above 250 K, which coincides with an increase in the U_{iso} of

oxygen in the O_2^{2-} anion for the ultra-slow-cooled state (Figure 5.20. (c)). However, the low intensity of the Bragg reflections of the tetragonal phase on warming above 250 K and the relatively large estimated errors in bond lengths make ultimate interpretation of the resulting structural details tricky. On the other hand, the anomaly seen in the tetragonal *a* and *c* lattice parameters above 250 K (Figure 5.16) could be correlated with this increase in the O_2^{2-} bond length.

The shortening of the superoxide bond length above 200 K could be attributed to the increase in the thermal and librational motion and does not necessarily mean a true change in bond length, considering the relatively large estimated errors in bond length at high temperatures. Whilst thermal displacements of the O_2^- and caesium in tetragonal Cs_4O_6 grew consistently on warming and became more pronounced above 200 K (Figure 5.20 . (c), (e)), which could be tentatively related to the pronounced increase in the torsion angles, thermal displacements of O_2^{2-} exhibited an almost linear temperature response.

We now turn to the variation in the O–O bond length and thermal displacements in cubic Cs_4O_6 with temperature. The bond length remained virtually unchanged up to 170 K (Figure 5.20(b)); however, at ~200 K, where the cubic phase fraction reached its minimum, there was a steep decrease in the bond length, which coincides with an anomaly seen in the variation of the Cs thermal displacements as well (Figure 5.20 and (f)). As it is apparent from Figure 5.20, there are significant correlations between the positional and the thermal parameters.
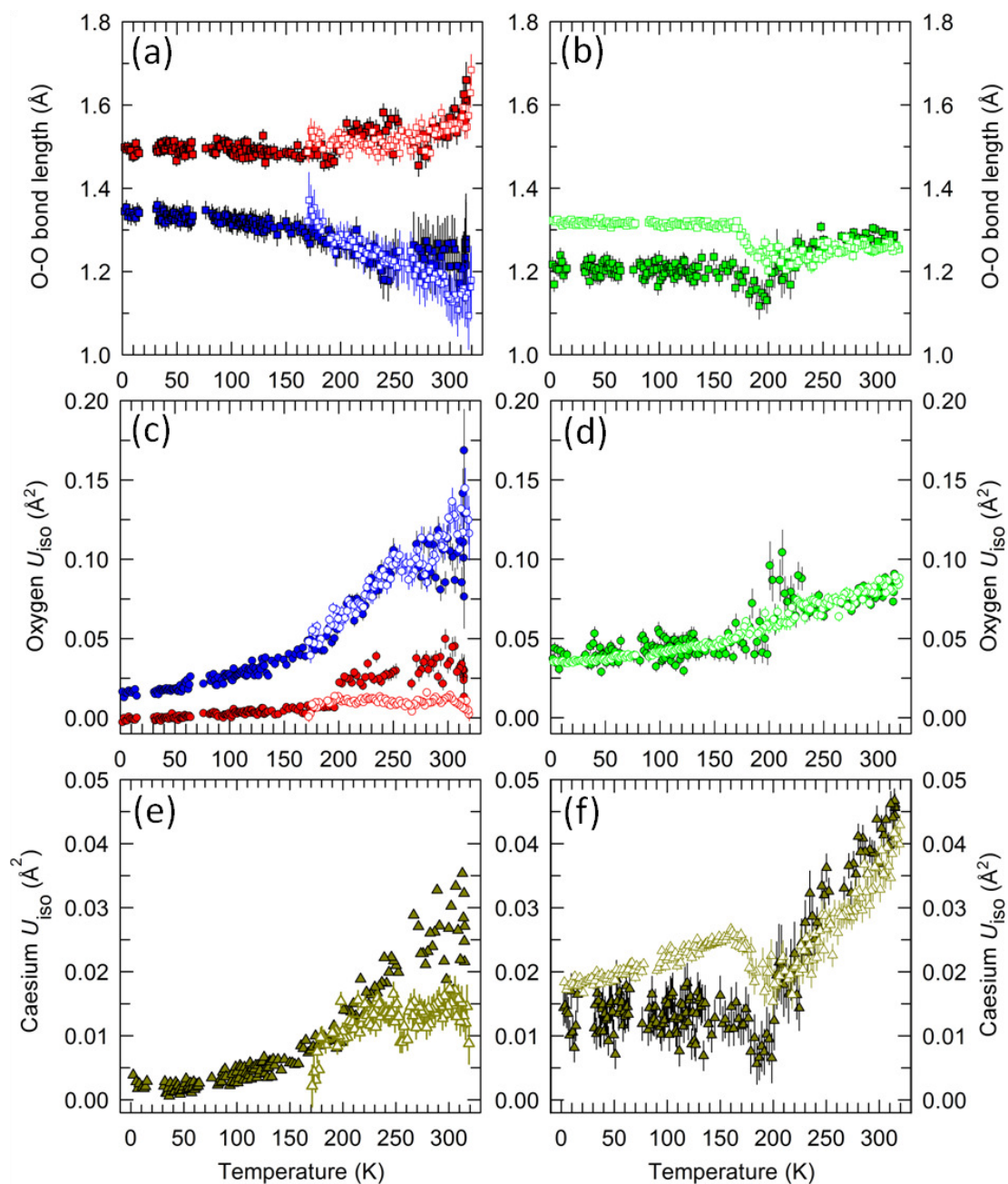
Figure 5.20 (a): Temperature response of the O–O bond lengths in tetragonal, and (b): in cubic Cs_4O_6. (c): Temperature response of U_{iso} for oxygen in tetragonal, and (d): in cubic Cs_4O_6. (e): Temperature response of U_{iso} for caesium in tetragonal, and (f): in cubic Cs_4O_6. Symbol and colour code: Solid and open symbols represent the data collected on warming after ultra-slow and rapid cooling, respectively. The red, blue, green and dark yellow colours represent the data for O_2^{2-}, O_2^{-}, $(O–O)^{(4/3)-}$ and Cs, respectively.

5.2.6 Discussion

A phase transition can be driven by many parameters, *i.e.* temperature, pressure, X-ray illumination, chemical composition, magnetic or electric field. Here in this section we used temperature as the driving force of the cubic-to-tetragonal phase transition. According to the kinetic classification of phase transitions, there are two distinct types: rapid or non-quenchable, and sluggish or quenchable transitions. Rapid transitions are fast and 'instantly' reversible. Conversely, sluggish phase transitions are sufficiently slow that the high temperature (or high pressure) phase can be 'quenched' or preserved as a metastable state at ambient conditions, and are not instantly reversible [231]. These transitions generally show large hysteresis caused by slow kinetics. From a structural point of view, phase transitions are divided into two main groups: displacive and reconstructive transitions. Displacive phase transitions are fast and barrierless; on the other hand, reconstructive ones are sluggish and slow due to some intermediate transitional changes [231], [232].

The cubic-to-tetragonal phase transition in Cs_4O_6 is extremely sluggish, the reverse transition is slow, there is phase co-existence and the transition is characterised by large hysteresis; therefore, the transition could be classified as first-order structural phase transition. It is a reconstructive transition as the volumes of the two phases are different at any given temperature and there are atomic rearrangements – 2/3 of the dioxygen units reorient to lie nearly along the *c*-axis. Buergers' definition of reconstructive phase transitions is: '*structures are so different that the only way a transformation can be effected is by disintegrating one structure into small units and constructing a new edifice from the units*' [233]. Such transitions are of first-order and expressed as sluggish as the material should traverse the intermediate state of a higher energy [232]. Indeed, the examination of the temperature response of the structure of Cs_4O_6 at ambient pressure implies the occurrence of intermediate changes.

In the present case, the only way to build up a tetragonal $I\bar{4}2d$ cell is the rearrangement of the oxygen dumbbells, otherwise no valence ordering is observed. Apparently, during the rearrangement of the oxygen dumbbells, the crystal is most likely broken into fragments, passing through the intermediate

state of a higher energy; therefore, this tetragonal-to-cubic conversion has showed a non-monotonic behaviour with changes in temperature, accompanied by different conversion rates upon warming above 170 K. The intermediate changes occurring in Cs_4O_6 due to the first-order nature of the cooperative phase transition have led to a competition between the electronic states of Cs_4O_6 upon warming above 170 K. These states shuttle between a higher and the most energetic state (Figure 5.21 (c) and (d)), leading to a slow highly hysteretic tetragonal-to-cubic phase transition. Almost all different types of phase transition mechanisms assume a cooperative structural rearrangement, and this cooperative interaction between the two phases creates an energy barrier. Once the thermal energy is close enough to the crossover energy between the metastable cubic and tetragonal phases, this barrier in the potential energy gradually disappears and eventually the high-temperature cubic phase returns to its ground state at 320 K.
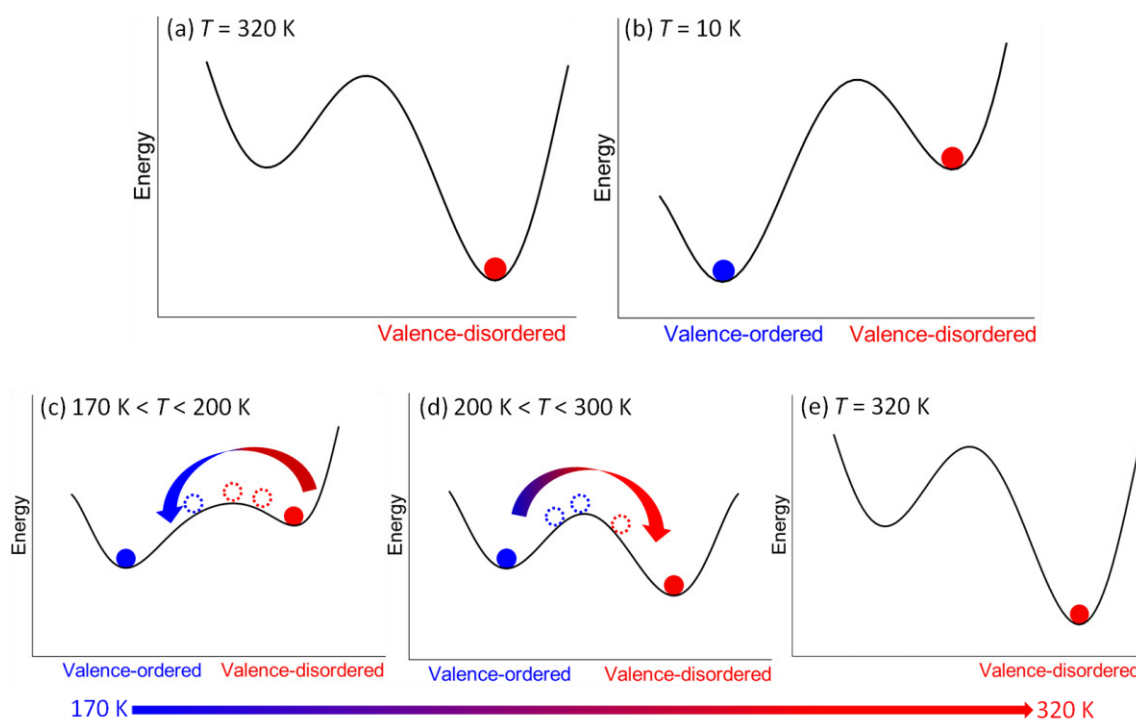
Figure 5.21 Schematic free-energy curves and arrows depict the direction of the temperature-induced transformation between the two metastable phases of Cs_4O_6.

These anomalies coincide well with those temperatures at which the temperature dependence of the molar magnetic susceptibility, $\chi_m(T)$, of Cs_4O_6 measured on warming after rapid cooling displayed some pronounced anomalies (*i.e.* between 200 and 250 K and at 320 K) [106]. Moreover, whilst between 350

and 200 K, the $\chi_m^{-1}(T)$ followed a Curie-Weiss behaviour, below 200 K, the $\chi_m^{-1}(T)$ deviated from linearity [106]. We have also found that 200 K is a critical temperature; the low-temperature tetragonal phase exists as a superheated phase and reaches its maximum weight fraction – 72.0(4) and 82.5(4) wt.% for the rapid and ultra-slow cooling protocols, respectively.

Examination of the torsion angles between the O_2^- and O_2^{2-} anions allowed us to track the evolution of the orientations of the O_2^- anions with temperature. We have found a non-monotonic response at temperatures between 200 and 300 K, (Figure 5.19) coinciding well with those temperatures at which some anomalies are observed in the temperature responses of the phase fractions (Figure 5.17) and of the magnetic susceptibility, as reported in ref. [106]. Because magnetic exchange interactions sensitively depend on molecular geometry, the orientation of the magnetically active O_2^- anions should sensitively affect the magnetism too.

5.2.7 Summary of temperature-induced valence disorder-order transition

The experimental data have shown that Cs_4O_6 at 320 K is isostructural to Rb_4O_6, crystallising in a disordered structure with cubic space group $I\bar{4}3d$. This high-temperature valence-disordered cubic structure transforms to a tetragonal structure (space group $I\bar{4}2d$) by ultra-slow-cooling to liquid helium temperatures. This symmetry-lowering structural transition is accompanied by a valency transition. In tetragonal $I\bar{4}2d$ unit cell, splitting of the oxygen atoms leads to the differentiation between the O_2^- and O_2^{2-} anions and hence to valence ordering. On the other hand, rapid cooling *via* deep quenching suppressed the emergence of the low temperature phase with the cubic phase surviving down to liquid helium temperatures, reveals that the high-temperature cubic phase is quenchable.

The evolution of the diffraction profiles with temperature has revealed the occurrence of extremely sluggish cubic-to-tetragonal phase transitions in Cs_4O_6. First-order nature of the transition between the two phases has been confirmed by phase-coexistence and large thermal hysteresis in the course of the sluggish reconstructive-type conversion. Because the two competing structures differ in the orientations of the dioxygen groups and that orientational ordering of the O_2^- units is coupled to the charge ordering, reorientational behaviour of the O_2^- anions could

play a role in driving the observed sluggish phase transition. Apparently, due to the anomalously large thermal displacement parameters of the O_2^- anions, which are tilted with respect to the tetragonal c axis, large amplitude reorientations of the O_2^- anions are evident above 170 K. The examination of the temperature variation of the torsion angles and phase fractions has demonstrated that there might be a correlation between the orientational ordering of the O_2^- anions and valence order-disorder phase transition.

The temperature evolution of the lattice parameters and unit cell volume of the two phases has revealed that the cubic phase has a larger volume than the tetragonal phase which anisotropically expands while transforming back to the cubic symmetry on heating.

5.3 Temperature- and X-ray illumination-induced valence order-disorder transitions

In the following sections, structural characterisation with synchrotron XRPD, employing Rietveld analysis, is described for Cs_4O_6 at room temperature and at 10 K. Firstly, a summary of experimental procedures is provided.

5.3.1 Experimental procedures

High-resolution synchrotron XRPD data were collected with the multidetector diffractometer on beamline ID31 at the ESRF. The overall setup was outlined in Section 2.5.1. A different batch of the sample from that used for the neutron tof diffraction studies was used for the XRPD data collections. The sample was sealed under ~300 mbar He in 6 different 0.5-mm diameter special glass capillaries for experiments at ambient and variable temperature. Different capillaries of the same sample were used for data collection at different temperatures after applying different cooling protocols.

An X-ray wavelength of $\lambda = 0.39996(4)$ Å ($E = 31$ keV) was used, and the horizontal beamwidth was set to ~1 mm to minimise the area of each capillary exposed to the X-ray beam. The position of the capillary was moved horizontally by ~2 mm for each collected dataset to minimise sample changes due to X-ray illumination. During the translation of the capillary, the radiation shutter was kept closed, to monitor the exposure time for each scan. Different numbers of scans were collected, over different angular ranges of 2θ and with the detector arm moving at 10°/min, depending on the data collection temperature, the applied cooling protocol and the degree of X-ray illumination-induced changes. Datasets were binned with a step size of 0.002° in 2θ. In the following sections, information on the experimental methods that were employed at different temperatures and cooling protocols are given, together with the structural results.

5.3.2 Cs_4O_6 at ambient temperature

Fourteen scans from 14 different positions of the same capillary were collected over an angular range of $2\theta = 0-20°$ at ambient temperature, with a 2 minute exposure time for each scan (with the detector arm moving at 10°/min),

using a capillary designated as number 6. These fourteen XRPD profiles of Cs_4O_6 are shown in Figure 5.22.
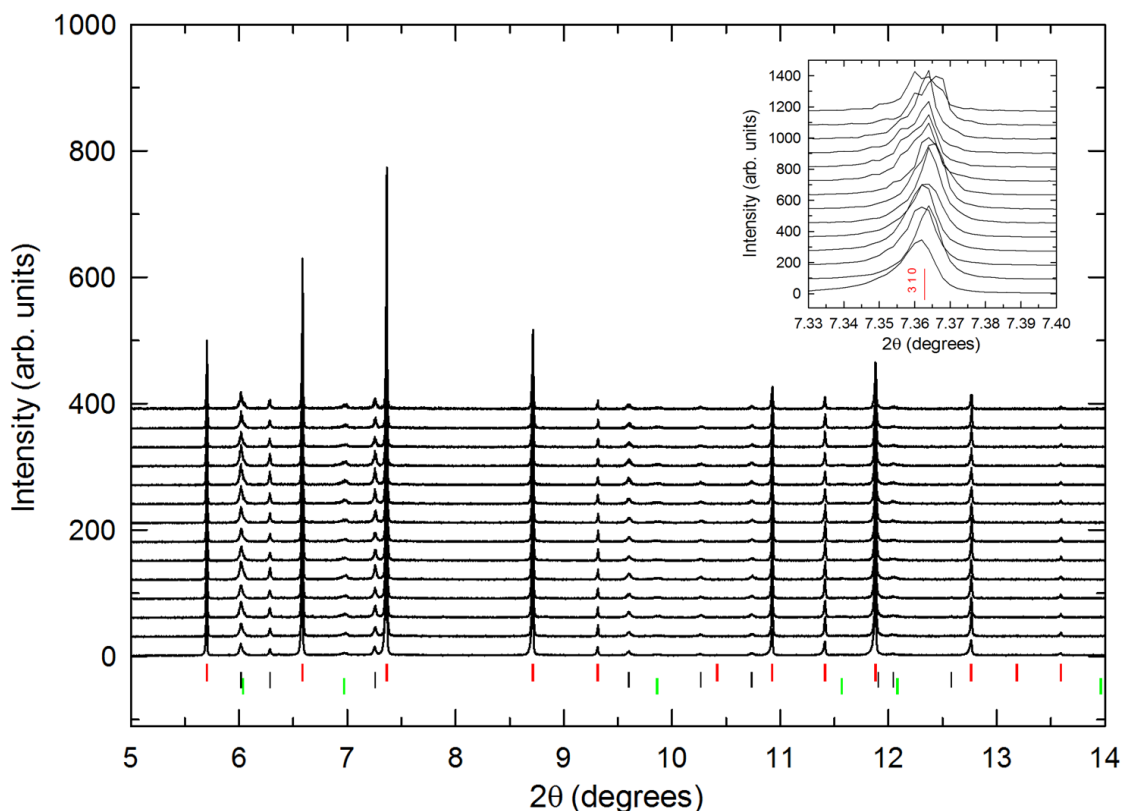
Figure 5.22 XRPD profiles of Cs_4O_6 collected from fourteen different positions of the same capillary at ambient temperature. Each single profile was collected with a 2 minute illumination time. Intensities are offset for clarity. The red, black and green tickmarks represent the cubic Cs_4O_6, cubic CsO_2 and tetragonal CsO_2 phases, respectively. The inset shows an expanded view focusing on the cubic (310) Bragg peak ($\lambda = 0.39996(4)$ Å).

Visual examination of the XRPD profiles of Cs_4O_6 at ambient temperature confirms that the majority phase can be indexed by a cubic space group, $I\bar{4}3d$. Two impurity phases were also detected: cubic CsO_2 (space group $Fm\bar{3}m$) and tetragonal CsO_2 (space group $I4/mmm$). The inset in Figure 5.22 focusing on the cubic (310) peak demonstrates that even though the position of the capillary was moved horizontally by ~ 2 mm for each collected profile, X-ray illumination-induced changes are still occuring. Therefore, to extract details in smaller time intervals, for the first profile which was illuminated by X-ray light for 120 s, the nine sub-profiles collected by the nine individual detectors (D0 to D8) of the diffractometer were examined (Figure 5.23). Due to sensitivity issues with detector 5, this was excluded in the subsequent treatment and analysis of the data.
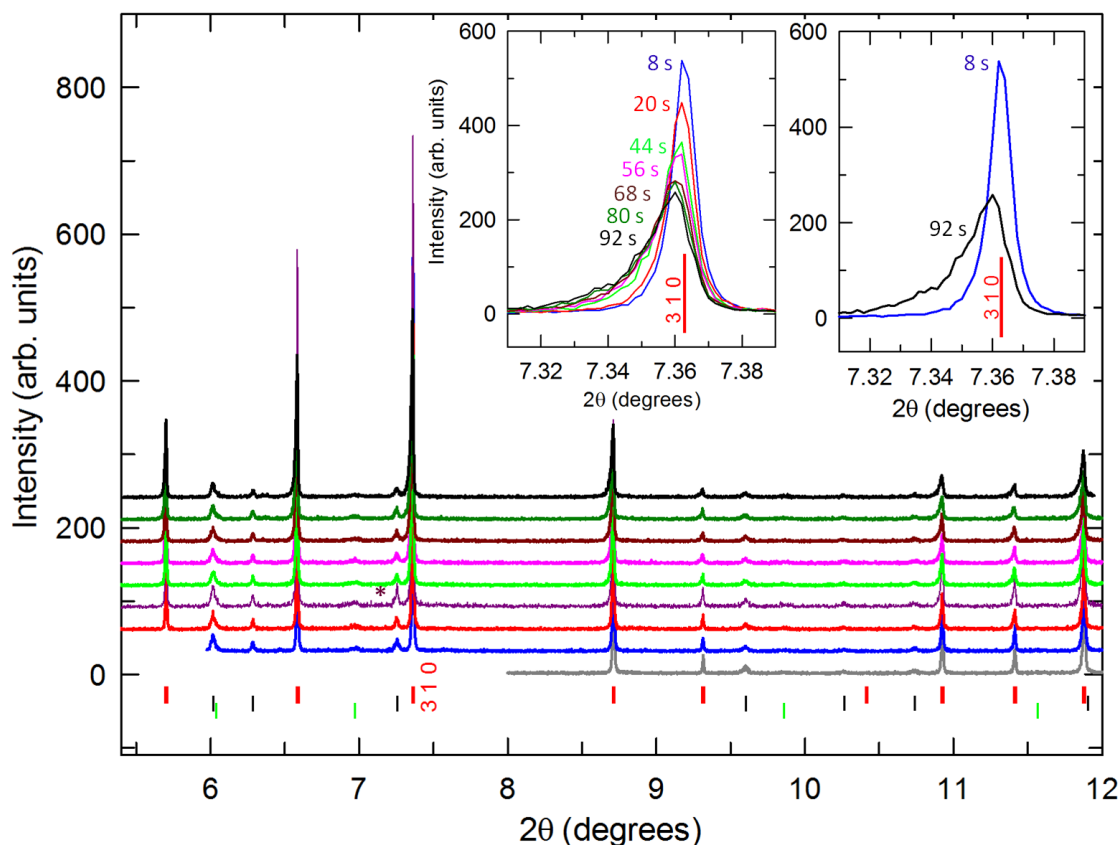
Figure 5.23 XRPD profiles of Cs_4O_6 collected by each individual detector (from bottom to top: D8, 7, 6, 5, 4, 3, 2, 1 and 0, respectively) at the same position of capillary at ambient temperature. Intensities are offset for clarity. The red, black and green tickmarks represent the cubic Cs_4O_6, cubic CsO_2 and tetragonal CsO_2 phases, respectively. The asterisk labels the pattern collected at D5 that was subsequently excluded from further analysis. Insets show the evolution of the cubic (310) Bragg peak ($\lambda = 0.39996(4)$ Å) with X-ray illumination time.

The insets in Figure 5.23 focusing on the cubic (310) peak demonstrate that the valence disordered phase of Cs_4O_6 is extremely sensitive to illumination by X-rays, as it is evident from peak broadening and shifts to lower angles. For a quantitative examination, the full-width-at-half-maximum (FWHM) and d-spacing of the cubic (310) reflection from each profile were extracted in the angular range between 7.32° and 7.38°. The angular region of $2\theta \leq 7.38°$ was fully covered by detectors D7 to D0 (Table 5.6). As the detector arm moves 1°/6 s and the angular difference of detectors are 2°, the angular region: $2\theta \leq 7.38°$ was illuminated for 92 s over the whole experiment.

Table 5.6 2θ positions of individual detectors at a given time within a 120 s illumination time of a single scan.

	Time (s)	0	12	24	36	48	60	72	84	96	108	120
	D0	-8	-6	-4	-2	0	2	4	6	8	10	12
	D1	-6	-4	-2	0	2	4	6	8	10	12	14
	D2	-4	-2	0	2	4	6	8	10	12	14	16
	D3	-2	0	2	4	6	8	10	12	14	16	18
$2\theta(°)$	D4	0	2	4	6	8	10	12	14	16	18	20
	D5	2	4	6	8	10	12	14	16	18	20	22
	D6	4	6	8	10	12	14	16	18	20	22	24
	D7	6	8	10	12	14	16	18	20	22	24	26
	D8	8	10	12	14	16	18	20	22	24	26	28

Even a brief 92 s illumination by X-ray light leads to significant broadening and shift of the cubic (310) peak (Figure 5.24).
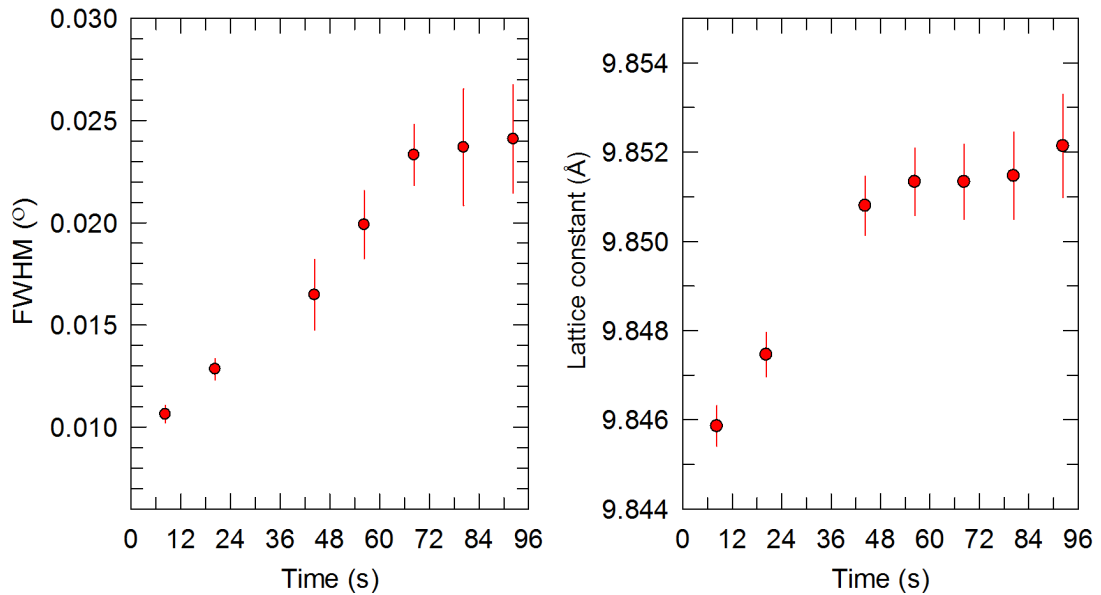
Figure 5.24 Left panel: The variation of the full-width-at-half-maximum (FWHM) for the (310) reflection of cubic Cs_4O_6 with X-ray illumination time. Right panel: Evolution with increasing X-ray illumination time of the lattice constant of cubic Cs_4O_6.

Although the structure remains cubic upon increasing illumination time, the Bragg reflections of the cubic phase broaden and shift to lower angles (lattice expansion). The observed peak broadening can occur in the presence of a distribution of lattice parameters: this in turn corresponds to the presence of inhomogeneous strain. Absorption of X-ray photons can produce photo-excited domains of different sizes embedded in the already existing parent cubic phase. This process can occur locally and give rise to inhomogeneous strain, and can be thought of as a phase segregation process through the formation of photo-converted domains with a

213

local structure different from that of the average bulk cubic structure. The observed lattice expansion in early times of illumination could be tentatively attributed to thermal effects induced by the X-ray light.

5.3.3 Rapid cooling of Cs_4O_6

Rapid cooling of the sample (capillary number 4) was achieved by introducing the capillary in a continuous-flow He cryostat directly at 100 K. This was followed by cooling to 10 K within 30 min. The procedure for the collection of XRPD profiles is given in Table 5.7. Due to experimental issues associated with data collection for scans 2, 3, 8, 9 and 10, corresponding data were not included in the following analysis.

Table 5.7 Data collection procedure for the sample rapidly cooled to 10 K (capillary no: 4).

scan #	Angular range (°)	Position (POS)	Exposure time
1	0-10	POS-1	60 s per scan
4 to 7	0-10	POS-1	60 s per scan
11 to 12	5-25	POS-2	120 s per scan
13 to 14	5-25	POS-3	120 s per scan

Visual examination of the XRPD profiles collected at POS-1, POS-2 and POS-3 after rapid cooling to 10 K revealed that the high-symmetry cubic Cs_4O_6 is retained, and no reflections of any impurity phase are present (Figure 5.25). The inset in Figure 5.25 shows the evolution of the cubic (310) peak with X-ray illumination time and demonstrates that the cubic phase is still sensitive to the X-ray light at 10 K, as peak broadenings and shifts to lower angles are still present. For scans collected at POS-1, the angular range of $2\theta \leq 7.46°$ was covered by detectors 7, 6, 5, 4 and 3, and for scans collected at POS-2 and POS-3, this angular region was covered by detectors 4, 3, 2, 1 and 0. Therefore cumulative illumination times for this angular region are 297 s at POS-1, and 183 s at POS-2 and POS-3, respectively.
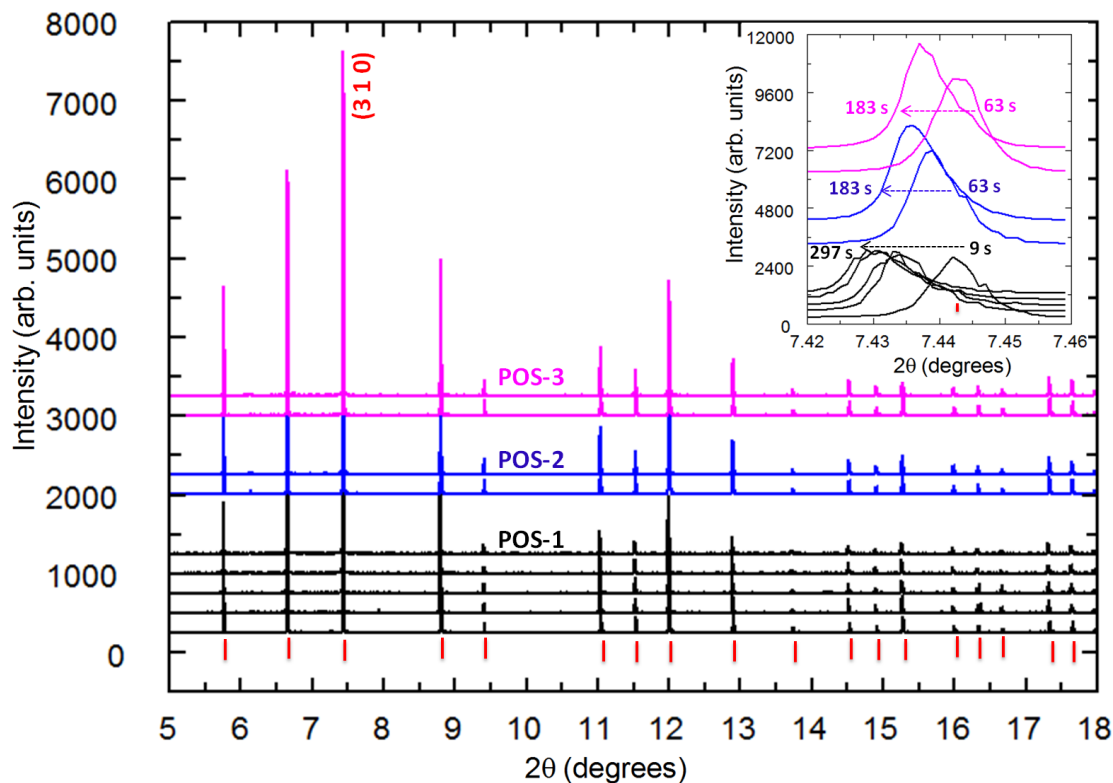
Figure 5.25 XRPD profiles collected at different positions of the capillary: POS-1, POS-2 and POS-3 (see table Table 5.7 for details) after rapid cooling to 10 K. Red tickmarks represent the reflection positions of cubic Cs_4O_6 ($\lambda = 0.39996(4)$ Å). Inset shows the evolution of the (310) reflection of cubic Cs_4O_6 with X-ray illumination at POS-1, POS-2 and POS-3. Intensities are offset for clarity.

We have also examined the individual profiles collected with each individual detector for scans 1, 4, 5, 6 and 7. For a 60 s exposure time, 6 sub-profiles, which were collected with detectors D8, 7, 6, 5, 4 and 3 are shown in Figure 5.26. Indeed, X-ray illumination-induced effects were clearly apparent at 10 K but the observed changes in the profiles - peak broadening and shifts to lower angles – were not as pronounced as at room temperature (Figure 5.27). Examination of the FWHM values and the lattice parameters of the cubic phase both at room temperature and at 10 K after fast cooling reveals that the effect of the X-ray beam is significantly reduced at low temperatures.
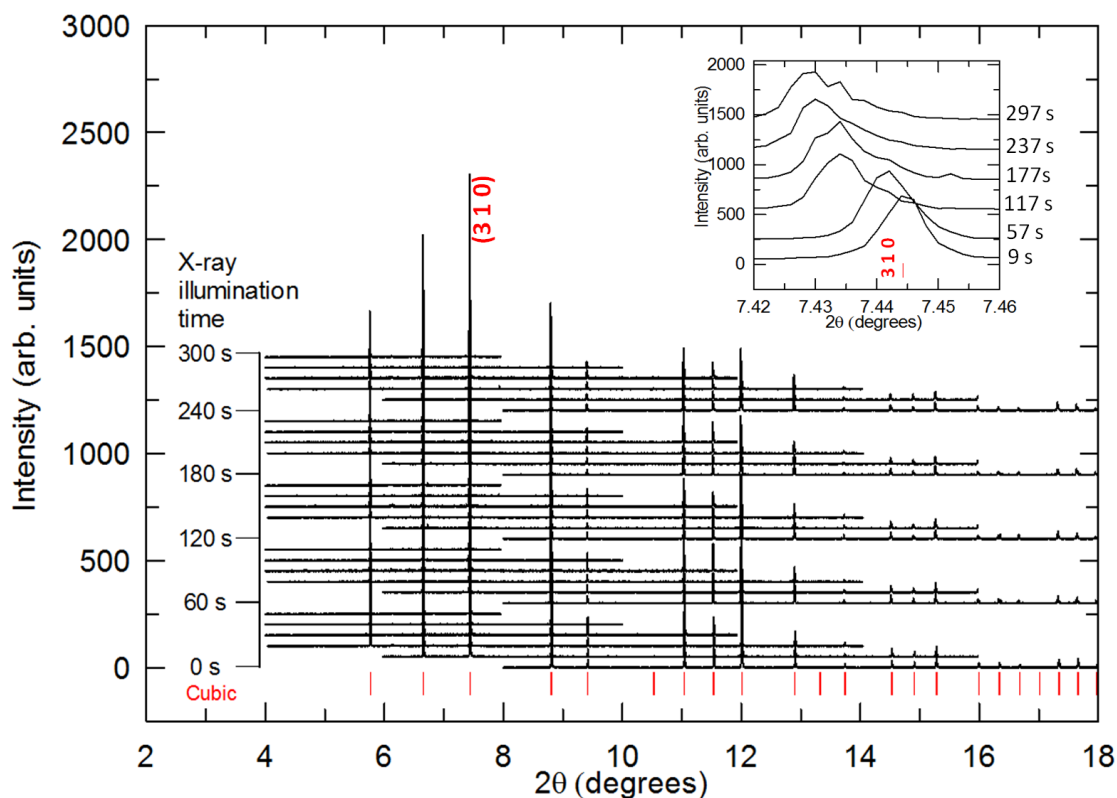
Figure 5.26 XRPD profiles of Cs_4O_6 collected at POS-1 with individual detectors after rapid cooling to 10 K. Profiles from bottom to top for each set of scans are collected with detectors 8, 7, 6, 5, 4 and 3, respectively. Inset shows the evolution of the (310) reflection of cubic Cs_4O_6 with X-ray illumination time over an angular range of $2\theta \leq 7.46°$. Red tickmarks represent the reflection positions of cubic Cs_4O_6 ($\lambda = 0.39996(4)$ Å). Intensities are offset for clarity.
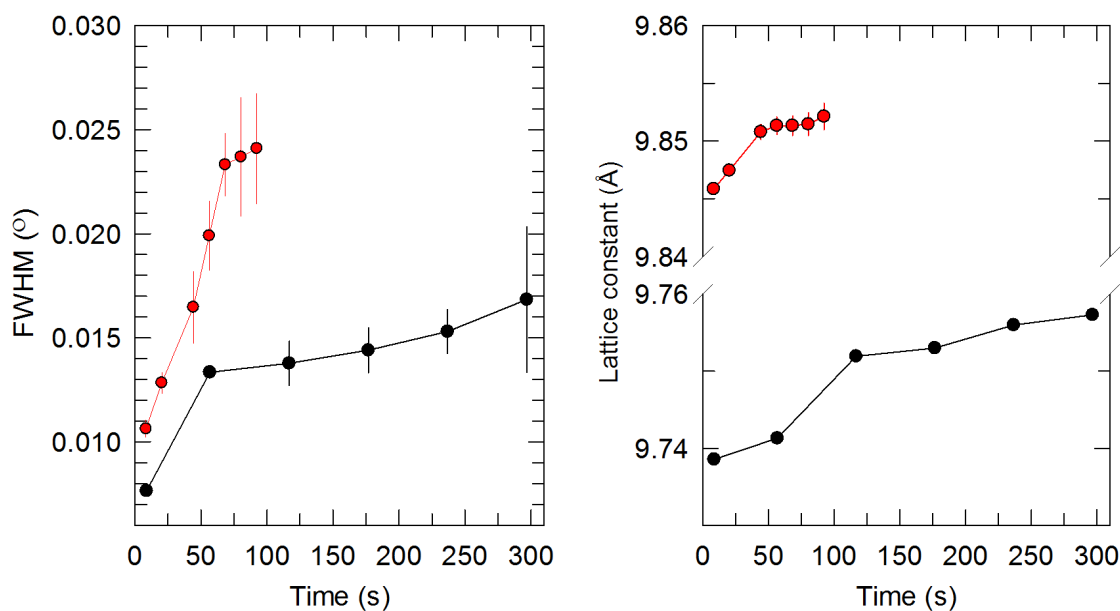
Figure 5.27 Left panel: Variation of the FWHM of the (310) reflection of cubic Cs_4O_6 with X-ray illumination time at room temperature (red circles) and at 10 K after rapid cooling (black circles). Right panel: Time evolution of the lattice constant of cubic Cs_4O_6 at room temperature (red circles) and at 10 K after fast cooling (black circles).

216

5.3.4 Slow cooling of Cs_4O_6

Slow cooling of the Cs_4O_6 sample (capillary number 2) was achieved by initial cooling to 180 K, followed by a 4-h dwelling period at this temperature in order to maximize the cubic-to-tetragonal structural transformation. This was then followed by cooling to 10 K within a 30-min period. A partial transformation from cubic to tetragonal Cs_4O_6 was observed after this procedure, as expected. To search for the existence of X-ray illumination-induced changes on the tetragonal phase, eight scans were collected at each of three different positions of the capillary, POS-1, POS-2 and POS-3 (~ 2 mm distance between each POS), over an angular range of $2\theta = 5$–$20°$, with a 90 s illumination time for each scan. The data collection protocol is summarized in Table 5.8.

Table 5.8 Data collection procedure for the sample slowly cooled to 10 K (capillary no: 2).

scan #	Angular range (°)	Position (POS)	Illumination time (s)
12 to 19	5-20	POS-1	90 s per scan
21 to 28	5-20	POS-2	90 s per scan
29 to 36	5-20	POS-3	90 s per scan

In order to improve the statistics of datasets collected with individual detectors, scans collected at different positions (POS-1, 2 and 3) along the capillary at the same illumination time were summed together (Table 5.9).

Table 5.9 Summing details of different scans collected at different positions along the Cs_4O_6 capillary at 10 K after slow cooling.

Sum of scan	comment
12, 21, 29	1st set of scans at each POS, designated as scan A
13, 22, 30	2nd set of scans at each POS, designated as scan B
14, 23, 31	3rd set of scans at each POS, designated as scan C
15, 24, 32	4th set of scans at each POS, designated as scan D

The time evolution of the XRPD profiles (Figure 5.28) collected after slow cooling to 10 K was investigated by examining the individual profiles collected with each detector of the triply-summed scans (summing details given in Table 5.9). An immediate feature of the datasets collected at 10 K with increasing exposure time is that X-ray illumination leads to an extremely fast transformation from tetragonal to cubic Cs_4O_6.
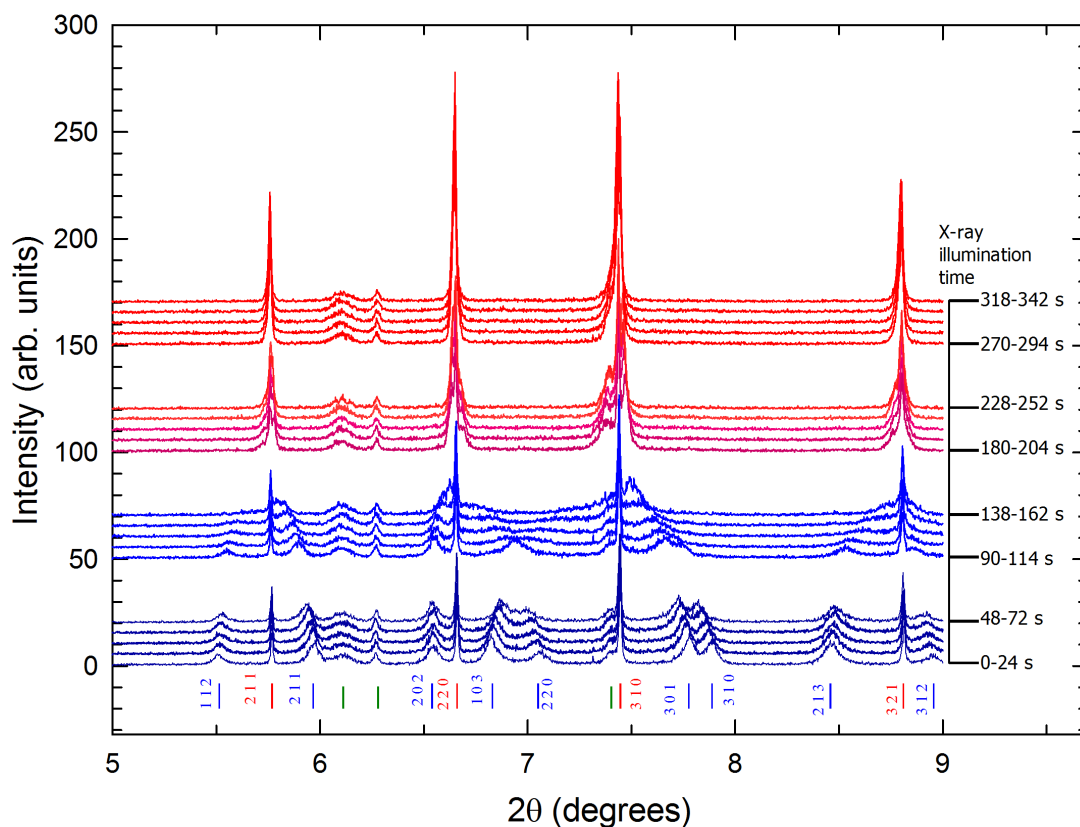
Figure 5.28 Time evolution of XRPD profiles collected after slow cooling to 10 K. Red, blue and green tickmarks represent the reflection positions of cubic and tetragonal Cs_4O_6, and the impurity tetragonal CsO_2 phase, respectively (λ = 0.39996(4) Å). Individual profiles are offset for clarity. The five XRPD profiles from bottom to top in the four set of scans are collected with D4, D3, D2, D1 and D0, respectively.

Rietveld analysis of the diffraction profiles was then undertaken. Only the first 4 scans collected from different positions of the capillary were included in the analysis as the following XRPD profiles were only indexed with cubic Cs_4O_6 and impurity CsO_2, and also due to the significant broadenings and shifts of the cubic Bragg peaks, Rietveld refinements could not proceed smoothly. The angular region: 2θ = 5°–9°, where the most intense tetragonal peaks appear (Figure 5.28), was included in the refinements. This region is fully covered by detectors 0, 1, 2, 3, and 4 (Table 5.10).

Table 5.10 2θ positions of individual detectors in the angular range of 2θ = 5°–9°, with corresponding illumination times.

	Time (s)	0	6	12	18	24	30	36	42	48	54	60	66	72
2θ(°)	D0	-3	-2	-1	0	1	2	3	4	5	6	7	8	9
	D1	-1	0	1	2	3	4	5	6	7	8	9	10	11
	D2	1	2	3	4	5	6	7	8	9	10	11	12	13
	D3	3	4	5	6	7	8	9	10	11	2	13	14	15
	D4	5	6	7	8	9	10	11	12	13	14	15	16	17

Table 5.11 X-ray illumination time ranges for individual scans and profiles collected by individual detectors (*i.e.* D4-profile) over an angular range of 2θ = 5°–9° at 10 K after slow cooling. The scans were collected from different positions of the capillary.

	t (s) for scan A	t (s) for scan B	t (s) for scan C	t (s) for scan D
D4-profile	0-24	90-114	180-204	270-294
D3-profile	12-36	102-126	192-216	282-306
D2-profile	24-48	114-138	204-228	294-318
D1-profile	36-60	126-150	216-240	306-330
D0-profile	48-72	138-162	228-252	318-342

We now move to the details of Rietveld analysis. Three crystallographic phases were included in the model: cubic (space group $I\bar{4}3d$) and tetragonal (space group $I\bar{4}2d$) Cs_4O_6 as major phases and a minority tetragonal CsO_2 ($I4/mmm$) phase. A pseudo-Voigt profile function was used (continuous wavelength profile function '3' in GSAS); profile shape coefficients GU, GV, GW, LX and LY were allowed to refine for the major phases. Low-angle peak asymmetry from axial divergence was modelled with coefficients $S/L = 0.00154$, $H/L = 0.00077$ [173]. A Chebyschev polynomial function (~20 terms) was used to fit the background. Consecutive cycles of improving profile shape coefficients with intermediate refinements of zero point and background were applied. The lattice parameters and scale factors of the crystallographic phases were also refined. The anomalous contributions to the X-ray form factors of oxygen (in e/atom): $f' = -0.002$, $f'' = 0.002$ and of caesium: $f' = -1.921$, $f'' = 0.758$ were included [174]. A cylindrical absorption correction, $\mu r/\lambda = 1.025$, was applied (linear absorption correction, $\mu = 16.44$ cm^{-1}).

Thermal displacement parameters for all atoms in the majority phases were modelled as isotropic and refined. As X-rays do not allow accurate refinement of the positions for light elements, the O–O bond lengths were restrained at the following values: O–O = 1.31 Å for cubic Cs_4O_6, and O1–O1 = 1.53 Å (indicating the bond distance in O_2^{2-}) and O2–O2 = 1.35 Å (indicating the bond distance in O_2^-) for tetragonal Cs_4O_6, as determined by the neutron tof diffraction studies at 10 K after rapid cooling and ultra-slow cooling, respectively. The fractional atomic coordinates of caesium and oxygen were allowed to refine using a 0.005 tolerance and a weight of 10 on the bond length restraints. The occupancies of the Cs and O in both major phases were kept at 1. Representative Rietveld fits of the 10 K XRPD

data collected within X-ray illumination times of 0-24 s, 138-162 s and 318-342 s and corresponding structural parameters obtained from the Rietveld analysis are shown in Figure 5.29 and Table 5.12, respectively.
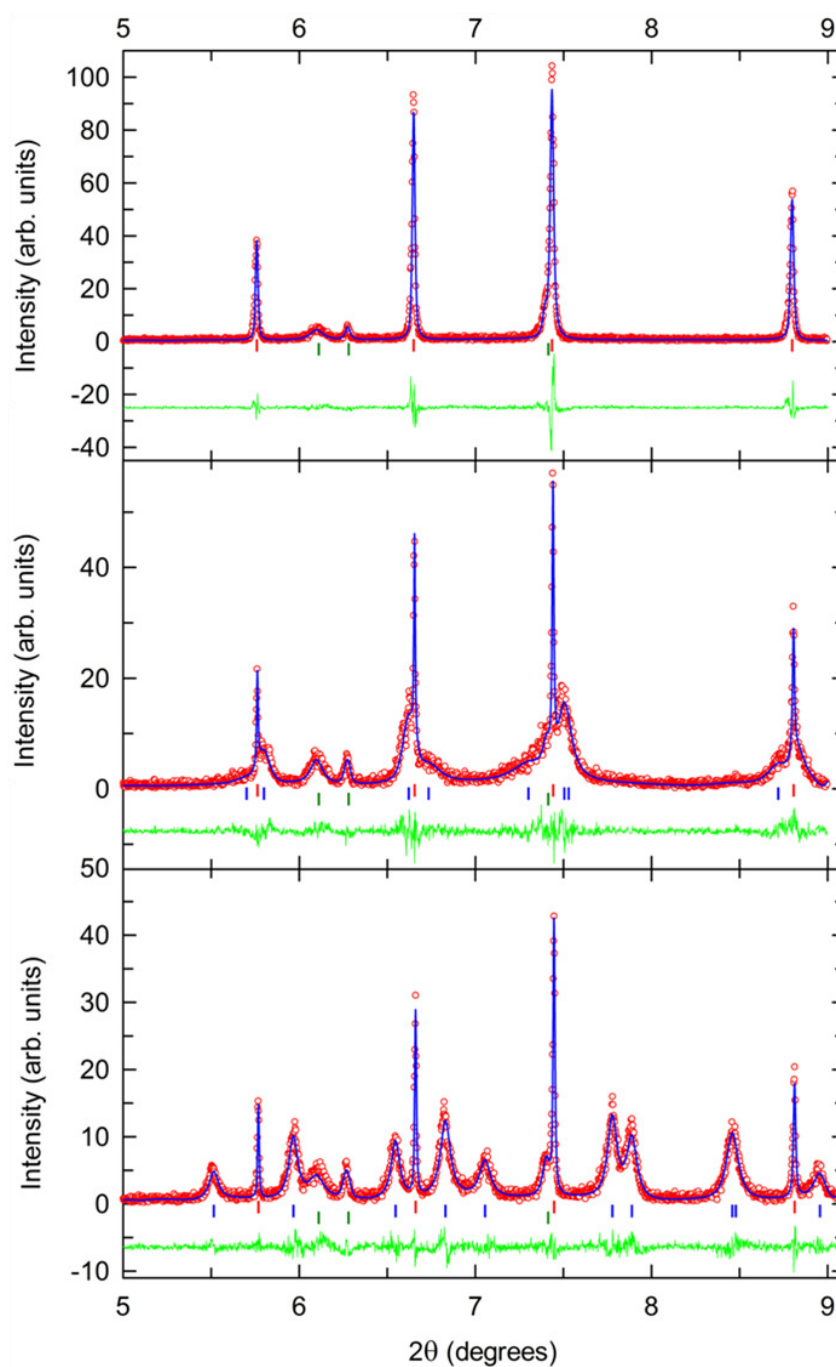
Figure 5.29 Rietveld refinements of the synchrotron XRPD data of Cs_4O_6 collected at 10 K after slow cooling (λ = 0.39996(4) Å). Red circles, blue lines and green lines represent the observed, calculated and difference profiles, respectively. From bottom to top data were collected within X-ray illumination times of 0-24 s, 138-162 s and 318-342 s, respectively. The red, blue and green tickmarks show the reflection positions of the cubic and tetragonal Cs_4O_6 and the impurity CsO_2 phases, respectively.

Table 5.12 Refined structural parameters for the cubic and tetragonal Cs_4O_6 phases from the Rietveld fits to XRPD data collected at 10 K after slow cooling and within X-ray illumination times of 0-24 s (R_{wp} = 19.2%, R_{exp} = 17.6%), 138-162 s (R_{wp} = 20.5%, R_{exp} = 18.3%) and 318-342 s (R_{wp} = 22.8%, R_{exp} = 18.8%). Values in parentheses are estimated errors from the least-squares fitting. Fractions of co-existing impurity CsO_2 ($Fm\bar{3}m$) phase within X-ray illumination times of 0-24 s, 138-162 s and 318-342 s are found as 12.3(2), 12.7(2) and 11.6(3)%, respectively.

Time (s)	0-24		138-162		318-342
Symmetry Space group (wt. %)	Cubic $I\bar{4}3d$ (16.7(2))	Tetragonal $I\bar{4}2d$ (71.83(2))	Cubic $I\bar{4}3d$ (20.6(2))	Tetragonal $I\bar{4}2d$ (62.9(2))	Cubic $I\bar{4}3d$ (88.55(7))
a (Å)	9.7451(1)	9.2002(6)	9.7456(1)	9.631 (1)	9.7591(1)
c (Å)	-	10.828(1)	-	9.967(3)	-
V (Å³)	925.45(4)	916.5(1)	927.03(4)	925.5(2)	929.46(3)
Cs Wyckoff site	16c	16e	16c	16e	16c
Cs x/a	0.9460(4)	0.302(1)	0.9457(6)	0.296(1)	0.9469(2)
Cs y/b	-	0.051(1)	-	0.053(1)	-
Cs z/c	-	0.046(1)	-	0.040(2)	-
Cs U_{iso} (Å²)	0.025(3)	0.049(2)	0.025	0.031(3)	0.042(1)
O(1) Wyckoff site	24d	8c	24d	8c	24d
O(1) x/a	0.55778(9)	0	0.55779(9)	0	0.55788(9)
O(1) y/b	0	0	0	0	0
O(1) z/c	0.75	0.06972(8)	0.75	0.07442(9)	0.75
O(2) Wyckoff site	-	16e	-	16e	-
O(2) x/a	-	0.359(9)	-	0.333(6)	-
O(2) y/b	-	0.76(1)	-	0.73(1)	-
O(2) z/c	-	0.187(1)	-	0.190(3)	-

After slow-cooling to 10 K, Cs_4O_6 had partially transformed to the tetragonal phase: at this temperature within 0-24 s exposure to X-ray light, the weight fractions of the cubic and tetragonal Cs_4O_6 phases and of the CsO_2 impurity were 16.7(2), 71.83(2) and 12.3(2)%, respectively. The response of the majority tetragonal Cs_4O_6 phase to continued X-ray illumination is very pronounced. The tetragonal Bragg peaks disappear after ~5 min of illumination – within an X-ray illumination time range of 318-342 s, the phase fractions of the co-existing cubic Cs_4O_6 and impurity CsO_2 are 88.55(7) and 11.6(3)%, respectively.

Examination of Figure 5.30 and Figure 5.31 reveals that there are three regimes in the structural response of tetragonal Cs_4O_6 to X-ray illumination. As seen in Figure 5.31 (a), the tetragonal-to-cubic transformation-time curve adopts a characteristic '*S-shape*'. The first regime manifests itself in the incubation time period, t_0. During t_0, within a ~2 min of illumination, all diffraction peaks associated with the valence-ordered tetragonal phase continuously broaden and anisotropically shift evidencing the occurrence of an anisotropic expansion (Figure 5.31 (c). In contrast, the Bragg reflections of the minority cubic phase are barely affected during this period. These broadenings and shifts could be attributed to the formation of photoexcited valence-disordered domains whose size rapidly grows with X-ray illumination time; however, in this incubation period, there are no indications of the occurrence of a structural transformation involving the bulk of the sample. These X-ray induced effects happening within t_0 can be described as a process of phase segregation through the formation of local valence-disordered domains within the tetragonal phase with a local structure different from that of the average tetragonal structure.

Following this incubation period, in the intermediate regime, the percolation threshold is reached, the fraction and size of the photo-converted valence-disordered domains increase rapidly at the expense of the valence-ordered phase leading to a first-order phase transformation to the bulk cubic phase through the rearrangements of the dioxygen units. In this regime, therefore, the fraction of the cubic phase grows rapidly with time. All these changes are clearly reflected in the time evolution of the diffraction profiles (Figure 5.28 and Figure 5.30): the Bragg reflections of the tetragonal phase begin to merge with those of the cubic and hence diminish in intensity very rapidly while those of the cubic phase grow.
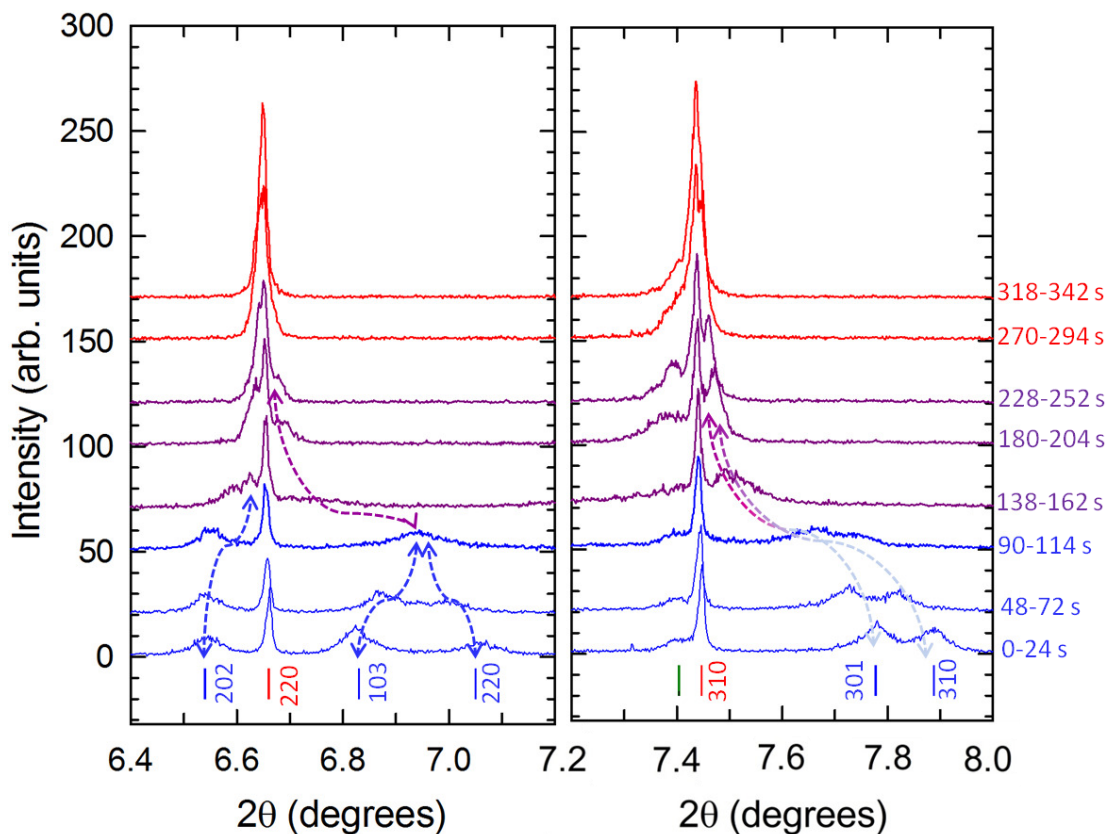
Figure 5.30 Evolution of the tetragonal (202), (103), (220), (301) and (310) Bragg peaks (labelled by their (*hkl*) Miller indices, blue tickmarks) of Cs_4O_6 with X-ray illumination time collected at 10 K after slow cooling. Red tickmarks depict the cubic (220) and (310) Bragg peaks. Diffraction profiles in blue, dark pink and red colour represent the initial regime within the incubation time period where strong peak broadenings are observed, the intermediate regime where the percolation threshold is reached and a phase transformation to the bulk cubic phase sets in, and the final regime where the bulk transformation is essentially complete.

Toward the end of the transformation, the conversion rate is slow and eventually the bulk transformation is essentially complete within an additional ~3 min of X-ray illumination, leaving only cubic Cs_4O_6 together with the impurity CsO_2 (phase fractions within an illumination time of 270-294 s are 88.27(7) and 11.7(2)%, respectively). Upon increasing X-ray illumination time, the tetragonal structure expands (Figure 5.31 (b)) anisotropically with the tetragonal *a* lattice constant increase accompanied by a decrease in *c* (Figure 5.31 (c), (d)).
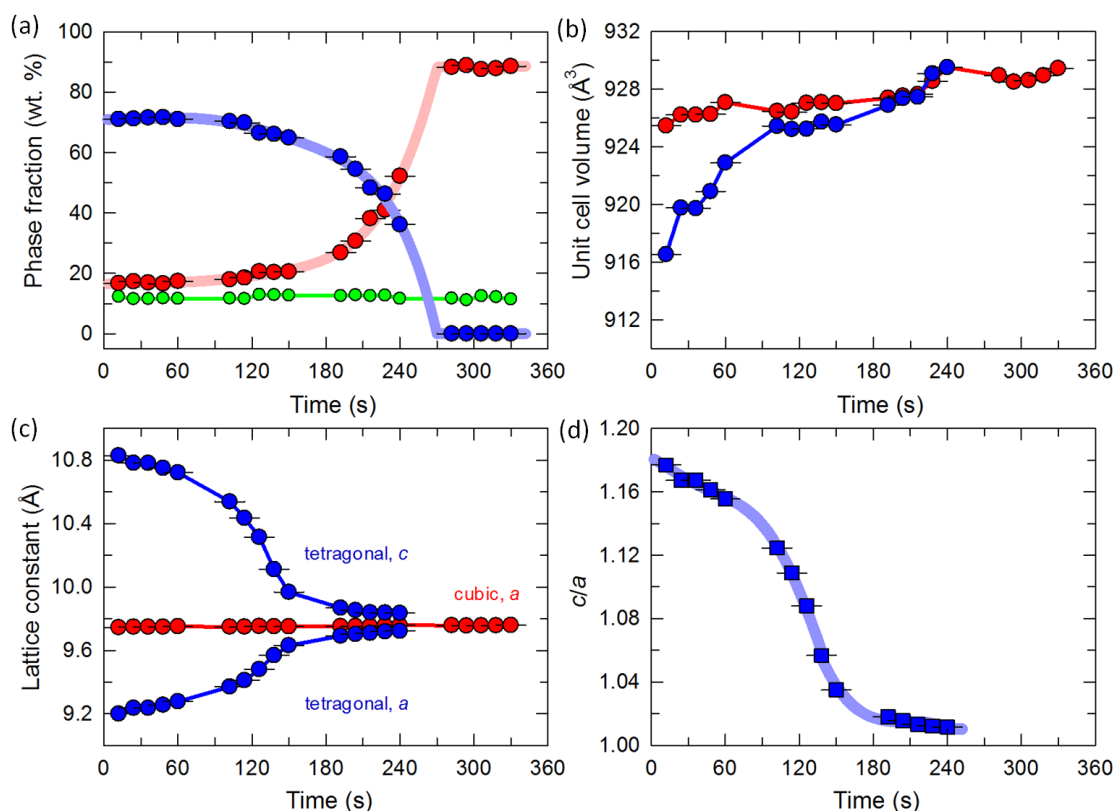
Figure 5.31 Time evolution of the structural parameters extracted from Rietveld analysis of XRPD data collected at 10 K after slow cooling: (a) phase fractions, (b) unit cell volumes and (c) lattice constants of the cubic (red circles) and tetragonal Cs_4O_6 (blue circles) phases, and (d) tetragonal distortion, c/a, in tetragonal Cs_4O_6. Green circles represent the impurity CsO_2 phase. Solid lines are guides to the eye.

In the course of this, in the cubic phase, aside from rapid growth in intensity of the diffraction peaks, very small peak shifts to lower angles are observed. This small lattice expansion was also observed at room temperature and at 10 K after rapid cooling, and attributed to structural rearrangement effects caused by the X-ray light: this was found to be accompanied by pronounced peak broadenings signifying the development of significant structural inhomogeneities. In sharp contrast, this time, pronounced broadenings of the cubic peaks are not observed. Figure 5.32 shows the time evolution of the isolated cubic (321) Bragg peak. In the presence of the tetragonal phase (majority phase), the cubic peaks are hardly affected by the X-ray light as essentially there is no change in the peak linewidths with illumination time within error (Figure 5.33) consistent with a photo-induced phase transition in the bulk.
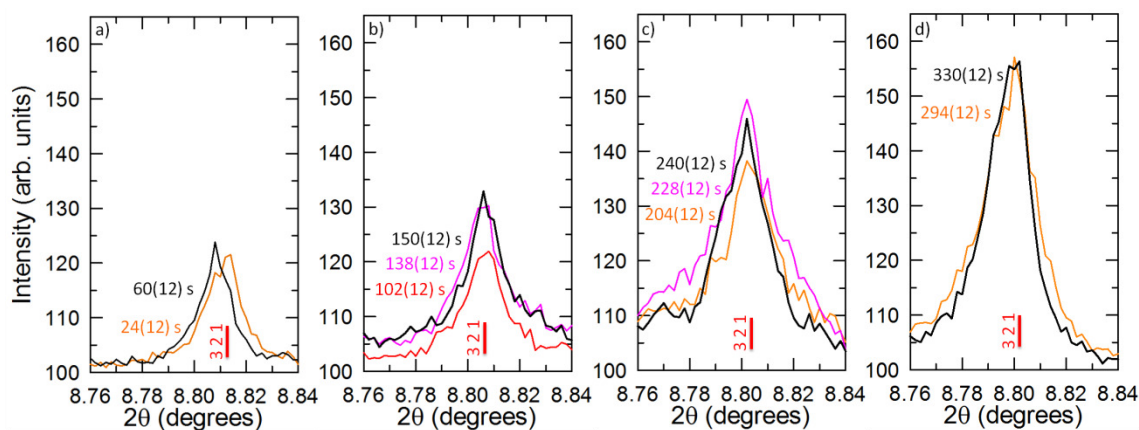
Figure 5.32 Evolution of the cubic (321) Bragg peak of Cs_4O_6 with X-ray illumination time at 10 K after slow cooling.
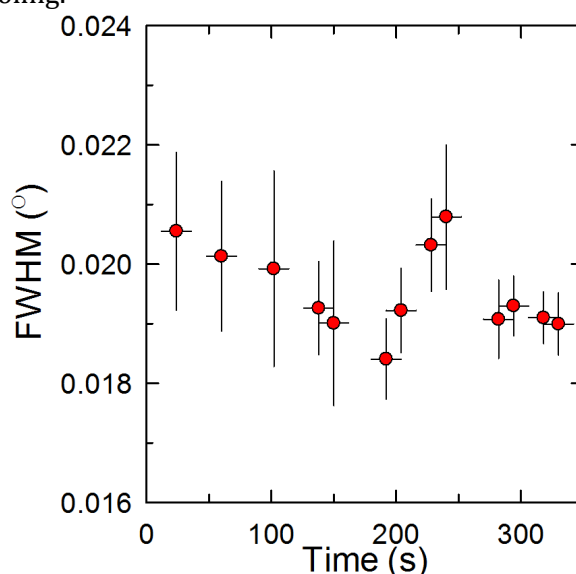
Figure 5.33 The variation of the full-width-at-half-maximum (FWHM) for the (321) reflection of cubic Cs_4O_6 with X-ray illumination time at 10 K after slow cooling.

5.3.5 Discussion

Illumination of matter by light can induce electronic excitations thanks to the existence of photo-excited atomic or molecular units, and lead to photo-induced transitions *via* some cooperative structural rearrangements. Photo-converted new structures can exhibit different electronic and/or magnetic properties [234], [235]. For instance, inter-valence electron transfer in mixed-valence metal cyanides (*i.e.* Prussian blue analogues) [236]–[239] and spin transitions in Fe-based spin crossover complexes [240] can be induced reversibly through illumination by visible, UV or X-ray light. We recall some key examples of X-ray light-induced transitions: in one of the mixed valence Prussian blue analogues, $Rb_{1.8}Co_4[Fe(CN)_6]_{3.3}\cdot13H_2O$, metal-to-metal charge transfer was induced by X-ray

light at low temperatures mediated by a phase transformation [241]. Such a sensitivity to X-ray light with an interconversion between the ground and excited states, accompanied by a variety of internal charge-transfer processes and spin transitions through phase transformations was also reported in cubic mixed valence $Rb_{0.7}Mn^{II}_{1.15}[Fe^{III}(CN)_6]\cdot 2H_2O$ [239]. In another member of the cubic mixed valence Prussian blue analogue $CsFe^{II}[Cr^{III}(CN)_6]$, an abrupt isosymmetric phase transition through Fe^{II} spin transitions from the high spin to the low spin configuration was also triggered by X-ray light illumination [240]. All the materials summarized above contain electronically-active d-electrons, which have been widely studied and are typically well understood. However, experimental investigations of effects of X-ray light illumination on p-electron-based structural, electronic and magnetic properties are much rarer. This is mostly due to the limited number of examples of such materials. In this study, we have experimentally investigated X-ray light-induced structural changes of the p-electron mixed valence system Cs_4O_6 and reported an abrupt X-ray light-induced structural transition from tetragonal to cubic Cs_4O_6, accompanied by charge transition.

Interestingly, the process of this X-ray illumination induced valence order-disorder transition in the Cs_4O_6 analogue is reminiscent of that reported for the Prussian blue analogues, $Rb_{0.7}Mn^{II}_{1.15}[Fe^{III}(CN)_6]\cdot 2H_2O$ [239] and $CsFe^{II}[Cr^{III}(CN)_6]$ [240]. In tetragonal Cs_4O_6 and these two cubic Prussian blue analogues, during the incubation time period, pronounced broadenings and shifts of the diffraction peaks were observed even though the associated phase conserves its structure as it is upon illumination. These X-ray induced effects before the bulk transition takes place, as in the present study, were attributed to a phase segregation process through the formation of photo-converted units [239], [240]. In Cs_4O_6 and in these Prussian blue analogues, a cooperative first-order phase transformation has been abruptly triggered as soon as the percolation threshold was exceeded and the phase transformations were accompanied by charge and/or spin transitions. These X-ray light-induced transitions in the Prussian blue analogues resulted in large lattice contraction: this was attributed to strong coupling between the spin and lattice degrees of freedom (strong electron–phonon coupling). Previous theoretical and experimental investigations of Rb_4O_6 and Cs_4O_6 analogues [100], [103], [106]

have proposed the importance of electron-electron correlations, and the presence of strong coupling between the charge, orbital and spin degrees of freedom in this open-shell p-electron systems which are proposed to be magnetically-frustrated insulators and to behave like other correlated $3d$- or $4f$-electron systems. As the magnetic properties of the temperature- and photo-induced tetragonal and cubic phases have not been probed in the present diffraction experiments, we can only propose that there could be a coupling between the charge and lattice degrees of freedom in this molecular solid.

5.3.6 Summary of temperature- and X-ray illumination-induced valence disorder-order transition

Our X-ray diffraction studies at ambient pressure have revealed that manipulation of the sesquioxide Cs_4O_6 by X-ray light can induce significant structural changes. At room temperature, while the structure remains cubic, X-ray illumination has led to broadenings and shifts of the cubic Bragg peaks but no structural transformation was observed in the bulk. The high-temperature cubic phase partially survives at 10 K upon quenching, while slow cooling to 10 K has resulted in the appearance of the tetragonal phase as the major component. Tetragonal Cs_4O_6 is extremely sensitive to X-ray radiation at 10 K: after a $\sim$5 min of exposure of the slowly cooled sample to the X-ray beam has resulted in the reverse tetragonal-to-cubic transformation.

This transformation develops in time through two processes. The first process manifests itself within a $\sim$2 min of incubation time with a progressive increase in the width of the tetragonal Bragg peaks and an anisotropic change in the tetragonal unit cell dimensions. The second process manifests itself in the intermediate region of the 'S-shaped' transformation-time curve with a first-order phase transformation to the valence-disordered cubic phase. In this region, the transformation occurs in the bulk, the Bragg reflections of the cubic phase grow in intensity at the full expense of those of the tetragonal phase with an additional $\sim$3 min of exposure.

5.4 Pressure-induced valence order-disorder transitions

In the following sections, the structural characterisation of Cs_4O_6 under high pressure at both room temperature and 13.4 K is described.

5.4.1 Experimental procedures

High-pressure synchrotron XRPD measurements were undertaken at 13.4 K and at room temperature with the diffractometer on beamline BL10XU, SPring-8, Japan. The overall setup of the beamline, experimental and 2D image integration details were provided in Section 2.5.2. The powdered sample was loaded in a helium-gas-driven membrane diamond anvil cell (MDAC), which was equipped with a stainless steel gasket and placed in a closed-cycle-helium refrigerator. All sample manipulations were carried out within the inert atmosphere of an argon glove-box (H_2O and O_2 < 0.1 ppm). The diameter of the diamond culet was 500 μm, and the powdered sample was introduced in a hole made in the stainless steel gasket of 100 μm depth and 200 μm in diameter. Helium gas in the MDAC was used as a pressure medium. The applied pressure was increased by controlling the He gas pressure at the membrane of the MDAC, and was measured with the ruby fluorescence method. The diffraction patterns were collected using a monochromatic X-ray beam with a slit size of 50 and 20 μm for the data collection at room and low temperature, respectively, with a wavelength of $\lambda = 0.41325(5)$ Å. Images were collected using a flat image plate detector. The beam spot size for the data collection was 20 μm and the illumination time was limited to 5 s, due to beam sensitivity.

With the knowledge that the Cs_4O_6 sample is extremely sensitive to the X-ray beam, data collection at each pressure was undertaken both at a fresh position and at a consecutively exposed position of the sample, in order to inspect any possible X-ray illumination-induced structural changes. The distance between each fresh position was approximately 20 μm.

5.4.2 High-pressure room temperature diffraction experiments

High-pressure synchrotron X-ray powder diffraction data were collected at room temperature at pressures between 0.5 and 9.9 GPa. While 4 datasets were collected at the same position of the sample on increasing pressure up to 1.7 GPa,

the MDAC was moved by ~20 μm upon further change in pressure. Six datasets were thus collected at fresh positions. The pressure evolution of the XRPD profiles is shown in Figure 5.34.
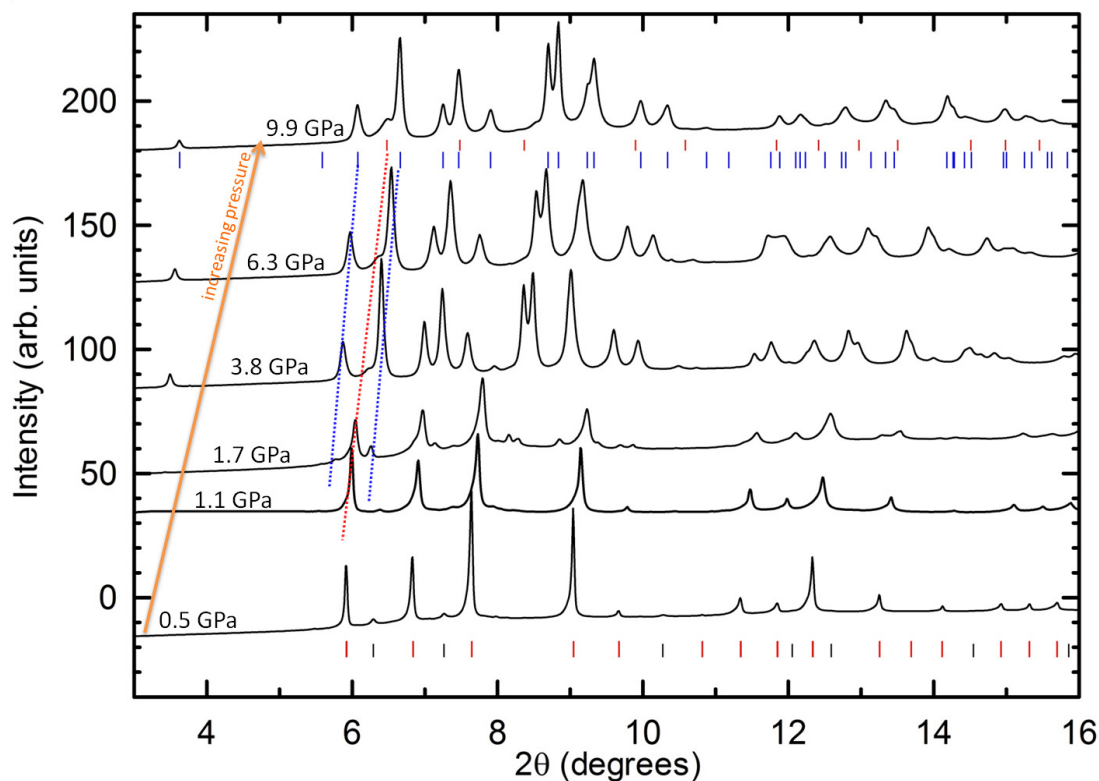
Figure 5.34 The evolution of synchrotron XRPD profiles with pressure at room temperature ($\lambda = 0.41325(5)$ Å). The profiles are offset and the background contribution is subtracted for clarity. Red, blue and black tickmarks represent the reflection positions of the cubic and tetragonal Cs_4O_6 and impurity CsO_2 phases, respectively. The 3 dotted lines from left to right mark the positions of the tetragonal (112), cubic (211) and tetragonal (211) Bragg peaks.

Inspection of the XRPD profiles confirms that the patterns can be indexed with a cubic cell ($I\bar{4}3d$) up to a pressure of 1 GPa. The presence of an impurity cubic superoxide CsO_2 (space group $Fm\bar{3}m$) phase is also confirmed. Further pressurisation led to the emergence of the tetragonal phase (space group $I\bar{4}2d$). Visual examination of the profiles revealed that, at pressures between 1 and 4 GPa, the tetragonal phase grew in intensity, reaching a maximum fraction at ~4 GPa that did not increase upon further pressurisation to 9.9 GPa. The cubic-to-tetragonal conversion is almost complete as it is evident from the very weak intensity of the remaining cubic (211) peak, discernible as a shoulder of the tetragonal (211) Bragg reflection (Figure 5.34, red dotted line).

5.4.3 High-pressure low temperature diffraction experiments

Slow cooling of the sample was achieved by initially cooling to 180 K in the cryostat and dwelling there for 4 hours, to maximize the cubic-to-tetragonal structural transition. This was then followed by cooling to 13.4 K within 30 min. To examine the effects of both X-ray illumination and pressure on the structure, XRPD data were collected at both fresh positions and a consecutively exposed position (POS-1) on pressurising between 0.6 and 11.7 GPa. Figure 5.35 demonstrates the difference in the pressure evolution of the diffraction profiles collected at fresh positions and at POS-1.
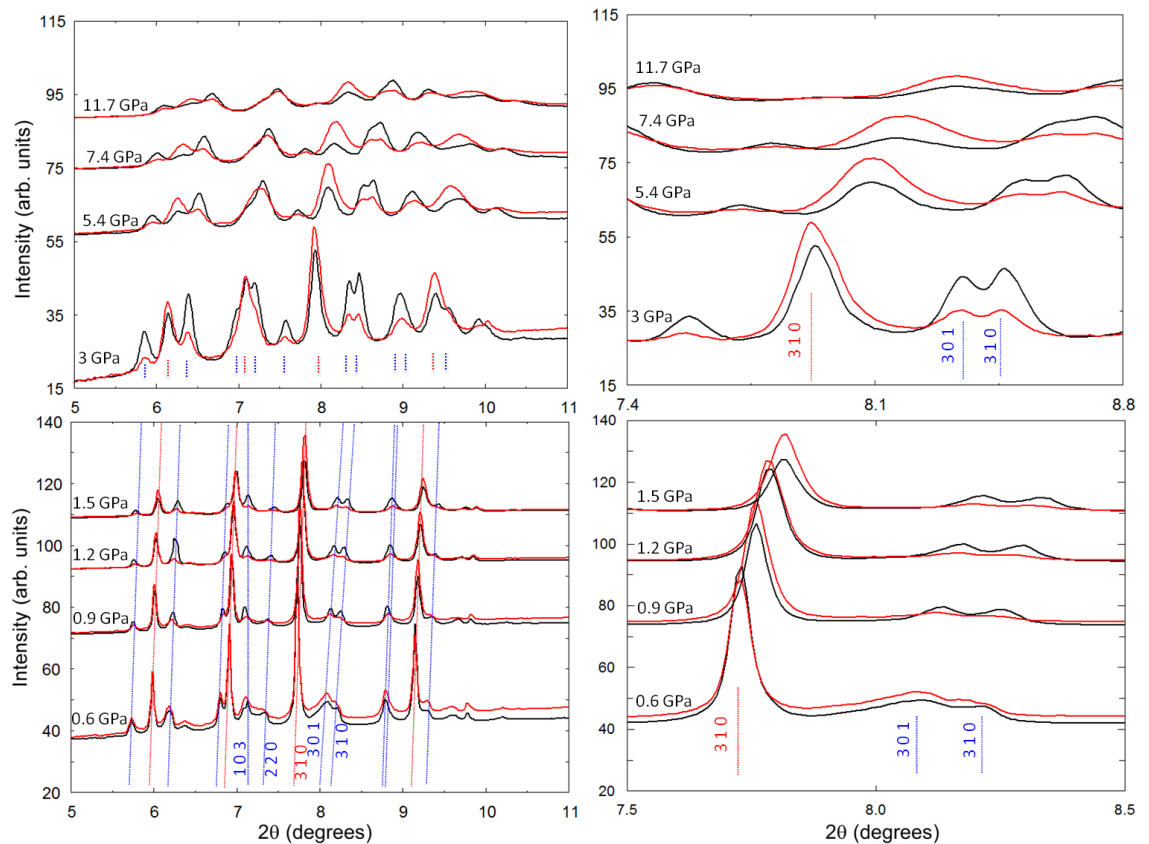
Figure 5.35 Pressure evolution of the synchrotron X-ray powder diffraction data collected at 13.4 K. Right panels are expanded views of the left panels. Diffraction profiles in black and red colour represent the profiles collected at fresh positions and at a continuously exposed position (POS-1), respectively. Red and blue dotted lines depict the reflection positions of the cubic and tetragonal Cs_4O_6 phases, respectively. Selected observed Bragg peaks are labelled by their (hkl) Miller indices with the same tickmark colours.

The data collected at POS-1 show that the temperature-induced cubic-to-tetragonal transition was reversed by X-ray illumination at pressures between 0.6 and 1.2 GPa, as evidenced from an increase in the intensity of the Bragg reflections

of the cubic phase. However on further pressurization, the X-ray-induced structural changes were partially suppressed by the applied pressure, resulting in a cubic-to-tetragonal transition. It is evident that X-ray illumination retards the transition from cubic to tetragonal structure, as seen in Figure 5.35: the XRPD data collected at fresh positions at each pressure (shown in black colour) are characterized by more intense Bragg reflections of the tetragonal phase than those collected at POS-1 (in red colour).

5.4.4 Structural results and compressibility behaviour at high pressures

Rietveld analysis was undertaken of the synchrotron XRPD data (fresh sample positions) collected at room temperature and 13.4 K upon pressurisation. The structural model employed was identical to that used to model the ambient pressure XRPD data given in section 5.3.4. The low-angle peak asymmetry from axial divergence was modelled here with coefficients $S/L = 0.001$ and $H/L = 0.0005$ [173]. Fitting of the background was achieved using a 15-term Chebyschev polynomial function. Consecutive cycles of improving profile shape coefficients in steps with intermediate refinements of zero point and background function were employed. The lattice parameters and scale factors of all three crystallographic phases present were refined up to ~3 GPa. However, significant pressure-induced peak broadening resulted in an almost complete loss of the intensity of the CsO_2 impurity peaks above ~3 GPa and the CsO_2 phase was thereafter excluded from the refinements. Thermal displacement factors were modelled as isotropic, were only refined at the lowest pressure and were fixed to these values at all elevated pressures. The anomalous contributions to the X-ray form factors of oxygen ($f' = -0.001$, $f'' = 0.002$ e/atom) and of caesium ($f' = -1.810$, $f'' = 0.793$ e/atom) were included. No absorption correction was used. Representative observed, calculated and difference diffraction profiles from Rietveld analysis at selected pressures are shown in Figure 5.36. Derived structural parameters at the lowest and highest pressure at room temperature and at 13.4 K are summarised in Table 5.13 and Table 5.14.
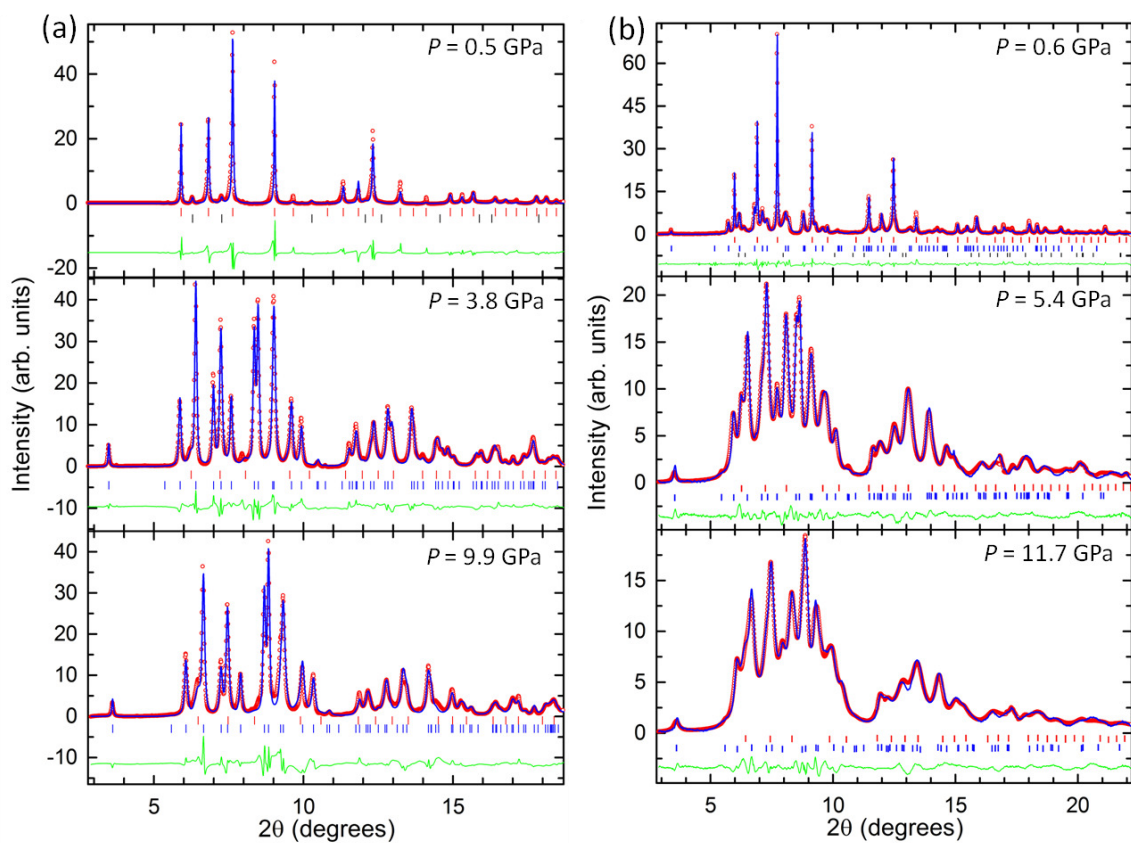
Figure 5.36 Rietveld refinements of high-pressure synchrotron X-ray powder diffraction data collected at room temperature (a) and at 13.4 K (b). Red circles, blue lines and green lines represent the observed, calculated and difference profiles, respectively. Red, blue and black tickmarks represent the reflection positions of the cubic and tetragonal Cs_4O_6, and impurity CsO_2 phases, respectively. The fitted background contribution has been subtracted for clarity.

Table 5.13 Refined structural parameters for the cubic and tetragonal Cs_4O_6 phases from the Rietveld fits to XRPD data collected at room temperature at 0.5 GPa (R_{wp} = 4.0%, R_{exp} = 0.8%) and at 9.9 GPa (R_{wp} =4.0%, R_{exp} = 0.9%). Values in parentheses are estimated errors from the least-squares fitting. Fraction of the impurity CsO_2 ($Fm\bar{3}m$) phase at 0.5 GPa is 4.6(4)%. CsO_2 phase is excluded from the refinements due to an almost complete loss of the intensity of Bragg peaks above ~3 GPa. Due to the small phase fraction of the cubic Cs_4O_6 phase above ~4 GPa, the lattice parameters and atomic fractional coordinates were not refined, and kept fixed to values found at 3.8 GPa at all elevated previous as given in the table for 9.9 GPa.

Pressure (GPa)	0.5	9.9	
Symmetry, Space group (wt. %)	Cubic, $I\bar{4}3d$ (95.402(6))	Cubic, $I\bar{4}3d$ (6.6(2))	Tetragonal, $I\bar{4}2d$ (93.360(3))
a (Å)	9.8102(3)	9.4750	8.4847(4)
c (Å)	-	-	10.2717(2)
V (Å^3)	944.13(7)	850.6	739.42(8)
Cs　Wyckoff site	*16c*	*16c*	*16e*
x/a	0.9413(2)	0.9579	0.3115(3)
y/b	-	-	0.0658(4)
z/c	-	-	0.0402(3)
U_{iso} (Å^2)	0.056(2)	0.056	0.029
O(1)　Wyckoff site	*24d*	*24d*	*8c*
x/a	0.5577(4)	0.5539	0
y/b	0	0	0
z/c	0.75	0.75	0.0745(4)
O(2)　Wyckoff site	-	-	*16e*
x/a	-	-	0.371(2)
y/b	-	-	0.789(2)
z/c	-	-	0.183(1)

Table 5.14 Refined structural parameters for the cubic and tetragonal Cs_4O_6 phases from the Rietveld fits to XRPD data collected at 13.4 K at 0.6 GPa (R_{wp} = 1.3%, R_{exp} = 2.1%) and 11.7 GPa (R_{wp} = 2.5%, R_{exp} = 1.5%). Values in parentheses are estimated errors from the least-squares fitting. Fraction of co-existing impurity CsO_2 ($Fm\bar{3}m$) phase at 0.6 GPa is 6.6(4)%. Atomic fractional coordinates of the tetragonal Cs_4O_6 phase were only refined for $P \le 3.6$ GPa, above that they were fixed to values found at 3.6 GPa as given in the table for 11.7 GPa.

Pressure (GPa)		0.6		11.7	
Symmetry, Space group, (wt. %)		Cubic, $I\bar{4}3d$ (51.098(8))	Tetragonal, $I\bar{4}2d$ (42.29(2))	Cubic, $I\bar{4}3d$ (28.8(3))	Tetragonal, $I\bar{4}2d$ (71.23(1))
a (Å)		9.69782(8)	9.077(1)	8.982(1)	8.3283(8)
c (Å)		-	10.791(2)	-	10.230(1)
V (Å³)		912.06(2)	889.1(3)	724.7(3)	709.5(2)
Cs	Wyckoff site	*16c*	*16e*	*16c*	*16e*
	x/a	0.9446(1)	0.3039(4)	0.9407(9)	0.3093
	y/b	-	0.0488(6)	-	0.0657
	z/c	-	0.0506(3)	-	0.0409
	U_{iso} (Å²)	0.029(3)	0.026(2)	0.029	0.026
O(1)	Wyckoff site	*24d*	*8c*	*24d*	*8c*
	x/a	0.55746(5)	-	0.5523(1)	-
	y/b	-	-	0	-
	z/c	0.75	0.07142(4)	0.75	0.07214
O(2)	Wyckoff site	-	*16e*	-	*16e*
	x/a	-	0.419(3)	-	0.424
	y/b	-	0.748(3)	-	0.763
	z/c	-	0.18773(8)	-	0.188

The evolution of the phase fractions with pressure at both temperatures is given in Figure 5.37. At room temperature, the structural conversion from cubic to tetragonal Cs_4O_6 starts at 1 GPa and is complete at ~4 GPa, with only ~4% of the cubic phase remaining. On the other hand, the pressure dependence of the phase fractions at 13.4 K shows that the pressure-induced cubic-to-tetragonal transition occurs gradually between 0.6 and ~4 GPa but at a much reduced rate. The weight fractions of the cubic and tetragonal phases at 13.4 K and 0.6 GPa were 51.098(8) and 42.29(2)%, respectively, finally reaching 73.259(9)% at 7.4 GPa for the

tetragonal phase. Whilst almost a complete conversion was achieved at room temperature, at low temperature, only ~24% of the cubic phase converted into the tetragonal structure. On further pressurisation at 13.4 K, the weight fractions of the two phases remained the same (~73%) up to the highest pressure of the present experiments.
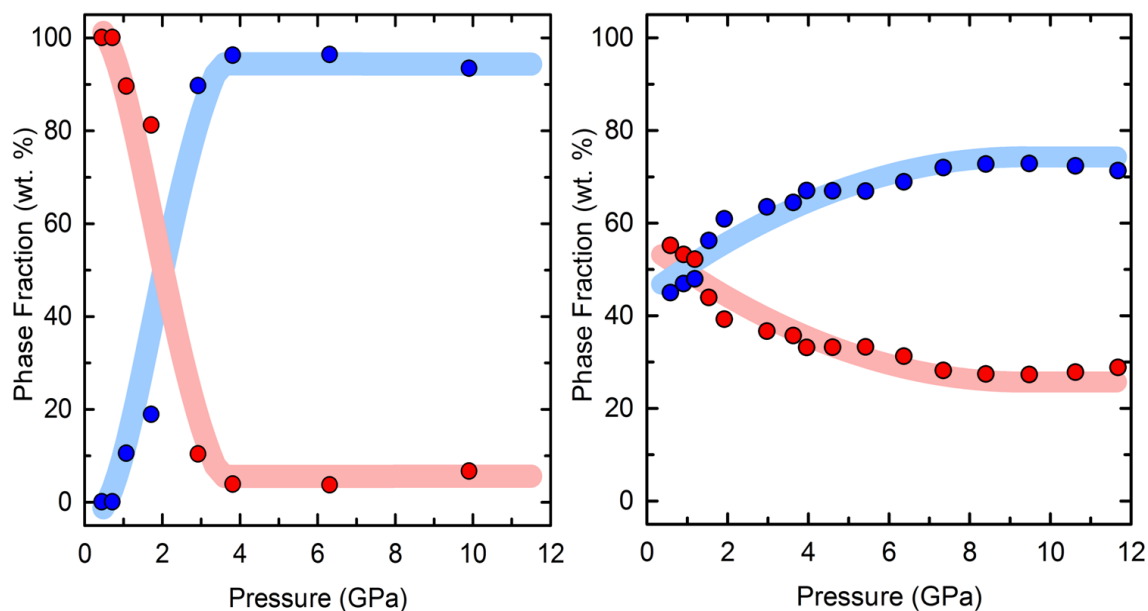
Figure 5.37 Evolution of the cubic and tetragonal Cs_4O_6 phase fractions with pressure at room temperature (left panel) and at 13.4 K (right panel). Red and blue circles represent the cubic and tetragonal phases, respectively. The XRPD datasets were collected at fresh positions at each pressure. Solid lines are guides to the eye. The impurity CsO_2 phase is excluded from the refinements due to an almost complete loss of the intensity of Bragg peaks above ~3 GPa; therefore the extracted relative weight fractions of the cubic and tetragonal Cs_4O_6 phases below 3 GPa were rounded to 100.

Figure 5.38 shows the pressure evolution of the unit cell volumes of the cubic and tetragonal Cs_4O_6, V, together with the results of least-squares fits to the third-order Birch-Murnaghan EoS (Equation 2.30). The resulting refined EoS parameters are given in Table 5.15.
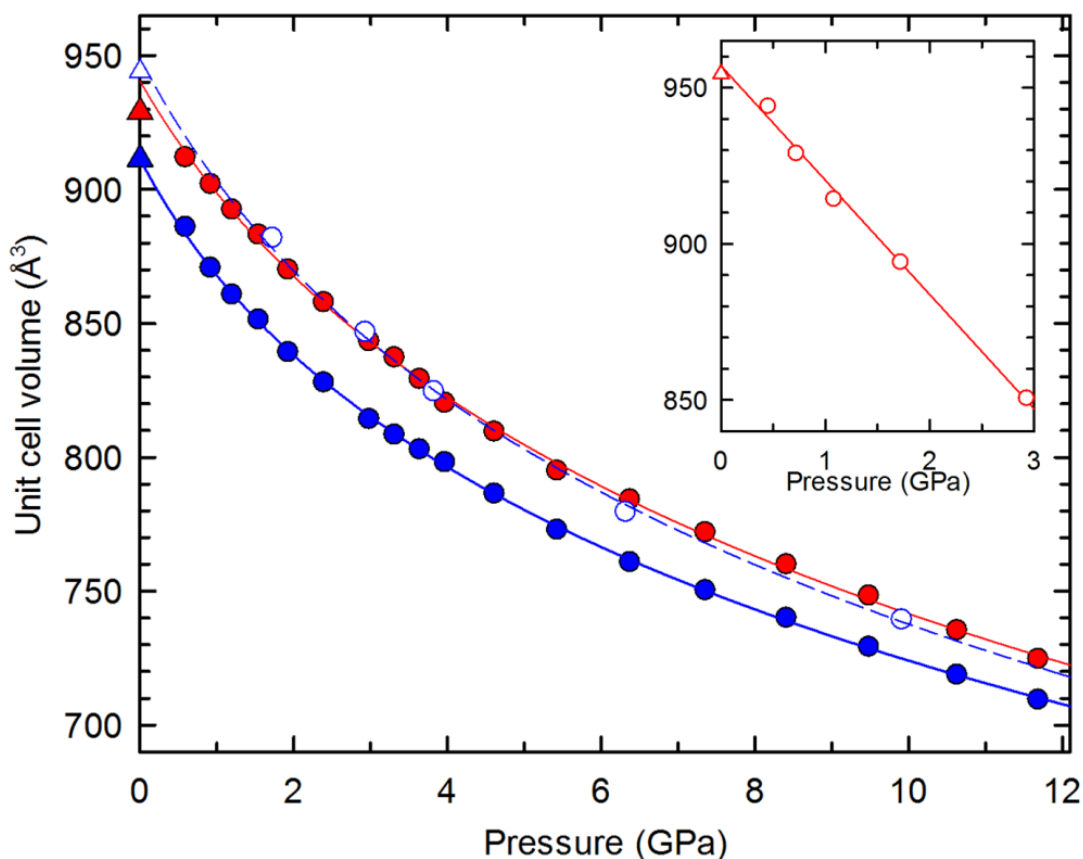
Figure 5.38 Pressure evolution of the unit cell volumes of tetragonal (blue) Cs_4O_6 at room temperature (open blue circles) and at 13.4 K (filled blue circles), and of cubic (red) Cs_4O_6 at 13.4 K (filled red circles), together with least-squares fits to the third-order Birch-Murnaghan EoS (see Table 5.15 for details). Triangles are the unit cell volumes at 300 K (open triangles) and at 10 K (solid triangles), taken from the ambient-pressure neutron tof powder diffraction studies. Inset shows the pressure evolution of the unit cell volume of cubic Cs_4O_6 at room temperature; the solid line through the data points is a linear fit, yielding a value of $dV/dP = -37(1)$ Å^3 GPa^{-1} and $V_0 = 957(2)$ Å^3.

The volume compressibilities of the cubic and tetragonal phases extracted from the Birch-Murnaghan EoS fits to the 13.4 K $V(P)$ data are essentially identical within error $\kappa = 0.053(4)$ and $\kappa = 0.063(4)$ GPa^{-1}, respectively (Table 5.15). The unit cell volumes of the tetragonal phase at room temperature and of the cubic phase at 13.4 K show the same response up to the highest pressure of the present experiments. Due to the very weak intensity of the cubic (211) peak (discernible as a shoulder; Figure 5.34, red dotted line) above ~4 GPa, the unit cell volume of the cubic phase could not be extracted from the Rietveld analysis of the XRPD data above 4 GPa; therefore, only low-P volume compressibility is extracted at room temperature (Figure 5.38, inset). Linear fit to the '*Cubic, V(P)*' data, for $P < 3$, has yielded linear average compressibility of 0.038(1) GPa^{-1}.

Table 5.15 Details of the third-order Birch-Murnaghan EoS fits to the 13.4 K and room temperature $V(P)$ data for cubic and tetragonal Cs_4O_6. Numbers in parentheses for the K_0 and K_0' indicate statistical errors from the least-squares-fitting.

		K_0 (GPa)	K_0'	$\kappa = dlnV/dP$ (GPa^{-1})	V_0 (Å^3)
13.4 K	Cubic, $V(P)$	19(2)	7.1(6)	0.053(4)	940(4)
	Tetragonal, $V(P)$	16(1)	9.7(6)	0.063(4)	913(3)
RT	Tetragonal, $V(P)$	17(3)	7(1)	0.06(1)	949(7)

The pressure dependence of the lattice parameters of the tetragonal and cubic Cs_4O_6 phases together with the corresponding EoS fits and results of the EoS fits are shown in Figure 5.39 (a) and Table 5.16, respectively.
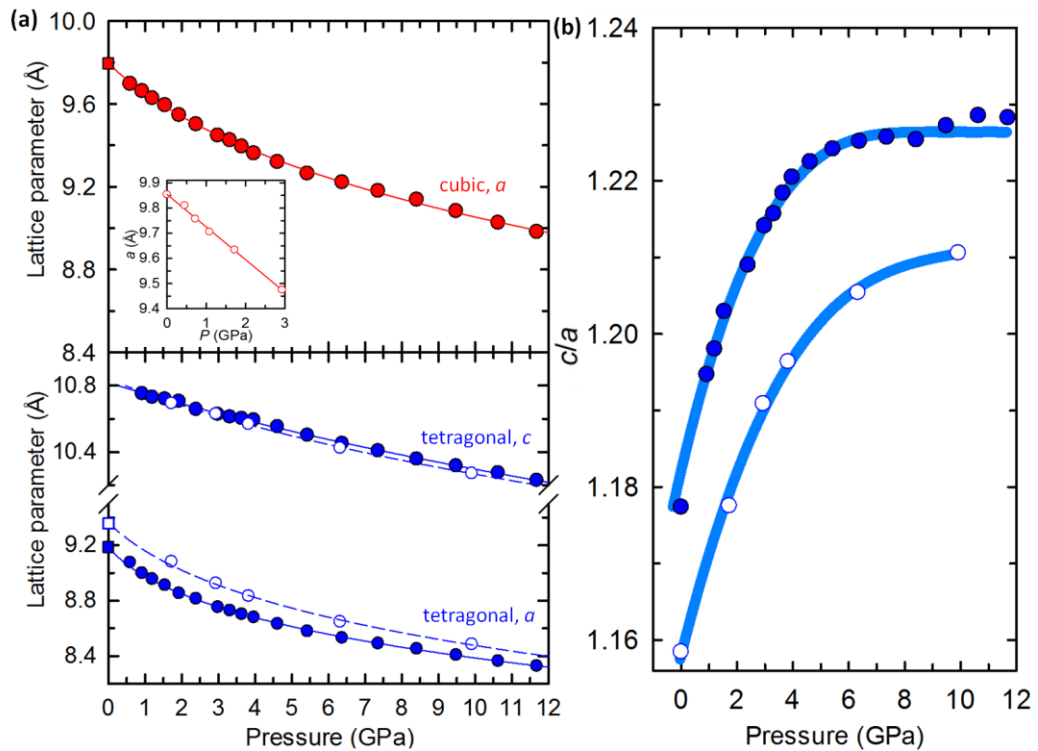
Figure 5.39 (a): Pressure evolution of the lattice parameters of cubic and tetragonal Cs_4O_6 at room temperature (open circles) and at 13.4 K (filled circles). The solid and dashed lines through the data points show results from least-squares fits to the modified Birch–Murnaghan equation for axial compression. For the lattice parameters, the values of K_x and K_x' are those obtained by fitting to the cubes of the lattice parameters. The zero-pressure data points, a_0, presented with squares kept at these values in the least-squares-fitting (for details see text). Inset shows the variation of the lattice parameter of cubic Cs_4O_6 at room temperature; solid line through the data points is a linear fit, yielding a value of $da/dP = -0.123(2)$ Å GPa^{-1} (b): Pressure dependence of the tetragonal distortion, c/a at room temperature (open circles) and at 13.4 K (filled circles). The lines through the data points are guides to the eye.

To determine the axial compressibilities, K_x and K_x' (x = a, c), a parameterised form of the Birch-Murnaghan EoS was used: the individual axes are cubed and fitted as volumes. The value of 'K_x' obtained from fitting the lattice parameters in this way is related to the zero-pressure axial compressibility by $\kappa_x = 1/3K_x$ [242]. The zero-pressure data point, a_0, of the cubic phase at 13.4 K was derived from the Birch-Murnaghan fit to the 13.4 K $V(P)$ data ($a_{0,\,13.4K}$ = 9.80(1) Å) and at room temperature it was derived from the linear fit to the $V(P)$ data ($a_{0,RT}$ = 9.854(8) Å). a_0s for the tetragonal phase were extracted using the derived c_0 and V_0 from the EoS; $a_{0,13.4K}$ = 9.19(2) Å, $a_{0,RT}$ = 9.36(3) Å. All a_0s for the tetragonal and cubic phases were kept fixed at these values in the least-squares-fittings (Table 5.16), only c_0 and axial compressibility parameters were refined, as refinement of the a_0 did not result in physically meaningful values.

Table 5.16 Details of the third-order Birch-Murnaghan EoS (modified for axial compression) fits to the cubes of the lattice parameters of cubic and tetragonal Cs_4O_6 at room temperature and 13.4 K. Numbers in parentheses for c_0, K_x and K_x' (x = a, c) indicate statistical errors from the least-squares-fitting. For the fixed values of a_0 see text above.

		K_x (GPa)	K_x'	$\kappa = 1/3K_x$ (GPa^{-1})	a_0 (Å)	c_0 (Å)
13.4 K	cubic, a	19.06(6)	7.0(4)	0.0175(6)	9.80	-
	tetragonal, a	9.7(3)	11.2(5)	0.034(1)	9.19	-
	tetragonal, c	54(3)	3.2(5)	0.0062(3)	-	10.817(8)
RT	tetragonal, a	12(1)	7.1(9)	0.028(2)	9.36	-
	tetragonal, c	41(1)	4.9(8)	0.0081(6)	-	10.84(1)

The anisotropic compressibility of the tetragonal structure is quantitatively confirmed by the refined EoS parameters and by inspection of Figure 5.39 (b) at both 13.4 K and room temperature: the tetragonal phase is least compressible along the c axis along which the peroxide anions lie at a small tilt, with K_c being 54(3) GPa (at 13.4 K), and most compressible in the ab plane (K_a = 9.7(3) GPa at 13.4 K). The interlayer compressibility κ_c = 0.0062(3) GPa^{-1} is ~5.5 times smaller than κ_a, consistent with an increasing tetragonal distortion upon pressurization. Our data has revealed that the pressure response of the c axis at room temperature

238

and at 13.4 K is essentially the same, with no obvious contraction in the length of the c axis by lowering the temperature. The temperature-induced volume contraction of the tetragonal structure is thus a result of the contraction of the a axis. The corresponding value of κ_a of the cubic phase straddles those of the tetragonal phase consistent with the disordered nature of the oxygen dumbbells.

5.4.5 Discussion

In addition to external perturbations such as temperature and X-ray light, pressure is also an important thermodynamic parameter that can completely redistribute electronic densities and change the nature of the chemical bonds *via* changing the free energy of materials, which exceed those of the strongest chemical bonds present at ambient pressure (>10 eV), leading to profound changes in materials [243].

A theoretical study of the pressure response of mixed-valent Rb_4O_6, which is isostructural to Cs_4O_6 at room temperature, has predicted an unexpected sequence of phase transitions between strongly correlated antiferromagnetic insulator, ferromagnetic insulator, moderately correlated ferromagnetic half-metal and finally itinerant nonmagnetic metal; it also stated that the external pressure reportedly destroys the charge-ordered insulating state by enabling the valence fluctuations between non-magnetic peroxide and magnetic superoxide molecules, and that at high pressures (~75 GPa), the system approaches the insulator-metal transition [244]. However, these results are virtually conflicting, as the experimental studies have not found such long-range magnetic ordering, but suggested magnetic correlations in the low-temperature range due to $2p$ electrons of the superoxide anions [100], [106]. To our knowledge, no experimental high-pressure XRPD studies of alkali sesquioxides have hitherto been reported. Our high-pressure XRPD studies have clearly demonstrated that external pressure drives a nearly complete phase transformation from cubic to tetragonal Cs_4O_6.

5.4.6 Summary of pressure-induced valence disorder-order transition

The pressure response of the structural properties of the valence-disordered sesquioxide Cs_4O_6 has revealed that, at room temperature, there is an almost complete valence disorder-to-order transition at pressures between 1 and 4 GPa.

On further pressurisation up to 10 GPa, no additional transformation occurs. A temperature-induced cubic-to-tetragonal structural transition was again observed by cooling the sample slowly to 13.4 K. Pressurisation at 13.4 K resulted in an increase in the intensities of the Bragg reflections of the tetragonal phase. However, no complete valence-ordering was induced by pressure at 13.4 K with only ~24% of the cubic phase converted to tetragonal in sharp contrast to the situation encountered at room temperature. The compressibility behaviour of the cubic and tetragonal Cs_4O_6 solids at 13.4 K and at room temperature has revealed that the tetragonal Cs_4O_6 is slightly more compressible than the cubic. The anisotropic compressibility of the tetragonal structure was confirmed by the refined EoS parameters: it is least compressible along the c axis, along which the peroxide anions lie, and more compressible in the ab plane.

5.5 Conclusion

In conclusion, we have presented a comprehensive study of the temperature, X-ray light and pressure response of the structure of Cs_4O_6 using neutron tof and X-ray powder diffraction. Our temperature-dependent datasets collected at ambient pressure have revealed that Cs_4O_6 adopts two distinct crystal structures, *i.e.* high-temperature cubic (space group $I\bar{4}3d$) and low-temperature tetragonal (space group $I\bar{4}2d$) phases, depending on the cooling protocol employed, and that valence ordering takes place in the tetragonal lattice, where splitting of the oxygens into two crystallographically-separate sites with a ratio of 2:1 is allowed. Our study is the first experimental crystallographic evidence for the presence of two localized valence states of dioxygen in sesquioxides. The detailed analysis of the temperature- and cooling-protocol-dependent neutron tof powder diffraction datasets collected on warming has shown that a cooperative first-order phase transformation between the cubic and tetragonal phases is triggered, and this transformation process is very sluggish, slow and highly hysteretic due to some intermediate transitional changes occurring in the course of the reorientations of the dioxygen units.

We have also discovered that whilst a partial valence localisation can be achieved in Cs_4O_6 by slow cooling to 10 K, at this temperature, X-ray light has

reversed this and led to a complete phase transformation from tetragonal to cubic structure resulting in a complete valence delocalisation in the bulk within a ~5 min of X-ray illumination. Finally, an almost complete pressure-induced valence disorder-to-order transition was observed at ambient temperature at pressures between 1 and 4 GPa. Pressurisation at low temperature has also induced partial transformation from cubic to tetragonal phase: ~24% of the cubic phase converted to tetragonal at 13.4 K. The compressibility behaviour of the two phases has revealed that the valence localisation does not lead to a big discrepancy in the compressibility of Cs_4O_6.

Chapter 6 Summary, conclusions and future directions

6.1 Results of work presented in this thesis

One of the directions taken in this work was to gain further understanding on the structural and electronic properties of fcc A_3C_{60} superconductors with compositions $K_xCs_{3-x}C_{60}$ and $Rb_xCs_{3-x}C_{60}$, extending from close to the strongly correlated Mott-Jahn-Teller insulator (MJTI) Cs_3C_{60} to the conventional BCS-type superconducting fullerides (underexpanded regime) (Chapters 3 and 4). The other key aim of this work was to resolve the ambiguous reports on the structural properties of the mixed valency molecular oxide, Cs_4O_6 and ascertain the true crystallographic symmetry of the valence ordered state under non-ambient conditions employing high-resolution neutron tof and X-ray powder diffraction techniques (Chapter 5).

Chapter 3 focused on the structural and magnetic properties of the fcc-structured $K_xCs_{3-x}C_{60}$ fullerides with particular attention to the comparison with the fcc $Rb_xCs_{3-x}C_{60}$ analogues to investigate cation specific effects on the electronic properties of fcc $A_xCs_{3-x}C_{60}$ system. Compositions with refined K-content, x_K, varied between 0.22 and 2, were synthesized covering the key region of the electronic phase diagram between that of the underexpanded A_3C_{60} superconductors and highly-expanded MJTI fcc Cs_3C_{60}. This regime had been previously accessed by physical pressurization of Cs_3C_{60} [28] before the recent access at ambient pressure *via* the application of chemical pressure through substitution of Cs^+ in Cs_3C_{60} by the smaller Rb^+ cation [67]. In this work, instead of Rb^+, smaller K^+ has been used to chemically pressurise fcc Cs_3C_{60}.

Ambient pressure high-resolution synchrotron XRPD studies of the family of $K_xCs_{3-x}C_{60}$ at 300 K have revealed that although both the size mismatch between the doped K^+ and the T_d site, and the incompatibility of the large Cs^+ cation size with the size of the T_d site have led to a significant deviation of the refined K-content from its nominal value, a systematic increase of the fcc unit cell volume has been verified with decreasing x, obeying Vegard's law.

Low-field magnetisation measurements at ambient pressures have demonstrated a 'dome' shaped scaling of T_c with x in this system, in agreement with earlier study [67]: T_c initially increases, reaches a maximum with optimally expanded composition, following the conventional BCS-like scaling of T_c with $N_{\varepsilon(F)}$, and then starts decreasing at large intermolecular distances on approaching the Mott boundary. Combination of high pressure structural and magnetization data has allowed us to track the T_c dependence on C_{60} packing density ($T_c(V)$) in fcc $K_xCs_{3-x}C_{60}$ at low temperature. Although the $T_c(V)$ follows the universal superconductivity dome, a significant decrease has been observed in the maximum T_c with increasing x; this has been attributed to the cation size disorder arising from the size mismatch between the substituted cations occupying the tetrahedral sites. Cation disorder has been quantified by the cation size variance at the T_d site and it has been shown that the cation specific detrimental effects should not be ignored in the description of the electronic properties of the A_3C_{60} superconductors, *i.e.* smaller ionic radius of K^+ yields a bigger detrimental effect on T_c compared to that of Rb^+ due to the greater size mismatch between the cations occupying the T_d site.

In contrast to the monotonic thermal contraction of Cs_3C_{60} and underexpanded A_3C_{60} (*e.g.* A = K, Rb) analogues, the compositions in proximity to the Mott insulator-metal boundary, *i.e.* $x_K = 0.35$, 0.64 and 0.87, displayed a characteristic isostructural volume collapse upon cooling at certain temperatures above the superconducting T_c. In addition, these compositions, including $x_K = 0.22$, did not exhibit a temperature-independent Pauli susceptibility term, χ, revealed by magnetic susceptibility measurements. Instead, the overexpanded $x_K = 0.22$ and 0.35 displayed distinct cusps with maxima at certain temperatures. The maximum of the cusp for $x = 0.35$ coincides closely with that at which the volume collapse was observed. Compositions with K-content of $x_K = 0.53$, 0.64 and 0.87 did not show cusps as clear as the more expanded ones, but they did not exhibit a smooth Pauli metallic behaviour either. Conversely, underexpanded compositions far from the Mott insulator-metal boundary showed a Pauli metallic behaviour. Both characterisation techniques have revealed that on approaching the underexpanded regime of the phase diagram from the Mott insulator-metal boundary through decreasing intermolecular distances (increasing x_K), the onset temperature of the

volume collapses and of the maxima of the cusps increases and becomes significantly broadened over a wider temperature range. Finally, smooth thermal contraction and nearly temperature-independent Pauli metallic behaviour are restored in the underexpanded regime, consistent with a metallic ground state from which conventional superconductivity emerges on cooling. Furthermore, at high temperatures, overexpanded and optimally expanded $K_xCs_{3-x}C_{60}$ compositions ($0.22 \leq x \leq 0.87$) follow the Curie-Weiss law with negative Weiss temperatures. These compositions have effective magnetic moments per C_{60}^{3-} ($\sim 1.2 - 1.6$ μ_B) comparable to those in MJTI Cs_3C_{60} and in overexpanded $Rb_xCs_{3-x}C_{60}$ compounds [28], [67], implying that they also adopt $S = \frac{1}{2}$ localized electron ground state with antiferromagnetic correlations. However, below the cusps, the magnetic susceptibility of those is temperature-dependent, indicating an unconventional paramagnetic metallic state. These anomalies emerging as volume collapses and cusps in fcc $K_xCs_{3-x}C_{60}$ ($0.22 \leq x \leq 0.87$) compositions have been taken as evidence of isostructural crossover from Mott insulating to metallic state at ambient pressure and at temperatures well-above superconducting T_c.

These results have shown that, although, T_c and Mott insulator-to-metal crossover temperatures, T' of fcc $A_xCs_{3-x}C_{60}$ materials could be tuned *via* bandwidth control through application of chemical pressure by adjusting the A^+/Cs^+ dopant ratio ($A^+ = K^+$ or Rb^+), cation specific effects (*i.e.* cation disorder) play a crucial role in the electronic properties of those, besides altering the unit cell dimensions. Even though the global trend of the variation of critical temperatures (T' and T_c) with fcc unit cell volume is essentially identical in both series of fcc $K_xCs_{3-x}C_{60}$ and $Rb_xCs_{3-x}C_{60}$, greater cation disorder in the K-substituted system induces grater unfavourable effects on critical temperatures.

Availability of very large masses of high quality fcc-structured underexpanded Rb_2CsC_{60} and overexpanded $Rb_{0.5}Cs_{2.5}C_{60}$ superconductors has allowed us to investigate the Hebel-Slichter (HS) coherence peak suppression across the superconductivity dome and to estimate the superconducting gap magnitude upon approaching the MI boundary (Chapter 4). While the HS peak has been observed in underexpanded Rb_2CsC_{60} as a small enhancement of the muon spin-relaxation rate below T_c, it may be suppressed at large interfullerene

separation in $Rb_{0.5}Cs_{2.5}C_{60}$, which has been already defined as an unconventional superconductor forming from the strongly correlated metallic regime (Jahn-Teller metal) [67]. Moreover, although s-wave symmetry is retained, an anomalously large coupling strength has been found in $Rb_{0.5}Cs_{2.5}C_{60}$ with ratio of superconducting gap to T_c, $2\Delta/k_BT_c$ approaching 5. This implies that the strong cooperation between the electron correlations and the electron-phonon interactions, as in MJTI Cs_3C_{60} [86], influences the superconducting state and is responsible for the high-T_c s-wave superconductivity in the family of overexpanded fcc A_3C_{60} superconductors [67], [204]. Our results have also revealed that $2\Delta/k_BT_c$ increases to 4.53(9)(for $Rb_{0.5}Cs_{2.5}C_{60}$) upon approaching the MI boundary where effects of the JTM are maximal [67], in agreement with earlier studies [67], [70], [75]. This trend contrasts with the 'dome' shaped scaling of T_c with interfullerene separation. These findings could stimulate further experimental and theoretical studies with extended numerical solutions to gain further understanding of the size and symmetry of the superconducting gap in the unconventional superconducting state which forms from a strongly correlated metallic regime.

In Chapter 5, we reported the first experimental crystallographic evidence for the presence of two localized valence states of dioxygen in the sesquioxide Cs_4O_6. Our comprehensive study of the structure of Cs_4O_6 at both ambient and low temperatures using neutron tof and X-ray powder diffraction techniques has revealed that Cs_4O_6 adopts two distinct crystal structures, *i.e.* high-temperature valence-disordered cubic and low-temperature valence-ordered tetragonal phases, and all the extreme external perturbations used in this study have induced valence order-disorder transitions in Cs_4O_6.

At ambient temperature, Cs_4O_6 adopts a high-symmetry cubic cell (space group $I\bar{4}3d$) in which all oxygen atoms reside on the same Wyckoff position: this in turn creates symmetry-equivalent valency-delocalised $(O–O)^{(4/3)-}$ dumbbells. However, ultra-slow cooling has led to a symmetry-lowering structural transition. This low-temperature phase crystallises with a tetragonal cell (space group $I\bar{4}2d$) where splitting of the oxygen atoms into two crystallographically-distinct sites is allowed. This splitting leads to the differentiation between the paramagnetic O_2^-

and diamagnetic O_2^{2-} anions, evident from the two clearly different sets of bond distances. This results in valency ordering, and the molecular formula of the compound is writen as $(Cs^+)_4(O_2^-)_2(O_2^{2-})$. These two structures differ in the orientations of the O_2 molecules: in the valence-ordered Cs_4O_6, the O_2^{2-} anions are oriented parallel to the *a* and *b* axes but O_2^- anions are directed at an angle to the tetragonal *c* axis. In the cubic phase, all $(O-O)^{(4/3)-}$ anions are oriented parallel to the crystallographic axes. On the other hand, rapid cooling has led to the molecular orientation of the $(O-O)^{(4/3)-}$ anions to quench on their original positions generated by the $I\bar{4}3d$ symmetry.

Neutron tof powder diffraction datasets collected on warming after rapid- and ultra-slow-cooling have revealed fascinating structural responses. These non-trivial responses of the cubic and tetragonal phases to temperature are most likely due to the cooperative structural rearrangements happening during the slow reorientations of the dioxygen units. This cooperative interaction condenses either cubic or tetragonal structures, generating large thermal hysteresis. Our experimental data have demonstrated that the high-temperature cubic and the low-temperature tetragonal Cs_4O_6 coexist as quenched and superheated phases at low and high temperatures, respectively. All these observations in the course of the sluggish reconstructive-type conversion confirm that this valence disorder-to-order transition is of first order.

We have also found that Cs_4O_6 is extremely sensitive to X-ray illumination at ambient temperature and at 10 K. At room temperature, illumination of cubic Cs_4O_6 by X-ray light has resulted in pronounced peak broadenings and shifts to lower angles but no structural transformation has occurred in the bulk. These observations signify the growth of significant structural inhomogeneities and the presence of structural rearrangement effects induced by the X-ray light. After slow cooling to 10 K, cubic-to-tetragonal transformation occurred: fractions of the coexisting cubic, tetragonal and impurity CsO_2 phases after a 12(12) s illumination time were found as 16.7(2), 71.83(2) and 12.3(2)%, respectively. At this temperature, a ~5 min of exposure of the slowly cooled Cs_4O_6 to the X-ray beam has resulted in the reverse tetragonal-to-cubic transformation. This transformation develops in time through two distinct steps. The first one manifests

itself within a ~2 min of incubation time with a progressive increase in the width of the tetragonal Bragg peaks and an anisotropic change in the tetragonal unit cell dimensions. The second process manifests itself in the intermediate region with a first-order phase transformation to the valence-disordered cubic phase. In this region, the transformation occurs in the bulk, the Bragg reflections of the cubic phase grow in intensity at the full expense of those of the tetragonal phase with an additional ~3 min of exposure. This photo-induced phase transition in the bulk has been confirmed by the observation that the cubic peaks are not broadened in the course of the transformation, contrasting with the observed effects of X-ray light on the cubic phase encountered at room temperature.

Moreover, at ambient temperature, pressurisation of Cs_4O_6 up to 4 GPa has led to an almost complete cubic-to-tetragonal structural transformation. The pressure response after slow cooling to 13.4 K has been also studied. We found that application of pressure increases the weight fraction of the tetragonal phase which was induced by slow cooling; however, in sharp contrast to the situation encountered at room temperature, only ~24% of the cubic phase converted to tetragonal at 13.4 K.

Magnetic and molecular orderings are typically strongly coupled to each other, and there are significant correlations between the adopted structure and the magnetic properties. Therefore, it is a fundamental requirement to establish the temperature evolution of the two competing phases of Cs_4O_6 for a reliable magnetic characterization. These results could therefore motivate further theoretical calculations and experimental studies by other techniques to gain an advance understanding of the magnetic behaviour of this family of materials.

6.2 Future directions

The present work conducted on fcc A_3C_{60} fullerides has offered a comprehensive understanding of the rich electronic phase diagram of fulleride superconductors. To structurally further characterise the crossover between the insulator and the metal, aside from X-ray powder diffraction technique, studies by complementary techniques, such as combined X-ray and neutron powder diffraction (NPD), maximum entropy method (MEM), pair distribution function (PDF) analysis and X-ray absorption fine structure (EXAFS) measurements could be undertaken.

Since the Mott insulator-to-metal transition (MIT) is of first order, a phase co-existence is expected; however, in the structural XRPD investigations of fcc $A_xCs_{3-x}C_{60}$ (A = K or Rb) with temperature reported in this thesis and in ref. [67], no anomalous structural changes that would imply a phase co-existence were observed at the insulator-to-metal crossover. Because carbon has a weak X-ray scattering power, in the course of the XRPD data analysis, the fractional coordinates of the C atoms in the fcc phase were not allowed to refine. They were only rescaled as the temperature varied to the refined lattice metrics and thus the molecular shape remained unaltered. NPD data analysis allows the refinement of the C atom fractional coordinates, allowing appropriate altering of the molecular shape of the C_{60} units and hence to elucidate any subtle structural changes happening at the MIT.

MEM analysis would allow us to track any changes in electron distribution at the MIT in overexpanded fcc $A_xCs_{3-x}C_{60}$ by determination of three-dimensional electron densities from high-resolution XRPD and NPD data. PDF analysis of high-statistics XRPD data with high Q would also facilitate to characterise the local structural changes at the MIT. Strong preferential site occupation of substituted cations, *i.e.* the octahedral site is entirely occupied by Cs^+ and the tetrahedral one is occupied by a disordered A^+/Cs^+ mixture, allows a separate structural analysis of the tetrahedral and octahedral sites through EXAFS measurements at the alkali ions K, Rb, and Cs, and thus allows a quantitative investigation of cation specific effects on the critical temperatures.

Aside from the investigation of cation specific effects on the electronic properties of fcc $A_xCs_{3-x}C_{60}$ fullerides, the effects of tetrahedral alkali-metal vacancies could be probed as well. For instance, in $Sm_{2.75}C_{60}$ and $Yb_{2.75}C_{60}$, tetrahedral rare-earth metal vacancies exhibit long-range ordered arrangement, generating superstructure [245], [246]. Such structural response to cation-vacancy could be encountered in fcc $A_xCs_{3-x}C_{60}$ fullerides, altering the electronic properties of this system. For example, starting conceptually from fcc K_2CsC_{60} (or Rb_2CsC_{60}), K^+ (or Rb^+) can be increasingly substituted non-stoichiometrically by a smaller cation, *i.e.* Ba^{2+}, with such a general formula: $[\ ]_{x/2}Ba_{x/2}K_{1-x})_2CsC_{60}$, $[\ ]$ representing vacant tetrahedral sites. Vacancy ratios with simple fractions might generate cation-vacancy ordering in fcc A_3C_{60} fullerides.

The availability of very large masses of high quality overexpanded fcc $Rb_xCs_{3-x}C_{60}$ samples with Rb-content $x = 2$ and 0.5 allowed us to investigate strong correlations in proximity to the Mott boundary by measurements of the temperature dependence of the longitudinal-field muon spin relaxation (LF-µSR) rate of endohedrally-formed muonium. These samples cover the either side of the superconductivity dome; however, the analysis of the temperature dependence of the LF-µSR data of the optimally-expanded $RbCs_2C_{60}$ could not be undertaken because of time limitations. For an ultimate investigation, it is essential to search for the existence or not of a Hebel-Slichter (HS) coherence peak and to determine the superconducting gap magnitude of this composition and of overexpanded $Rb_{0.35}Cs_{2.65}C_{60}$. In the present work we employed Arrhenius law for the estimation of Δ and the temperature dependence of $1/T_1T$ has not been modelled. Here more realistic models can be employed, *e.g.* the Hebel-Slichter theory formulation with a broadened BCS density of states.

In addition of the temperature-dependent LF-µSR studies, field-dependent measurements could be undertaken to determine the critical field of the suppression of HS coherence peak in this system, as high fields are known to suppress the HS peak. Spin-lattice relaxation rate, $1/T_1$ can be also extracted through NMR studies using smaller masses of samples but this requires significantly higher magnetic fields than the LF-µSR technique, resulting in the suppression of the HS peak.

Moving to the sesquioxide Cs_4O_6, there are many different types of techniques that could provide complementary information on the structural and magnetic properties of this molecular system. In the course of the XRPD study of Cs_4O_6, we found that X-ray light illumination leads to significant structural changes but we did not investigate these effects in any detail as the primary aim of the structural studies was the accurate identification of its structure. To obtain fine details about the interconversion, time-resolved X-ray diffraction could be used for simultaneous complete structural determination, X-ray absorption spectroscopy (XAS) for metal valence states determination, high-resolution angle-resolved photoemission spectroscopy (ARPES) for valence-band structure determination, and EXAFS to explore temperature dependent local displacements.

Since the transformation between the cubic and tetragonal phases involves large amplitude reorientations of the oxygen dumbbells, a study of molecular motion of dioxygen units might be needed. Inelastic neutron scattering could be an option to study the molecular motion and dynamics in this system. This technique could also provide some quantitative information on the magnetic properties. MEM analysis could be also undertaken to probe any changes in electron distribution at critical temperatures where two molecular metastable phases shows complex conversion in between.

In addition, though high-pressure XRPD investigations of Cs_4O_6 were undertaken, it is necessary to examine the structural changes with high-pressure NPD studies at ambient temperature to eliminate X-ray light induced changes and to isolate the tetragonal phase at room temperature. Furthermore, to determine the thermodynamic properties of the cubic and tetragonal phases with the aim of a quantitative investigation of the mechanism of sluggish phase transition between cubic and tetragonal Cs_4O_6, specific heat and differential scanning calorimetry (DSC) measurements could be employed.

From magnetic characterization perspective, temperature- and time-dependent magnetisation experiments should be undertaken, employing the cooling protocols that applied in the present study. The emergence of the low-temperature tetragonal phase is essential for an accurate determination of the magnetic behavior of this phase; therefore ultra-slow cooling must be employed.

Aside from magnetisation experiment, μSR measurements could be undertaken for a detailed search of the existence or not of magnetic ordering. As typical magnetic resonance experiments is dependent on the temperature and magnetic field, and the initial spin polarisation is not as high as that of the μSR technique, μSR technique can lead to quantitatively more accurate results.

Finally, similar structural and magnetic characterisation techniques should be undertaken for the sesquioxide Rb_4O_6 to search whether they exhibit comparable properties with Cs_4O_6 and to resolve the contradictory reports on the structural and magnetic properties of Rb_4O_6.

References

[1]   H. W. Kroto, J. R. Heath, S. C. O'Brien, R. F. Curl, and R. E. Smalley, *Nature*, vol. 318, no. 6042, pp. 162–163, 1985.

[2]   W. Kratschmer, L. D. Lamb, K. Fostiropoulos, and D. R. Huffman, *Nature*, vol. 347, no. 6291, pp. 354–358, 1990.

[3]   R. Taylor, J. P. Hare, A. K. Abdul-Sada, and H. W. Kroto, *J. Chem. Soc. Chem. Commun.*, no. 20, pp. 1423–1425, 1990.

[4]   H. Ajie, M. M. Alvarez, S. J. Anz, R. D. Beck, F. Diederich, K. Fostiropoulos, D. R. Huffman, W. Kraetschmer, Y. Rubin, and . et al., *J. Phys. Chem.*, vol. 94, no. 24, pp. 8630–8633, 1990.

[5]   M. Prato, *J. Mater. Chem.*, vol. 7, no. 7, pp. 1097–1109, 1997.

[6]   O. Gunnarsson, *Alkali-Doped Fullerides: Narrow-Band Solids with Unusual Properties*. World Scientific Publishing, 2004.

[7]   W. I. F. David, R. M. Ibberson, J. C. Matthewman, K. Prassides, T. J. S. Dennis, J. P. Hare, H. W. Kroto, R. Taylor, and D. R. M. Walton, *Nature*, vol. 353, no. 6340, pp. 147–149, 1991.

[8]   P. Heiney, J. Fischer, A. McGhie, W. Romanow, A. Denenstein, J. McCauley Jr., A. Smith, and D. Cox, *Phys. Rev. Lett.*, vol. 66, no. 22, pp. 2911–2914, 1991.

[9]   R. Tycko, R. C. Haddon, G. Dabbagh, S. H. Glarum, D. C. Douglass, and A. M. Mujsce, *J. Phys. Chem.*, vol. 95, no. 2, pp. 518–520, 1991.

[10]   R. Tycko, G. Dabbagh, R. M. Fleming, R. C. Haddon, A. V. Makhija, and S. M. Zahurak, *Phys. Rev. Lett.*, vol. 67, no. 14, pp. 1886–1889, 1991.

[11]   C. S. Yannoni, R. D. Johnson, G. Meijer, D. S. Bethune, and J. R. Salem, *J. Phys. Chem.*, vol. 95, no. 1, pp. 9–10, 1991.

[12]   C. S. Yannoni, P. P. Bernier, D. S. Bethune, G. Meijer, and J. R. Salem, *J. Am. Chem. Soc.*, vol. 113, no. 8, pp. 3190–3192, 1991.

[13]   D. A. Neumann, J. R. D. Copley, R. L. Cappelletti, W. A. Kamitakahara, R. M. Lindstrom, K. M. Creegan, D. M. Cox, W. J. Romanow, N. Coustel, J. P. McCauley, N. C. Maliszewskyj, J. E. Fischer, and A. B. Smith, *Phys. Rev. Lett.*, vol. 67, no. 27, pp. 3808–3811, 1991.

[14]   R. F. Kiefl, J. W. Schneider, A. MacFarlane, K. Chow, T. L. Duty, T. L. Estle, B. Hitti, R. L. Lichti, E. J. Ansaldo, C. Schwab, P. W. Percival, G. Wei, S. Wlodek, K. Kojima, W. J. Romanow, J. P. McCauley, N. Coustel, J. E. Fischer, and A. B. Smith, *Phys. Rev. Lett.*, vol. 68, no. 9, pp. 1347–1350, 1992.

[15]   R. F. Kiefl, J. W. Schneider, A. MacFarlane, K. Chow, T. L. Duty, T. L. Estle, B. Hitti, R. L. Lichti, E. J. Ansaldo, C. Schwab, P. W. Percival, G. Wei, S. Wlodek, K. Kojima, W. J.

Romanow, J. P. McCauley, N. Coustel, J. E. Fischer, and A. B. Smith, *Phys. Rev. Lett.*, vol. 68, no. 17, pp. 2708–2711, 1992.

[16] W. I. F. David, R. M. Ibberson, T. J. S. Dennis, J. P. Hare, and K. Prassides, *Europhys. Lett.*, vol. 18, no. 3, pp. 219–225, 1992.

[17] W. I. F. David, R. M. Ibberson, T. J. S. Dennis, J. P. Hare, and K. Prassides, *Europhys. Lett.*, vol. 18, no. 8, pp. 735–736, 1992.

[18] D. W. Murphy, M. J. Rosseinsky, R. M. Fleming, R. Tycko, A. P. Ramirez, R. C. Haddon, T. Siegrist, G. Dabbagh, J. C. Tully, and R. E. Walstedt, *J. Phys. Chem. Solids*, vol. 53, pp. 1321–1332, 1992.

[19] S. Saito and A. Oshiyama, *Phys. Rev. Lett.*, vol. 66, no. 20, pp. 2637–2640, 1991.

[20] A. Hirsch and M. Brettreich, *Fullerenes: Chemistry and Reactions*. Wiley-VCH, 2006.

[21] R. C. Haddon, A. F. Hebard, M. J. Rosseinsky, D. W. Murphy, S. J. Duclos, K. B. Lyons, B. Miller, J. M. Rosamilia, R. M. Fleming, A. R. Kortan, S. H. Glarum, A. V Makhija, A. J. Muller, R. H. Eick, S. M. Zahurak, R. Tycko, G. Dabbagh, and F. A. Thiel, *Nature*, vol. 350, no. 6316, pp. 320–322, 1991.

[22] A. F. Hebard, M. J. Rosseinsky, R. C. Haddon, D. W. Murphy, S. H. Glarum, T. T. M. Palstra, A. P. Ramirez, and A. R. Kortan, *Nature*, vol. 350, pp. 600–601, 1991.

[23] K. Holczer, O. Klein, S. M. Huang, R. B. Kaner, K. J. Fu, R. L. Whetten, and F. Diederich, *Science*, vol. 252, no. 5009, pp. 1154–1157, 1991.

[24] P. W. Stephens, L. Mihaly, P. L. Lee, R. L. Whetten, S. M. Huang, R. Kaner, F. Diederich, and K. Holczer, *Nature*, vol. 351, pp. 632–634, 1991.

[25] M. J. Rosseinsky, A. P. Ramirez, S. H. Glarum, D. W. Murphy, R. C. Haddon, A. F. Hebard, T. T. M. Palstra, A. R. Kortan, S. M. Zahurak, and A. V. Makhija, *Phys. Rev. Lett.*, vol. 66, no. 21, pp. 2830–2832, 1991.

[26] K. Tanigaki, T. W. Ebbesen, S. Saito, J. Mizuki, J. S. Tsai, Y. Kubo, and S. Kuroshima, *Nature*, vol. 352, pp. 222–223, 1991.

[27] A. Y. Ganin, Y. Takabayashi, Y. Z. Khimyak, S. Margadonna, A. Tamai, M. J. Rosseinsky, and K. Prassides, *Nat. Mater.*, vol. 7, pp. 367–371, 2008.

[28] A. Y. Ganin, Y. Takabayashi, P. Jeglič, D. Arčon, A. Potočnik, P. J. Baker, Y. Ohishi, M. T. McDonald, M. D. Tzirakis, A. McLennan, G. R. Darling, M. Takata, M. J. Rosseinsky, and K. Prassides, *Nature*, vol. 466, pp. 221–227, 2010.

[29] M. J. Rosseinsky, D. W. Murphy, R. M. Fleming, R. Tycko, A. P. Ramirez, T. Siegrist, G. Dabbagh, and S. E. Barrett, *Nature*, vol. 356, pp. 416–418, 1992.

[30] K. Tanigaki, I. Hirosawa, T. W. Ebbesen, J. Mizuki, Y. Shimakawa, Y. Kubo, J. S. Tsai, and S. Kuroshima, *Nature*, vol. 356, pp. 419–421, 1992.

[31]   M. Kosaka, K. Tanigaki, K. Prassides, S. Margadonna, A. Lappas, C. M. Brown, and A. N. Fitch, *Phys. Rev. B*, vol. 59, pp. R6628–R6630, 1999.

[32]   O. Zhou, R. M. Fleming, D. W. Murphy, M. J. Rosseinsky, A. P. Ramirez, R. B. Vandover, and R. C. Haddon, *Nature*, vol. 362, pp. 433–435, 1993.

[33]   T. Yildirim, L. Barbedette, J. E. Fischer, C. L. Lin, J. Robert, P. Petit, and T. T. M. Palstra, *Phys. Rev. Lett.*, vol. 77, pp. 167–170, 1996.

[34]   A. R. Kortan, N. Kopylov, S. Glarum, E. M. Gyorgy, A. P. Ramirez, R. M. Fleming, F. A. Thiel, and R. C. Haddon, *Nature*, vol. 355, pp. 529–532, 1992.

[35]   M. Baenitz, M. Heinze, K. Lüders, H. Werner, R. Schlögl, M. Weiden, G. Sparn, and F. Steglich, *Solid State Commun.*, vol. 96, pp. 539–544, 1995.

[36]   C. M. Brown, S. Taga, B. Gogia, K. Kordatos, S. Margadonna, K. Prassides, Y. Iwasa, K. Tanigaki, A. N. Fitch, and P. Pattison, *Phys. Rev. Lett.*, vol. 83, pp. 2258–2261, 1999.

[37]   Y. Iwasa, H. Hayashi, T. Furudate, and T. Mitani, *Phys. Rev. B*, vol. 54, pp. 14960–14962, 1996.

[38]   Y. Iwasa, M. Kawaguchi, H. Iwasaki, T. Mitani, N. Wada, and T. Hasegawa, *Phys. Rev. B*, vol. 57, no. 21, pp. 13395–13398, 1998.

[39]   Y. Iwasa and T. Takenobu, *J. Phys. Condens. Matter*, vol. 15, no. 13, pp. R495–R519, 2003.

[40]   M. S. Dresselhaus, G. Dresselhaus, and P. C. Eklund, *Science of Fullerenes and Carbon Nanotubes*. Academic Press, 1996.

[41]   R. M. Fleming, A. P. Ramirez, M. J. Rosseinsky, D. W. Murphy, R. C. Haddon, S. M. Zahurak, and A. V. Makhija, *Nature*, vol. 352, no. 6338, pp. 787–788, 1991.

[42]   M. S. Deshpande, S. C. Erwin, S. Hong, and E. J. Mele, *Phys. Rev. Lett.*, vol. 71, no. 16, pp. 2619–2622, 1993.

[43]   K. Prassides, C. Christides, I. M. Thomas, J. Mizuki, K. Tanigaki, I. Hirosawa, and T. W. Ebbesen, *Science*, vol. 263, no. 5149, pp. 950–954, 1994.

[44]   J. P. McCauley, Q. Zhu, N. Coustel, O. Zhou, G. Vaughan, S. H. J. Idziak, J. E. Fischer, S. W. Tozer, D. M. Groski, N. Bykovetz, C. L. Lin, A. R. McGhie, B. H. Allen, W. J. Romanow, A. M. Denenstein, and A. B. Smith, *J. Am. Chem. Soc.*, vol. 113, no. 22, pp. 8537–8538, 1991.

[45]   H. H. Wang, A. M. Kini, B. M. Savall, K. D. Carlson, J. M. Williams, K. R. Lykke, P. Wurz, D. H. Parker, M. J. Pellin, D. M. Gruen, U. Welp, W. K. Kwok, S. Fleshler, and G. W. Crabtree, *Inorg. Chem.*, vol. 30, no. 14, pp. 2838–2839, 1991.

[46]   H. H. Wang, A. M. Kini, B. M. Savall, K. D. Carlson, J. M. Williams, M. W. Lathrop, K. R. Lykke, D. H. Parker, P. Wurz, and . et al., *Inorg. Chem.*, vol. 30, no. 15, pp. 2962–2963, 1991.

[47]   D. R. Buffinger, R. P. Ziebarth, V. A. Stenger, C. Recchia, and C. H. Pennington, *J. Am. Chem. Soc.*, vol. 115, no. 20, pp. 9267–9270, 1993.

[48]   R. D. D. Boss, J. S. S. Briggs, E. W. W. Jacobs, T. E. E. Jones, and P. A. A. Mosier-Boss, *Phys. C-Superconductivity Its Appl.*, vol. 243, no. 1–2, pp. 29–34, 1995.

[49]   S. Cooke, S. Glenis, X. Chen, C. L. Lin, and M. M. Labes, *J. Mater. Chem.*, vol. 6, no. 1, pp. 1–3, 1996.

[50]   A. Y. Ganin, Y. Takabayashi, C. A. Bridges, Y. Z. Khimyak, S. Margadonna, K. Prassides, and M. J. Rosseinsky, *J. Am. Chem. Soc.*, vol. 128, no. 46, pp. 14784–5, 2006.

[51]   X. H. Liu, W. C. Wan, S. M. Owens, and W. E. Broderick, *J. Am. Chem. Soc.*, vol. 116, no. 12, pp. 5489–5490, 1994.

[52]   X. Chen, Y. Maniwa, C. A. Kuper, S. Glenis, C. L. Lin, and M. M. Labes, *Chem. Mater.*, vol. 9, no. 12, pp. 3049–3051, 1997.

[53]   P. Dahlke, M. S. Denning, P. F. Henry, and M. J. Rosseinsky, *J. Am. Chem. Soc.*, vol. 122, no. 49, pp. 12352–12361, 2000.

[54]   S. P. Kelty, C. C. Chen, and C. M. Lieber, *Nature*, vol. 352, no. 6332, pp. 223–225, 1991.

[55]   T. T. M. Palstra, O. Zhou, Y. Iwasa, P. E. Sulewski, R. M. Fleming, and B. R. Zegarski, *Solid State Commun.*, vol. 93, no. 4, pp. 327–330, 1995.

[56]   A. G. McLennan, A. Y. Ganin, Y. Takabayashi, R. H. Colman, R. H. Zadik, M. J. Rosseinsky, and K. Prassides, *Faraday Discuss.*, vol. 173, pp. 95–103, 2014.

[57]   J. Bardeen, L. N. Cooper, and J. R. Schrieffer, *Phys. Rev.*, vol. 108, no. 5, pp. 1175–1204, 1957.

[58]   O. Gunnarsson, *Rev. Mod. Phys.*, vol. 69, no. 2, pp. 575–606, 1997.

[59]   C. H. Pennington and V. A. Stenger, *Rev. Mod. Phys.*, vol. 68, no. 3, pp. 855–910, 1996.

[60]   C. M. Varma, J. Zaanen, and K. Raghavachari, *Science*, vol. 254, no. 5034, pp. 989–992, 1991.

[61]   G. Baskaran and E. Tosatti, *Curr. Sci.*, vol. 61, no. 1, pp. 33–39, 1991.

[62]   S. Chakravarty and S. Kivelson, *Europhys. Lett.*, vol. 16, no. 8, pp. 751–756, 1991.

[63]   S. Chakravarty, M. P. Gelfand, and S. Kivelson, *Science*, vol. 254, no. 5034, pp. 970–974, 1991.

[64]   W. L. McMillan, *Phys. Rev.*, vol. 167, no. 2, pp. 331–344, 1968.

[65]   M. J. Rosseinsky, *Chem. Mater.*, vol. 10, no. 10, pp. 2665–2685, 1998.

[66] M. T. McDonald, "Structural and electronic properties of fulleride superconductors," Department of Chemistry, Durham University, 2010.

[67] R. H. Zadik, Y. Takabayashi, G. Klupp, R. H. Colman, A. Y. Ganin, A. Potocnik, P. Jeglic, D. Arcon, P. Matus, K. Kamaras, Y. Kasahara, Y. Iwasa, A. N. Fitch, Y. Ohishi, G. Garbarino, K. Kato, M. J. Rosseinsky, and K. Prassides, *Sci. Adv.*, vol. 1, no. e1500059, pp. 1–9, 2015.

[68] C. Christides, D. A. Neumann, K. Prassides, J. R. D. Copley, J. J. Rush, M. J. Rosseinsky, D. W. Murphy, and R. C. Haddon, *Phys. Rev. B*, vol. 46, pp. 12088–12091, 1992.

[69] B. Mitrović, C. R. Leavens, and J. P. Carbotte, *Phys. Rev. B*, vol. 21, no. 11, pp. 5048–5054, 1980.

[70] A. Potočnik, A. Krajnc, P. Jeglič, Y. Takabayashi, A. Y. Ganin, K. Prassides, M. J. Rosseinsky, and D. Arčon, *Sci. Rep.*, vol. 4, p. 5, 2014.

[71] Z. Zhang, C. Chen, S. P. Kelty, H. Dai, and C. M. Lieber, *Nature*, vol. 353, no. 6342, pp. 333–335, 1991.

[72] P. Jess, S. Behler, M. Bernasconi, V. Thommen, H. P. Lang, M. Baenitz, K. Lüders, and H. Güntherodt, *Phys. C Supercond.*, vol. 235–240, no. 4, pp. 2499–2500, 1994.

[73] R. Kiefl, W. MacFarlane, K. Chow, S. Dunsiger, T. Duty, T. Johnston, J. Schneider, J. Sonier, L. Brard, R. Strongin, J. Fischer, and A. Smith, *Phys. Rev. Lett.*, vol. 70, no. 25, pp. 3987–3990, 1993.

[74] W. MacFarlane, R. Kiefl, S. Dunsiger, J. Sonier, J. Chakhalian, J. Fischer, T. Yildirim, and K. Chow, *Phys. Rev. B*, vol. 58, no. 2, pp. 1004–1024, 1998.

[75] P. Wzietek, T. Mito, H. Alloul, D. Pontiroli, M. Aramini, and M. Ricco, *Phys. Rev. Lett.*, vol. 112, p. 5, 2014.

[76] R. W. Lof, M. A. van Veenendaal, B. Koopmans, H. T. Jonkman, and G. A. Sawatzky, *Phys. Rev. Lett.*, vol. 68, no. 26, pp. 3924–3927, 1992.

[77] A. Georges, G. Kotliar, W. Krauth, and M. J. Rozenberg, *Rev. Mod. Phys.*, vol. 68, no. 1, pp. 13–125, 1996.

[78] O. Gunnarsson, E. Koch, and R. M. Martin, *Phys. Rev. B*, vol. 54, no. 16, pp. 11026–11029, 1996.

[79] G. R. Darling, A. Y. Ganin, M. J. Rosseinsky, Y. Takabayashi, and K. Prassides, *Phys. Rev. Lett.*, vol. 101, no. 13, 2008.

[80] Y. Takabayashi, A. Y. Ganin, P. Jeglic, D. Arcon, T. Takano, Y. Iwasa, Y. Ohishi, M. Takata, N. Takeshita, K. Prassides, and M. J. Rosseinsky, *Science*, vol. 323, no. 5921, pp. 1585–1590, 2009.

[81] M. Capone, M. Fabrizio, C. Castellani, and E. Tosatti, *Rev. Mod. Phys.*, vol. 81, no. 2, pp. 943–958, 2009.

[82] Y. Iwasa, *Nature*, vol. 466, pp. 191–192, 2010.

[83] V. Brouet, H. Alloul, S. Gàràj, and L. Forrò, "NMR studies of insulating, metallic, and superconducting fullerides: Importance of correlations and Jahn-Teller distortions," in *Fullerene-Based Materials: Structures and Properties*, vol. 109, K. Prassides, Ed. Springer, 2004, pp. 165–199.

[84] M. Capone, M. Fabrizio, C. Castellani, and E. Tosatti, *Science*, vol. 296, no. 5577, pp. 2364–2366, 2002.

[85] Y. Ihara, H. Alloul, P. Wzietek, D. Pontiroli, M. Mazzani, and M. Ricco, *Phys. Rev. Lett.*, vol. 104, no. 25, p. 4, 2010.

[86] G. Klupp, P. Matus, K. Kamarás, A. Y. Ganin, A. McLennan, M. J. Rosseinsky, Y. Takabayashi, M. T. McDonald, and K. Prassides, *Nat. Commun.*, vol. 3, no. 912, 2012.

[87] R. J. Meier and R. B. Helmholdt, *Phys. Rev. B*, vol. 29, no. 3, pp. 1387–1393, 1984.

[88] Y. Akahama, H. Kawamura, D. Häusermann, M. Hanfland, and O. Shimomura, *Phys. Rev. Lett.*, vol. 74, no. 23, pp. 4690–4693, 1995.

[89] K. Shimizu, K. Suhara, M. Ikumo, M. I. Eremets, and K. Amaya, *Nature*, vol. 393, no. 6687, pp. 767–769, 1998.

[90] Y. A. Freiman and H. J. Jodl, *Phys. Rep.*, vol. 401, no. 1–4, pp. 1–228, 2004.

[91] I. N. Goncharenko, O. L. Makarova, and L. Ulivi, *Phys. Rev. Lett.*, vol. 93, no. 5, 2004.

[92] W. Hesse, M. Jansen, and W. Schnick, *Prog. Solid State Chem.*, vol. 19, no. 1, pp. 47–110, 1989.

[93] A. Helms and W. Klemm, *Zeitschrift für Anorg. und Allg. Chemie*, vol. 242, no. 2, pp. 201–214, 1939.

[94] M. Jansen and N. Korber, *Zeitschrift für Anorg. und Allg. Chemie*, vol. 598, no. 1, pp. 163–173, 1991.

[95] M. Jansen, R. Hagenmayer, N. Korber, and J. Rouxel, *Comptes Rendus l'Académie des Sci. - Ser. IIC - Chem.*, vol. 2, no. 11–13, pp. 591–594, 1999.

[96] M. Labhart, D. Raoux, W. Känzig, and M. A. Bösch, *Phys. Rev. B*, vol. 20, no. 1, pp. 53–70, 1979.

[97] M. Ziegler, M. Rosenfeld, W. Känzig, and P. Fischer, *Helv. Phys. Acta*, vol. 49, no. 1, pp. 57–90, 1976.

[98] A. Zumsteg, M. Ziegler, W. Känzig, and M. Bösch, *Phys. Condens. Matter*, vol. 17, no. 4, pp. 267–291, 1974.

[99] M. Rosenfeld, M. Ziegler, and W. Känzig, *Helv. Phys. Acta*, vol. 51, no. 2, pp. 298–320, 1978.

[100] J. Winterlik, G. Fecher, C. Jenkins, S. Medvedev, C. Felser, J. Kübler, C. Mühle, K. Doll, M. Jansen, T. Palasyuk, I. Trojan, M. Eremets, and F. Emmerling, *Phys. Rev. B*, vol. 79, no. 214410, pp. 1–6, 2009.

[101] J. J. Attema, G. A. de Wijs, G. R. Blake, and R. A. de Groot, *J. Am. Chem. Soc.*, vol. 127, no. 46, pp. 16325–16328, 2005.

[102] J. Winterlik, G. H. Fecher, C. Felser, C. Mühle, and M. Jansen, *J. Am. Chem. Soc.*, vol. 129, no. 22, pp. 6990–6991, 2007.

[103] J. Winterlik, G. H. Fecher, C. A. Jenkins, C. Felser, C. Mühle, K. Doll, M. Jansen, L. M. Sandratskii, and J. Kübler, *Phys. Rev. Lett.*, vol. 102, no. 016401, p. 016401, 2009.

[104] C. Urano, M. Nohara, S. Kondo, F. Sakai, H. Takagi, T. Shiraki, and T. Okubo, *Phys. Rev. Lett.*, vol. 85, no. 5, pp. 1052–1055, 2000.

[105] G. Khaliullin, P. Horsch, and A. M. Oleś, *Phys. Rev. Lett.*, vol. 86, no. 17, pp. 3879–3882, 2001.

[106] D. Arčon, K. Anderle, M. Klanjšek, A. Sans, C. Mühle, P. Adler, W. Schnelle, M. Jansen, and C. Felser, *Phys. Rev. B*, vol. 88, no. 224409, pp. 1–7, 2013.

[107] P. Debye and P. Scherrer, *Phys. Zeitschrift*, vol. 17, pp. 277 – 283, 1916.

[108] P. Debye and P. Scherrer, *Phys. Zeitschrift*, vol. 18, pp. 291 – 301, 1917.

[109] H. M. Rietveld, *J. Appl. Crystallogr.*, vol. 2, no. 2, pp. 65–71, 1969.

[110] C. Kittel, *Introduction to Solid State Physics*, 8th ed. Wiley, 2005.

[111] T. Hahn, *International Tables for Crystallography, Space-Group Symmetry*. Wiley, 2005.

[112] P. Ewald, *Zeitschrift für Krist.*, vol. 56, no. 2, pp. 129–156, 1921.

[113] V. K. Pecharsky and P. Y. Zavalij, *Fundamentals Of Powder Diffraction And Structural Characterization Of Materials*. Springer, 2004.

[114] R. Dinnebier and S. Billinge, "Principles of Powder Diffraction," in *Powder Diffraction: Theory and Practice*, R. E. Dinnebier and S. J. L. Billinge, Eds. Cambridge: Royal Society of Chemistry, 2008, pp. 1 – 582.

[115] R. C. Reynolds, "Principles of Powder Diffraction," in *Modern Powder Diffraction*, vol. 20, D. L. Bish and J. E. Post, Eds. 1989.

[116] J. K. Cockcroft and A. N. Fitch, "Chapter 2 Experimental Setups," in *Powder Diffraction: Theory and Practice*, The Royal Society of Chemistry, 2008, pp. 20–57.

[117] M. T. Hutchings and C. G. Windsor, "25. Industrial Applications," in *Neutron Scattering*, vol. Volume 23, Academic Press, 1987, pp. 405–482.

[118] *International Tables for Crystallography, Mathematical, Physical and Chemical Tables.* Springer Science & Business Media, 2004.

[119] B. Buras and L. Gerward, *Acta Crystallogr. Sect. A*, vol. 31, no. 3, pp. 372–374, 1975.

[120] R. A. Young, "Introduction to the Rietveld method," in *The Rietveld method*, R. A. Young, Ed. Oxford University Press, 1993, pp. 1–38.

[121] L. B. McCusker, R. B. Von Dreele, D. E. Cox, D. Louër, and P. Scardi, *J. Appl. Crystallogr.*, vol. 32, no. 1, pp. 36–50, 1999.

[122] B. H. Toby, *J. Appl. Crystallogr.*, vol. 34, no. 2, pp. 210–213, 2001.

[123] R. A. Young, P. E. Mackie, and R. B. von Dreele, *J. Appl. Crystallogr.*, vol. 10, no. 4, pp. 262–269, 1977.

[124] A. Albinati and B. T. M. Willis, *J. Appl. Crystallogr.*, vol. 15, no. 4, pp. 361–374, 1982.

[125] P. Thompson, D. E. Cox, and J. B. Hastings, *J. Appl. Crystallogr.*, vol. 20, no. 2, pp. 79–83, 1987.

[126] R. A. Young and D. B. Wiles, *J. Appl. Crystallogr.*, vol. 15, no. 4, pp. 430–438, 1982.

[127] A. C. Larson and R. B. Von Dreele, "General Structure Analysis System (GSAS)," Los Alamos National Laboratory Report LAUR 86-748, 2004.

[128] R. Smith, "Refinement of time-of-flight Profile Parameters in GSAS," *Crystallography Group, ISIS Facility, Rutherford Appleton Laboratory*, Oxford, pp. 1–4.

[129] B. H. Toby, *Powder Diffr.*, vol. 21, no. December 2005, pp. 67–70, 2006.

[130] R. M. Hazen, R. T. Downs, and C. T. Prewitt, "Principles of comparative crystal chemistry," in *High-Temperature and High-Pressure Crystal Chemistry*, vol. 41, Mineralogical Society of America, 2000, pp. 1–33.

[131] R. J. Angel, "Equations of state," in *High-Temperature and High-Pressure Crystal Chemistry*, vol. 41, Mineralogical Society of America, 2000, pp. 35–59.

[132] F. D. Murnaghan, *Proc. Natl. Acad. Sci. U. S. A.*, vol. 30, pp. 244–247, 1944.

[133] F. Birch, *Phys. Rev.*, vol. 71, no. 11, pp. 809–824, 1947.

[134] F. Sayetat, P. Fertey, and M. Kessler, *J. Appl. Crystallogr.*, vol. 31, no. 2, pp. 121–127, 1998.

[135] P. Debye, *Ann. Phys.*, vol. 39, no. 14, pp. 789–839, 1912.

[136] S. F. J. Cox, *J. Phys. C Solid State Phys.*, vol. 20, no. 22, pp. 3187–3319, 1987.

[137] S. J. Blundell, *Chem. Rev.*, vol. 104, no. 11, pp. 5717–36, 2004.

[138] S. F. J. Cox, *Reports Prog. Phys.*, vol. 72, no. 11, 2009.

[139] A. Yaouanc and P. D. de Réotier, *Muon Spin Rotation, Relaxation, and Resonance: Applications to Condensed Matter*. Oxford University Press, 2011.

[140] P. J. C. King, R. De Renzi, S. P. Cottrell, A. D. Hillier, S. F. J. Cox, R. de Renzi, S. P. Cottrell, A. D. Hillier, and S. F. J. Cox, *Phys. Scr.*, vol. 88, no. 6, 2013.

[141] A. Zorko, F. Bert, P. Mendels, K. Marty, and P. Bordet, *Phys. Rev. Lett.*, vol. 104, no. 5, 2010.

[142] S. R. Giblin, J. D. M. Champion, H. D. Zhou, C. R. Wiebe, J. S. Gardner, I. Terry, S. Calder, T. Fennell, and S. T. Bramwell, *Phys. Rev. Lett.*, vol. 101, no. 23, 2008.

[143] T. Lancaster, S. Blundell, D. Andreica, M. Janoschek, B. Roessli, S. Gvasaliya, K. Conder, E. Pomjakushina, M. Brooks, P. Baker, D. Prabhakaran, W. Hayes, and F. Pratt, *Phys. Rev. Lett.*, vol. 98, no. 19, 2007.

[144] P. Mendels, F. Bert, M. A. de Vries, A. Olariu, A. Harrison, F. Duc, J. C. Trombe, J. S. Lord, A. Amato, and C. Baines, *Phys. Rev. Lett.*, vol. 98, no. 7, 2007.

[145] J. Friedman and V. Telegdi, *Phys. Rev.*, vol. 105, no. 5, pp. 1681–1682, 1957.

[146] V. Storchak and N. Prokof'ev, *Rev. Mod. Phys.*, vol. 70, no. 3, pp. 929–978, 1998.

[147] B. D. Patterson, E. Holzschuh, W. Kündig, P. F. Meier, W. Odermatt, J. P. F. Sellschop, and M. C. Stemmet, *Hyperfine Interact.*, vol. 18, no. 1–4, pp. 605–610, 1984.

[148] R. F. Kiefl, T. L. Duty, J. W. Schneider, A. MacFarlane, K. Chow, J. Elzey, P. Mendels, G. D. Morris, J. H. Brewer, E. J. Ansaldo, C. Niedermayer, D. R. Noakes, C. E. Stronach, B. Hitti, and J. E. Fischer, *Phys. Rev. Lett.*, vol. 69, no. 13, pp. 2005–2008, 1992.

[149] J. E. Sonier, "Muon Spin Rotation/Relaxation/Resonance (μSR) Brochure," *Simon Fraser University*, pp. 1–16, 2002.

[150] B. D. Patterson, *Rev. Mod. Phys.*, vol. 60, no. 1, pp. 69–159, 1988.

[151] K. H. Chow, R. L. Lichti, R. F. Kiefl, S. Dunsiger, T. L. Estle, B. Hitti, R. Kadono, W. A. MacFarlane, J. W. Schneider, D. Schumann, and M. Shelley, *Phys. Rev. B*, vol. 50, no. 12, pp. 8918–8921, 1994.

[152] A. Schenck, *Muon spin rotation spectroscopy*. Bristol: Adam Hilger, 1985.

[153] W. A. Macfarlane, "MuSR Studies of the Metallic Alkali Fullerides," The University of British Colombia, 1997.

[154] "Introduction to the ESRF for Journalists," 2013.

[155] A. N. Fitch, *Solid State Phenom.*, vol. 130, pp. 7–14, 2007.

[156] J. P. Wright, G. B. M. Vaughan, and A. N. Fitch, "Merging data from a multi-detector continuous scanning powder diffraction system," vol. 1. IUCr Computing Commision Newsletter, p. 92, 2003.

[157] "ID31." [Online]. Available: http://www.esrf.eu/home/UsersAndScience/Experiments/Beamlines/content/content/id31.html. [Accessed: 27-Mar-2015].

[158] K. Kato, R. Hirose, M. Takemoto, S. Ha, J. Kim, M. Higuchi, R. Matsuda, S. Kitagawa, M. Takata, R. Garrett, I. Gentle, K. Nugent, and S. Wilkins, "The RIKEN Materials Science Beamline at SPring-8: Towards Visualization of Electrostatic Interaction," in *SRI 2009, 10th International Conference on Radiation Instrumentation*, 2010, vol. 1234, no. 1, pp. 875–878.

[159] Y. Ohishi, N. Hirao, N. Sata, K. Hirose, and M. Takata, *High Press. Res.*, 2008.

[160] H. K. Mao, J. Xu, and P. M. Bell, *J. Geophys. Res.*, vol. 91, no. B5, p. 4673, 1986.

[161] H. Fujihisa, *Rev. High Press. Sci. Technol.*, vol. 15, no. 1, pp. 29–35, 2005.

[162] "Research at ISIS," *Education in Chemistry*, pp. 180–184, Nov-2011.

[163] "Neutron Training Course Manual," Didcot, Oxford, pp. 1–92, 2014.

[164] N. J. Rhodes, M. W. Johnson, and E. M. Schooneveld, "The Development of Neutron Detectors for the GEM Instrument at ISIS," in *15th Meeting of the International Collaboration on Advanced Neutron Sources*, 2001, pp. 645–653.

[165] A. D. Hillier, D. J. Adams, P. J. Baker, A. Bekasovs, F. C. Coomer, S. P. Cottrell, S. D. Higgins, S. J. S. Jago, K. G. Jones, J. S. Lord, A. Markvardsen, P. G. Parker, J. N. T. Peck, F. L. Pratt, M. Tftelling, and R. E. Williamson, "Developments at the ISIS muon source and the concomitant benefit to the user community," in *13th International Conference on Muon Spin Rotation, Relaxation and Resonance*, 2014, vol. 551.

[166] O. Arnold, J. C. Bilheux, J. M. Borreguero, and A. Buts, *Nucl. Instruments Methods Phys. Res. Sect. A Accel. Spectrometers, Detect. Assoc. Equip.*, vol. 764, no. 0, pp. 156–166, 2014.

[167] Z. Salman, P. J. Baker, S. J. Blundell, S. P. Cottrell, S. R. Giblin, a. D. Hillier, B. H. Holsman, P. J. C. King, T. Lancaster, J. S. Lord, I. McKenzie, J. Nightingale, F. L. Pratt, and R. Scheuermann, *Phys. B Condens. Matter*, vol. 404, no. 5–7, pp. 978–981, 2009.

[168] F. Pratt, *Phys. B Condens. Matter*, vol. 289–290, pp. 710–714, 2000.

[169] M. McElfresh, "Fundamentals of Magnetism and Magnetic Measurements featuring Quantum Design's Magnetic Property Measurement System," 1994.

[170] B. D. Cullity and C. D. Graham, "Magnetic properties of superconductors," in *Introduction to Magnetic Materials*, 2nd ed., John Wiley & Sons, 2011, p. 568.

[171] *easyLab Mcell 10 User Guide*. easyLab Technologies Limited, 2006.

[172] J. Diederichs, A. K. Gangopadhyay, and J. S. Schilling, *Phys. Rev. B*, vol. 54, pp. R9662–R9665, 1996.

[173] L. W. Finger, D. E. Cox, and A. P. Jephcoat, *J. Appl. Crystallogr.*, vol. 27, pp. 892–900, 1994.

[174] J. Laugier and B. Bochu, "LMGP-Suite Suite of Programs for the interpretation of X-ray Experiments." ENSP/Laboratoire des Matériaux et du Génie Physique, 1999.

[175] O. Zhou and D. E. Cox, *J. Phys. Chem. Solids*, vol. 53, pp. 1373–1390, 1992.

[176] O. Zhou, J. E. Fischer, N. Coustel, S. Kycia, Q. Zhu, A. R. McGhie, W. J. Romanow, J. P. McCauley, A. B. Smith, and D. E. Cox, *Nature*, vol. 351, no. 6326, pp. 462–464, 1991.

[177] A. Potočnik, "Magnetic Resonance of Molecular Superconductors Bordering the Antiferromagnetic Mott-Insulating State," University of Ljubljana, 2013.

[178] P. Dahlke, P. F. Henry, and M. J. Rosseinsky, *J. Mater. Chem.*, vol. 8, pp. 1571–1576, 1998.

[179] A. Lappas, M. Kosaka, K. Tanigaki, and K. Prassides, *J. Am. Chem. Soc.*, vol. 117, pp. 7560–7561, 1995.

[180] J. P. Attfield, A. L. Kharlanov, and J. A. McAllister, *Nature*, vol. 394, no. 6689, pp. 157–159, 1998.

[181] J. A. McAllister and J. P. Attfield, *Phys. Rev. B*, vol. 66, no. 1, pp. 1–10, 2002.

[182] A. K. Kundu, M. M. Seikh, K. Ramesha, and C. N. R. Rao, *J. Phys. Condens. Matter*, vol. 17, no. 26, pp. 4171–4180, 2005.

[183] A. K. Kundu and C. N. R. Rao, *Solid State Commun.*, vol. 134, no. 5, pp. 307–311, 2005.

[184] J. B. Goodenough, *Localized to Itiner. Electron. Transit. Perovskite Oxides*, vol. 98, pp. 1–16, 2001.

[185] H. D. Zhou and J. B. Goodenough, *Phys. Rev. B*, vol. 71, p. 6, 2005.

[186] A. Jayaraman, D. B. McWhan, J. P. Remeika, and P. D. Dernier, *Phys. Rev. B*, vol. 2, no. 9, pp. 3751–3756, 1970.

[187] O. Zhou, Q. Zhu, J. E. Fischer, N. Coustel, G. B. Vaughan, P. A. Heiney, J. P. McCauley, and A. B. Smith, *Science*, vol. 255, no. 5046, pp. 833–5, 1992.

[188] A. A. Sabouri-Dodaran, M. Marangolo, C. Bellin, F. Mauri, G. Fiquet, G. Loupias, M. Mezouar, W. Crichton, C. Hérold, F. Rachdi, and S. Rabii, *Phys. Rev. B*, vol. 70, 2004.

[189] V. Buntar and H. W. Weber, *Supercond. Sci. Technol.*, vol. 9, pp. 599–615, 1996.

[190] V. Buntar, M. Riccò, L. Cristofolini, H. W. Weber, and F. Bolzoni, *Phys. Rev. B*, vol. 52, pp. 4432–4437, 1995.

[191] G. Sparn, J. D. Thompson, R. L. Whetten, S. M. Huang, R. B. Kaner, F. Diederich, G. Grüner, and K. Holczer, *Phys. Rev. Lett.*, vol. 68, pp. 1228–1231, 1992.

[192] K. Holczer, O. Klein, G. Grüner, J. D. Thompson, F. Diederich, and R. L. Whetten, *Phys. Rev. Lett.*, vol. 67, no. 2, pp. 271–274, 1991.

[193] K. Tanigaki and K. Prassides, *J. Mater. Chem.*, vol. 5, pp. 1515–1527, 1995.

[194] G. A. Bain and J. F. Berry, *J. Chem. Educ.*, vol. 85, pp. 532–536, 2008.

[195] K. Prassides, S. Margadonna, D. Arcon, A. Lappas, H. Shimoda, and Y. Iwasa, *J. Am. Chem. Soc.*, vol. 121, no. 48, pp. 11227–11228, 1999.

[196] M. Capone, M. Fabrizio, and E. Tosatti, *Phys. Rev. Lett.*, vol. 86, no. 23, pp. 5361–5364, 2001.

[197] M. Lüders, A. Bordoni, N. Manini, A. D. Corso, M. Fabrizio, and E. Tosatti, *Philos. Mag. B*, vol. 82, no. 15, pp. 1611–1647, 2002.

[198] M. Fabrizio and E. Tosatti, *Phys. Rev. B*, vol. 55, no. 20, pp. 13465–13472, 1997.

[199] K. Tanigaki, M. Kosaka, T. Manako, Y. Kubo, I. Hirosawa, K. Uchida, and K. Prassides, *Chem. Phys. Lett.*, vol. 240, pp. 627–632, 1995.

[200] G. J. Burkhart and C. Meingast, *Phys. Rev. B*, vol. 54, no. 10, pp. R6865–R6868, 1996.

[201] V. P. Antropov, I. I. Mazin, O. K. Andersen, A. I. Liechtenstein, and O. Jepsen, *Phys. Rev. B*, vol. 47, pp. 12373–12376, 1993.

[202] A. P. Ramirez, M. J. Rosseinsky, D. W. Murphy, and R. C. Haddon, *Phys. Rev. Lett.*, vol. 69, pp. 1687–1690, 1992.

[203] G. Sparn, J. D. Thompson, S. M. Huang, R. B. Kaner, F. Diederich, R. L. Whetten, G. Grüner, and K. Holczer, *Science*, vol. 252, no. 5014, pp. 1829–31, 1991.

[204] Y. Nomura, S. Sakai, M. Capone, and R. Arita, *Sci. Adv.*, vol. 1, no. 7, pp. e1500568–e1500568, 2015.

[205] F. Kagawa, K. Miyagawa, and K. Kanoda, *Nature*, vol. 436, no. 7050, pp. 534–7, 2005.

[206] N. A. Babushkina, L. M. Belova, O. Y. Gorbenko, A. R. Kaul, A. A. Bosak, V. I. Ozhogin, and K. I. Kugel, *Nature*, vol. 391, pp. 159–161, 1998.

[207] P. Hammel, M. Takigawa, R. Heffner, Z. Fisk, and K. Ott, *Phys. Rev. Lett.*, vol. 63, no. 18, pp. 1992–1995, 1989.

[208] Y. Kitaoka, K. Ishida, F. Fujiwara, T. Kondo, K. Asayama, M. Horvatic, Y. Berthier, P. Butaud, P. Segransan, C. Berthier, H. Katayama-Yoshida, Y. Okabe, and T. Takahashi, "NMR Study of High-Tc Superconductors," in *Strong Correlation and Superconductivity*, vol. 89, Springer Berlin Heidelberg, 1989, pp. 262–273.

[209] L. C. Hebel and C. P. Slichter, *Phys. Rev.*, vol. 113, no. 6, pp. 1504–1519, 1959.

[210] V. A. Stenger, C. H. Pennington, D. R. Buffinger, and R. P. Ziebarth, *Phys. Rev. Lett.*, vol. 74, no. 9, pp. 1649–1652, 1995.

[211] M. Telling, "Muon Data Analysis: Introduction to Mantid Muon Data Analysis Getting Started," 2014.

[212] F. Pratt, "WiMDA Manual," 2005.

[213] I. McKenzie, *Phys. Chem. Chem. Phys.*, vol. 16, no. 22, pp. 10600–6, 2014.

[214] R. Tycko, G. Dabbagh, M. Rosseinsky, D. Murphy, A. Ramirez, and R. Fleming, *Phys. Rev. Lett.*, vol. 68, no. 12, pp. 1912–1915, 1992.

[215] L. Coffey, *Phys. Rev. Lett.*, vol. 64, no. 9, p. 1071, 1990.

[216] P. B. Allen and D. Rainer, *Nature*, vol. 349, no. 6308, pp. 396–398, 1991.

[217] R. Akis and J. P. Carbotte, *Solid State Commun.*, vol. 78, no. 5, pp. 393–396, 1991.

[218] J. R. Clem, *Ann. Phys. (N. Y).*, vol. 40, no. 2, pp. 268–295, 1966.

[219] R. C. Dynes, V. Narayanamurti, and J. P. Garno, *Phys. Rev. Lett.*, vol. 41, no. 21, pp. 1509–1512, 1978.

[220] H. Y. Choi, *Phys. Rev. Lett.*, vol. 81, no. 2, pp. 441–444, 1998.

[221] R. Kiefl, T. Duty, J. Schneider, A. MacFarlane, K. Chow, J. Elzey, P. Mendels, G. Morris, J. Brewer, E. Ansaldo, C. Niedermayer, D. Noakes, C. Stronach, B. Hitti, and J. Fischer, *Phys. Rev. Lett.*, vol. 70, no. 9, pp. 1353–1353, 1993.

[222] L. Degiorgi, P. Wachter, G. Grüner, S.-M. Huang, J. Wiley, and R. B. Kaner, *Phys. Rev. Lett.*, vol. 69, no. 20, pp. 2987–2990, 1992.

[223] Z. Shen, D. Dessau, B. Wells, D. King, W. Spicer, A. Arko, D. Marshall, L. Lombardo, A. Kapitulnik, P. Dickinson, S. Doniach, J. DiCarlo, T. Loeser, and C. Park, *Phys. Rev. Lett.*, vol. 70, no. 10, pp. 1553–1556, 1993.

[224] K. Tanaka, W. S. Lee, D. H. Lu, A. Fujimori, T. Fujii, Risdiana, I. Terasaki, D. J. Scalapino, T. P. Devereaux, Z. Hussain, and Z.-X. Shen, *Science*, vol. 314, no. 5807, pp. 1910–3, 2006.

[225] Y. M. Xu, P. Richard, K. Nakayama, T. Kawahara, Y. Sekiba, T. Qian, M. Neupane, S. Souma, T. Sato, T. Takahashi, H. Q. Luo, H. H. Wen, G. F. Chen, N. L. Wang, Z. Wang, Z. Fang, X. Dai, and H. Ding, *Nat. Commun.*, vol. 2, p. 394, 2011.

[226] H. Seyeda and M. Jansen, *J. Chem. Soc. Dalt. Trans.*, no. 6, pp. 875–876, 1998.

[227] T. Bremm and M. Jansen, *Zeitschrift für Anorg. und Allg. Chemie*, vol. 610, no. 4, pp. 64–66, 1992.

[228] V. Y. Dudarev, A. B. Tsentsiper, and M. S. Dobrolyubova, *Kristallografiya*, vol. 18, no. 4, pp. 759–763, 1973.

[229] A. Sans, J. Nuss, G. H. Fecher, C. Mühle, C. Felser, and M. Jansen, *Zeitschrift fur Anorg. und Allg. Chemie*, vol. 640, no. 7, pp. 1239–1246, 2014.

[230] D. Cox, E. Samuelsen, and K. Beckurts, *Phys. Rev. B*, vol. 7, no. 7, pp. 3102–3111, 1973.

[231] R. Roy, "A Syncretist Classification of Phase Transitions," in *Phase Transitions - 1973: Proceedings of the Conference on Phase Transitions and Their Applications in Materials Science, University Park, Pennsylvania, May 23-25, 1973*, Elsevier, 2013, pp. 13–37.

[232] Y. Mnyukh, "On the Phase Transitions that cannot Materialize," *American Journal of Condensed Matter Physics*, vol. 4, no. 1. Scientific & Academic Publishing, pp. 1–12, 2014.

[233] M. J. Buerger, *Acta Crystallogr.*, vol. 4, no. 6, pp. 531–544, 1951.

[234] K. Nasu, Ed., *Relaxations of Excited States and Photo-Induced Structural Phase Transitions*, vol. 124. Berlin, Heidelberg: Springer Berlin Heidelberg, 1997.

[235] K. Prassides, *Nat. Chem.*, vol. 2, no. 7, pp. 517–9, 2010.

[236] O. Sato, T. Iyoda, A. Fujishima, and K. Hashimoto, *Science*, vol. 272, no. 5262, pp. 704–5, 1996.

[237] P. Gütlich, Y. Garcia, and T. Woike, *Coord. Chem. Rev.*, vol. 219–221, pp. 839–879, 2001.

[238] A. Bleuzen, C. Lomenech, V. Escax, F. Villain, F. Varret, C. Cartier dit Moulin, and M. Verdaguer, *J. Am. Chem. Soc.*, vol. 122, no. 28, pp. 6648–6652, 2000.

[239] S. Margadonna, K. Prassides, and A. N. Fitch, *Angew. Chemie*, vol. 116, no. 46, pp. 6476–6479, 2004.

[240] D. Papanikolaou, S. Margadonna, W. Kosaka, S. Ohkoshi, M. Brunelli, and K. Prassides, *J. Am. Chem. Soc.*, vol. 128, no. 25, pp. 8358–63, 2006.

[241] V. Escax, A. Bleuzen, J. P. Itié, P. Munsch, F. Varret, and M. Verdaguer, *J. Phys. Chem. B*, vol. 107, no. 20, pp. 4763–4767, 2003.

[242] R. J. Angel, "Equations of state," in *High-Temperature and High-Pressure Crystal Chemistry*, vol. 41, Mineralogical Society of America, 2000, pp. 35–59.

[243] F. J. Manjón and D. Errandonea, *Phys. Status Solidi B-Basic Solid State Phys.*, vol. 246, pp. 9–31, 2009.

[244] S. Naghavi, S. Chadov, C. Felser, G. H. Fecher, J. Kübler, K. Doll, and M. Jansen, *Phys. Rev. B*, vol. 85, no. 20, p. 205125, 2012.

[245] J. Arvanitidis, K. Papagelis, S. Margadonna, K. Prassides, and A. N. Fitch, *Nature*, vol. 425, no. 6958, pp. 599–602, 2003.

[246] E. Özdaş, A. R. Kortan, N. Kopylov, A. P. Ramirez, T. Siegrist, K. M. Rabe, H. E. Bair, S. Schuppler, and P. H. Citrin, *Nature*, vol. 375, no. 6527, pp. 126–129, 1995.

[247] Y. Yoshinari, H. Alloul, V. Brouet, G. Kriza, K. Holczer, and L. Forro, *Phys. Rev. B*, vol. 54, no. 9, pp. 6155–6166, 1996.

[248] H. Alloul, K. Holczer, Y. Yoshinari, and O. Klein, *Phys. C Supercond.*, vol. 235–240, pp. 2509–2510, 1994.

A. Appendix

High-resolution synchrotron X-ray powder diffraction data were collected for fcc-structured $K_xCs_{3-x}C_{60}$ compositions under variable temperature and pressure conditions, as described in detail in Chapter 3. Due to space limitations, only representative data were included in Chapter 3, and thus further data for the remaining compositions will be presented in this Appendix.

I. Ambient-pressure synchrotron X-ray powder diffraction

The observed, calculated and difference profiles and the derived structural parameters for fcc-structured $K_xCs_{3-x}C_{60}$ compositions obtained from the Rietveld analysis of synchrotron XRPD data are presented in the following figures and tables, as summarised in table below. Analogous data at 300 K for samples with K-content of $x_K = 0.64(1)$ and $x_K = 1.28(1)$ (Table 3.1 and Figure 3.5), and at 10 K for compositions with K-content of $x_K = 0.64(1)$ and $x_K = 0.87(1)$ (Table 3.5 and Figure 3.10) were provided in section 3.3.2 and section 3.3.3, respectively.

Figure	Table	K-content, x_K	XRPD data collection temperature
Figure A.1	Table A.1	0.22(1) 0.53(1)	300 K
Figure A.2	Table A.2	0.87(1)	300 K
Figure A.3	Table A.3	1.626(4) 2	300 K
Figure A.4	Table A.4	0.35(1)	40 K 300 K
Figure A.5	Table A.5	1.28(1)	100 K 300 K

The description of the models employed for the Rietveld analysis of the ambient-pressure XRPD data collected at 300 K and at low-temperature was provided in section 3.3.2 and 3.3.3, respectively.
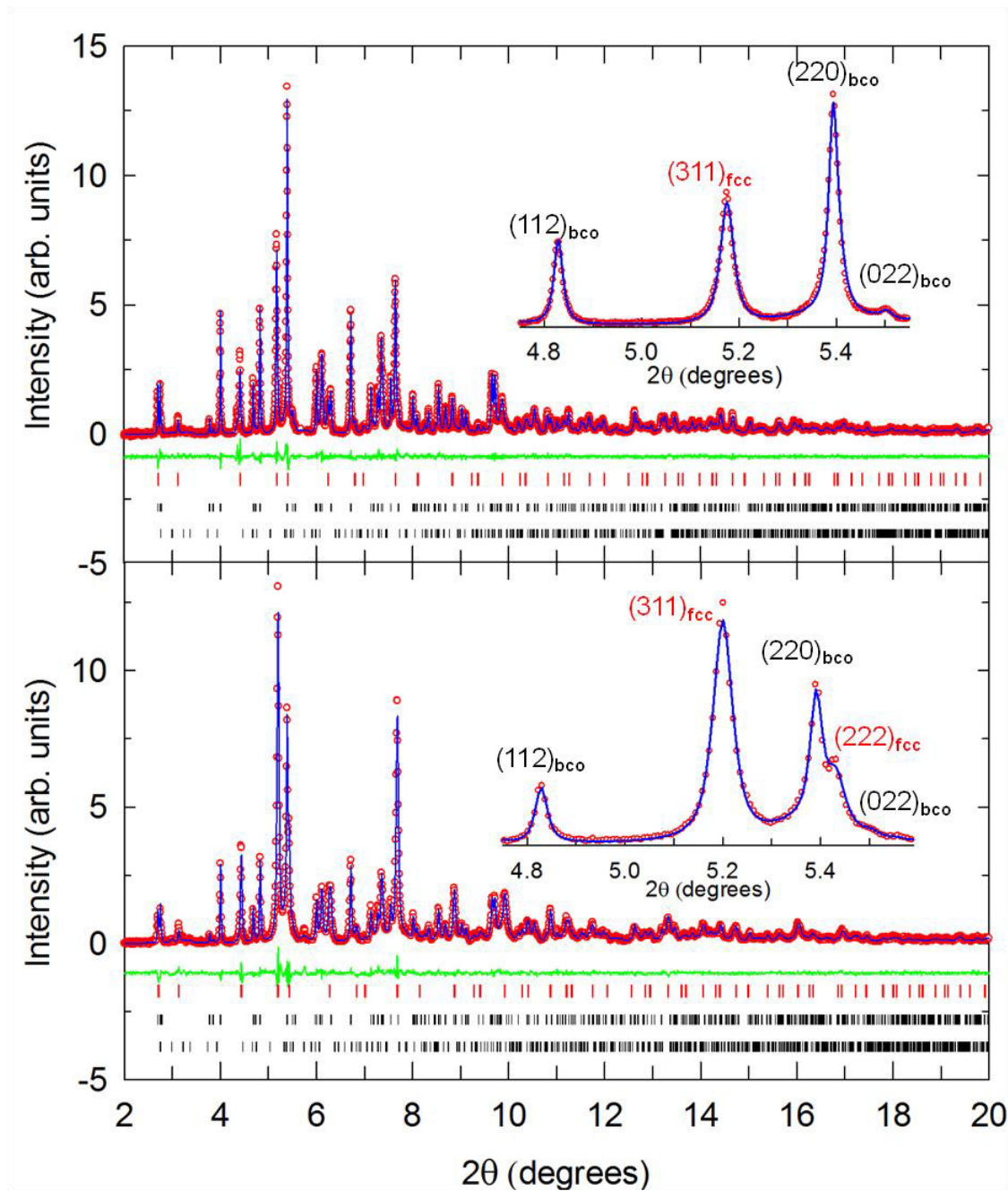
Figure A.1 Rietveld fits to synchrotron XRPD data collected at 300 K for fcc-structured $K_xCs_{3-x}C_{60}$ samples with K-content of $x_K = 0.22(1)$ (upper panel, $\lambda = 0.39999$ Å), and of $x_K = 0.53(1)$ (lower panel, $\lambda = 0.39984$ Å). Red circles, blue lines and green lines represent the observed, calculated and difference profiles. Ticks mark the reflection positions, from top-to-bottom, of co-existing fcc (red ticks), body-centered-orthorhombic (bco) and CsC_{60} phases. Both insets display expanded regions of the respective diffraction profiles; observed Bragg peaks are labelled by their (*hkl*) Miller indices.

Table A.1 Refined structural parameters for fcc-structured $K_xCs_{3-x}C_{60}$ samples with K-content of x_K = 0.22(1) and 0.53(1), from Rietveld analysis of synchrotron XRPD data collected at 300 K, with wavelengths of 0.39999 Å and 0.39984 Å, respectively (see Table 3.3 for details). Site multiplicities are listed in column M. Values in parentheses are estimated errors from the least-squares fitting. As detailed in section 3.3.2, the C–C bond lengths of the C_{60} units were kept fixed at 1.42 Å. The fractional cation occupancies, N of the tetrahedral interstitial site were refined (for details see the sub-section of Chapter 3 titled as '*Fractional site occupancy studies at 300 K*'). The weighted-profile and expected R-factors are R_{wp} = 4.9% and R_{exp} = 3.4% (x_K = 0.22(1)), and R_{wp} = 4.11% and R_{exp} = 2.96% (x_K = 0.53(1)), respectively. The lattice constants for x_K = 0.22(1) and 0.53(1) are 14.7011(2) Å and 14.6262(5) Å, respectively. The co-existing phase fractions for x_K = 0.22(1) are fcc = 31.5(2)%, Cs_4C_{60} = 52.69(7)% and CsC_{60} = 14.9(2)%, and for x_K = 0.53(1) are fcc = 54.0(2)%, Cs_4C_{60} = 29.9(2)% and CsC_{60} = 16.1(3)%.

| x_K =0.22(1)	x/a	y/b	z/c	M	N	B_{iso} (Å²)
K	0.25	0.25	0.25	8	0.109(6)	1.28(2)
Cs(1)	0.25	0.25	0.25	8	0.891(6)	1.28(2)
Cs(2)	0.5	0.5	0.5	4	1.0	5.82(4)
C(1)	0	0.048357	0.234528	96	0.5	0.29(5)
C(2)	0.204709	0.078176	0.096518	192	0.5	0.29(5)
C(3)	0.174695	0.156254	0.048357	192	0.5	0.29(5)
x_K =0.53(1)	x/a	y/b	z/c	M	N	B_{iso} (Å²)
K	0.25	0.25	0.25	8	0.263(6)	1.17(3)
Cs(1)	0.25	0.25	0.25	8	0.737(6)	1.17(3)
Cs(2)	0.5	0.5	0.5	4	1.0	5.60(4)
C(1)	0	0.048605	0.235729	96	0.5	0.71(4)
C(2)	0.205758	0.078576	0.097013	192	0.5	0.71(4)
C(3)	0.175589	0.157054	0.048605	192	0.5	0.71(4)
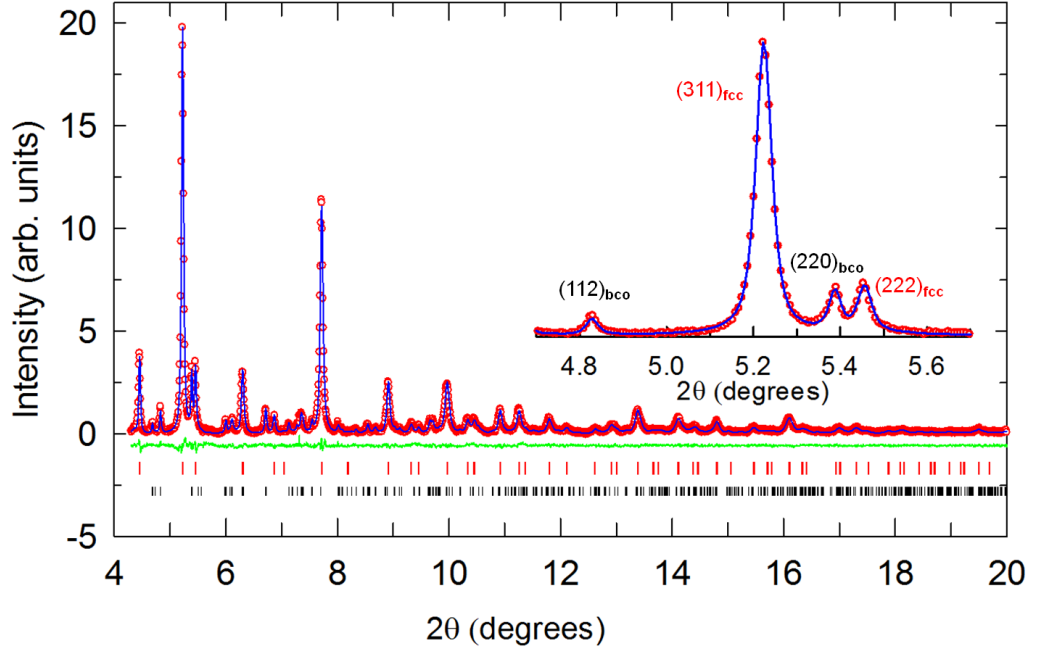
Figure A.2 Rietveld fits to synchrotron XRPD data collected at 300 K for fcc-structured $K_xCs_{3-x}C_{60}$ composition with K-content of $x_K = 0.87(1)$ ($\lambda = 0.39984$ Å). Red circles, blue lines and green lines represent the observed, calculated and difference profiles. Ticks mark the reflection positions of co-existing fcc (red ticks), and body-centered-orthorhombic (bco) phases. Both insets display expanded regions of the respective diffraction profiles; observed Bragg peaks are labelled by their (hkl) Miller indices.

Table A.2 Refined structural parameters for fcc-structured $K_xCs_{3-x}C_{60}$ sample with K-content of $x_K = 0.87(1)$ from Rietveld analysis of synchrotron XRPD data collected at 300 K, with wavelength of 0.39984 Å. Site multiplicities are listed in column M. Values in parentheses are estimated errors from the least-squares fitting. The weighted-profile and expected R-factors are $R_{wp} = 3.55\%$ and $R_{exp} = 2.60\%$, respectively. The fcc lattice constant is 14.5576(2) Å. The fractions of the co-existing fcc and Cs_4C_{60} phases are 85.18(7)% and 14.8(1)%, respectively.

| $x_K =0.87(1)$	x/a	y/b	z/c	M	N	B_{iso} (Å²)
K	0.25	0.25	0.25	8	0.435(6)	1.09(3)
Cs(1)	0.25	0.25	0.25	8	0.565(6)	1.09(3)
Cs(2)	0.5	0.5	0.5	4	1.0	4.59(5)
C(1)	0	0.048834	0.236840	96	0.5	0.57(5)
C(2)	0.206727	0.078947	0.097470	192	0.5	0.57(5)
C(3)	0.176417	0.157794	0.048834	192	0.5	0.57(5)
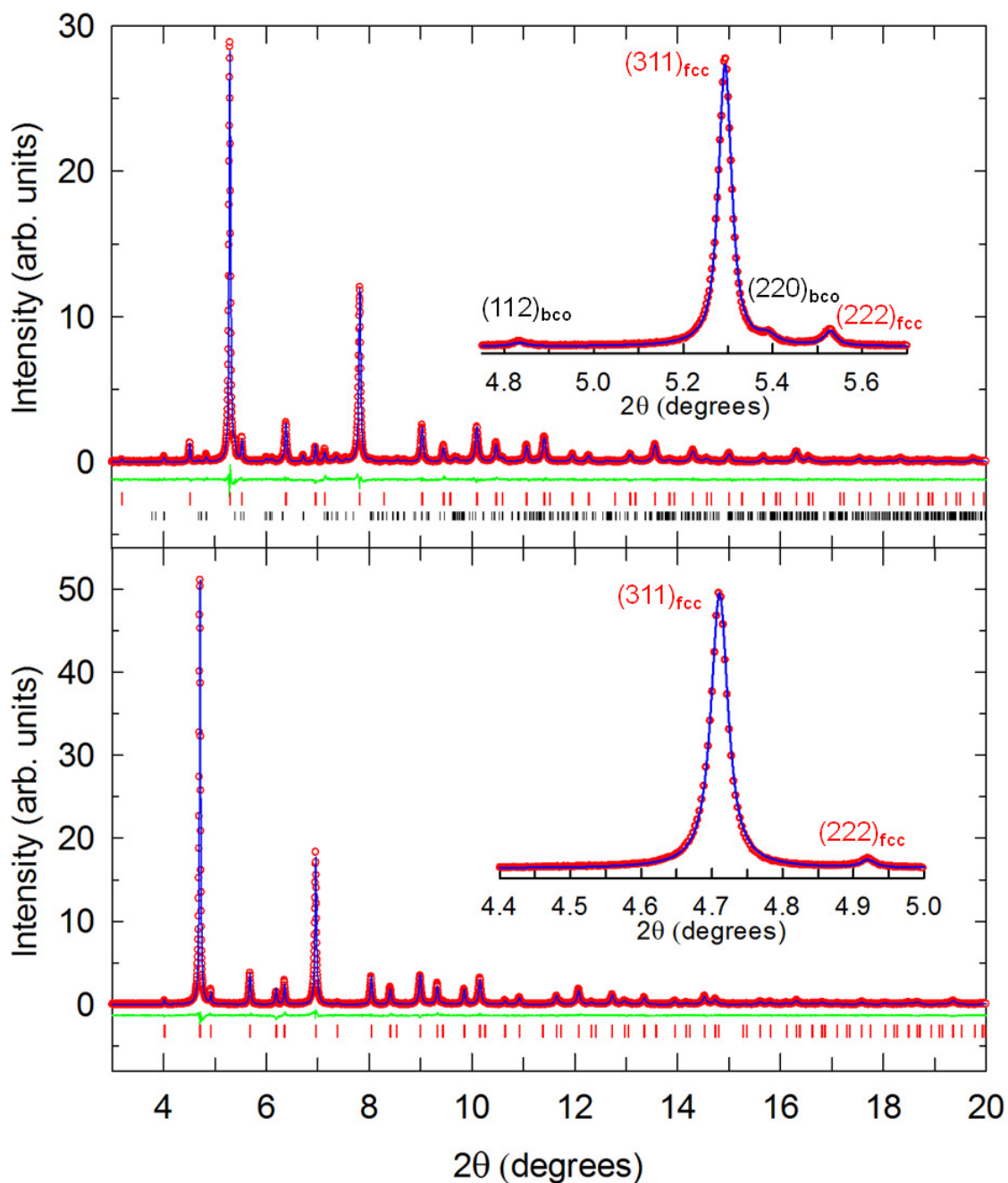
Figure A.3 Rietveld fits to synchrotron XRPD data collected at 300 K for fcc-structured $K_xCs_{3-x}C_{60}$ samples with refined K-content of x_K = 1.626(4) (upper panel, λ = 0.39996 Å) and with nominal K-content of x = 2 (refined x_K = 1.996(6)) (lower panel, λ = 0.35419 Å). Red circles, blue lines and green lines represent the observed, calculated and difference profiles. Ticks mark the reflection positions of co-existing fcc (red ticks), and body-centered-orthorhombic (bco) (black ticks, only observable in x_K = 1.626(4)) phases. Both insets display expanded regions of the respective diffraction profiles; observed Bragg peaks are labelled by their (*hkl*) Miller indices.

Table A.3 Refined structural parameters for fcc-structured $K_xCs_{3-x}C_{60}$ samples with K-content of $x_K = 1.626(4)$ and with nominal K-content of $x_K = 2$ (refined to $x_K = 1.996(6)$, single fcc phase), from Rietveld analysis of synchrotron XRPD data collected at 300 K, with wavelengths of 0.39996 Å and 0.35419 Å, respectively. Site multiplicities are listed in column M. Values in parentheses are estimated errors from the least-squares fitting. The R-factors are: $R_{wp} = 4.55\%$ and $R_{exp} = 3.41\%$ ($x_K = 1.626(4)$), and $R_{wp} = 3.76\%$ and $R_{exp} = 2.74\%$ ($x_K = 2$). The lattice constants for $x_K = 1.626(4)$ and $x = 2$ are 14.37345(8) Å and 14.28571(7) Å, respectively. The fractions of the co-existing fcc and Cs_4C_{60} phases for $x_K = 1.626(4)$ are 94.05(1)% and 5.95(7)%, respectively.

$x_K = 1.626(4)$	x/a	y/b	z/c	Site	N	B_{iso} (Å²)
K	0.25	0.25	0.25	8	0.813(3)	1.19(2)
Cs(1)	0.25	0.25	0.25	8	0.187(3)	1.19(2)
Cs(2)	0.5	0.5	0.5	4	1.0	3.31(1)
C(1)	0	0.049460	0.239874	96	0.5	0.46(5)
C(2)	0.209376	0.079958	0.098719	192	0.5	0.46(2)
C(3)	0.178677	0.159816	0.049460	192	0.5	0.46(2)
$x_K = 2$	x/a	y/b	z/c	M	N	B_{iso} (Å²)
K	0.25	0.25	0.25	8	1.0	0.99(1)
Cs	0.5	0.5	0.5	4	1.0	2.85(1)
C(1)	0	0.049763	0.241348	96	0.5	0.37(1)
C(2)	0.210662	0.080449	0.099325	192	0.5	0.37(1)
C(3)	0.179774	0.160797	0.049763	192	0.5	0.37(1)
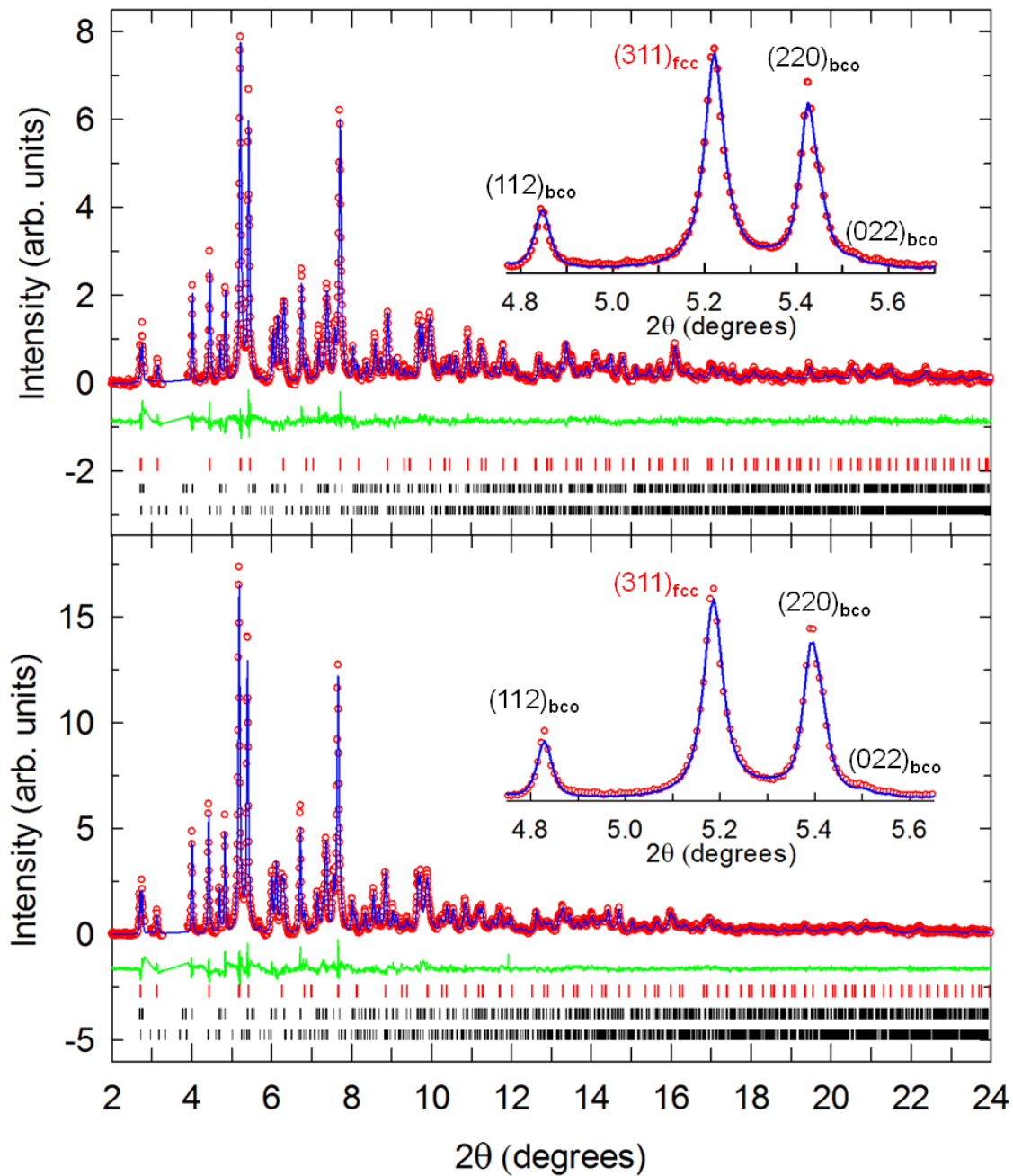
Figure A.4 Rietveld fits to synchrotron XRPD data collected at 40 K (upper panel) and 300 K (lower panel) for fcc-structured $K_xCs_{3-x}C_{60}$ sample with K-content of $x_K = 0.35$ ($\lambda = 0.39999$ Å). Red circles, blue lines and green lines represent the observed, calculated and difference profiles. Ticks mark the reflection positions, from top-to-bottom, of co-existing fcc (red ticks), body-centered-orthorhombic (bco) and CsC_{60} phases. Both insets display expanded regions of the respective diffraction profiles; observed Bragg peaks are labelled by their (hkl) Miller indices. Two broad peaks arising from the cryostat were visible at low angles (<4°), and these regions were excluded from the fitting.

Table A.4 Refined structural parameters for fcc-structured $K_xCs_{3-x}C_{60}$ sample with K-content of $x_K = 0.35$ from Rietveld analysis of synchrotron XRPD data collected at 40 K and 300 K, with wavelength of 0.39999 Å. Site multiplicities are listed in column *M.* The fractional site occupancies, *N* of the tetrahedral site were fixed to values obtained from the analysis of 300 K high statistics data. Values in parentheses are estimated errors from the least-squares fitting. The *R*-factors are $R_{wp} = 5.41\%$ and $R_{exp} = 3.52\%$ at 40 K, and $R_{wp} = 5.34\%$ and $R_{exp} = 4.47\%$ at 300 K. The lattice constants are 14.5762(3) Å at 40 K and 14.6736(2) Å at 300 K. The fractions of the co-existing fcc, Cs_4C_{60}, and CsC_{60} phases at 300 K are 53.0(2)%, 40.9(2)%, and 5.7(3), respectively: the relative phase fractions at 40 K were fixed to these values.

T = 40 K	x/a	y/b	z/c	M	N	B_{iso} (Å^2)
K	0.25	0.25	0.25	8	0.176	0.72(3)
Cs(1)	0.25	0.25	0.25	8	0.824	0.72(3)
Cs(2)	0.5	0.5	0.5	4	1.0	1.45(5)
C(1)	0	0.048772	0.236537	96	0.5	0.03(6)
C(2)	0.206463	0.078846	0.097345	192	0.5	0.03(6)
C(3)	0.176191	0.157592	0.048772	192	0.5	0.03(6)
T = 300 K	x/a	y/b	z/c	M	N	B_{iso} (Å^2)
K	0.25	0.25	0.25	8	0.176(7)	1.36(2)
Cs(1)	0.25	0.25	0.25	8	0.824(7)	1.36(2)
Cs(2)	0.5	0.5	0.5	4	1.0	5.44(7)
C(1)	0	0.048448	0.234968	96	0.5	0.34(6)
C(2)	0.205093	0.078323	0.096699	192	0.5	0.34(6)
C(3)	0.175022	0.156547	0.048448	192	0.5	0.34(6)
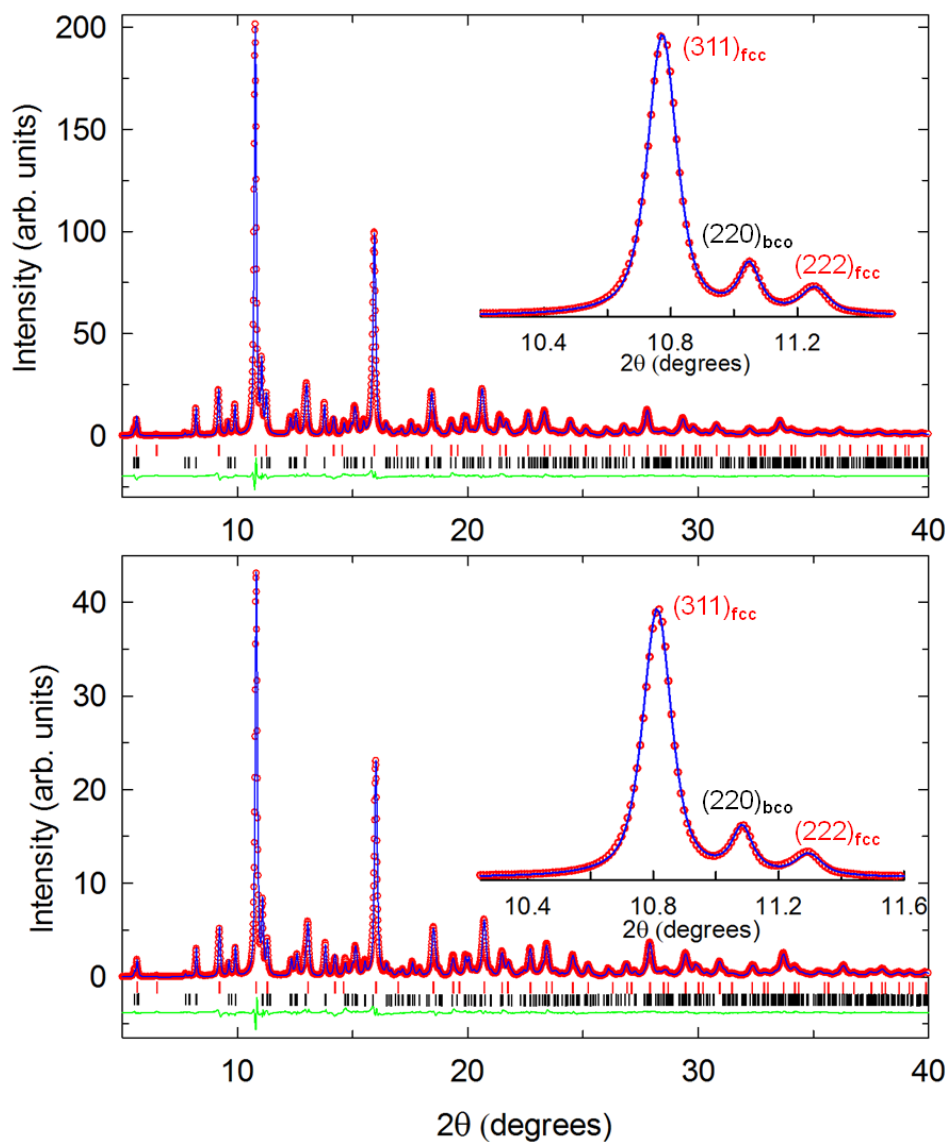
Figure A.5 Rietveld fits to synchrotron XRPD data collected at 300 K (upper panel) and 112 K (lower panel) on beamline BL44B2 for fcc-structured $K_xCs_{3-x}C_{60}$ sample with K-content of $x_K = 1.28$ ($\lambda = 0.81887$ Å). Red circles, blue lines and green lines represent the observed, calculated and difference profiles. Red and black ticks mark the reflection positions of co-existing fcc and body-centered-orthorhombic (bco) phases. Both insets display expanded regions of the respective diffraction profiles; observed Bragg peaks are labelled by their (hkl) Miller indices.

Table A.5 Refined structural parameters for fcc-structured $K_xCs_{3-x}C_{60}$ sample with K-content of $x_K = 1.28$ from Rietveld analysis of synchrotron XRPD data collected at 112 and 300 K, with wavelength of 0.81887 Å, on beamline BL44B2. Site multiplicities are listed in column M. The fractional site occupancies, N of the tetrahedral site were fixed to values obtained from the analysis of 300 K high statistics data collected on beamline ID31 with λ = 0.354197 Å. The fcc phase structural parameters obtained from the refinements and Rietveld fits to the XRPD data collected on beamline ID31 were shown in Table 3.1 and Figure 3.5, respectively. Values in parentheses are estimated errors from the least-squares fitting. The R-factors are R_{wp} = 3.9% and R_{exp} = 2.6% at 112 K, and R_{wp} = 3.3% and R_{exp} = 1.2% at 300 K. The lattice constants are 14.4006(3) Å at 112 K and 14.4614(1) Å at 300 K. The fractions of the co-existing fcc and Cs_4C_{60} phases at 300 K are 81.74(3)% and 18.3(1), respectively: the relative phase fractions at 112 K were fixed to these values (Relative phase fractions from the analysis of 300 K ID31 data were found as: fcc = 83.34(4)% and Cs_4C_{60} = 16.69(9)%).

T = 112 K	x/a	y/b	z/c	M	N	B_{iso} (Å^2)
K	0.25	0.25	0.25	8	0.641	0.26(1)
Cs(1)	0.25	0.25	0.25	8	0.359	0.26(1)
Cs(2)	0.5	0.5	0.5	4	1.0	1.89(1)
C(1)	0	0.049366	0.239422	96	0.5	0.18(2)
C(2)	0.208981	0.079807	0.098533	192	0.5	0.18(2)
C(3)	0.178340	0.159515	0.049366	192	0.5	0.18(2)
T = 300 K	x/a	y/b	z/c	M	N	B_{iso} (Å^2)
K	0.25	0.25	0.25	8	0.641	1.17(1)
Cs(1)	0.25	0.25	0.25	8	0.359	1.17(1)
Cs(2)	0.5	0.5	0.5	4	1.0	4.12(2)
C(1)	0	0.049159	0.238416	96	0.5	0.78(2)
C(2)	0.208103	0.079472	0.098118	192	0.5	0.78(2)
C(3)	0.177590	0.158844	0.049159	192	0.5	0.78(2)

II. High-pressure synchrotron X-ray powder diffraction at 7 K

Rietveld fits to the XRPD data for fcc-rich $K_{0.87}Cs_{2.13}C_{60}$ and $K_{1.28}Cs_{1.72}C_{60}$ (Figures 3.15 and 3.16) at low and high pressure, and the corresponding structural

parameters of fcc-structured $K_{0.87}Cs_{2.13}C_{60}$ (Table 3.6) were presented in section 3.3.5. Here the observed, calculated and difference profiles and the derived structural parameters for fcc $K_{0.35}Cs_{2.65}C_{60}$ obtained from the Rietveld analysis of synchrotron XRPD data are presented in Figure A.6 and Table A.6. Refined structural parameters of fcc-structured $K_{1.28}Cs_{1.72}C_{60}$ are presented in Table A.7.
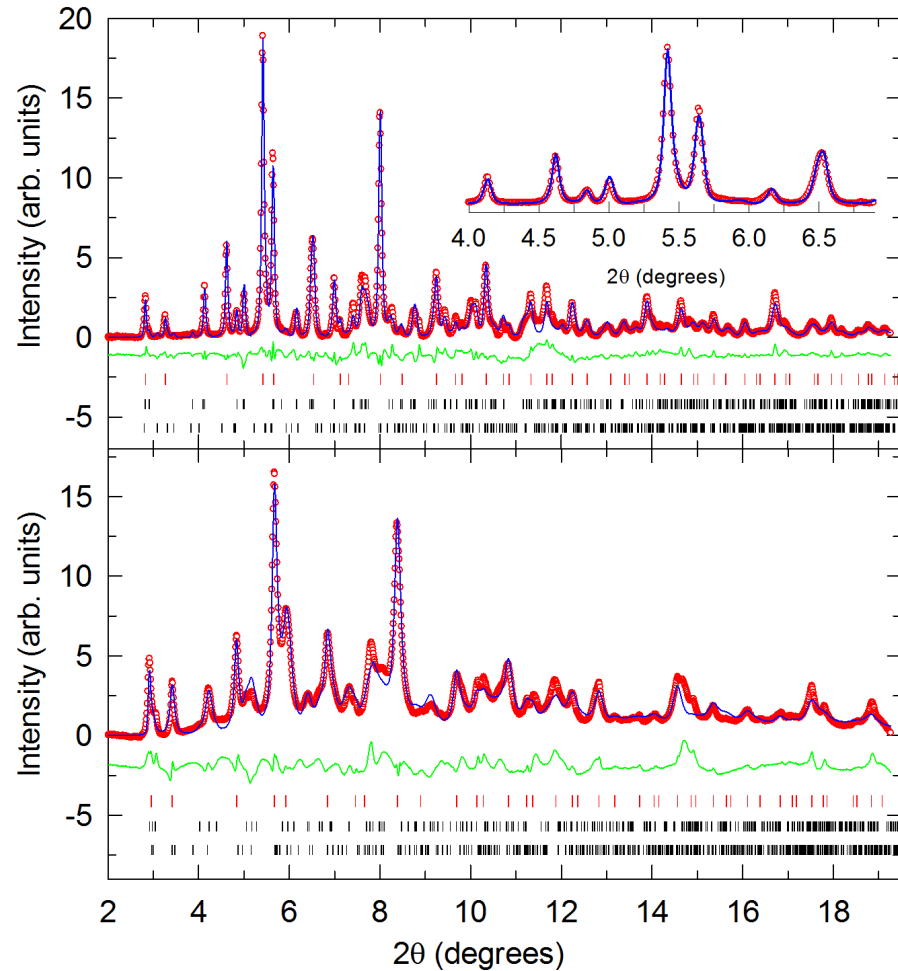

Figure A.6 Rietveld fits to high-pressure synchrotron XRPD data collected at 7 K for fcc $K_{0.35}Cs_{2.65}C_{60}$ at 0.6 GPa (upper panel) and 6.2 GPa (lower panel), with $\lambda = 0.41260$ Å. Red circles, blue lines and green lines represent the observed, calculated and difference profiles. Ticks mark the reflection positions, from top-to-bottom, of co-existing fcc (red ticks), body-centered-orthorhombic (bco) and CsC_{60} phases. Inset displays an expanded region of the respective diffraction profile. The fitted background contribution has been subtracted for clarity.

Table A.6 Refined structural parameters for fcc-structured $K_{0.35}Cs_{2.65}C_{60}$ from Rietveld analysis of synchrotron XRPD data collected at 7 K at 0.6 and 6.2 GPa ($\lambda = 0.41260$ Å). Values in parentheses are statistical errors from Rietveld refinement. The R-factors are $R_{wp} = 0.45\%$ and $R_{exp} = 0.45\%$ (at 0.6 GPa), and $R_{wp} = 0.78\%$ and $R_{exp} = 0.44\%$ (at 6.2 GPa). The lattice constants are 14.4742(4) Å at 0.6 GPa and 13.800(1) Å at 6.2 GPa. The fractions of the co-existing phases at 0.6 GPa are fcc = 54.3(1)%, $Cs_4C_{60} = 35.0(2)\%$ and $CsC_{60} = 10.7(4)\%$: the relative phase fractions were fixed to these values at all other

pressures. The fractional cation occupancies, N of the tetrahedral interstitial site were fixed to values refined from the 300 K ambient pressure data for the same sample, as described in section 3.3.5. Thermal displacement parameters were fixed to values refined from the 40 K ambient pressure data for the same sample, as with the data quality available these could not be meaningfully refined together with the profile shape parameters necessary to describe the pressure-induced peak broadening (the effect of pressure on isotropic thermal displacement parameters should be relatively small [1]).

$K_{0.35}Cs_{2.65}C_{60}$, $a_{7K, 0.6 GPa}$ = 14.4742(4) Å, fcc phase fraction: 54.3(1)%					
P = 0.6 GPa	x/a	y/b	z/c	N	B_{iso} (Å^2)
K	0.25	0.25	0.25	0.435	0.72
Cs(1)	0.25	0.25	0.25	0.565	0.72
Cs(2)	0.5	0.5	0.5	1.0	1.45
C(1)	0	0.049115	0.238205	0.5	0.03
C(2)	0.207919	0.079402	0.098032	0.5	0.03
C(3)	0.177433	0.158703	0.049115	0.5	0.03

$K_{0.35}Cs_{2.65}C_{60}$, $a_{7K, 6.2 GPa}$ = 13.800(1) Å					
P = 6.2 GPa	x/a	y/b	z/c	N	B_{iso} (Å^2)
K	0.25	0.25	0.25	0.435	0.72
Cs(1)	0.25	0.25	0.25	0.565	0.72
Cs(2)	0.5	0.5	0.5	1.0	1.45
C(1)	0	0.051515	0.249842	0.5	0.03
C(2)	0.218076	0.083281	0.102821	0.5	0.03
C(3)	0.186102	0.166457	0.051515	0.5	0.03

[1] R. M. Hazen, R. T. Downs, and C. T. Prewitt, "Principles of comparative crystal chemistry," in *High-Temperature and High-Pressure Crystal Chemistry*, vol. 41, Mineralogical Society of America, 2000, pp. 1–33.

Table A.7 Structural parameters for the majority fcc phase of $K_{1.28}Cs_{1.72}C_{60}$ extracted from Rietveld analysis of synchrotron XRPD data collected at 7 K at 0.3 and 9.8 GPa (λ = 0.41238 Å). The fractional site occupancies, N of the tetrahedral site were fixed to values obtained from the analysis of 300 K high statistics data, as described earlier (Table 3.3). Values in parentheses are statistical errors from Rietveld refinement. The R-factors are: R_{wp} = 0.42% and R_{exp} = 0.39% (at 0.3 GPa), and R_{wp} = 0.44% and R_{exp} = 0.41% (at 9.8 GPa). Refined fcc and bco phase fractions at 0.3 GPa are 82.739(3)% and 17.26(1)%,

respectively. The thermal displacement parameters of the C atoms could not refine to physically meaningful values, so were fixed to values of appropriate magnitude and of the tetrahedral and octahedral interstitial sites were only refined at 0.3 GPa and kept fixed to those values found at all other pressures.

$K_{1.28}Cs_{1.72}C_{60}$, $a_{7K, 0.3 GPa}$ = 14.3491(1) Å, fcc phase fraction: 82.739(3)%

P = 0.3 GPa	x/a	y/b	z/c	N	B_{iso} (Å^2)
K	0.25	0.25	0.25	0.64	0.52(3)
Cs(1)	0.25	0.25	0.25	0.36	0.52(3)
Cs(2)	0.5	0.5	0.5	1.0	0.93(3)
C(1)	0	0.04954	0.24028	0.5	0.13
C(2)	0.20973	0.08009	0.09889	0.5	0.13
C(3)	0.17898	0.16009	0.04954	0.5	0.13

$K_{1.28}Cs_{1.72}C_{60}$, $a_{7K, 9.8 GPa}$ = 13.5299(3) Å

P = 9.8 GPa	x/a	y/b	z/c	N	B_{iso} (Å^2)
K	0.25	0.25	0.25	0.64	0.52
Cs(1)	0.25	0.25	0.25	0.36	0.52
Cs(2)	0.5	0.5	0.5	1.0	0.93
C(1)	0	0.05254	0.25483	0.5	0.13
C(2)	0.22243	0.08494	0.10487	0.5	0.13
C(3)	0.18981	0.16978	0.05254	0.5	0.13

III. ^{133}Cs and ^{39}K NMR spectra of $A_xCs_{3-x}C_{60}$ compounds

The ^{133}Cs NMR spectra of selected $A_xCs_{3-x}C_{60}$ samples at 300 K, by our collaborators, are shown in Figure A7.
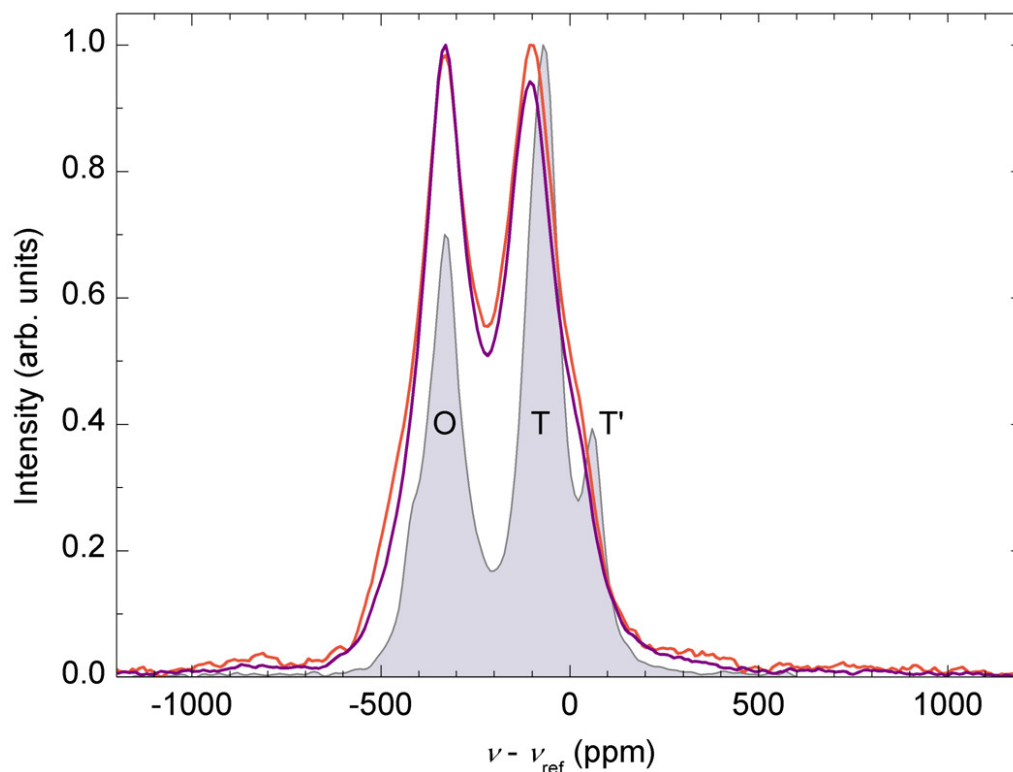

Figure A.7 The ^{133}Cs NMR spectra of $K_{0.53}Cs_{2.47}C_{60}$, $K_{0.64}Cs_{2.37}C_{60}$ and $Rb_{0.35}Cs_{2.65}C_{60}$ at 300 K presented with red, purple and gray lines, respectively. O, T and T' represent the octahedral and tetrahedral fcc interstitial site peaks, respectively. Whilst overexpanded $Rb_{0.35}Cs_{2.65}C_{60}$ shows a very clear splitting of the tetrahedral sites, T' peak is almost invisible for samples of $x_K = 0.53$ and 0.64, showing only a broad hump on the T line, consistent with the previous NMR results of K_3C_{60}. This behaviour can be ascribed to an increased distortion in the $K_xCs_{3-x}C_{60}$ system compared to the $Rb_xCs_{3-x}C_{60}$ due to the greater cation size variance at the tetrahedral sites.

The ^{39}K NMR measurements were also performed on selected K$_x$Cs$_{3-x}$C$_{60}$ compounds at 300 K, including K$_3$C$_{60}$; in addition, the temperature dependence of ^{39}K line-shape for K$_2$CsC$_{60}$ was investigated at temperatures between 100 and 300 K (Figure A8).

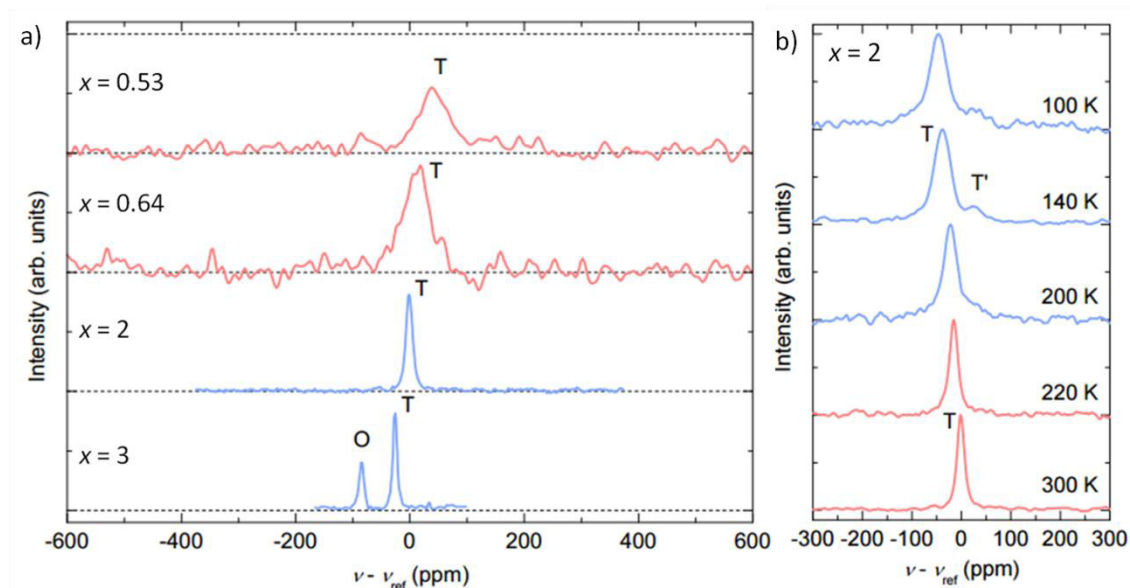Figure A.8 a) The ^{39}K NMR spectra of K$_x$Cs$_{3-x}$C$_{60}$ samples at 300 K. b) Temperature dependence of ^{39}K NMR spectrum of K$_2$CsC$_{60}$. O, T and T' represent the octahedral and tetrahedral fcc interstitial site peaks, respectively. For K$_3$C$_{60}$, only O and T lines are apparent at 300 K, consistent with previous NMR measurements [247], and no O and T' lines are apparent for any of K$_x$Cs$_{3-x}$C$_{60}$ samples, indicating K$^+$ cations only reside in the tetrahedral sites, and the octahedral site is fully occupied only by Cs. Temperature dependence of the ^{39}K line-shape for K$_2$CsC$_{60}$ reveals that, the T' line is clearly resolved below 200 K on the NMR timescale where molecular rotational motion freezes as well. In the complementary ^{39}K NMR spectra of K$_3$C$_{60}$, only an asymmetric broadening of the T line could be detected at low temperatures without really seeing a resolved T' line [247], [248].